



HAL
open science

The formation of multimetallic molecular nanocontainers

Ivan Khariushin

► **To cite this version:**

Ivan Khariushin. The formation of multimetallic molecular nanocontainers. Other. Université de Strasbourg; Kazanskij gosudarstvennyj universitet im. V. I. Ul'janova (Kazan), 2023. English. NNT : 2023STRAF020 . tel-04225723

HAL Id: tel-04225723

<https://theses.hal.science/tel-04225723>

Submitted on 3 Oct 2023

HAL is a multi-disciplinary open access archive for the deposit and dissemination of scientific research documents, whether they are published or not. The documents may come from teaching and research institutions in France or abroad, or from public or private research centers.

L'archive ouverte pluridisciplinaire **HAL**, est destinée au dépôt et à la diffusion de documents scientifiques de niveau recherche, publiés ou non, émanant des établissements d'enseignement et de recherche français ou étrangers, des laboratoires publics ou privés.

ÉCOLE DOCTORALE DES SCIENCES CHIMIQUE
UMR 7140, Chimie de la matière complexe

THÈSE présentée par :
Ivan KHARIUSHIN

soutenue le : 8 juin 2023

pour obtenir le grade de : **Docteur de l'université de Strasbourg**
Discipline/ Spécialité : Chimie supramoléculaire

**Formation de nanocontainers multimétalliques
moléculaires**

THÈSE dirigée par :

Pr. FERLAY Sylvie
Pr. BULACH Véronique

Professeur, Université de Strasbourg
Professeur, Université de Strasbourg

Co-directeurs :

Dr. OVSYANNIKOV Alexander
Pr. ANTIPIIN Igor

Chargé de recherche, Kazan Federal University
Professeur, Kazan Federal University

RAPPORTEURS :

Dr. GOEB Sébastien
Pr. THERRIEN Bruno

Directeur de recherches, Université d'Angers
Professeur, Université de Neuchâtel

AUTRES MEMBRES DU JURY :

Pr. GIUSEPPONE Nicolas

Professeur, Université de Strasbourg

Table of contents

Acknowledgements	7
Résumé	9
Chapter I. Introduction	17
I. Historical review of covalent and coordination cage	19
I.1. Crown-ethers of Pedersen	19
I.2. Cryptands of Dietrich, Lehn and Sauvage	20
I.3. Macrooligocycle of Kiggen.....	20
I.4. Quan's hemicarcerand capable to encapsulate organic molecules.....	21
I.5. The first metal-organic cages and their development through decades	22
II. Non-calixarene MOCs: classification and properties	26
II.1. Strategies for synthetic approaches.....	26
II.2. Geometrical analysis	28
II.3. Reported properties of MOCs.....	33
III. Calixarene-based MOCs.....	38
III.1. Generalities on calix[4]arene.....	38
III.2. First calixarene-based metal-organic cage	39
III.3. Calixarene-based MOCs: formation and synthesis	40
III.4. Calixarene-based MOCs: geometry.....	42
III.5. Calixarene-based MOCs based on organic connectors: properties	46
III.6. Calixarene-based MOC with Metal-Organic connectors	53
IV. Conclusion.....	55
V. Presentation of the scientific project.....	56
Chapter II. Synthesis of the connectors	57
I. Generalities.....	59
II. Dipyrin-based metal-organic connectors family	62
II.1. Triangular and linear dipyrin connectors.....	62
II.2. Synthesis of racemic triangular tris(dipyrin) connectors ($\text{rac-M}(\text{HL}_1)_3$, $\text{rac-Co}(\text{HL}_2)_3$)	66
II.3. Chiral resolution of the triangular connector $\text{rac-M}(\text{HL}_1)_3$ ($\Lambda\text{-M}(\text{HL}_1)_3$ and $\Delta\text{-M}(\text{HL}_1)_3$)	70
II.4. The synthesis of linear dipyrin connectors ($\text{Pd}(\text{HL}_1)_2$, $\text{Ni}(\text{H}_2\text{L}_3)$).....	73
III. Phenanthroline-based metal-organic connector.....	77
III.1. Complexes of phenanthroline: review	77

III.1. Phenanthroline connector: size, geometry and properties	78
III.2. The synthesis of triangular phenanthroline connector ($[\text{rac-Fe}(\text{HL}_4)_3][\text{PF}_6]_2$).....	79
IV. Terpyridine-based metal-organic connectors family.....	81
IV.1. Terpyridine complexes: review	81
IV.2. Linear terpyridine connectors: properties, size and geometry	82
IV.3. The synthesis of linear terpyridine connectors ($[\text{M}(\text{HL}_5)_2][\text{PF}_6]_2$)	83
V. Porphyrin-based metal-organic connector.....	85
V.1. Porphyrin macrocycles: review	85
V.2. Porphyrin connector: size, geometry and properties	86
V.3. The synthesis of the linear porphyrin connector ($\text{Ni}(\text{H}_2\text{L}_6)$)	88
VI. Corrole-based metal-organic connector	90
VI.1. Corrole macrocycle: review	90
VI.2. Corrole connector: size, geometry and properties.....	90
VI.3. The synthesis of triangular corrole connector ($\text{Co}(\text{H}_3\text{L}_7)$).....	91
VII. Organic connectors	93
VII.1. Triazine core: review	94
VII.2. Triazine connectors: size, geometry and properties.....	95
VII.3. The synthesis of triangular 1,3,5-triazine connectors (H_3L_8 , H_3L_9 , H_3L_{10})	96
VII.4. 1,3,5-trifluorobenzene connector: size, geometry and properties.....	97
VII.5. The synthesis of triangular 1,3,5-trifluorobenzene connector (H_3L_{11})	98
VIII. Conclusion	100
Chapter III. Formation and structural investigations of MOCs.....	103
I. Synthesis of crystalline molecular cages.....	105
I.1. Determination of the synthetic conditions	106
I.2. Synthesis of crystalline cages using metal-organic connectors	111
I.3. Synthesis of crystalline cages using organic connectors (H_3L_8 - H_3L_{11})	115
II. Structural investigation of racemic dipyrin-based MOCs: XRD analysis.....	116
II.1. Crystalline data	116
II.2. Metal environment.....	118
II.3. Cages metrics	119
II.4. Packing of the dipyrin-based MOCs in the unit cell	122
III. Structural investigation of chiral dipyrin-based MOCs: XRD analysis.....	124
IV. Additional characterizations techniques for dipyrin-based MOCs	125
IV.1. CD and chiral HPLC of enantiomerically pure cages	126
IV.2. MS characterization in solution.....	127
IV.3. XRPD in the solid state for racemic cages	129

IV.4. TGA measurements and IR analysis of the racemic cages	130
IV.5. Conclusion.....	131
V. Structural investigation of MOCs based on organic connectors	133
V.1. Crystalline data for $[M_4SO_2TCA(\mu_4-OH_2)]_6[L_8]_8$ ($M = Co^{II}, Ni^{II}$)	133
V.2. Cages metrics.....	134
V.3. Packing of the Cages	135
V.4. TGA and IR for triazine-based MOCs.....	136
VI. Conclusion.....	138
Chapter IV. Gas adsorption properties of synthesized calixarene-based MOCs	139
I. Generalities.....	141
I.1. Context of the study	141
I.2. The performed measurements on the synthesized MOCs	142
I.3. Activation of samples.....	143
II. Adsorption properties of triazine-based MOC.....	144
II.1. Behaviour of the sample after activation	144
II.2. $N_{2(g)}$ adsorption and surface area evaluation.....	146
II.3. CO_2 adsorption.....	148
III. Adsorption properties of dipyrin-based MOCs.....	149
III.1. Behaviour of the samples after activation	149
III.2. $N_{2(g)}$ adsorption and surface area investigation	152
III.3. Adsorption of other small molecules.....	156
III.4. Estimation of gas adsorption selectivity.....	159
IV. Conclusion.....	162
General conclusion	163
I. Results of the work.....	165
II. Perspectives for this work.....	166
II.1. Improvement of the synthesis for the formation of MOCs.....	166
II.2. Further investigation of gas adsorption properties of the reported MOCs	167
II.3. Investigation of catalytic properties.....	167
II.4. Investigation of the molecular recognition properties	168
II.5. Other properties	168
Experimental part	171
I. Synthesis of calixarenes	178

I.1. Synthesis of (5,26,27,28-tetrahydroxy-5,11,17,23-tetra-tert-butyl-2,8,14,20-tetrasulfonyl[4]arene (H ₄ SO ₂ TCA)	178
II. Synthesis of connectors.....	179
II.1. Synthesis of dipyrin connectors.....	179
II.2. Synthesis of phenanthroline connector	197
II.3. Synthesis of terpyridine connectors	200
II.4. Synthesis of porphyrin connector	204
II.5. Synthesis of corrole connector.....	207
II.6. Synthesis of organic connectors.....	210
III. Synthesis of MOCs in the crystalline form	215
Solvothermal technique	215
Liquid-liquid diffusion technique	215
[Co ₄ SO ₂ TCA] ₆ [rac-Co(L ₁) ₃] ₈ •nDMF•mH ₂ O	216
[Ni ₄ SO ₂ TCA] ₆ [rac-Co(L ₁) ₃] ₈ •nDMF•mH ₂ O	217
[Co ₄ SO ₂ TCA] ₆ [Λ-Co(L ₁) ₃] ₈ •nDMF•mH ₂ O	218
[Co ₄ SO ₂ TCA] ₆ [Δ-Co(L ₁) ₃] ₈ •nDMF•mH ₂ O.....	219
[Ni ₄ SO ₂ TCA] ₆ [Λ-Co(L ₁) ₃] ₈ •nDMF•mH ₂ O	220
[Ni ₄ SO ₂ TCA] ₆ [Δ-Co(L ₁) ₃] ₈ •nDMF•mH ₂ O	221
[Co ₄ SO ₂ TCA] ₆ [rac-Fe(L ₁) ₃] ₈ •nDMF•mH ₂ O	222
[Ni ₄ SO ₂ TCA] ₆ [rac-Fe(L ₁) ₃] ₈ •nDMF•mH ₂ O.....	223
[Co ₄ SO ₂ TCA] ₆ [rac-Rh(L ₁) ₃] ₈ •nDMF•mH ₂ O	224
[Ni ₄ SO ₂ TCA] ₆ [rac-Rh(L ₁) ₃] ₈ •nDMF•mH ₂ O	225
[Co ₄ SO ₂ TCA] ₆ [L ₈] ₈ •nDMF•mH ₂ O	226
[Ni ₄ SO ₂ TCA] ₆ [L ₈] ₈ •nDMF•mH ₂ O	227
References	229
Annexes.....	247
I. Crystallographic part.....	249
I.1. Crystallographic data of MOCs.....	249
I.2. Crystallographic data of metallocalixarenes	256
I.3. Crystallographic data of metal-organic complexes	258
II. Gas adsorption	259
II.1. Isotherms fit by virial equation	259
II.2. Calculations of Henry constants	261
II.3. Calculations of heats of adsorption.....	261
II.4. Calculations of IAST selectivity of adsorption.....	262

Acknowledgements

That is really hard to express my gratitude to all the people helped me during this PhD work. That was tough, but nevertheless, happy time.

I thank Pr. Sébastien Goeb, Pr. Bruno Therrien and Pr. Nicolas Giuseppone for kindly accepting to be members of my thesis committee and their interest in my work. Their feedback and constructive criticism will help me to refine my research project further.

I grateful to the team of SFAM laboratory (Strasbourg University), who provided me with outstanding research resources and equipment necessary for my experiments. In addition, their support, guidance, and extremely friendly attitude was making me happy every hour I spent in the laboratory.

I would like to express my sincere thanks to the team at Laboratory of Calixarene Chemistry of Arbuzov IOPC (Kazan, Russia) And especially I would like to thank A. Ovsyannikov, I. Antipin and Z. Akhmetzyanova for their invaluable contribution to my chemistry education and opening me the way to this PhD project

I would like to thank Strasbourg University for providing me with a comprehensive research experience. I am also grateful to the University for its support for Russian and Ukrainian students during the darkest times of war.

I appreciate the contribution of collaborators to my work, without who this project could have not been possible. I am thankful to group of Pr. Kari Rissanen (Jyväskylä University, Finland), Dr. Elina Kalenius (Jyväskylä University, Finland) and group of Pr. V. Fedin (Nikolaev Institute of Inorganic Chemistry, Russia)

I would like to express my heartfelt gratitude to my friends for their unwavering support and encouragement throughout my research journey: Evgenii O., Jean-Baptist F., Jaison C., David P., Aleksei Sh., Aleksei D., Danil K., Mikhail M., Tagir Akh. Their companionship and encouragement have been a source of motivation throughout the problems during my doctoral program. Thanks to all international team of StrasAir: Rokas, Tatjana, Victoriia, Nizami, Teodor and Sven. I am deeply grateful to my partner Iryna, who has been a pillar of support throughout the hardest part of my doctoral program and whose constant support was making me go forwards during this time.

Finally, I would like to express my sincere thanks to my supervisors Pr. Sylvie Ferlay and Pr. Véronique Bulach. There are no words in the world to express my gratitude to you. Thank you for the guidance, scientific discussions, corrections, remarks, and encouragement. I truly appreciate the scientific experience you gave me and the constant support thorough these years. Separately, I want to thank you for your patience and will to work with me.

Lastly, I would like to thank my mother. Спасибо тебе, мама, за все твои старания и жертвы, вложенные в меня. Без тебя я бы никогда не поступил в лицей, затем в Казанский университет, а затем в Страсбургский. Без тебя я бы никогда не защитил эту научную степень. Спасибо за то, что открыла мне дорогу в жизнь и за постоянную самоотверженную поддержку в течение этих 26 лет.

Résumé

Introduction

Le domaine de recherche lié aux cages supramoléculaires est très actif, avec des applications dans les domaines de la catalyse, des matériaux ou du transport de molécules par exemple, ces assemblages ayant la capacité d'encapsuler et de libérer sélectivement des molécules invitées. Les cages supramoléculaires sont des structures auto-assemblées formées grâce à l'utilisation d'interactions non-covalentes entre les différents composants, telles que les liaisons hydrogène, les liaisons de coordination et les forces de van der Waals, etc.¹ Ces dernières années, on recense de nombreux progrès concernant la conception et la synthèse de cages supramoléculaires avec des tailles, des formes et des fonctionnalités contrôlables.

Une variété de cages supramoléculaires particulièrement intéressante est les Cages Métallo-Organiques (MOC). Les MOC sont généralement synthétisées par auto-assemblage d'ions métalliques et de ligands organiques (connecteurs), qui forment spontanément une structure auto-assemblée présentant la forme d'une cage. La taille, la géométrie ainsi que la capacité de coordination du centre métallique, de même que la nature et le nombre de ligands impliqués, peuvent être ajustés afin d'obtenir des MOC présentant des propriétés souhaitées.² Parmi tous les types de MOC reportés dans la littérature, on note des MOC construits à partir de macrocycles de type calixarène (calix[4]arène, thiacalix[4]arène et tetrasulfonylcalix[4]arène): ils combinent les propriétés structurales uniques inhérentes aux calixarènes et les propriétés fonctionnelles des ions métalliques et des ligands constituant la cage. Un avantage majeur de l'utilisation de calixarènes est, entre autre, leur grande stabilité thermique.³ En conséquence, les applications possibles des MOC à base de calixarènes ne sont pas limitées par la stabilité thermique des calixarènes, ce qui offre un large éventail d'applications, telles que la catalyse à haute température et le stockage de gaz. En outre, l'utilisation de connecteurs métallo-organiques au lieu de connecteurs purement organiques pour la synthèse de MOC à base de calixarène, ouvre de nouvelles possibilités d'applications, telles que la catalyse en espace confiné.⁴

Les MOC sont synthétisées au cours d'une réaction d'auto-assemblage entre des nœuds et des connecteurs qui forment une structure discrète et cohérente maintenue par des liaisons de coordination. De très nombreuses géométries des MOC résultants peuvent être observées : cubiques, octaédriques, tétraédriques, etc. Dans ce travail, des connecteurs linéaires et triangulaires ont été utilisés pour l'auto-assemblage de MOC, et nous nous sommes centrés sur la formation de MOC adoptant une géométrie octaédrique. Selon les connecteurs utilisés, il est possible d'obtenir différents types de cages. Dans le cas de l'utilisation d'un connecteur linéaire bidentate, un MOC



octaédrique de type "Edge-panelled" est obtenu, alors que dans le cas de l'utilisation d'un connecteur trigonal, un MOC octaédrique de type "Face-panelled" est observé, comme représenté en Figure 1.²

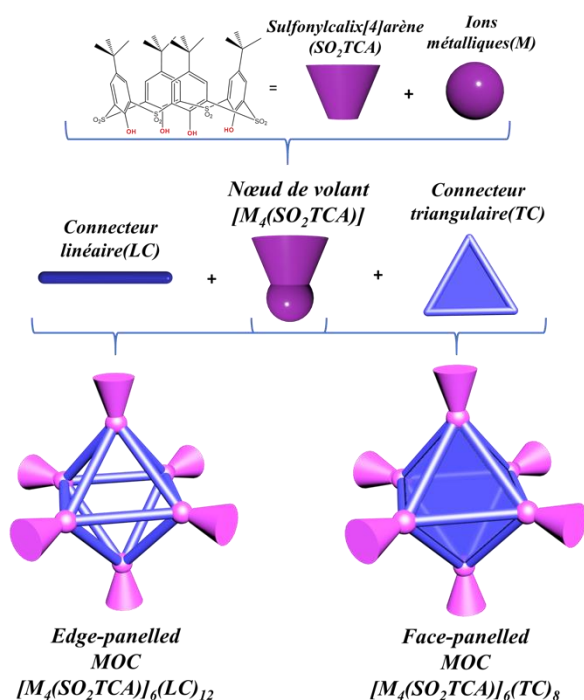


Figure 1 Les réactions d'auto-assemblage des ions métalliques, des connecteurs et des sulfonycalix[4]arènes pour la formation de MOC présentant une géométrie octaédrique

Pour la formation de MOC à base de l'entité calixarène, on utilise le plus souvent les thiacalix[4]arènes et les sulfonycalix[4]arènes, en raison de la présence d'atomes de soufre et d'atomes d'oxygène sur le macrocycle, ce qui leur confère de meilleures propriétés de coordination vis-à-vis des métaux et en fait des candidats parfaits pour la formation de MOC multimétalliques.

Ce travail, qui consiste en la formation et l'étude des propriétés des MOC à base de sulfonycalix[4]arènes et plus particulièrement en utilisant des connecteurs métallo-organiques. Cette approche a jusqu'à présent été très peu explorée. L'intérêt de tels MOC réside dans leur utilisation potentielle dans le stockage et la séparation de gaz en raison de la porosité inhérente des calixarènes et la formation de cages à larges cavités. De plus, la présence de connecteurs métallo-organiques permet d'envisager des applications potentielles de ces cages en catalyse.

Résultats et discussion

1) Choix et synthèse des nouveaux connecteurs utilisés

Afin d'obtenir de nouvelles cages multimétalliques octaédriques à partir de calixarènes et de connecteurs métallo-organiques, en utilisant le schéma de synthèse présenté figure 1, le choix des connecteurs appropriés est crucial. Dans ce travail, plusieurs familles de connecteurs ont été synthétisées (Figure 2). Ils ont été choisis selon certains critères :

- La nombre et la position des groupements coordinants. Pour tous les connecteurs, les groupement carboxylates sont des sites de coordination qui permettent la formation de liaisons de coordination avec les nœuds métalliques des calixarènes.

- La géométrie des connecteurs. Les connecteurs tridentates ou bidentates doivent présenter respectivement une géométrie trigonale ou linéaire afin de former les MOC ciblés (MOC octaédrique de type "Edge-panelled" ou de type "Face-panelled", comme présenté Figure 1).

- Les propriétés intrinsèques des connecteurs (sites métalliques accessibles pour catalyse, luminescence) qui pourraient être amplifiées lorsque le connecteur est intégré dans le MOC.

La famille des connecteurs métallo-organiques de type tris(dipyrrine) et bis(dipyrrine) (Figure 2a) a été choisie en raison de la nature tridentate et de la géométrie triangulaire du connecteur **tris(dipyrrine)** : $\text{rac-M}(\text{HL}_1)_3$ ($\text{M} = \text{Co}^{\text{III}}, \text{Fe}^{\text{III}}$ and Rh^{III}) ; et de la nature bidentate et de la géométrie linéaire du connecteur **bis(dipyrrine)** : $\text{Pd}(\text{HL}_1)_2, \text{Ni}(\text{H}_2\text{L}_3)$. De plus, les complexes dérivés de ces connecteurs sont chiraux ($\Lambda\text{-Co}(\text{HL}_1)$, $\Delta\text{-Co}(\text{HL}_1)$) et peuvent ainsi conduire à la formation de cages chirales ($[\text{Co}_4\text{SO}_2\text{TCA}]_6[\Lambda\text{-Co}(\text{L}_1)]_8$; $[\text{Ni}_4\text{SO}_2\text{TCA}]_6[\Lambda\text{-Co}(\text{L}_1)]_8$; $[\text{Co}_4\text{SO}_2\text{TCA}]_6[\Delta\text{-Co}(\text{L}_1)]_8$; $[\text{Ni}_4\text{SO}_2\text{TCA}]_6[\Delta\text{-Co}(\text{L}_1)]_8$).⁵ Par ailleurs, il a été possible de synthétiser un connecteur tris(dipyrrine) élargi ($\text{rac-Co}(\text{L}_3)_3$) dans le but d'obtenir des MOC de plus grande taille et de modifier ainsi les propriétés d'adsorption.

Le connecteur de type **tris(phénanthroline)** (Figure 2b) ($[\text{rac-Fe}(\text{HL}_4)_3][\text{PF}_6]_2$) a été choisi pour les mêmes raisons. Il possède une nature ionique, de sorte que la cage obtenue pourrait être soluble dans l'eau, ce qui est important pour certaines applications. Enfin, le connecteur **tris(phénanthroline)** ($[\text{rac-Fe}(\text{HL}_4)_3][\text{PF}_6]_2$) est photosensible et pourrait être utilisé pour la photocatalyse.⁵

Le connecteur de type **porphyrine** ($\text{Ni}(\text{H}_2\text{L}_6)$) possédant deux fonctions acides carboxyliques en position *trans* (Figure 2c) présente une géométrie linéaire. L'analogue de type **corrole** tri-substitué ($\text{Co}(\text{H}_3\text{L}_7)$) présente une géométrie en T dont la flexibilité pourrait être suffisante pour conduire aux MOC ciblés (Figure 2d). Ces deux macrocycles tétrapyrroliques sont également photochimiquement actifs. De plus, les ions métalliques présents dans leur cavités ont des sites de coordination axiaux libres qui peuvent être utiles pour la coordination lors des réactions catalytiques.⁶

La famille des connecteurs de type **bis(terpyridine)** (Figure 2e): $[\text{M}(\text{HL}_5)_2][\text{PF}_6]_2$ ($\text{M} = \text{Fe}^{\text{II}}, \text{Co}^{\text{II}}, \text{Ru}^{\text{II}}$), de géométrie linéaire, sont de nature ionique et photochimiquement actifs : ils peuvent notamment être utilisés dans les réactions formation du dihydrogène.⁷

Enfin, parallèlement à ces différentes familles de connecteurs métallo-organiques, nous avons également synthétisé des nouveaux connecteurs organiques : les connecteurs de type **triazine** (Figure 2f) (H_3L_8 , H_3L_9 , H_3L_{10}) trisubstitués qui présentent une géométrie trigonale. Le cœur du groupement triazine présente une densité de charge positive qui peut être utilisée pour la π -reconnaissance d'anions,⁸ procurant ainsi aux cages formées des propriétés potentielles de reconnaissance inédites.

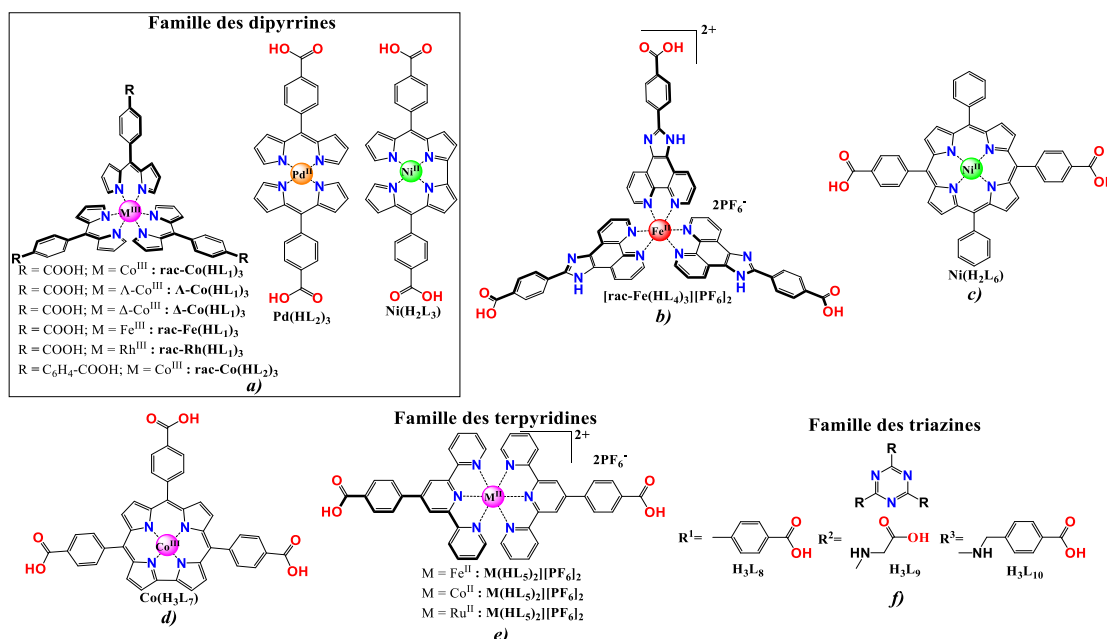


Figure 2 Les familles de connecteurs qui ont été utilisés pour la formation de cages octaédriques nanométriques

Tous les connecteurs mentionnés ci-dessus (Figure 2) ont été synthétisés avec succès et caractérisés par différentes techniques en solution et à l'état solide (spectroscopie RMN, spectrométrie de masse, spectroscopie IR, microanalyse).

2) Synthèse et caractérisation structurale des MOC

Les connecteurs obtenus ont ensuite été utilisés dans des réactions d'auto-assemblage avec des sels métalliques et l'espèce macrocyclique sulfonylcalix[4]arène en solution et à température ambiante (la diffusion liquide-liquide) ou en chauffant (la synthèse solvothermale), afin d'obtenir de nouvelles cages octaédriques multimétalliques à base de calixarène, comme présenté figure 1. Afin d'étudier la structure des cages obtenues, l'obtention de monocristaux afin d'effectuer des analyses de diffraction de RX sur monocristaux est indispensable.

Au cours de cette étude, il a été démontré que les familles de connecteurs les plus prometteuses pour la formation de MOC cristallines à base de calixarènes sont les connecteurs à base de **tris(dipyrrine)** (Figure 2a, connecteurs $rac-M(HL_1)_3$, $\Delta-Co(HL_1)_3$, $\Lambda-Co(HL_1)_3$) et un

dérivé de la famille de connecteurs de triazine (connecteur H_3L_8 , Figure 2f). Les cristaux obtenus ont un pouvoir diffractant faible, et les structures ont pu être obtenues en utilisant des diffractomètres puissants associés à des temps d'enregistrements importants, en collaboration avec le groupe du Pr. Kari Rissanen (Université de Jyväskylä, Finlande).

Ainsi, une série de 12 nouveaux MOC octaédriques a été obtenue et caractérisée à l'état solide par DRX. Ce sont des cages présentant la formule brute suivante : $[M_4SO_2TCA]_6[Cx]_8$ ($M = Co^{II}, Ni^{II}$; $Cx = rac-Co(L_1)_3, rac-Fe(L_1)_3, rac-Rh(L_1)_3, \Delta-Co(L_1)_3, \Lambda-C(L_1)_3, L_8$). Ils présentent tous les mêmes caractéristiques structurales : ils sont constitués de six unités tétranucléaires de sulfonylcalix[4]arène connectées les unes aux autres par l'intermédiaire de huit connecteurs triangulaires occupant les faces de la cage octaédriques, conduisant ainsi à des cages nanométriques octaédriques de type de type "Face-panelled", comme présenté Figure 3. Les MOC sont soit homo- soit hétéro-métalliques, selon la nature du cation métallique coordonné au calixarène et celui présent dans le connecteur métal-organique :

- 6 MOC isostructuraux dont 5 hétéro-métalliques basés sur des connecteurs à base de tris(dipyrrine) de Co^{III} , Fe^{III} , Rh^{III} : $[Co_4SO_2TCA]_6[rac-Co(L_1)_3]_8$, $[Ni_4SO_2TCA]_6[rac-Co(L_1)_3]_8$, $[Co_4SO_2TCA]_6[rac-Fe(L_1)_3]_8$, $[Ni_4SO_2TCA]_6[rac-Fe(L_1)_3]_8$, $[Co_4SO_2TCA]_6[rac-Rh(L_1)_3]_8$, $[Ni_4SO_2TCA]_6[rac-Rh(L_1)_3]_8$,
- 4 MOC octaédriques chiraux basés sur le connecteur chiral $\Lambda-Co(HL_1)_3$ and $\Delta-Co(HL_1)_3$: $[Co_4SO_2TCA]_6[\Lambda-Co(L_1)_3]_8$, $[Co_4SO_2TCA]_6[\Delta-Co(L_1)_3]_8$, $[Ni_4SO_2TCA]_6[\Lambda-Co(L_1)_3]_8$, $[Ni_4SO_2TCA]_6[\Delta-Co(L_1)_3]_8$,
- 2 MOC octaédrique isostructuraux basés sur le connecteur H_3L_8 , purement organique : $[Co_4SO_2TCA]_6[L_8]_8$, $[Ni_4SO_2TCA]_6[L_8]_8$.

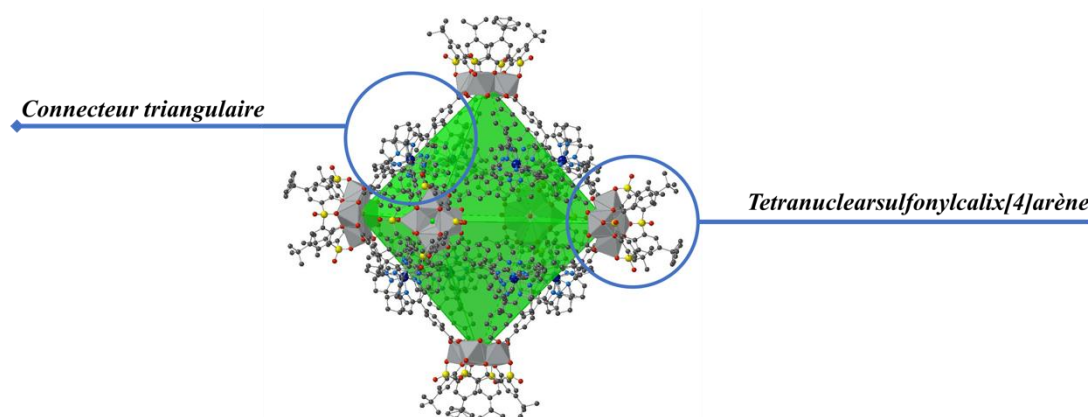


Figure 3 Un exemple de structure cristalline d'une cage octaédrique $[M_4SO_2TCA]_6[Cx]_8$ obtenue à partir de connecteurs métal-organiques triangulaires



Il convient de mentionner que la caractérisation par DRX des différents assemblages a été un grand défi, notamment avec les connecteurs rac-M(HL₁)₃. En effet, le volume de la maille est très important, et comme déjà mentionné les cristaux ont un faible pouvoir diffractant en raison de la présence d'une grande quantité de solvants désordonnés à l'intérieur et à l'extérieur de la cage.

Les cages octaédriques formées possèdent une cavité interne de grande taille (Figure 3) dont le diamètre est proche de 19 Å pour les cages à base de rac-M(HL₁)₃ et d'environ 16 Å pour les cages à base de H₃L₈. Les cages cristallisent dans le système hexagonal avec des volumes de maille : proche de 225 000 Å³ pour les cages à base de rac-M(HL₁)₃ et d'environ 65 000 Å³ pour les cages à base de H₃L₈.

Pendant le travail de doctorat, il n'a pas été possible d'obtenir la structure cristalline des MOC avec d'autres connecteurs que ceux mentionnés ci-dessus. Cependant, certaines de ces modifications ont conduit à la formation de nouveaux cristaux qui n'ont pas encore été analysés. Ces travaux sont toujours en cours, notamment en explorant de nouvelles voies de synthèse qui permettraient d'aboutir à la formation de cristaux souhaités. Par conséquent, les résultats actuels n'indiquent pas que ces connecteurs ne sont pas adaptés à la formation de nanoconteneurs multimétalliques, mais plutôt que la recherche est en cours et nécessite des investigations supplémentaires.

3) Propriétés des MOC

a) Propriétés optiques

Parmi les connecteurs métallo-organiques employés, certains présentent une chiralité liée à la présence du métal (Λ -Co(HL₁)₃, Δ -Co(HL₁)₃). Lors de la synthèse, les différents énantiomères ont pu être séparés et leur pureté a été démontrée par dichroïsme circulaire ainsi que par chromatographie chirale. Les cages correspondantes ([Co₄SO₂TCA]₆[Λ -Co(L₁)₃]₈, [Co₄SO₂TCA]₆[Δ -Co(L₁)₃]₈, [Ni₄SO₂TCA]₆[Λ -Co(L₁)₃]₈, [Ni₄SO₂TCA]₆[Δ -Co(L₁)₃]₈) énantiomériquement pures ont été préparées et caractérisées par DRX. L'activité optique de ces cages a également été mesurée.

Afin de mettre en évidence la reconnaissance d'espèces chirales de la part de ces cages énantiomériquement pures ([Co₄SO₂TCA]₆[Λ -Co(L₁)₃]₈, [Co₄SO₂TCA]₆[Δ -Co(L₁)₃]₈, [Ni₄SO₂TCA]₆[Λ -Co(L₁)₃]₈, [Ni₄SO₂TCA]₆[Δ -Co(L₁)₃]₈), des mesures d'adsorption sélective de solvants chiraux en phase vapeur (2-butanol, par exemple) sont en cours, en collaboration avec Pr. Beata Nowicka (Jagiellonian University, Cracovie, Pologne).

b) Propriétés d'adsorption de gaz

La présence d'espèces macrocycliques de type calixarène en conformation cône comme constituant des cages, ainsi que la formation de cavités de tailles nanométriques des cages laissent envisager qu'elles possèdent des propriétés d'adsorption de gaz accrues. En effet, la caractérisation structurale de ces entités a montré qu'elles peuvent présenter plus de 70% de vide du volume cristallin total. Après la synthèse, les cavités internes contiennent de nombreuses molécules de solvants, mais ces dernières peuvent être retirées par simple activation des cristaux sous vide, en préalable aux études de l'adsorption de gaz.

Les propriétés d'adsorption avec N₂ et CO₂ d'une cage de formule [Co₄SO₂TCA]₆[L₈]₈ ont été étudiées. Les mesures d'adsorption de diazote ont montré que les composés étudiés présentent des isothermes de type I avec de bonnes propriétés d'adsorption. Cette MOC a montré une surface BET élevée d'environ 742.6 m²/g

Les propriétés d'adsorption et de séparation des gaz des cages octaédriques [Co₄SO₂TCA]₆[rac-Co(L₁)₃]₈ et [Ni₄SO₂TCA]₆[rac-Co(L₁)₃]₈ ont été étudiées en collaboration avec le groupe du Pr. V. Fedin (Institut de chimie inorganique A.V. Nikolaev, Russie, Novosibirsk). Les mesures d'adsorption de diazote ont montré que les composés étudiés présentent des isothermes de type I avec de bonnes propriétés d'adsorption. Il a été calculé à partir des isothermes que les cages [Co₄SO₂TCA]₆[rac-Co(L₁)₃]₈ et [Ni₄SO₂TCA]₆[rac-Co(L₁)₃]₈ ont une surface BET de 416,9 m²/g et 445,2 m²/g respectivement.

Afin d'étudier la sélectivité d'adsorption de gaz, des expériences d'adsorption avec d'autres gaz (C₂H₂, CH₄, C₂H₄, C₂H₆, CO₂) ont été effectuées. Nous avons pu montrer que les cages obtenues ont une meilleure affinité pour l'acétylène C₂H₂ avec des valeurs d'adsorption de 2,25 mmol/g et 2,37 mmol/g pour les cages [Co₄SO₂TCA]₆[rac-Co(L₁)₃]₈ et [Ni₄SO₂TCA]₆[rac-Co(L₁)₃]₈ respectivement.

Les différences dans les propriétés d'adsorption des différents gaz permettent également d'envisager l'adsorption sélective IAST de mélanges de gaz. Il a été montré que les mélanges de gaz les plus prometteurs pour la séparation par les cages citées ci-dessus sont : C₂H₂/CH₄, C₂H₆/CH₄, CO₂/N₂. L'adsorption sélective IAST de ces mélanges dépasse de nombreux systèmes similaires décrits précédemment.^{9,10}



Conclusion

Au cours de ce travail, nous avons synthétisé plusieurs familles connecteurs dans le but de les impliquer dans la formation de cages moléculaires (MOC) octaédriques à base d'entités macrocycliques de type calixarène. Ces connecteurs sont de nature métallo-organiques ou purement organiques. Deux nouvelles familles de MOC (12 nouvelles cages) ont été obtenues: dix MOC à base de connecteurs dipyrrine métallo-organiques et deux MOC à base de connecteurs organiques triazine ont été mises en évidence. Ces cages ont été parfaitement caractérisées d'un point de vue structural.

Les cages octaédriques obtenues $[\text{Co}_4\text{SO}_2\text{TCA}]_6[\text{rac-Co}(\text{L}_1)_3]_8$ et $[\text{Ni}_4\text{SO}_2\text{TCA}]_6[\text{rac-Co}(\text{L}_1)_3]_8$ ont démontré, entre autre, de bonnes propriétés d'adsorption et d'excellentes propriétés de séparation de gaz IAST ($\text{C}_2\text{H}_2/\text{CH}_4$; $\text{C}_2\text{H}_6/\text{CH}_4$; CO_2/N_2).

En outre, la cage à base de triazine $[\text{Co}_4\text{SO}_2\text{TCA}]_6[\text{L}_8]_8$ a également démontré d'excellentes propriétés d'adsorption, surpassant de nombreuses MOC similaires ainsi que les MOC à base de dipyrrhine démontrées dans ce travail

Chapter I.

Introduction

Table of contents

<u>I. Historical review of covalent and coordination cage</u>	19
<u>I.1. Crown-ethers of Pedersen</u>	19
<u>I.2. Cryptands of Dietrich, Lehn and Sauvage</u>	20
<u>I.3. Macrooligocycle of Kiggen</u>	20
<u>I.4. Quan's hemicarcerand capable to encapsulate organic molecules</u>	21
<u>I.5. The first metal-organic cages and their development through decades</u>	22
<u>II. Non-calixarene MOCs: classification and properties</u>	26
<u>II.1. Strategies for synthetic approaches</u>	26
<u>II.2. Geometrical analysis</u>	28
<u>II.3. Reported properties of MOCs</u>	33
<u>III. Calixarene-based MOCs</u>	38
<u>III.1. Generalities on calix[4]arene</u>	38
<u>III.2. First calixarene-based metal-organic cage</u>	39
<u>III.3. Calixarene-based MOCs: formation and synthesis</u>	40
<u>III.4. Calixarene-based MOCs: geometry</u>	42
<u>III.5. Calixarene-based MOCs based on organic connectors: properties</u>	46
<u>III.6. Calixarene-based MOC with Metal-Organic connectors</u>	53
<u>IV. Conclusion</u>	55
<u>V. Presentation of the scientific project</u>	56



I. Historical review of covalent and coordination cage

Supramolecular cages are self-assembled structures that are formed through the use of noncovalent interactions, such as hydrogen bonding, metal coordination, and van der Waals forces that distinguishes them from purely covalent cages, mainly formed through covalent bonds.¹ Both supramolecular cages and covalent cages have the ability to selectively encapsulate and release guest molecules, making them useful in a wide range of applications including drug delivery, catalysis, and material science. In the recent years, there has been a large progress in the design and synthesis of supramolecular cages with controllable sizes, shapes, and functionalities.

The field of supramolecular cages is a rapidly expanding area of research that has the potential to fundamentally change the way we view materials and their related properties. Overall, the study of supramolecular cages is an exciting and rapidly growing field with a vast array of potential applications.

This brief introduction aims to provide an overview of supramolecular cages, beginning with the history of the first covalent cage-like structures and their subsequent evolution into coordination cages and sophisticated calixarene-based metal-organic cages. By tracing this developmental path, we can gain a better understanding concerning their properties and potential applications of these structures.

Below, a historical review with the beginning of recognition chemistry and some chosen examples (not an exhaustive list) will be provided.

I.1. Crown-ethers of Pedersen

The development of supramolecular cages has a history spanning over 50 years. The origins of this field can be traced back to the work of Pedersen *et al.*, reported in 1967.¹¹ In this work, 33 crown ethers were described for the first time. These macrocycles were found to form strong inclusion complexes with ions, including Li^+ , Na^+ , NH_4^+ , RNH_3^+ , K^+ , Rb^+ , Cs^+ , Ag^+ , Au^+ , Ca^{2+} , Sr^{2+} , Ba^{2+} , Cd^{2+} , Hg^+ , Hg^{2+} , La^{3+} , Tl^+ , Ce^{3+} , and Pb^{2+} . The preference for certain ions towards specific crown-ethers was explained by the cavity size of corresponding crown-ethers (Figure 4).

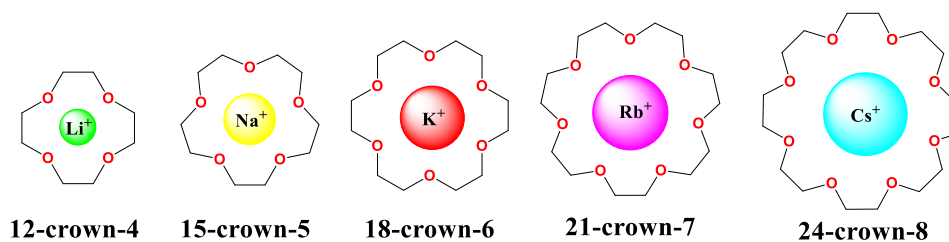


Figure 4 The most stable complexes for different sizes of crown-ethers¹²

There are several reasons why crown-ethers may be regarded as the first covalent cages. Firstly, crown-ethers possess an internal cavity that is able to be adapted. Secondly, it is demonstrated in Figure 4 that crown-ethers can selectively bind specific metal ions. In fact, crown-ethers can be considered as a type of "covalent organic cage", as they are composed of covalent bonds, have an inherent cavity and able to selectively bind certain species.

I.2. Cryptands of Dietrich, Lehn and Sauvage

The development of supramolecular cages was reported by the group of Dietrich, Lehn, and Sauvage in 1969.¹³ They described the synthesis of more sophisticated molecules, called "cryptands", suitable for host-guest interactions. Cryptands are macrobicycles (Figure 5) that allows them to form more stable complexes with ions compared to crown ethers. While crown ethers form a 2D cavity, macrobicycles form a 3D cavity that is suitable for bonding with spherical alkali and alkali earth cations. It was found that the bonding strength of macrobicycles (cryptands) exceeds the one of macrocycles (crown-ethers) by several orders of magnitude and the formation selectivity is much higher, depending on the size of the cavity and the hard-soft acids and bases affinity. These phenomena led to the concept of "spherical recognition", which is now a common type of supramolecular interaction based on non-covalent interactions.

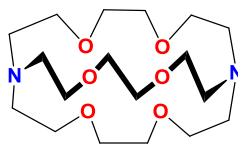


Figure 5 Structure of [2.2.2]cryptand

I.3. Macrooligocycle of Kiggen

In 1984, Kiggen *et al.* reported the first recognizable prototype of a supramolecular cage. This sophisticated ligand is a cage-like "macrooligocycle", which exhibits a cavity bounded on three sides and has functional groups suitable for the binding of metals (Figure 6). The synthesized ligand displays excellent complexation properties, able to dissolve Fe(0) and Ni(0) powders and even attack stainless steel. Additionally, the formation of large cages with large internal cavities opened up new possibilities for chemical reactions to occur within the cavity confined space.¹⁴

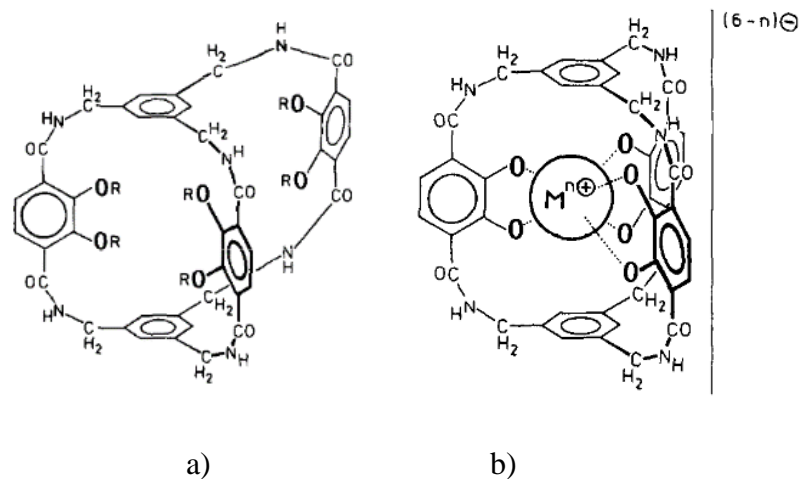


Figure 6 Structure of the Kiggen's macrooligocycle (a); Structure of octahedral anionic complex involving the macrooligocycle (b) (from ref. ¹⁴)

I.4. Quan's hemicarcerand capable to encapsulate organic molecules

A breakthrough in the field was made in 1991 by Quan *et al.*, who reported the first molecule able to encapsulate organic molecules and that inhibits dissociation of the formed complexes.¹⁵ This molecule, called a "hemicarcerand", has a barrel-shaped cage structure and is able to exhibit host-guest interactions with guests like anthraquinone, camphor, and anthracene (Figure 7). The hemicarcerand described by this group was the first recognizable cage structure and paved the way for the synthesis of larger structures suitable for encapsulating larger guest molecules.

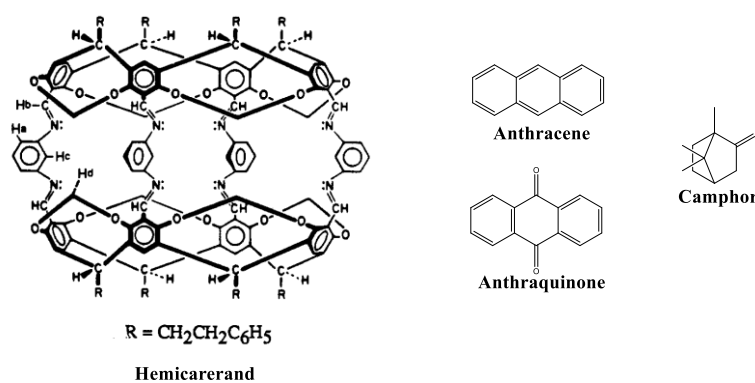


Figure 7 Structure of the first hemicarcerand and its guest molecules (from ref. ¹⁵)

I.5. The first metal-organic cages and their development through decades

The next major development in the field of supramolecular cages was the first report of the synthesis of Metal-Organic Cages (MOCs). The first pioneering work in this field was reported in 1988 by Saalfrank *et al.*¹⁶ The authors reported the formation of a Mg^{II} -based MOC that displays a tetrahedral shape (Figure 8). However, the reported MOC presents a small cavity (diameter is approximately 6Å) and did not demonstrate good host-guest interactions.

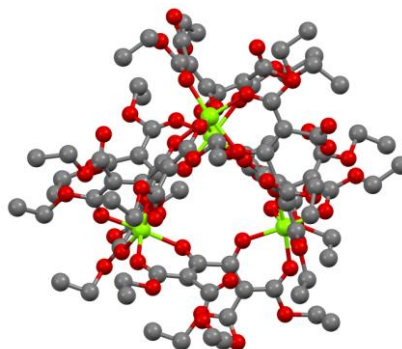


Figure 8 The structure of the first MOC reported by Saalfrank *et al.* in 1988 (from ref. ¹⁶)

The next breakthrough was done by Fujita *et al.* in 1990. In this pioneering work a water-soluble Pd^{II} -square “proto-MOC” was reported. This compound demonstrated great recognition properties in aqueous media with 1,3,5-trimethoxybenzene (Figure 9a).¹⁷ In 1995, the same group reported the first recognizable MOCs and their encapsulation properties were demonstrated. The authors reported the formation of three MOCs displaying an octahedral shape using tridentate ligands. One of the obtained MOC is a cage formed by 2,4,6-tri(pyridin-4-yl)-1,3,5-triazine, and *cis*-protected $Pd(NO_3)_2(en)$ through the process of self-assembly (Figure 9b).

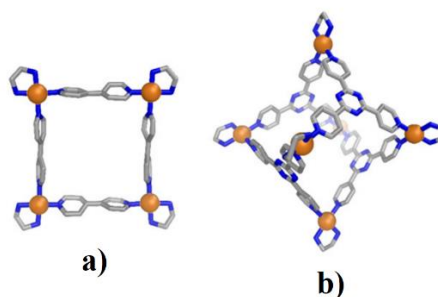


Figure 9 Proto-MOC(a); The first MOC presenting recognition properties (from ref. ¹⁸)

The octahedral shape assemblies present an ionic nature (the octahedron is charged positively, and anions are located inside and outside), making it water-soluble. Additionally, this MOC has a large accessible internal cavity with a diameter approximately of 12Å, suitable for recognition of relatively large species, for example, adamantyl carboxylate ions.

this family of MOCs, based on rigid pyridyl ligands, demonstrates the possibility to precisely tune the properties of the desired MOCs by manipulating rigid ligands geometry and especially the angle between the coordinating positions (Figure 11).

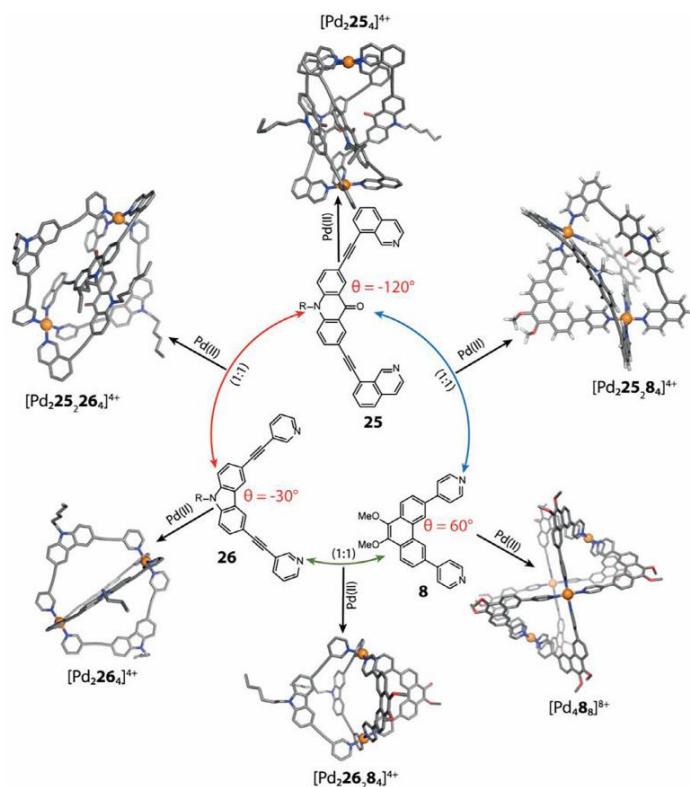


Figure 11 The formation of MOCs series from ligands with different angles between coordination sites (from the ref. ²¹)

The Fujita's approach also influenced another interesting class of MOCs developed in the last decades - water soluble MOCs based on charged ligands that focused applications on the fields of molecular recognition, chemical transport, catalysis, and guest stabilization.¹⁸ For example, Pr. Nitschke *et al.* reported tetrahedral Fe^{II} pyridyl-imine water soluble MOC.²² The authors reported "subcomponent self-assembly method" for MOCs synthesis involving the simultaneous formation of dynamic coordinative $\text{N} \rightarrow \text{M}$ and covalent $\text{C}=\text{N}$ bonds, leading to the *in situ* building of pyridyl-imine chelating ligands and their organization around metal ions acting as templates, forming the negatively charged MOCs (Figure 12). This method demonstrated its usefulness for the formation of many water-soluble cages.

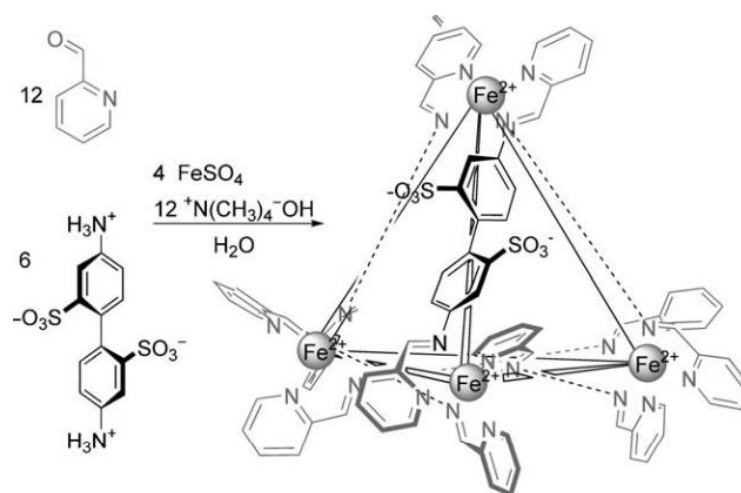


Figure 12 The synthesis of negatively charged MOC using the method of subcomponent self-assembly (from ref. ²²)

It is worth mentioning that MOCs structural developments can be provided not only through chemical modifications of the ligands but also of the “metal nodes” (point building units). For example, the increasing number of metal ions that forms one node has been reported.²³ The higher number of metal ions forming one node is usually related to larger MOCs with better thermal stability. However, this approach is facing a stability problem of the formed nodes. The most frequent way to stabilise these polymetallic nodes is to coordinate free coordination positions of metal with certain organic species: formation of metallocenic²⁴ or calixarene-based⁴ clusters. The calixarene-based approach will be discussed in details in the §III. of this chapter.

In conclusion, the field of metal-organic cages (MOCs) has rapidly expanded since the first pioneering work reported in 1988 by Saalfrank *et al.* The ground-breaking research conducted by Pr. M. Fujita *et al.* in the area of MOCs had a significant impact on the field, leading to the discovery of numerous types of MOCs with unique properties and new classes of MOCs. In the following sections of this chapter, we will discuss more in details different types of MOCs and especially their geometries and unique properties.



II. Non-calixarene MOCs: classification and properties

In order to correctly classify the different MOCs, useful concepts for their description will be defined here below:

Node – a point building unit in a supramolecular cage, where two or more connectors are joint/vertex of a polyhedron.

Connector – a prolonged building unit in a supramolecular cage, which links two or more nodes/surface or edge of a polyhedron.

As it was demonstrated in the previous section, many different MOCs were synthesized over the years. These cages display different connectors structure, different nodes composition and it is hard to strictly classify them. In this section, MOCs classification will be divided in accordance with the nature of the used nodes:

- Metal-organic cages based on non-calixarene nodes
- Metal-organic cages based on calixarene nodes, which is the topic of this work

II.1. Strategies for synthetic approaches

As previously mentioned, metal-organic cages (MOCs) belong to a class of porous materials that are composed of metal nodes and organic or metal-organic connectors, which form a cage-like structure under conditions suitable for self-assembly.

The size, the shape, and the properties of the resulting MOCs can be precisely controlled by manipulating the size and shape of the metal nodes and the connectors. MOCs have attracted interest due to their large internal cavity and as a consequence high surface area, which make them suitable for a range of applications. The size, shape and coordination ability of the metal centres, as well as the nature and number of ligands, can be tailored to obtain MOCs with desired properties.²

MOCs and metal-organic frameworks (MOFs) share a close relationship from a structural point of view since both involve the combination of metal ions or clusters with organic ligands. However, the primary distinction between them is that MOCs are formed through the self-assembly of specifically chosen metal ions and ligands, leading to discrete, finite structures, while MOFs are formed through the coordination of metal ions and ligands to form porous extended or infinite network.²

For the formation of MOCs, the choice of the nature of the metal ions and connectors is of utmost importance because the coordination ability of the metal ions and the geometry of the connectors determine the resulting cage geometry. The selection of metal ions and ligands in

MOCs is aimed at capping coordination sites, resulting to the formation of discrete molecular entities rather than extended frameworks. The most common metal ions used for MOCs synthesis are d-metals and f-metals, which have the ability to coordinate with ligands and form polyhedral structures while other elements are less commonly used due to their lower coordination number. Furthermore, as it was discussed in §I.5. of this chapter, it is possible to obtain MOCs based on clusters of d-metals forming a node.²³

On the other side, the selection of appropriate connectors is also crucial for the synthesis of MOCs, as they must be able to coordinate to metal ions and contribute to the overall stability of the cage structure. The most common coordinating groups that are used for MOCs synthesis are (Figure 13): carboxylate,^{24,25} pyridyl,^{26,27} or alcoholate,^{28,29} however, this is a non-exhaustive list.

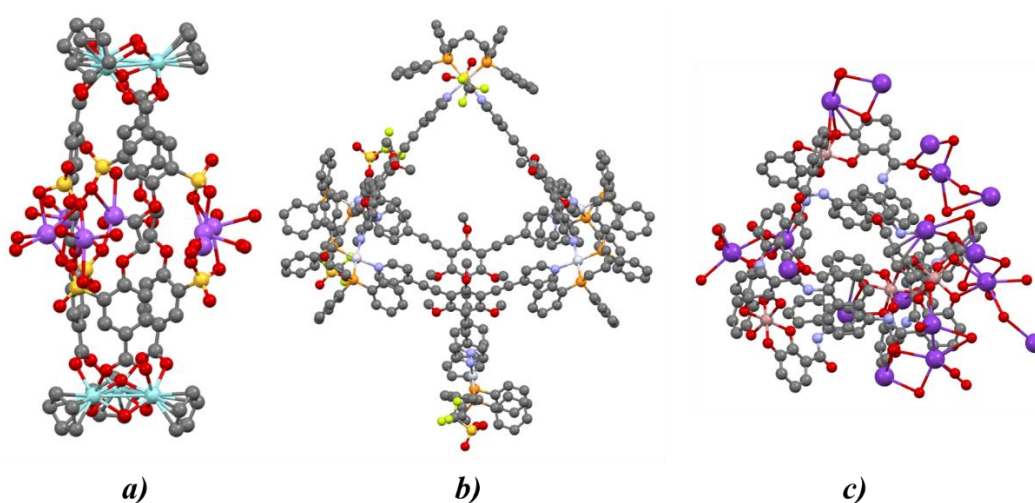


Figure 13 MOCs based on connectors with carboxylate(a),¹⁵ pyridyl(b)²⁰ or alcoholate (c)²⁹ coordinating groups

The formation of MOCs requires a well-designed combination of metal ions and connectors, as well as the use of allosteric and chelate cooperativity.³⁰ In order to comply to these conditions, there are several MOCs synthetic approaches used, which are detailed below:

- *The symmetry interaction approach* is a strategy that uses chelating connectors to occupy all coordination sites on metal centres while maintaining a closed structure. This approach is based on the proper alignment of both the coordinate vector of the connector and the chelate plane of the metal in order to achieve the desired structural outcome.^{31,32}
- *The directional bonding approach* is a strategy that involves the combination of connectors with specific orientations of donor atoms and metal atoms with fixed angle

in coordination sites. This approach aims to achieve precise geometry control over the chemical bonding interactions between the connectors and the metal centres.^{20,33}

- The third strategy for the formation of MOCs involves the *use of ligands as two-dimensional capping agents* on the faces of MOCs. This approach, known as the *face-panelling strategy*, differs from the symmetry interaction and directional bonding approaches, and primarily results in edge-panelled MOCs (Figure 14).

In both the directional bonding and face-panelling strategies, it is common to use additional ligands to block the unoccupied coordination sites on the metal centre, in order to stabilize the discrete nature of the structure.^{34,35}

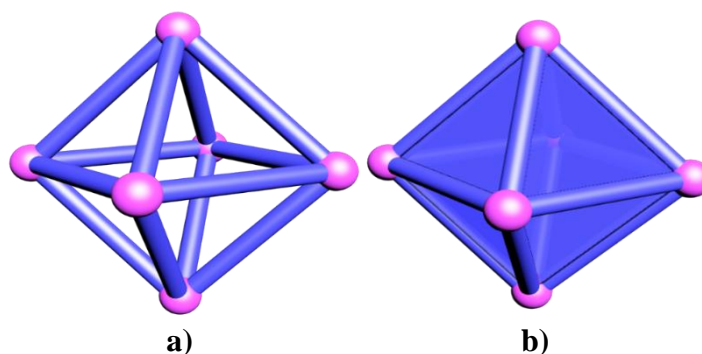
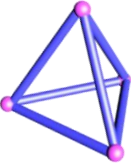
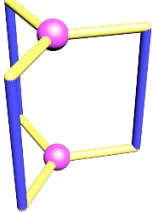
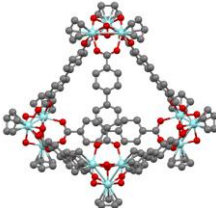
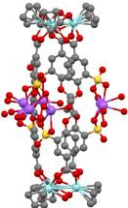
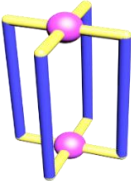
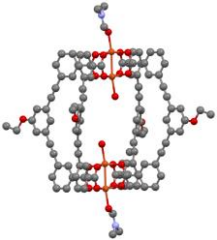
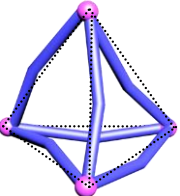
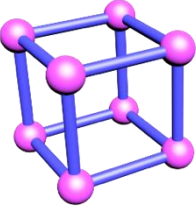
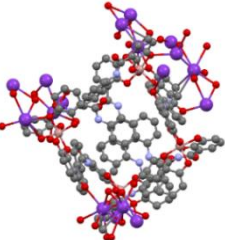
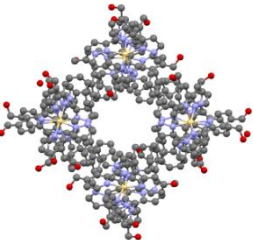
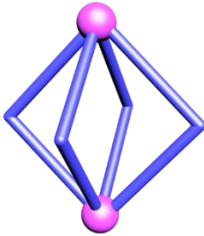
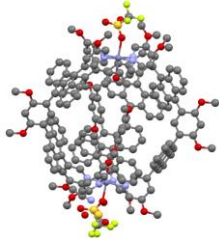
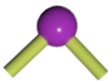
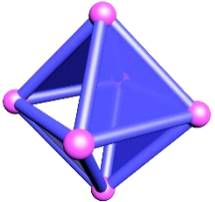
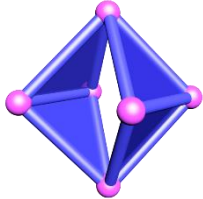
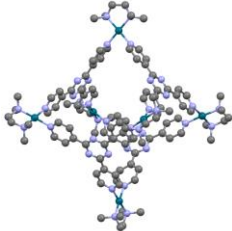
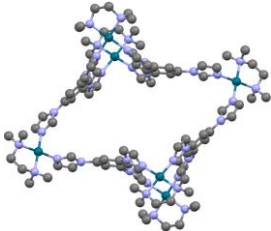
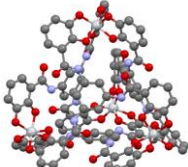
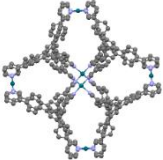


Figure 14 Edge-panelled MOC (a); Face-panelled MOC(b)

II.2. Geometrical analysis

There are numerous possible combinations of metal nodes and connectors, and it is also possible to use multiple types of connectors involved into the formation of MOCs. This results in a diverse range of stable cage geometries with varying sizes of internal cavities, suitable for hosting a wide range of guest molecules. Table 1 represents a summary of the most frequently observed combinations between metal node geometries and ligand geometries, the resulting cage geometries, and synthesized cages with their corresponding internal cavity diameters. They will be arranged from the simplest connectors to the most sophisticated connectors and connectors combinations. This is a non-exhaustive list and additional more geometries exist that are out of this classification (see the description after the Table 1).

Connectors geometry and number of binding positions	Metal nodes geometry with number of positions for coordination	Resulting cage geometry		Synthesized examples with cavity diameter	
 <p>Linear bidentate (Lin)</p>	 <p>Number of positions = 3 Complex trigonal (Ctrigon)</p>	 <p>Tetrahedron²⁴ Lin₆Ctrigon₄</p>	 <p>Barrel²⁵ Lin₃Ctrigon₂</p>	 <p>D=13Å (from ref. ²⁴)</p>	 <p>D=6Å (from ref. ²⁵)</p>
 <p>Linear bidentate (Lin)</p>	 <p>Number of positions = 4 Complex tetragonal (Ctetra)</p>	 <p>Barrel³⁶ Lin₄Ctetra₂</p>		 <p>D=9Å (from ref. ³⁶)</p>	
 <p>Angular bidentate (An)</p>	 <p>Number of positions = 3 Trigonal (Trigon)</p>	 <p>Tetrahedron²⁹ An₆Trigon₄</p>	 <p>Cube³⁷ An₁₂Trigon₈</p>	 <p>D=12Å (from ref. ²⁹)</p>	 <p>D=19Å (from ref. ³⁷)</p>

 <p>Angular bidentate (An)</p>	 <p>Number of positions = 4 Tetragonal (Tetra)</p>	 <p>Barrel³⁸ An₄Tetra₂</p>		 <p>D=9Å (from ref. ³⁸)</p>	
 <p>Tridentate (Tri)</p>	 <p>Number of positions = 2 V-shape (V)</p>	 <p>Octahedron²⁶ Tri₄V₆</p>	 <p>Octahedron³⁹ Tri₄V₆</p>	 <p>D=18Å (from ref. ²⁶)</p>	 <p>D=15Å (from ref. ³⁹)</p>
 <p>Tridentate (Tri)</p>	 <p>Number of positions = 3 Trigonal (Trigon)</p>	 <p>Tetrahedron⁴⁰ Tri₄Trigon₄</p>		 <p>D=10Å (from ref. ⁴⁰)</p>	
 <p>Tridentate (Tri)</p>	 <p>Number of positions = 4 Tetragonal (Tetra)</p>	 <p>Octahedron⁴¹ Tri₈Tetra₆</p>		 <p>D=25Å (from ref. ⁴¹)</p>	

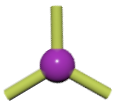
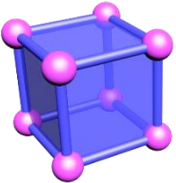
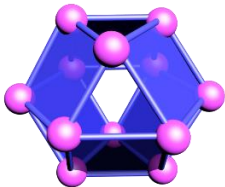
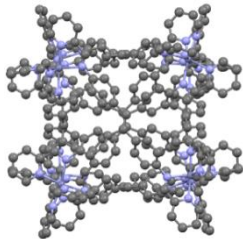
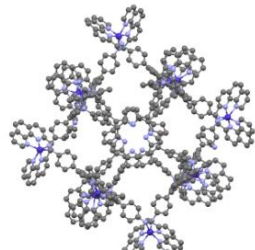
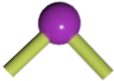
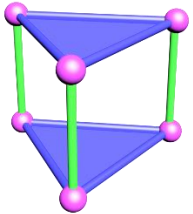
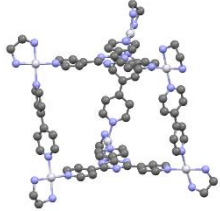
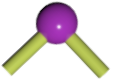
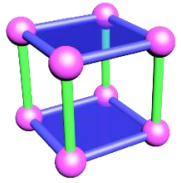
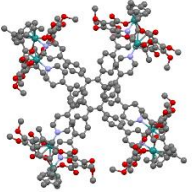
 <p>Tetradentate (Square)</p>		 <p>Number of positions = 3 Trigonal (Trigon)</p>	 <p>Cube⁴² Square₆Trigon₈</p>	 <p>Cuboctahedron⁴³ Square₆Trigon₁₂</p>	 <p>D=18Å (from ref. ⁴²)</p>	 <p>D=28Å (from ref. ⁴³)</p>
 <p>Linear bidentate (Lin)</p>	 <p>Tridentate (Tri)</p>	 <p>Number of positions = 2 V-shape (V)</p>	 <p>Trigonal prism⁴⁴ Lin₃Tri₂V₆</p>		 <p>D=10Å (from ref. ⁴⁴)</p>	
 <p>Linear bidentate (Lin)</p>	 <p>Tetradentate (Square)</p>	 <p>Number of positions = 2 V-shape (V)</p>	 <p>Tetragonal prism⁴⁵ Lin₄Square₂V₈</p>		 <p>D=10Å (from ref. ⁴⁵)</p>	

Table 1 *The most frequent combinations of metal nodes and connectors, resulted cage geometries and some examples with their internal cavity diameters*

The data presented in the Table 1 highlight the versatility of MOCs in terms of their geometry and internal cavity size that differs from 6 to 28 Å. The table shows that 14 different geometries are the most common:

- Three types of tetrahedra,
- Three types of barrels,
- Two types of cubes,
- Three types of octahedrons,
- Cuboctahedra,
- Trigonal prisms,
- Tetragonal prisms.

However, there were many other MOCs geometries reported in the literature starting with distorted version of the mentioned polyhedra and ending with the variety of sophisticated polyhedra from M_nL_{2n} family that are represented in Figure 11 and Figure 15

It is worth to mention that for non-calixarene based MOCs, precise combinations of *node/connector* usually do not lead to different MOCs geometry upon different synthetic conditions. However, it is possible to obtain MOCs with different geometries by minor alteration of the angle between coordination sites of the used connector, for example, even a small change of 3° can lead to completely different geometries of the resulting MOCs. It was well demonstrated by Fujita *et al.*, where they reported the formation of few giant MOCs using similar bis-monodentate connectors (Figure 15).⁴⁶

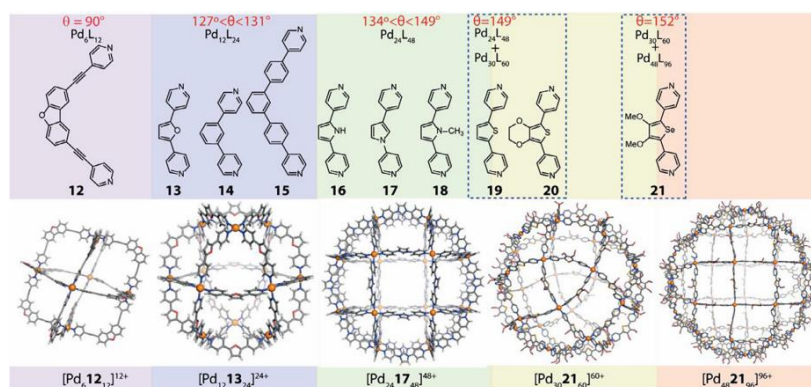


Figure 15 The formation of MOCs displaying different geometries, depending on the angle between coordination sites of the chosen connectors (from ref.²¹)

The successful formation of MOCs with a suitable internal cavity for specific guest molecules heavily relies on the careful selection of metal ions, connectors and self-assembly conditions. The ability to tune the size of the internal cavity is a critical factor which determines the properties and applications of MOCs, which will be further discussed.



II.3. Reported properties of MOCs

Unique MOCs properties are explained by their tunable internal cavity, the presence of metal ions in the structure and their discrete nature.

The tunable internal cavity of MOCs enables the formation of host-guest complexes with a wide range of desired guest molecules, leading to better fitting and stronger host-guest interactions.

The presence of metal ions in the structure of MOCs generates a possibility to exhibit magnetic and optical properties (for example, single-molecule magnet behaviour and sensing).⁴⁷

The discrete nature of MOCs allows them to be soluble without destruction of the building unit (cage) in solution.¹⁸ Cage solubility opens new horizons for their application, for example, water soluble charged cages are great candidates for the design of target drug delivery systems.^{18,48} In comparison, MOFs, which are extended structures, are composed of repeating units and thus have less control over the overall structure, making it harder to tailor the properties of the structures and to incorporate specific functional groups in process of post-functionalization.⁴⁹ Additionally, the discrete nature of MOCs also allows a strong control over the chemical functionalization of the cage structure. This can be used to introduce functional groups for specific applications, such as catalytic or sensing applications. The main reported applications will be discussed here below.

II.3.1. Catalytic activity

The catalytic activity of MOCs has been the subject of extensive research due to the potential for MOCs to act as efficient catalysts with the presence of the cavity and the possibility to use confined space. Various chemical reactions catalysed with MOCs have been reported in the homogeneous catalysis conditions, for example, hydrolysis of organophosphates esters⁵⁰ and Kemp elimination.⁵¹

The activity of MOCs in the homogeneous catalysis can be illustrated here by an example involving the use of Ga-based MOC.⁵² It was demonstrated that the use of this cage significantly increased the reaction rate, reaching a magnitude of seven orders, of the reductive elimination reaction from gold and platinum species with the formation of a C-C bond (Figure 16). In this reaction, the Ga-based MOC plays a role of catalyst and gold or platinum species provide methyl groups for the C-C bond formation.

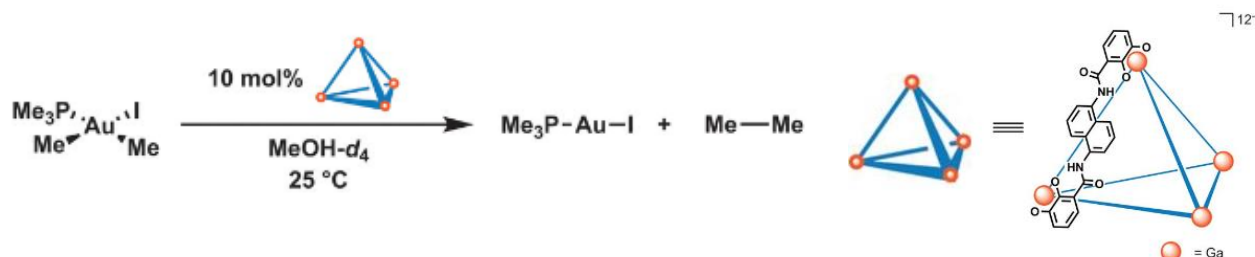


Figure 16 Cage catalysis in the reaction of reductive elimination (from ref. ⁵²)

The MOC's catalytic microenvironment, which acts as a functional enzyme mimic, plays a crucial role in this process. Reaction of the reductive elimination with Ga-MOC use brought to the mind an idea of introducing catalytic system with Ga-based MOC, where reductive elimination is one of the steps in the catalytic cycle. The idea was to force gold and platinum species not to act as reactants but as catalyst in the reaction mixture of other molecules that provide methyl groups for the C-C bond formation.

Previously described Ga-based MOC was sophisticated and introduced as a cocatalyst leading to dual system catalyst. The authors demonstrated the potential of the Ga-based MOC to stabilize the Pt⁺ transition state so Pt-species does not degrade as it was demonstrated on the Figure 16. This system, consisting of Pt-catalyst and tetrahedral Ga-based MOC cocatalyst, catalyses the reaction between iodomethane and tetramethyltin (two sources of methyl groups), in the presence of KF, where the reductive elimination from Pt-species is one of the steps in the catalytic cycle (Figure 17).

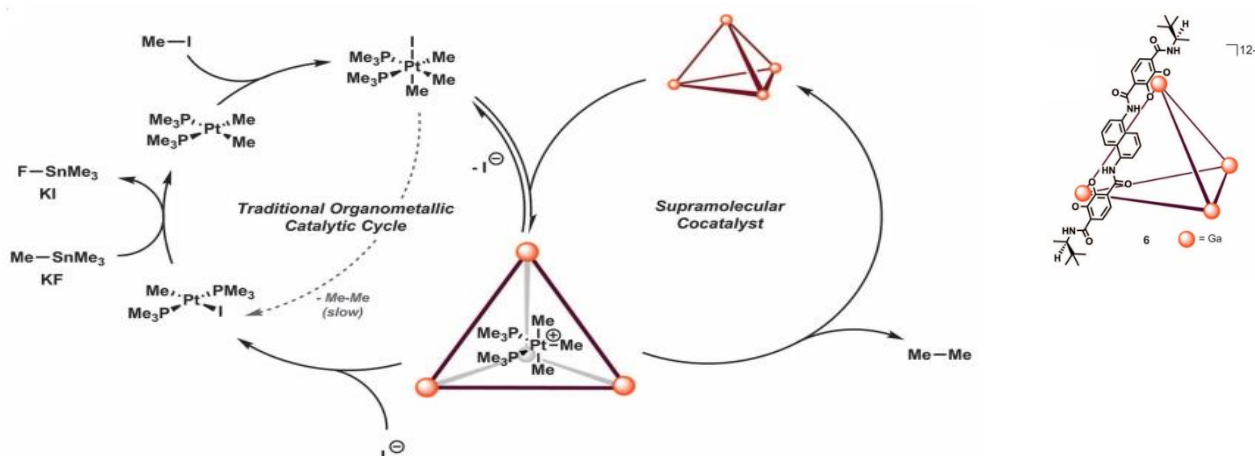


Figure 17 Demonstration of system Pt/Cage dual catalysis (from ref. ⁵²)

II.3.2. Separation properties

Due to their solubility and large, tunable internal cavities, MOCs have the ability to selectively bind and separate target molecules from a mixture. Additionally, the versatility of MOCs allows the functionalization of their internal surfaces, which further enhances their separation abilities. Here below, we will focus on few detailed examples.



The separation properties of MOCs have been widely demonstrated in various phases, such as liquid-liquid extractions, solid-liquid extractions, phase transfer, and enantiomers separation using chiral cages. One notable example of liquid-liquid extraction with MOCs is the study conducted by Nitschke *et al.*,⁵³ who synthesized a Fe^{II}-based positively-charged tetrahedral MOC using an azaphosphatrane-based ligand. This cage was able to selectively encapsulate ReO₄⁻ anion in a water solution through competitive guest exchange, in presence of many other ions such as F⁻, Cl⁻, Br⁻, I⁻, SO₄²⁻, ClO₄⁻, NO₃⁻, BF₄⁻, H₂PO₄⁻, and AcO⁻, with 97% ReO₄⁻ extraction efficiency.

In a follow-up study,⁵⁴ the same MOC was modified to be soluble in water-immiscible nitromethane, and this MOC demonstrated the ability to extract ReO₄⁻ from the water phase to the organic phase with an extraction efficiency of up to 97% (Figure 18).

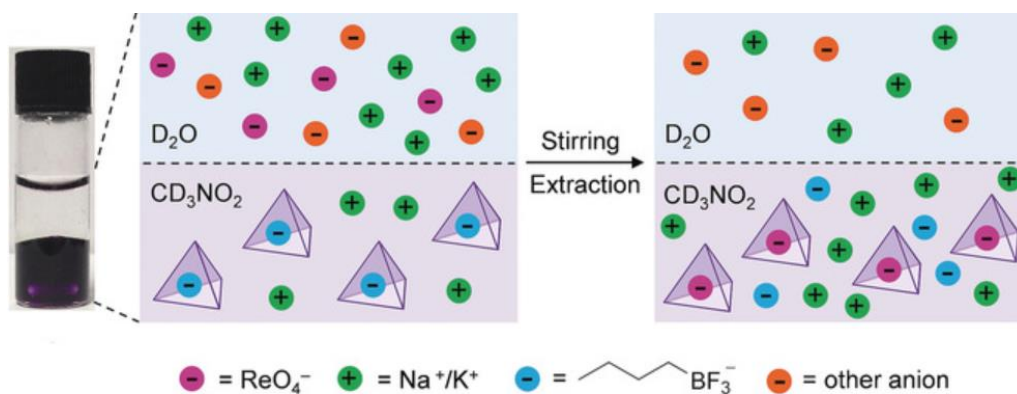


Figure 18 Selective extraction of ReO₄⁻ anion from water phase to organic phase (Tetrahedron represents Fe-based MOC) (from ref. ⁵⁴)

Another example of separation properties using MOCs is the study of Zhang *et al.*,⁵⁵ which demonstrated the separation of para-dihalogenated benzene derivatives, using a Rh-Ag MOC. This cage was able to selectively encapsulate para-isomers from an hexane to methanol solution. Photosensitivity of the described cage allows the release of encapsulated para-dihalogenated derivatives under light irradiation which destroys the cage.

Solid-liquid extraction was also well-demonstrated by the extraction of different fullerenes from a tetrachloroethane solution into a solid phase of MOC.⁵⁶ Authors have shown temperature-dependent binding preference of carcerand-like MOC for C₆₀ and C₇₀. It was shown that both complexes “C₆₀⊂carcerand” and “C₇₀⊂carcerand” form at temperatures below 110°C. However, C₆₀⊂carcerand exclusively formed at 130°C, leaving C₇₀ in solution which means the possibility to selectively extract fullerenes from the mixture. Furthermore, it is possible to release encapsulated fullerenes from the MOC in 4-dimethylaminopyridine.

Finally, one of the most interesting MOCs properties is the enantiomeric separation. Enantiomeric separation properties by MOCs were investigated by Su *et al.*, for instance, separation of R/S-BINOL and R/S-spiridol by octahedral Δ and Λ mixed Pd/Ru cages.⁵⁷ Extraction of R/S-BINOL and R/S-spiridol as guests from diethyl-ether solution, or uptake the guest to a solid state in the process of solid-liquid extraction into an aqueous solution of chiral cages led to stereoselective resolution of Δ -R and Λ -S host-guest complexes with enantiomeric excess up to 34% (Figure 19). Further, Su *et al.* demonstrated a new method for preparing enantiopure octahedral MOC from racemic Fe^{II}-based ligands by addition of R-BINOL during self-assembly process. Obtained enantiopure octahedral cages could then be used for R/S-BINOL separation with enantiomeric excess up to 88%.⁵⁸

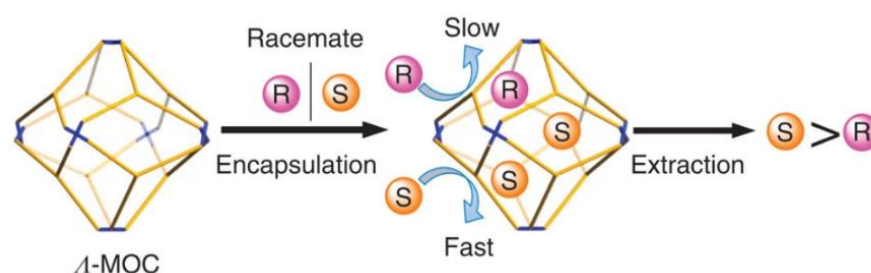


Figure 19 Proposed mechanism of R/S-BINOL enantiomers separation based on MOC (from ref.⁵⁷)

These examples demonstrate the infinite possibilities of MOCs for the separation properties in solution. It is possible to achieve a selectivity towards targeted guests by connectors and nodes modification which leads to the formation of MOCs with suitable cavities.

II.3.3. MOCs in medicine: drug carriers and imaging

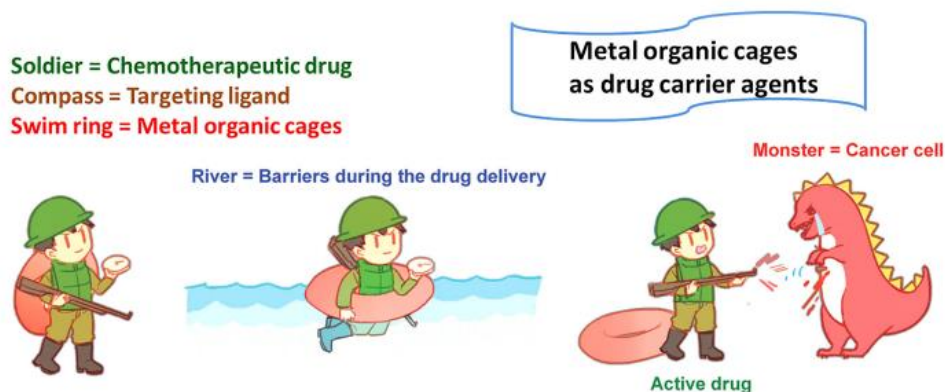


Figure 20 Cartoon representation of MOCs application in targeted drug delivery systems (from ref.⁵⁹)

The ionic nature of some water-soluble MOCs allows them to be widely used in biological applications, such as imaging and targeted drug delivery.¹⁸ It was shown that MOCs can have



applications in chemotherapy due to their distinctive guest capture ability.⁴⁸ For example, the solubility of some poorly soluble anticancer drugs can be significantly improved when incorporated in MOCs (Figure 20). Furthermore, many anticancer agents are not stable in the body environment, but the formation of host-guest complexes with MOCs can preserve their activity.⁵⁹ Besides, high accumulation of the anticancer agents in a tumour can be achieved from enrichment effect of MOCs, remarkably enhancing the efficiency of the supramolecular chemotherapeutic agents and reducing the side effects towards normal tissues.⁶⁰

One of the attractive features of MOCs as drug carriers is their ability to host multiple drug molecules, in contrast to traditional carriers like calixarenes or cyclodextrins that can only accommodate one molecule. This increased capacity can lead to higher concentrations of the therapeutic agent into targeted cells, potentially improving the efficiency of the treatment while also decreasing the overall chemical exposure of the organism by virtue of using smaller amounts of the carrier.⁵⁹

Another potential application of MOCs in biological fields is the selective sensing and imaging. With the outstanding sensing property, MOCs could work as chemosensors towards certain substrates, reactions or processes.⁶¹ Yu *et al.* reported the anion sensing of HSO_3^- in aqueous solution by hexametallic-organic cages.⁶² The cages were built from tris(4-(1H-pyrazol-3-yl) phenyl)amine as tripod connector, and di-Pd^{II} motifs as metal vertices. The structure of the resulting hexametal-organic cages can be adapted by selectively interacting with HSO_3^- anions and is illustrated as efficient fluorescence sensor. Mascaren's *et al.* reported the anion sensing of a tetrahedral MOC, which specifically binds to the pyronine moiety, that facilitates the supramolecular complex entering the cell.⁶³ This host-guest interaction enables the complex to pass the cell membrane, while none of the components, neither the host nor the guest, are able to cross the cell membrane on their own. Sun *et al.* also demonstrated a rare earth Eu (III)-based tetrahedral MOC with a record emission quantum yield of 23.1%. High sensitivity and selectivity are revealed for the cage in both turn-off luminescent sensing toward I^- and turn-on sensing toward Cu^{2+} .⁶⁴

In this part we provided many examples of MOCs together with their geometrical features and properties. The field of their applications is very large starting from the remarkable catalytic properties and ending with the design of targeted drug delivery systems.

In the next section we will focus on the main topic of this work: calixarene-based MOCs, their geometrical characteristics and applications.

III. Calixarene-based MOCs

MOCs based on calixarene is an intriguing research area because it combines the unique structural properties of macrocyclic calixarene moieties with the functional properties of metal ions. For example, the calixarene imposes to the MOCs a larger central cavity and the ability to form inclusion complexes with larger guest molecules in comparison with other reported MOCs, while the metal ions can introduce new chemical and physical properties, such as catalytic activity, magnetic behaviour, and optical properties, as already mentioned.^{47,65}

Here below, we will discuss special properties of calixarene moieties that make them excellent candidates for the MOCs formation.

III.1. Generalities on calix[4]arene

The calixarene derivatives, a well-known macrocyclic species, has been chosen to be one of the components for the formation of the MOCs, due to their peculiar structural features, their ability to be chemically modified, as well as their properties.⁶⁶

One of the most notable characteristics of the family of calixarene macrocyclic moieties is the ability to adopt different conformations in solution and in the solid state, which provides to them the versatility to perform a variety of functions. For example, calix[4]arenes display the conformations of cone, partial cone, 1,2-alterante, 1,3-alternate (Figure 21). Theoretically, this feature can be useful to control the shape of the building block while building MOCs. However, it was noticed from the literature analysis, that for the formation of calixarene-based MOCs, only the cone conformation was observed.

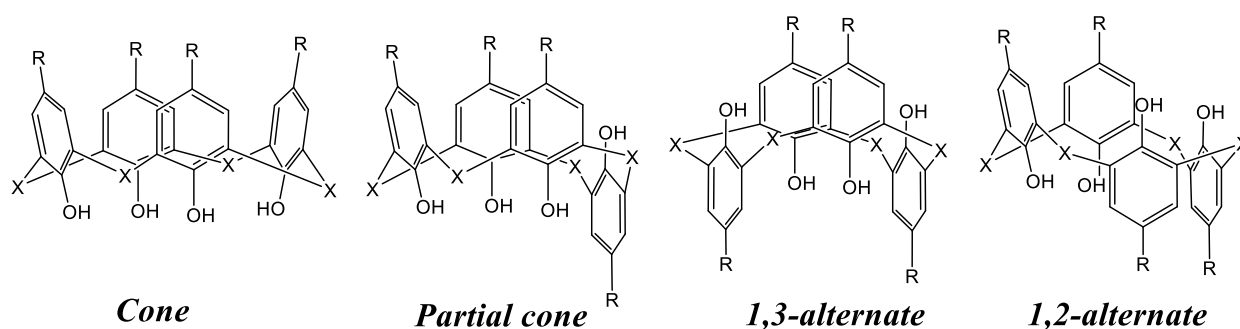


Figure 21 Calix[4]arene conformations

There are three different calixarene families that have been mostly used for the formation of calixarene-based MOCs: classical calix[4]arene,⁶⁷ thiacalix[4]arene⁶⁸ and sulfonylcalix[4]arenes⁶⁹ (Figure 22). Due to the presence of sulphur atoms and additional oxygen atoms, families of thiacalix[4]arenes and sulfonylcalix[4]arenes display better metal coordination properties. It was demonstrated that thiacalix[4]arene and sulfonylcalix[4]arenes are able to form complexes with the variety of d-metal ions.^{70,71} These complexes usually consists of one calixarene



species, four d-metal ions and, sometimes, one μ -water molecule located in the middle of the square formed by the metal ions.⁶⁴ This feature makes thiacalix[4]arenes and sulfonylcalix[4]arenes the best candidates for the formation of sophisticated metal nodes in the structure of MOCs, because that allows to increase the general number of metal ions involved in the structure of the desired MOCs, as it was mentioned in §I.5 of this chapter.

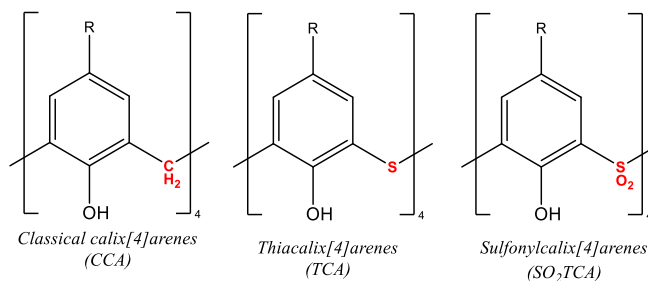


Figure 22 Calix[4]arene families most common in MOCs

In the following sections, we will examine the structure and geometry of MOCs based on calixarenes, as well as their advanced properties related to the presence of calixarene moieties in the structure.

III.2. First calixarene-based metal-organic cage

The idea of using calixarene moieties in the structure of MOCs was driven by the desire to improve the cage structure in order to achieve new properties. In this section, we will discuss the approaches that lead to the sophistication of metal nodes in the structure of the resulting MOCs.

One approach is the use of metal ions clusters instead of single metal ions, as described in several works.²³ Another possibility is to use calixarene-based clusters, as it was firstly reported in 2012.^{72,73} The authors used polynuclear metal clusters of *p-tert*-Butylthiacalix[4]arene as metal nodes. Previous studies^{70,74} have demonstrated that *p-tert*-Butylthiacalix tends to form tetranuclear complexes with transition metals, resulting in **shuttlecock-like building units** (Figure 23). This property to synthesize a series of octahedral calixarene-based MOC was exploited. The octahedral MOC synthesized consists of six tetracobalt-*p-tert*-Butylthiacalixarene units connected by tricarboxylate connectors of various sizes (Figure 23). The obtained calixarene-based MOC belongs to the class “face-panelled MOCs” discussed in §II.1. of this chapter.

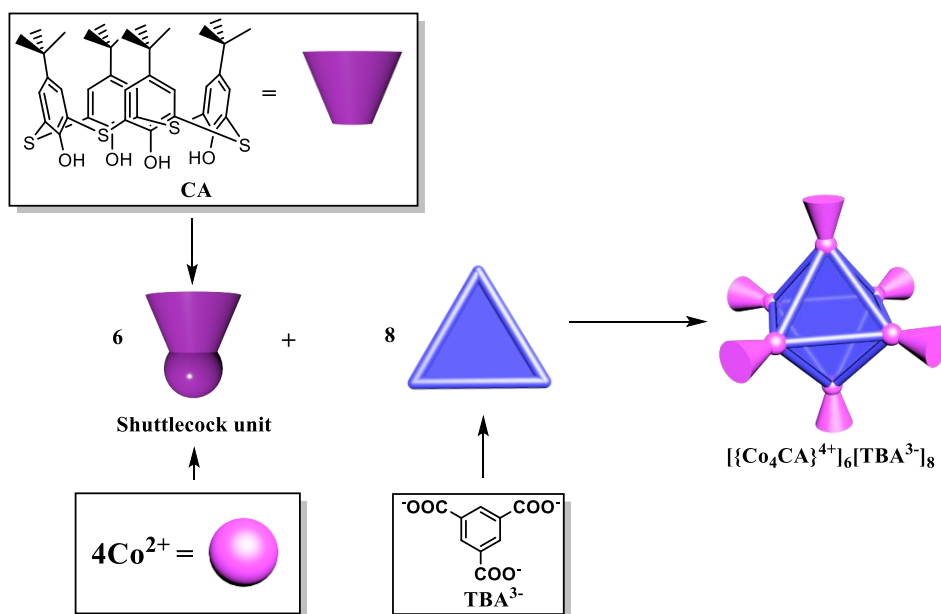


Figure 23 The process of supramolecular self-assembly of tetracobalt-*p*-*tert*-Butylthiacalix[4]arene and tricarboxylate linkers leading to the octahedral calixarene-based MOC

The use of calixarenes in the structure of MOCs allows to open new fields for structural varieties and applications. The benefits along with geometry and properties of calixarene-based MOCs will be discussed more in detail in the following section.

III.3. Calixarene-based MOCs: formation and synthesis

Calixarene moieties have been used for the formation of coordination cages for more than 10 years.^{72,73} As it was mentioned in §III.1., calixarenes can be observed as bowl-shaped molecules, in cone confirmation exclusively in the structure of MOCs (Figure 21). In MOCs, they display the feature to coordinate four d-metal ions (and sometimes also one μ -H₂O molecule) by one calixarene molecule (CA), leading to the formation of perfect **shuttlecock nodes** [M₄CA(μ -OH₂)]⁴⁺ (Figure 24).⁷¹

A connector is typically a ditopic ligand, able to coordinate the metals in the structure of the shuttlecock node [M₄CA(μ -OH₂)]⁴⁺, having free positions in their coordination spheres. The most frequently encountered connectors that are used for the cage formation present the carboxyl coordinating groups. The connectors can be linear,⁷⁵ angular⁷⁶ and triangular⁷⁷ with different number of binding positions. A non-exhaustive list of connectors is depicted in reference.⁷⁸

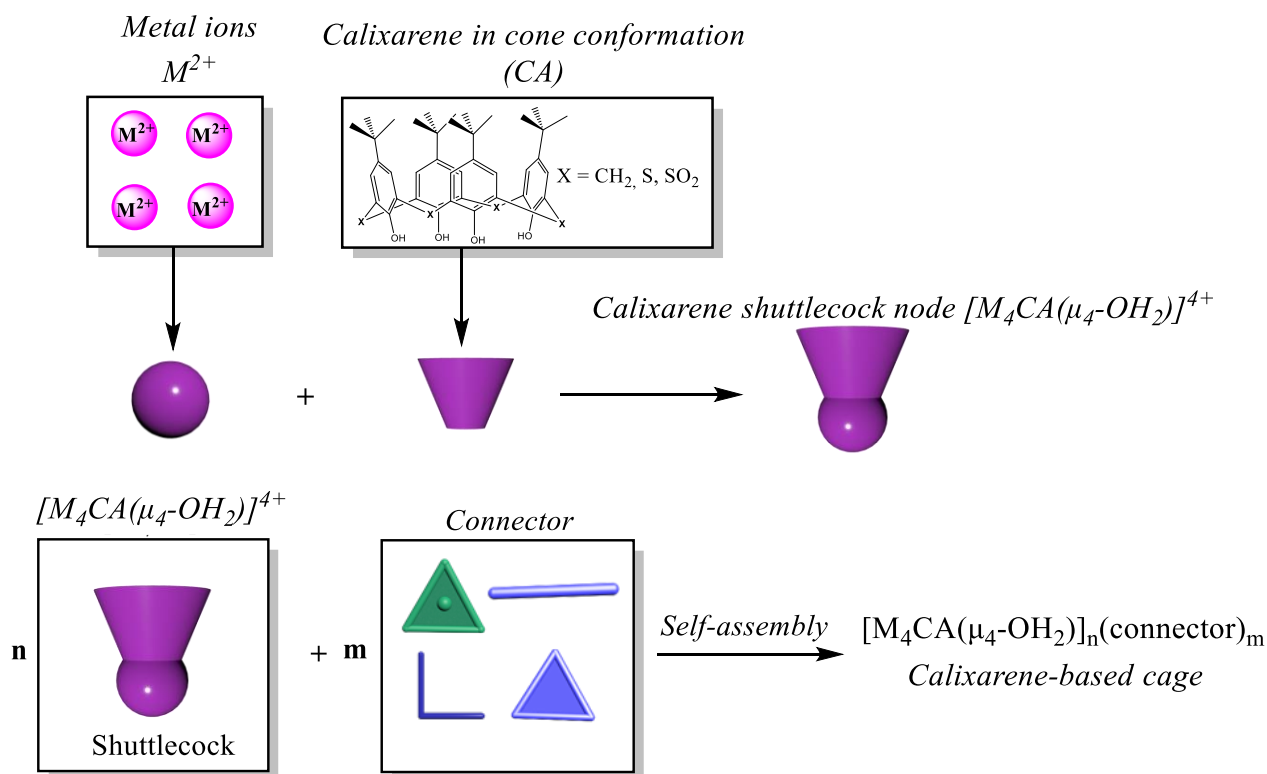


Figure 24 Formation of calixarene shuttlecock node $[M_4CA(\mu_4-OH_2)]^{4+}$; self-assembly process of shuttlecock nodes with connectors for the formation of calixarene-based cage

Various synthetic conditions must be considered. The choice of these conditions is crucial to achieve the desired cavity and the desired properties of the MOCs. The synthetic approaches for the formation of these MOCs have been extensively investigated, and solvothermal⁷⁹ methods have been demonstrated to be the most effective methods for synthesizing these cages. These methods involve the use of high temperatures and high pressure to ensure the formation of the desired MOCs. However, the solvents used in the calixarene-based MOCs synthesis are limited by the requirement to solubilize connectors, calixarenes, and metal salts. Among the commonly used solvents, dimethyl sulfoxide, N,N-dimethylformamide, acetonitrile and N,N-dimethylacetamide have demonstrated a great potential for the efficient synthesis of MOCs.

It should be noted that the choice of the synthetic parameters, such as temperature, pressure, and solvent, can greatly affect the structure and properties of the resulting MOCs. Therefore, the optimization of these conditions is critical in order to obtain MOCs with the desired properties. Moreover, while solvothermal methods are commonly used for the MOC synthesis, alternative methods such as microwave-assisted synthesis⁸⁰ have also been reported, which may provide more efficient and sustainable approaches for the synthesis of MOCs.

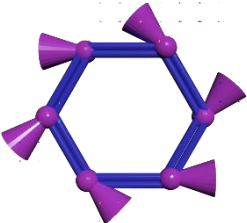
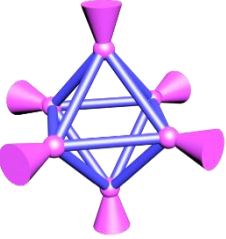
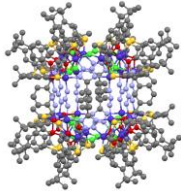
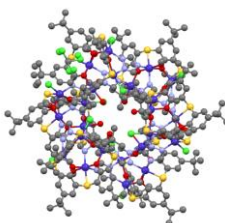
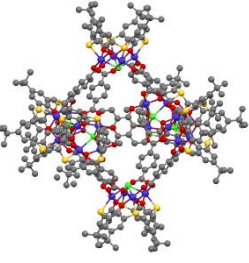
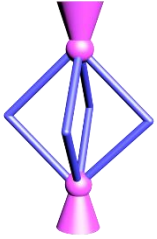
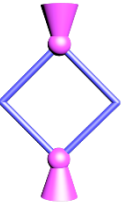
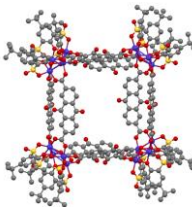
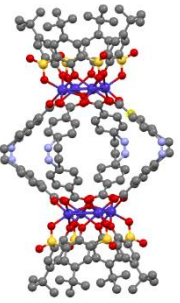
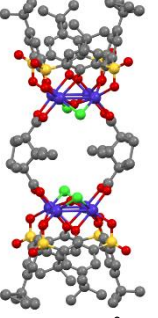
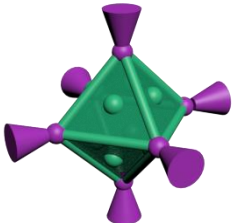
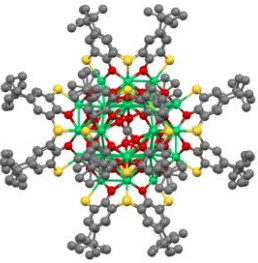
As a conclusion, the synthesis of the calixarene-based MOCs is the result of a **three-components** process, as shown in Figure 24: during the synthesis, the shuttlecock nodes



$[M_4CA(\mu_4-OH_2)]^{4+}$ are formed, and they are suitable to interact through coordination bonds with connectors, behaving like “complex as ligand”, to lead to the formation of large cages.

III.4. Calixarene-based MOCs: geometry

Having in hands a three-components system when forming MOCs based on calixarenes, the number of reachable stable geometries is rather limited. And there are specific parameters that are orienting the type of cages that can be obtained using the combination of metals, calixarenes and connectors. The nature and geometry of the connectors along with the used stoichiometry connector/node play a significant role in determining the overall geometry of the resulting MOC.⁷⁸ In Table 2 we summarized the already reported cages obtained from the combination of metals, calixarenes and connectors, along with their geometrical characteristics. This list is non exhaustive, though most of the examples have been reported.

Connector nature	Node nature	Resulted cage geometry			Synthesized examples with cavity diameters		
 <p>Linear bidentate (LB)</p>	 <p>Complex calixarene node M_4CA</p>	 <p>Cube⁷⁵ [M_4CA]₈LB₁₂</p>	 <p>Macrocyclic⁸¹ [M_4CA]₆LB₁₂</p>	 <p>Octahedron^{82,83} [M_4CA]₆LB₁₂</p>	 <p>D=14Å (from ref. ⁷⁵)</p>	 <p>D=9Å (from ref. ⁸¹)</p>	 <p>D=16Å (from ref. ⁸²)</p>
 <p>Angular bidentate (AB)</p>	 <p>Complex calixarene node M_4TCA</p>	 <p>Truncated Cuboctahedron⁸⁴⁻⁸⁷ [M_4CA]₄AB₈</p>	 <p>Barrel⁸⁸⁻⁹¹ [M_4CA]₂AB₄</p>	 <p>Barrel⁷⁶ [M_4CA]₂AB₂</p>	 <p>D=18Å (from ref. ⁸⁴)</p>	 <p>D=11Å (from ref. ⁸⁸)</p>	 <p>D=6Å (from ref. ⁷⁶)</p>
 <p>d-metal ions, Co^{2+}, Ni^{2+} (M)</p>	 <p>Complex calixarene node M_4TCA</p>	 <p>Octahedron⁹² [M_4CA]₆M₈</p>			 <p>D=7Å (from ref. ⁹²)</p>		

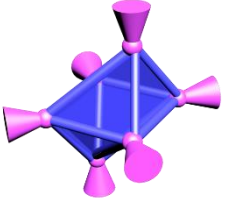
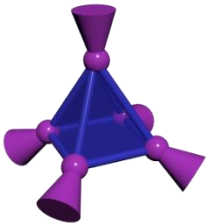
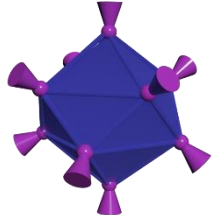
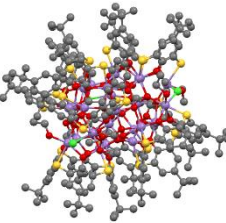
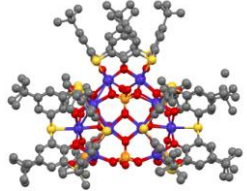
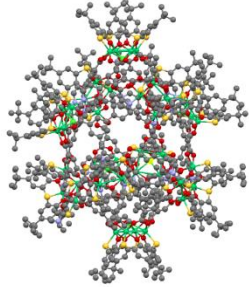
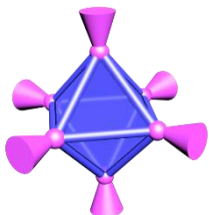
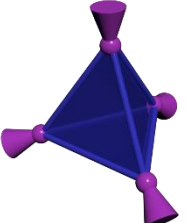
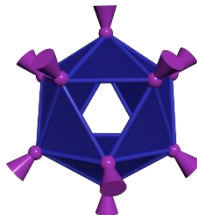
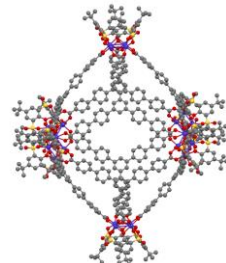
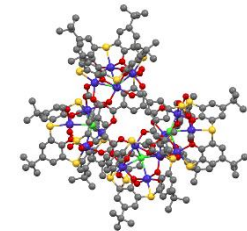
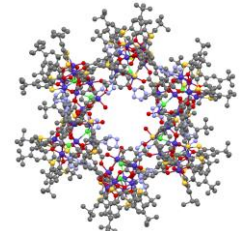
 Tridentate (T)	 Complex calixarene node M ₄ TCA	 Distorted octahedron ⁷⁷ [M ₄ CA] ₆ T ₈	 Tetragonal pyramid ⁹³ [M ₄ CA] ₅ T ₈	 Hexadecahedron ⁹⁴ [M ₄ CA] ₁₀ T ₁₆	 D=7Å (from ref. ⁷⁷)	 D=9Å (from ref. ⁹³)	 D=21Å (from ref. ⁹⁴)
		 Octahedron ^{84,95-97,98} [M ₄ CA] ₆ T ₈	 Tetrahedron ⁹⁹ [M ₄ CA] ₄ T ₄	 Icosahedron ¹⁰⁰ [M ₄ CA] ₁₂ T ₂₀	 D=27Å (from ref. ⁹⁸)	 D=8Å (from ref. ⁹⁹)	 D=22Å (from ref. ¹⁰⁰)

Table 2 *The most frequently observed combinations of (Metals + calixarenes + connectors), and resulting calixarene-based MOCs, their geometry and their internal cavity diameters*

The data represented in Table 2 reveal that the calixarene shuttlecock nodes usually serve as vertices in the formation of polyhedral cages, and the final geometry of the cage is mostly dependent upon the flexibility, geometry, number of binding positions and angle between binding positions of the used connectors. Based on our literature review, we have documented the presence of 12 distinct geometries of calixarene-based MOCs with internal cavity diameters ranging from 7 Å to 27 Å:

- Face-panelled and edge-panelled octahedra,
- Distorted octahedra,
- Tetrahedra,
- Icosahedra,
- Hexadecahedra,
- Tetragonal pyramids,
- Truncated cuboctahedra,
- Two types of barrels,
- Macrocycles,
- Cubes.

The most frequently encountered geometry for calixarene-based MOCs is the octahedral one, which consists of an octahedron-like cage with shuttlecock units at each of the six vertices. Controlling the geometry of the calixarene-based MOCs can be challenging as it depends on a combination of several factors. However, some control can be achieved by modifying the synthetic conditions: among them the nature of the used connectors, the concentration of components, and the reaction time. Additionally, the nature of the calixarene derivatives and metal ions can also influence the geometry of the resulting MOC.

A significant amount of calixarene-based MOCs display internal cavity diameters exceeding 10Å, indicating that they are generally characterized by large internal cavities that are well-suited for host-guest interactions with a range of molecular species.

The geometry of calixarene-based MOCs has a direct impact on their properties and potential applications. In the following section, we will discuss some of these properties and focus our attention on the possible calixarene-based MOCs applications.



III.5. Calixarene-based MOCs based on organic connectors: properties

Besides the ability to form tetranuclear clusters with a large variety of d-metals, another one major advantage of using thiacalix[4]arenes and sulfonylcalix[4]arenes usage for the formation of MOCs, is to improve the thermal stability of the self-assembled species compared to the one of classical calixarenes.³ This opens a wide range of applications, such as high-temperature catalysis and gas storage. Additionally, these molecules present a higher acidity, which allows a larger affinity towards metal ions and a higher metal-loading capacity.

Calixarenes moieties are famous for their natural shape as cone, and their ability to form host-guest complexes due to their macrocyclic nature, which provides perfect pores for encapsulation of small molecules, like for example, methane.¹⁰¹ They present a high adsorption activity towards gas inherent to their geometry. Furthermore, calixarenes moieties have demonstrated unique properties for molecular separation, for example, extraction of organic molecules from water, selective gas adsorption, selective inclusion of organic molecules, etc.¹⁰²

The unique physical characteristics of thiacalix[4]arenes and sulfonylcalix[4]arenes, that form MOCs, confer to MOCs properties: like higher surface area, improved gas adsorption properties and ability to host larger guests.⁹⁸ These unique properties of calixarene-based MOCs will be discussed in the following section.

III.5.1. Gas adsorption properties

Gas adsorption properties of calixarene-based MOCs will be discussed in depth in §I.1. of **Chapter IV**. In this section we intend to provide a generalised understanding of the gas adsorption properties of MOCs and discuss the influence of a connector structure on these properties.

The adsorption properties of thiacalix[4]arene-based and sulfonylcalix[4]arene-based MOCs have been already studied, however this field is relatively underexplored. In comparison with MOFs, MOCs usually demonstrate smaller Surface Area. For instance, MOFs frequently exceed BET surface area of 3000 or even 4000 m²/g. On the same time, BET surface area of the largest synthesized calixarene-based MOCs do not exceed 1300 m²/g.¹⁰³ However, the adsorption properties of MOCs can be modulated through the use of specific connectors.

For example, the formation of a series of octahedral MOCs (Figure 25) based on the enlarged tetracobaltthiacalix[4]arene shuttlecock units and tricarboxylate connectors with BET surface area 605 m²/g has been reported.⁷² This is relatively high when compared to the structurally similar calixarene-based MOCs.⁹⁸

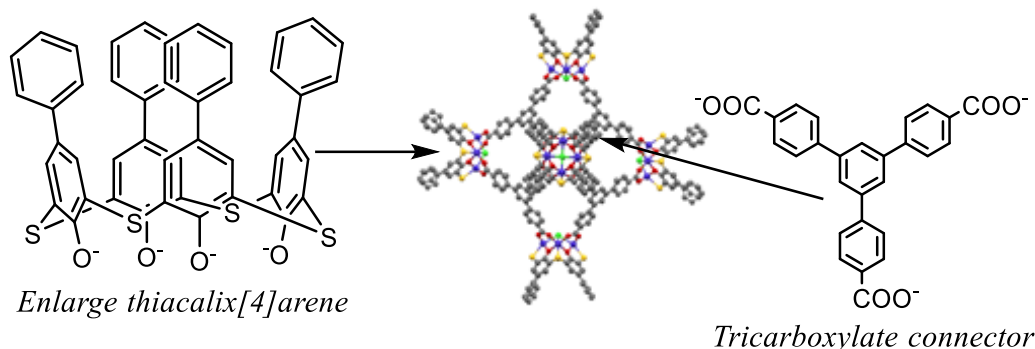


Figure 25 Octahedral cage base on enlarged tetracobaltthiocalix[4]arene shuttlecock units (from ref.⁷²)

In a noteworthy study,⁹⁸ the formation of isorecticular MOCs (presenting the same coordination pattern and also the same connectivity) using various sizes of tridentate connectors (Figure 26a,b) was demonstrated. It was observed that the use of larger connectors provided MOCs with improved adsorption properties, as evidenced by the higher BET surface areas observed for the larger cage CIAC-114 with cavity diameter of 27Å (558 m²/g) compared to the smaller one CIAC-106 with cavity diameter of 19Å (410 m²/g). These results highlight the potential of tailoring the connector shape in order to improve adsorption properties.

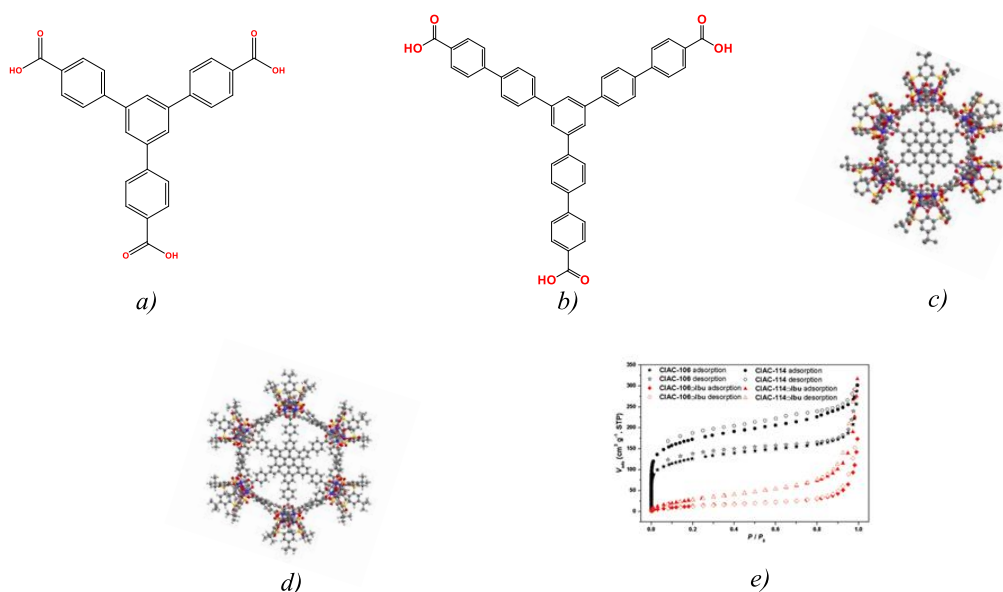


Figure 26 CIAC-106 connector structure (a); CIAC-114 connector structure (b); Structure of CIAC-106 calixarene-based MOC (c); Structure of CIAC-114 calixarene-based MOC (d); Nitrogen adsorption-desorption isotherm of cages CIAC-106 and CIAC-114 (e) (from ref.⁹⁸)

III.5.2. Recognition properties

Observation of good gas adsorption properties accounts for the fact that calixarene-based MOCs have large internal cavity that could be exploited not only for gas adsorption but also for encapsulation of other molecules in a process of recognition

Guest recognition properties of calixarene-based MOCs are widely described in the literature. For example, host-guest properties were investigated on guest molecules as methylene blue,⁸⁷ that is widely used for the investigation of adsorption properties of MOFs, and also on eosin Y.⁹¹ Not only model compounds were employed to study the host-guest properties of MOCs. Also calixarene-based MOC exhibiting excellent binding properties with amine derivatives was recently described.⁹⁰ In 2014, Wang *et al.* reported the host-guest properties of an octahedral MOCs based on tetranuclear-sulfonylcalix[4]arene units ($M = Ni^{II}, Co^{II}, Mg^{II}$) and terephthalic acid towards methylene blue and acetylsalicylic acid using various methods, including homogeneous-solution guest binding, liquid-liquid extraction, solid-liquid adsorption, and solid-gas adsorption.¹⁰⁴ The occurrence of host-guest interactions was demonstrated, among others, through the shift in absorbance on the UV-vis spectra observed during the titration of a MOC solution with methylene blue solution (Figure 27a). The transition of methylene blue, which is more soluble in water, to the chloroform phase in the presence of MOCs during a liquid-liquid extraction experiment was also observed (Figure 27b). The solid-liquid adsorption experiment showed that MOCs could effectively adsorb a large amount of methylene blue from the aqueous solution (5 molecules of methylene blue by the one cage) (Figure 27c).

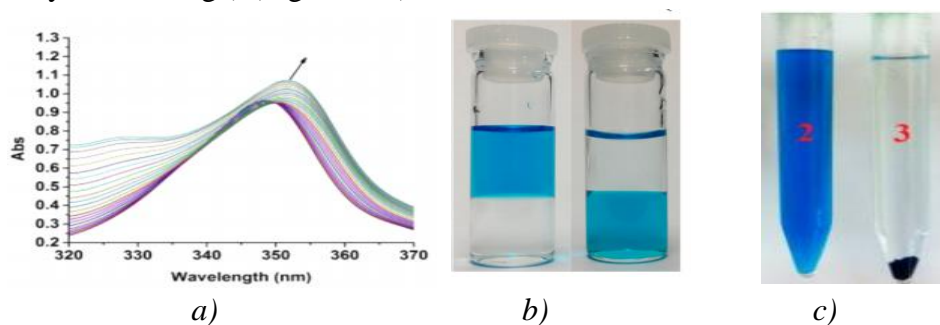


Figure 27 Experiments of octahedral calixarene-based MOCs solution titration with methylene blue (MB) solution(a); results of liquid-liquid extraction experiment(b); results of liquid-solid adsorption experiment(c), where 2 is the solution of MB before addition of cage and 3 is the solution of MB after addition of MB. (from ref. ¹⁰⁴)

Furthermore, applying of stimuli-responsive connectors (pH responsive amino-groups,¹⁰⁵ solvent responsive polyaromatic systems¹⁰⁶), for the formation of calixarene-based MOCs, leads to stimuli-responsive MOCs. A calixarene-based MOC suitable for proton recognition based on connector with stimuli-responsive luminescent properties was reported,⁸⁶ exhibiting pH-dependent luminescence (Figure 28) that can be modulated by the addition of proton excess and quenched under addition of base, with multiple repetition of cycle switch on/off.

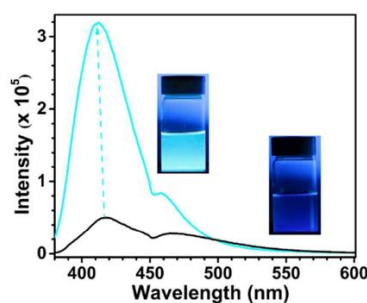


Figure 28 Fluorescent emission spectra of MOC 1-Zn before addition of an excess amount of proton (black) and after (cyan) (from ref. ⁸⁶)

A very recent work demonstrated the formation of MOC based on tetramagnesium-sulfonylcalix[4]arene and benzene-1,3,5-tribenzoic acid that exhibits excellent luminescent properties.¹⁰⁷ These properties allow the cages to be an efficient luminescent sensor for various species in the aqueous media. For example, this cage exhibits high sensitivity towards Fe^{3+} and MnO_4^- ions, nitrobenzene and 2,4-dinitrophenol. It was demonstrated by dramatic decreasing of luminescence with the addition of guests in small quantities (Figure 29).

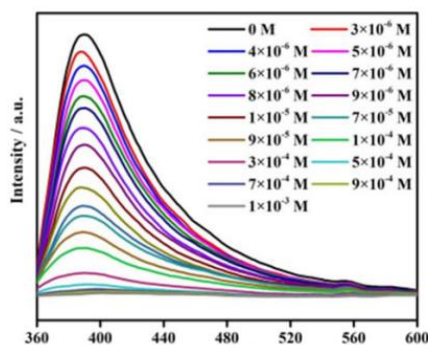


Figure 29 The emission spectra of calixarene-based Mg^{II} -MOCs excited at 328 nm with different concentrations of Fe^{3+} showing its sensor capacity to Fe^{3+} ions (from ref. ¹⁰⁷)

III.5.3. Drug delivery

As already mentioned, one of the advantages of calixarene-based MOCs is also their ability to accommodate large guests due to their spacious internal cavities. This ability has been demonstrated using the therapeutic guest *ibuprofen*, which was shown to be successfully hosted by MOCs through the decrease of nitrogen adsorption observed following *ibuprofen* adsorption (as depicted in the red adsorption-desorption isotherms of Figure 26e).⁹⁸

Calixarene-based MOCs have been mixed with biological active compounds in order to design target drug delivery. For example, octahedral calixarene based MOCs were tested with aspirin.¹⁰⁴ The results of this investigation, depicted in Figure 30a, showed a UV-titration profile similar to what is usually observed for substrate binding to enzymes. At low guest equivalents, nearly all of the added aspirin binds to the MOCs in a linear fashion, as indicated by the initial tangent of the curve (Figure 30). However, as the concentration of aspirin increases, only a portion of the guest binds to the MOCs due to weaker binding strength, leading to a deviation from the initial tangent. This suggests that binding to calixarene-based MOCs may be an effective way to greatly enhance the local concentration of drug molecules.

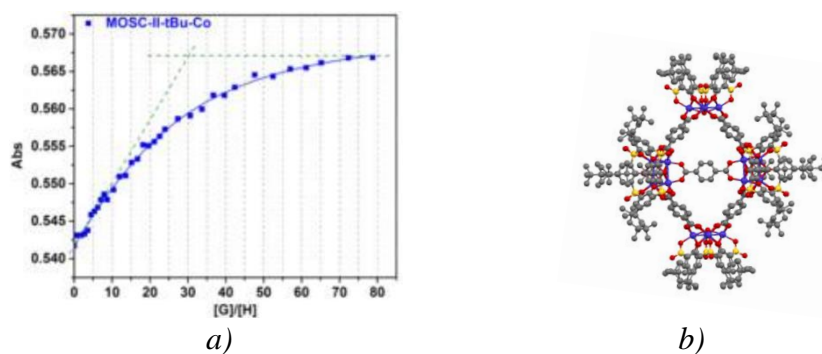


Figure 30 Change of the absorbance maximum at $\lambda = 348$ nm by changing the aspirin(G)/cage(H) ratio, representing an enzyme-like behavior (a); structure of the used octahedral cage $[M_4SO_2TCA]_6[H_2BDC]_{12}$ (from ref. ¹⁰⁴)

These observations demonstrate the potential of calixarene-based MOCs as drug carriers capable of delivering a wide range of large active molecules under different stimuli.

III.5.4. Catalysis

The host-guest interactions properties of MOCs play a significant role in determining their catalytic properties. The ability of MOCs to selectively and strongly bind guest molecules, as demonstrated in previous studies,^{98,104} opens up opportunities for the stabilization of catalytic species within the internal cavity during the catalytic process, in a confined space. By designing MOCs with optimized host-guest interactions, the conditions for catalysis can be effectively controlled, in confined media, leading to improved catalytic activity. Geometrical and electronic structure of discrete calixarene-based MOCs, allow them to participate to homogeneous catalytic reactions. Moreover, it was shown that highly hydrophobic upper rim of *p*-tert-butylsulfonylcalix[4]arene is helpful to prevent the hydroxide attack on the tetranuclearcalixarene moieties, thus improves the stability of the coordination containers for some reactions, for instance, oxygen evolution reactions, that could be useful for catalysis under hard conditions.¹⁰⁸

Catalytic activity of chiral octahedral calixarene-based MOC based on tetracarboxylate connectors with free phosphate group was demonstrated, for example, for the asymmetric Friedel-Crafts reaction of N-sulfonyl aldimines with indole (*ee* is up to 99%) and asymmetric [3+2] coupling reaction (*ee* is up to 99%).¹⁰³ Catalytic activity of dimeric calixarene-based MOC with barrel-like shape was also investigated for Knoevenagel reactions as represented in the Figure 31.⁸⁹ In some cases (for example, for pyrene-1-carbaldehyde), an increase of the yields up to nearly quantitative (95%) was observed in this cage. The catalytic activity appears to be linked with the shape and not the size of the used aldehydes.

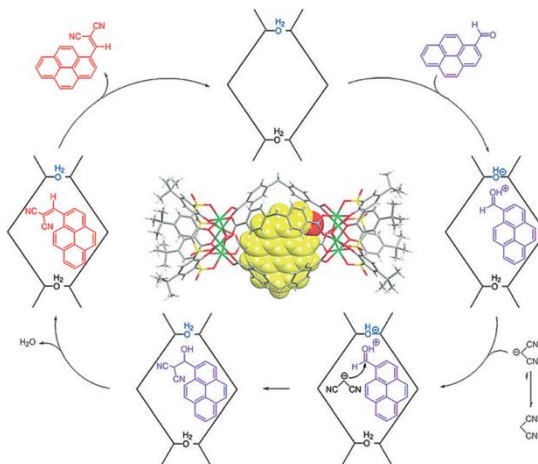


Figure 31 Proposed mechanism of the Knoevenagel condensation catalysed by a barrel-like shaped dimeric calixarene-based MOC (from ref. ⁸⁹)

Calixarene-based MOCs presenting the same geometry were reported to be also highly efficient electrocatalysts for the oxygen evolution reaction.¹⁰⁸

The photocatalytic activity of octahedral and cubic calixarene-based MOCs with anthraquinone connector was recently demonstrated. It was shown that it is possible to use these cages as efficient catalysts for the reaction of photocatalytic selective [2+2] cycloaddition of α,β -unsaturated carbonyl compounds, while obtaining corresponding cyclobutanes.⁸⁴

Catalytic activity of calixarene-based MOC can be also demonstrated by the stabilization of certain catalytically active species inside the internal cavity with perseverance of their catalytic activity.^{97,109} This outstanding calixarene-based MOCs property was well demonstrated using a trigonal prism calixarene-based MOC with thiophene-2,5-dicarboxylic acid connector. This cage is suitable for the stabilization of Pt-nanocluster, containing less than 18 Pt atoms inside the MOC cavity (Figure 32).¹⁰⁹ This system exhibits higher electrocatalytic activity than commercial Pt/C towards hydrogen evolution reaction due to large accessible surface area of Pt-nanoclusters that are stabilised inside the cavity of the MOC.

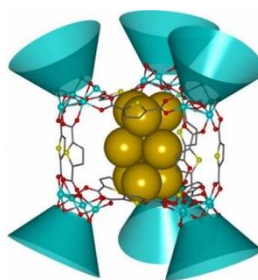


Figure 32 Stabilization of Pt nanocluster (yellow spheres) inside a trigonal prism shaped calixarene-based MOC (from ref. ¹⁰⁹)

Great adsorption properties of certain calixarene-based MOCs leads to possibilities for catalytic reactions involving trapped gases. For example, an imidazolium-functionalized calixarene-based cage presents suitable sites for CO₂ coordination that provides possibility to catalyse CO₂ cycloaddition reactions without cocatalyst. The catalytic activity of this calixarene-based MOC was investigated through the reaction of CO₂ cycloaddition with epichlorohydrin, achieving conversion rates up to 95% and yields up to 93% which opens outstanding perspectives for applying cages in CO₂ capture systems (Figure 33).⁸³

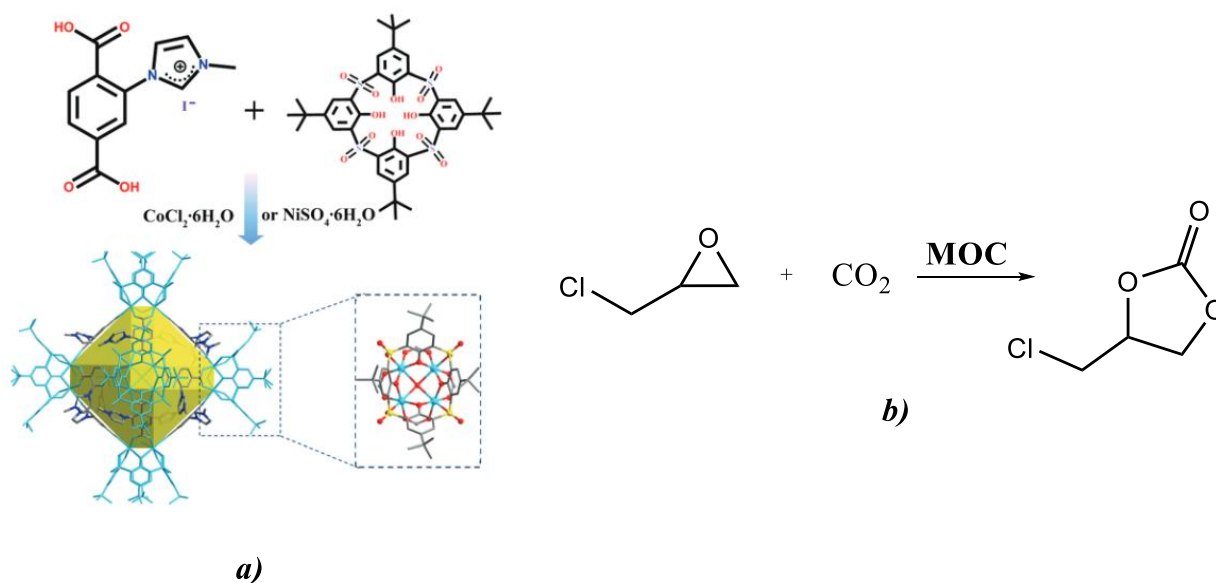


Figure 33 The structure of imidazolium-functionalized octahedral calixarene-based MOC (a) (from ref. ⁸³); The MOC catalysed reaction of CO₂ cycloaddition with epichlorohydrin (b)

III.6. Calixarene-based MOC with Metal-Organic connectors

The aforementioned calixarene-based MOCs were built using only organic connectors. The use of metal-organic connectors instead of purely organic connectors in MOCs offers promising perspectives for several reasons. Firstly, metal-organic connectors increase the number and density of metal centres around the formed cage, providing new coordination positions that may be beneficial for catalysis. Additionally, metal-organic complexes are typically larger than organic connectors, offering the potential for the formation of larger cages.

Despite the potential advantages offered by the use of metal-organic connectors in MOCs, there is currently only one reported example till now (2022) of a calixarene-based MOC using such connectors - the octahedral MOC based on 6 tetrazincsulfonylcalix[4]arene units linked by 12 linear chiral Mn(II) salen connectors (Figure 34).⁴ This chiral MOC is particularly interesting from the perspective of asymmetric catalysis due to several reasons.

Firstly, Mn(II) metal ions in the salen connector presents unoccupied coordination positions in the axial positions, exhibiting significant potential for catalytic applications. Secondly, Mn(II) salen metal organic connector is chiral and consequently, the formed MOC is expected to be also chiral. Thirdly, formed MOCs features a large hydrophobic cavity ($D = 19\text{\AA}$) decorated with catalytically active chiral metallosalen species.

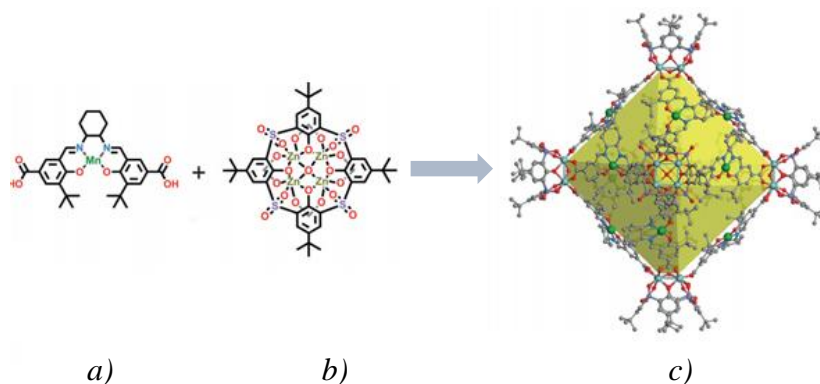


Figure 34 Structure of Mn (II) salen connector (a); structure of tetrazincsulfonylcalix[4]arene unit (b); Structure of the chiral octahedral cage $[Zn_4(SO_2TCA)]_6[MnL]_{12}$ (from ref. ⁴)

The catalytic activity of this MOC was demonstrated through alcohol oxidation and epoxidation reactions. In these experiments, racemic secondary alcohols and alkenes were used and the catalytic activity of the MOC was compared to the one of the Mn(II) salen connector alone in order to establish the superior catalytic activity of the MOC. It was established that the enantiomeric excess could be increased up to 99% in the case of alcohol oxidation and up to 96% in the case of epoxidation. Additionally, the presence of small amounts of the chiral MOC in the



reaction mixture led to an increase in conversion compared to the use of Mn(II) salen alone. These results can be attributed to the deactivation of the Mn(II) salen catalyst during the reaction process. The inclusion of Mn(II) salen in the cage structure helps to preserve the catalyst from deactivation along with providing an hydrophobic cavity to concentrate the reactants, contributing to the observed enhancement in catalytic activity.

This example is particularly noteworthy due to its focus on metal-organic connectors in octahedral calixarene-based MOCs. As already mentioned, to the best of our knowledge, this is the only reported work using such connectors in MOCs, making it an important contribution to the field. The authors have demonstrated the potential of these connectors in MOC synthesis and have provided a detailed investigation of their catalytic activity. This work highlights the promising possibilities for the use of metal-organic connectors in MOCs and the potential for further exploration of their properties and applications.



IV. Conclusion

The investigation of supramolecular calixarene-based MOCs appears important. Firstly, MOCs have the potential to be used as homogeneous catalysts in chemical reactions, as they can selectively bind and activate reactants. This could lead to the development of more efficient and selective catalysts (for homogeneous and heterogeneous catalysis), which would have a significant impact on many industrial processes. Additionally, the study of the catalytic activity of MOCs can provide insight into the mechanisms of chemical reactions at the molecular level in confined space, leading to an in-depth understanding of chemical transformations. The development of MOCs with tuneable catalytic properties could lead to the creation of novel materials and technologies, with applications ranging from energy production to environmental remediation.

Secondly, these structures have the potential to be used as drug delivery carriers, as they can encapsulate and release therapeutic agents in a controlled manner. This could greatly improve the efficacy and specificity of drug treatment, reducing side effects and increasing patient compliance. The study of MOCs can provide insight into the fundamental principles of self-assembly and molecular recognition, leading to a deeper understanding of chemical and biological systems.

The development of MOCs with tailored properties and functionality could lead to the creation of novel materials and technologies. The field of calixarene-based MOCs using metal-organic connectors is relatively under-explored. This study aims to contribute to the expansion of this area by synthesizing novel calixarene-based MOCs using metal-organic connectors. The significance of this research lies in the potential applications of these cages in catalysis, as the high density of metal centres within the structure allows for efficient catalytic reactions, and in gas storage and separation, as the large internal cavity volume allows for ample storage capacity. Overall, the investigation of MOCs has the potential to have significant impact in a variety of fields, from medicine to materials science.

V. Presentation of the scientific project

The topic of "Formation of multimetallic molecular nanocontainers" is a fascinating and cutting-edge area of research that has the potential to be developed further. Synthesis of multimetallic cages base on metal-organic connector is of particular interest due to unexplored research field. This work focuses on the expansion of the octahedral MOCs family, specifically the $[M_4SO_2TCA(\mu_4-H_2O)]_6[connector]_8$ ($M = Co^{II}, Ni^{II}$) series, with the aim of enhancing catalytic, optical, and separation properties through the incorporation of various metals in the cage structure. The primary objective of this research is to investigate the synthesis of MOCs using different families of metal-organic connectors, including Co^{III} -, Fe^{III} -, Rh^{III} , Pd^{II} , Ni^{II} -dipyrrin complexes, Ni^{II} -porphyrin, Co^{III} -corrole, Fe^{II} -phenanthroline complex and Co^{II} , Fe^{II} , Ru^{II} -terpyridine complexes. This is illustrated on the Figure 35. The structure, chirality, and separation properties of these MOCs will be studied in-depth in the coming chapters.

The research will be conducted through the following steps:

- Synthesis and characterisation of metal-organic and organic connectors
- Synthesis of octahedral MOCs using various metal-organic and organic connectors
- Characterization of the MOCs, including structural analysis and confirmation of chirality when applicable
- Investigation of the gas adsorption and gas separation potential abilities of the obtained octahedral MOCs

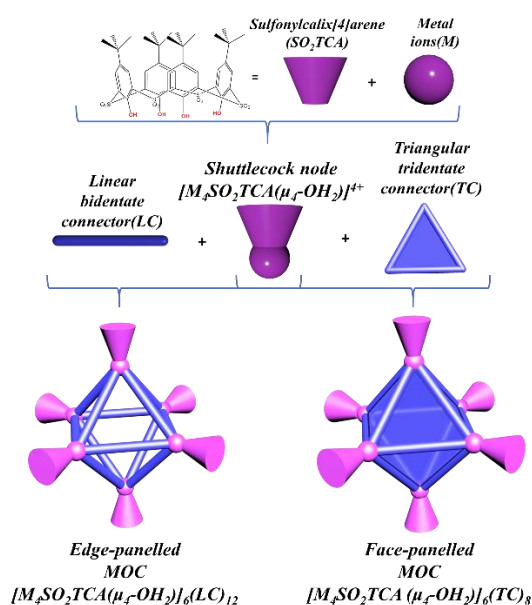


Figure 35 The scientific project: formation of octahedral calixarene-based MOCs from calixarene shuttlecock nodes and different types of connectors

Chapter II.

Synthesis of the connectors

Table of contents

<u>I. Generalities</u>	59
<u>II. Dipyrin-based metal-organic connectors family</u>	62
<u>II.1. Triangular and linear dipyrin connectors</u>	62
<u>II.2. Synthesis of racemic triangular tris(dipyrin) connectors ($\text{rac-M}(\text{HL}_1)_3$, $\text{rac-Co}(\text{HL}_2)_3$)</u>	66
<u>II.3. Chiral resolution of the triangular connector $\text{rac-M}(\text{HL}_1)_3$ ($\Lambda\text{-M}(\text{HL}_1)_3$ and $\Delta\text{-M}(\text{HL}_1)_3$)</u>	70
<u>II.4. The synthesis of linear dipyrin connectors ($\text{Pd}(\text{HL}_1)_2$, $\text{Ni}(\text{H}_2\text{L}_3)$)</u>	73
<u>III. Phenanthroline-based metal-organic connector</u>	77
<u>III.1. Complexes of phenanthroline: review</u>	77
<u>III.1. Phenanthroline connector: size, geometry and properties</u>	78
<u>III.2. The synthesis of triangular phenanthroline connector ($[\text{rac-Fe}(\text{HL}_4)_3][\text{PF}_6]_2$)</u>	79
<u>IV. Terpyridine-based metal-organic connectors family</u>	81
<u>IV.1. Terpyridine complexes: review</u>	81
<u>IV.2. Linear terpyridine connectors: properties, size and geometry</u>	82
<u>IV.3. The synthesis of linear terpyridine connectors ($[\text{M}(\text{HL}_5)_2][\text{PF}_6]_2$)</u>	83
<u>V. Porphyrin-based metal-organic connector</u>	85
<u>V.1. Porphyrin macrocycles: review</u>	85
<u>V.2. Porphyrin connector: size, geometry and properties</u>	86
<u>V.3. The synthesis of the linear porphyrin connector ($\text{Ni}(\text{H}_2\text{L}_6)$)</u>	88
<u>VI. Corrole-based metal-organic connector</u>	90
<u>VI.1. Corrole macrocycle: review</u>	90
<u>VI.2. Corrole connector: size, geometry and properties</u>	90
<u>VI.3. The synthesis of triangular corrole connector ($\text{Co}(\text{H}_3\text{L}_7)$)</u>	91
<u>VII. Organic connectors</u>	93
<u>VII.1. Triazine core: review</u>	94
<u>VII.2. Triazine connectors: size, geometry and properties</u>	95
<u>VII.3. The synthesis of triangular 1,3,5-triazine connectors (H_3L_8, H_3L_9, H_3L_{10})</u>	96
<u>VII.4. 1,3,5-trifluorobenzene connector: size, geometry and properties</u>	97
<u>VII.5. The synthesis of triangular 1,3,5-trifluorobenzene connector (H_3L_{11})</u>	98
<u>VIII. Conclusion</u>	100



I. Generalities

According to the introduction, one of the main goals of this PhD work is the synthesis of new octahedral calixarene-based MOCs using metal-organic connectors or purely organic connectors with specific properties. To obtain MOCs based on calixarenes, appropriate connectors must be chosen.

In this work, several families of connectors were chosen, based on specific criteria:

- Nature of coordinating groups: among all coordinating groups used for the MOCs formation, carboxyl group is the most preferable for the formation of calixarene-based MOCs as previously discussed in the introduction. This group allows the formation of strong bonds between calixarene nodes and connectors.

- Geometry of the connectors: in addition to the stoichiometry *calixarene node/connector* used for the formation of MOCs, the geometry and the size of the connectors must be taken into account. In this work, we focused on the formation of octahedral MOCs. As a consequence, connectors must comply with either triangular tridentate geometry or linear bidentate geometry to form octahedral calixarene-based face-panelled or edge-panelled MOCs respectively.

- Inherent properties of connectors: each of the chosen connectors must possess properties that make these connectors relevant for the formation of MOCs. Thus, it is important to identify the unique properties of each connector and consequently magnify them when incorporated into the MOCs structure. The inherent properties of each connector will be discussed in detail in the corresponding sections of this chapter.

- Charge of the connectors: since the desired MOCs is limited by one type of calixarenes node of formula $[M^{\text{II}}_4\text{SO}_2\text{TCA}(\mu\text{-OH}_2)]^{4+}$, the charge of the MOCs depends on the charge of the connectors used in the cage synthesis (structure of calixarene nodes discussed in details in **Chapter IV**). For example, if the neutral connectors of formula H_2L_x (bidentate) or H_3L_y (tridentate) are used in the MOCs formation, that leads to the neutral MOCs (Figure 36). On the other hand, ionic nature (charged) of connectors leads to the formation of charged MOCs.

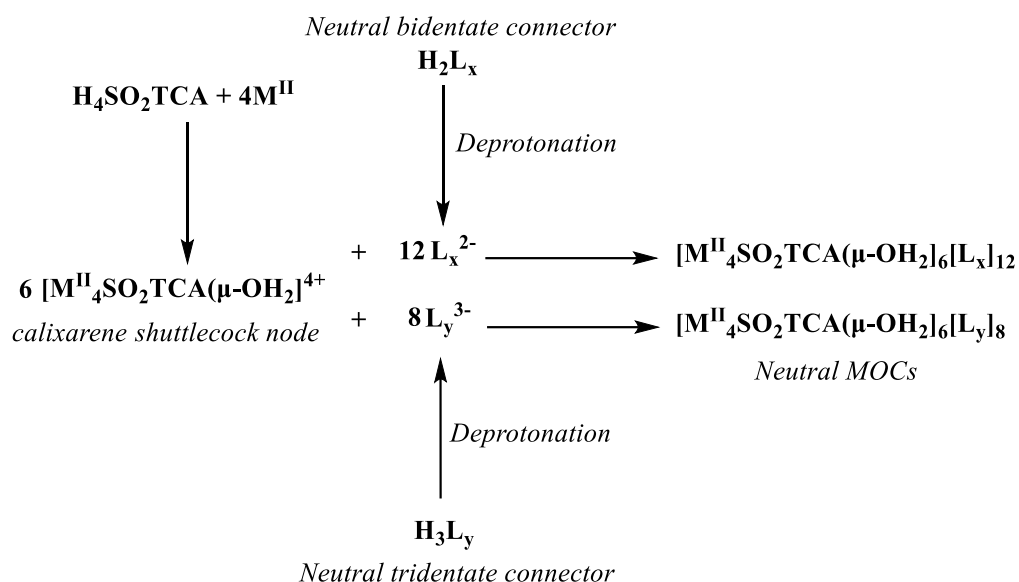


Figure 36 Influence of connectors charge on the charge of the desired MOCs

In order to correctly classify targeted connectors and compare them with literature examples, it is crucial to define useful concepts that will be discussed in detail for each targeted connector:

The connector size (length) is the C-C distance between carbon atoms of two different carboxyl groups ($-\text{COOH}$).

The angle between coordinating positions is defined as the angle in degrees($^\circ$) between two bonds R-C of two different carboxyl groups (R-COOH)

These characteristics allow us to compare different connectors and estimate the size of the expected calixarene-based MOCs. Furthermore, it is also possible to compare different types of connectors (linear and triangular) in terms of the size. Since, the expected geometry of calixarene-based MOCs is octahedral, **the connector size** is a characteristic that define the length of the octahedron edge, regardless the connector type (linear or triangular) used. Both connectors characteristics are measured from the XRD data available in the literature or estimated from XRD data of similar species.

It is essential to compare the targeted connectors with those previously reported in the synthesis of octahedral calixarene-based MOCs to evaluate their geometrical characteristics which determine the expected size of the final cage (Table 3).



Denticity/size	Tridentate	Bidentate	Metal-organic bidentate
Smallest	<p>5Å 120° Triangular <i>a)</i></p>	<p>5.8Å 180° Linear <i>b)</i></p>	<p>13.8Å 180° <i>e)</i></p>
Largest	<p>19.5Å 120° Triangular <i>c)</i></p>	<p>10Å 145° Angular <i>d)</i></p>	

Table 3 Geometrical characteristics of the largest and smallest bidentate and tridentate organic connectors that were reported for the formation of calixarene-based MOCs (*a-d*)^{84,96,98,104}; Structure of the only one metal-organic connector that was used for the formation of octahedral calixarene-based MOC (*e*)⁴

The most preferable angles between coordinating sites for the formation of face-panelled and edge-panelled octahedral MOCs are 120° (triangular connectors) and 180° (linear connectors), respectively. As given in the Table 3c, the largest triangular tridentate connector used for the formation of calixarene-based MOCs has an equilateral triangle shape and a distance between coordinating groups equal to 19.5Å. For the smallest triangular tridentate connector, this distance is equal to 5Å (Table 3a). In the case of bidentate connectors, the size of the smallest linear one was measured 5.8Å (Table 3b), while the size of the largest one was estimated at 10Å (Table 3d). However, MOC based on the largest bidentate connector (Table 3d) does not demonstrate an octahedral shape but a square shape due to angular nature (145°) of the connector.

As given in Table 3e, the only one metal-organic connector used in the synthesis of octahedral calixarene-based MOC is relatively large (13.8Å) and linear bidentate.⁴

In the following section, we will present the synthesis of 18 targeted connectors (dipyrrin, phenanthroline, terpyridine, porphyrin, corrole and triazine connectors) and discuss their size, geometry, and inherent properties. Most of these connectors were reported in the literature, and thus, a small review of each type will be provided with discussion of their potential properties that make them suitable candidates for the formation of new octahedral calixarene-based MOCs. It is also important to consider whether these connectors or similar species have been previously used for the formation of supramolecular species, for instance, MOFs, or non-calixarene MOCs, which provides strong support for the possibility to obtain new calixarene-based MOCs.

II. Dipyrrin-based metal-organic connectors family

II.1. Triangular and linear dipyrrin connectors

II.1.1. Complexes of dipyrrin: review

The family of dipyrrin complexes comprises a variety of metal-organic structures based on bidentate dipyrrin ligands coordinated to a metal ion. There are several types of dipyrrin complexes with different geometries reported in the literature: mono(dipyrrin), bis(dipyrrin) and tris(dipyrrin) complexes of transition and alkaline earth metals. Dipyrrin ligands have a unique electronic structure, with two pyrrole rings connected by a meso-carbon bridge. This structure leads to a strong electron donation from the ligand to the metal centre, resulting in high stability and robustness of the metal-organic complexes.¹¹⁰

Among all the dipyrrin complexes, we focused on bis(dipyrrin) (Figure 37a) and tris(dipyrrin) (Figure 37b) complexes for the formation of calixarene-based MOCs due to their geometrical characteristics. In bis(dipyrrin) complexes coordinating groups (RCOOH) can be presented at an angle close to 180°. On the other hand, for tris(dipyrrin) complexes they are positioned at an angle close to 120°. As a result, bis(dipyrrin) and tris(dipyrrin) complexes appear to be respectively suitable for the formation of new edge-panelled and face-panelled calixarene-based MOCs.

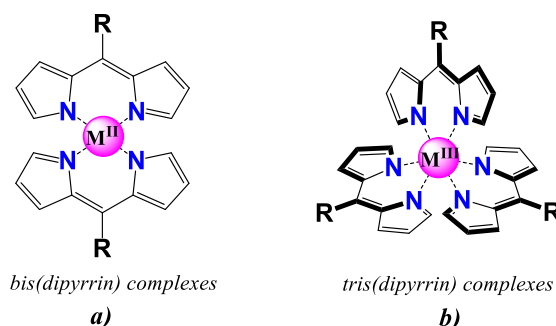


Figure 37 The structure of bis(dipyrrin) and tris(dipyrrin) complexes

Many bis(dipyrrin) and tris(dipyrrin) complexes have been already reported in the literature. For example, dipyrrin complexes of trivalent (Co^{III} , Fe^{III} , Rh^{III} , Ga^{III} , In^{III})^{111–113} and divalent (Ni^{II} , Pd^{II} , Zn^{II} , Cu^{II})¹¹⁴ metals have been described. These complexes are interesting for the MOCs formation due to their inherent properties. For example, many dipyrrin complexes exhibit optical properties : bis(dipyrrin) complexes of Pd^{II} and tris(dipyrrin) complexes of Rh^{III} have intense absorption bands in the visible region due to π - π^* transitions of the dipyrrin chromophores,¹¹² tris(dipyrrin) complexes of In^{III} and Ga^{III} exhibit luminescent behaviour.¹¹⁵ These optical properties lead to many possible applications, such as photosensitizing or sensing.¹¹²



In addition, tris(dipyrrin) complexes have propeller-like arrangement which means that they exist in two enantiomeric forms: Λ and Δ . As a result tris(dipyrrin) complexes exhibit chiral properties (Figure 38).¹¹⁶

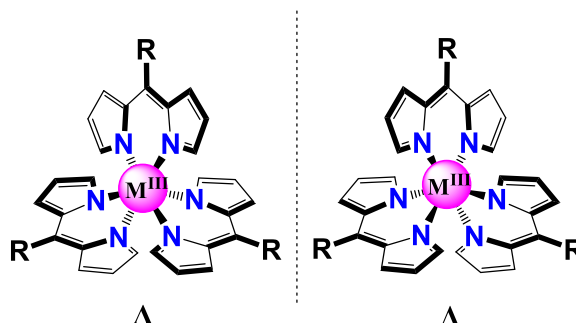


Figure 38 Λ - and Δ - enantiomers of tris(dipyrrin) complexes

Dipyrrin complexes might exhibit other properties, which are mostly related to the type of the metal ion in the structure. For instance, tris(dipyrrin) complex of Fe^{III} demonstrated redox^{117,118} properties in the cyclic voltammetry experiments, making them suitable for electrochemical applications. Thus, properties of dipyrrin complexes can be tuned by the nature of the metal.

The most intriguing field of the dipyrrin complexes application is the formation of extended symmetrical structures. There are many examples of MOFs formation with different dipyrrin complexes.¹¹⁹ For example, tris(dipyrrin) complexes of Ga^{III} and In^{III} demonstrated the formation of 2D-MOFs when combined with silver ions (Figure 39).¹¹³ In addition, numerous other heterometallic dipyrrin compounds have been described in the literature.¹²⁰ Furthermore, the majority of dipyrrin complexes found in MOFs are highly stable and have a variety of shapes and metal ions, resulting in a broad range of optical and electrochemical characteristics.



Figure 39 The formation of MOFs by tris(dipyrrin) complex of Ga^{III} (from ref. ¹¹³)

Thus, tris(dipyrrin) and bis(dipyrrin) complexes are promising candidates for the formation of new MOCs due to their inherent properties and the possibility to arrange the coordinating groups at angles close to 120° and 180° , which is essential for the formation of octahedral face-panelled

and edge-panelled calixarene-based MOCs respectively. As it was discussed in §I. suitable coordinating groups for cages formation are carboxyl groups.

According to these constraints Bis[5-(4-Carboxyphenyl)-4,6-dipyrrinato]M(II) and Tris[5-(4-Carboxyphenyl)-4,6-dipyrrinato]M(III) complexes were selected for the synthesis of new calixarene-based MOCs. We limited tris(dipyrrin) complexes with complexes of Co^{III}, Fe^{III} and Rh^{III} (**rac-M(HL₁)₃**, **rac-Co(HL₂)₃**) and bis(dipyrrin) complexes with Pd^{II} and Ni^{II} (**Pd(HL₁)₂** and **Ni(H₂L₃)**) due to their robustness and inherent properties.

II.1.2. Triangular and linear dipyrrin connectors: size, geometry and properties

We targeted 6 dipyrrin complexes as connectors, 4 or which are tris(dipyrrin) complexes.

Triangular tris(dipyrrin) connectors (Figure 40a) are perfect for the formation of face-panelled MOCs due to their triangular tridentate nature with an angle between coordinating groups of 120°. The length of the connectors **rac-Co(HL₁)₃**, **rac-Fe(HL₁)₃**, and **rac-Rh(HL₁)₃** was estimated approximately to 16Å from X-ray data for **rac-Rh(HL₁)₃** connector (Figure 40a)¹¹², which is suitable for the formation of large MOCs. However, it was not possible to estimate the length of the connector **rac-Co(HL₂)₃** due to the absence of X-ray data for this connector or similar species.

Tris[5-(4-Carboxyphenyl)-4,6-dipyrrinato]Co(III) (**rac-Co(HL₁)₃**) can be easily separated into two pure enantiomers¹¹⁶ that could be useful for the formation of chiral MOCs with unique properties (Figure 40a), this will be discussed in §II.3. of this chapter. Moreover, we expected the enlarged tris(dipyrrin) connector of Co^{III} (**rac-Co(HL₂)₃**) to have modified gas adsorption properties due to the enlarged size (Figure 40a).

Tris[5-(4-Carboxyphenyl)-4,6-dipyrrinato]Fe(III) (**rac-Fe(HL₁)₃**) is expected to present electrochemical properties related to the presence of Fe^{III} in the structure.^{117,118} (Figure 40a).

Tris[5-(4-Carboxyphenyl)-4,6-dipyrrinato]Rh(III) (**rac-Rh(HL₁)₃**) is expected to present photosensitivity due to the presence of photosensitive Rh^{III} ion.¹¹² As a result, great photocatalytic activity of related MOCs may be observed due to combination of Rh^{III} ions photosensitivity with the enclosed space of the MOCs (Figure 40a).

Bis(dipyrrin) connectors (Figure 40b and 4c) are linear bidentate connectors with tetracoordinated metal ions in the planar or distorted planar geometry.^{112,121} The angle between coordinating groups is close to 180° which is perfect for the formation of edge-panelled MOCs. X-ray data for **Pd(HL₁)₂** and **Ni(H₂L₃)** demonstrated the length of the connectors to be close to



19Å (Figure 40b and 4c) that might lead to MOCs that are larger than MOCs based on triangular tris(dipyrrin) connectors.¹²²

As represented in the Figure 40c, steric hindrances between α -pyrrolic protons (**H₁**) of opposite pyrrolic rings lead to the distortion from perfect linear geometry of **Ni(H₂L₃)**. This leads to the deviations from 180° between coordinating positions for **Ni(H₂L₃)** (170°). This phenomenon is discussed in details in §II.4. of this chapter.

Concerning the properties, bis[5-(4-Carboxyphenyl)-4,6-dipyrrinato]Pd(II) (**Pd(HL₁)₂**) is also highly photosensitive complex.¹¹² As it was mentioned for the **rac-Rh(HL₁)₃**, we could expect great photocatalytic properties from the MOCs based on **Pd(HL₁)₂** due to its photosensitivity and enclosed space of the formed MOCs (Figure 40b). Bis(dipyrrin) complex of Ni^{II} (**Ni(H₂L₃)**) is expected to have intriguing optical properties due to the distinct structure and presence of semi-opened cavity in this complex (Figure 40c).

Notably, all the targeted connectors are not charged, and as a result, the MOCs formed by bis(dipyrrin) and tris(dipyrrin) connectors are expected to be neutral species.

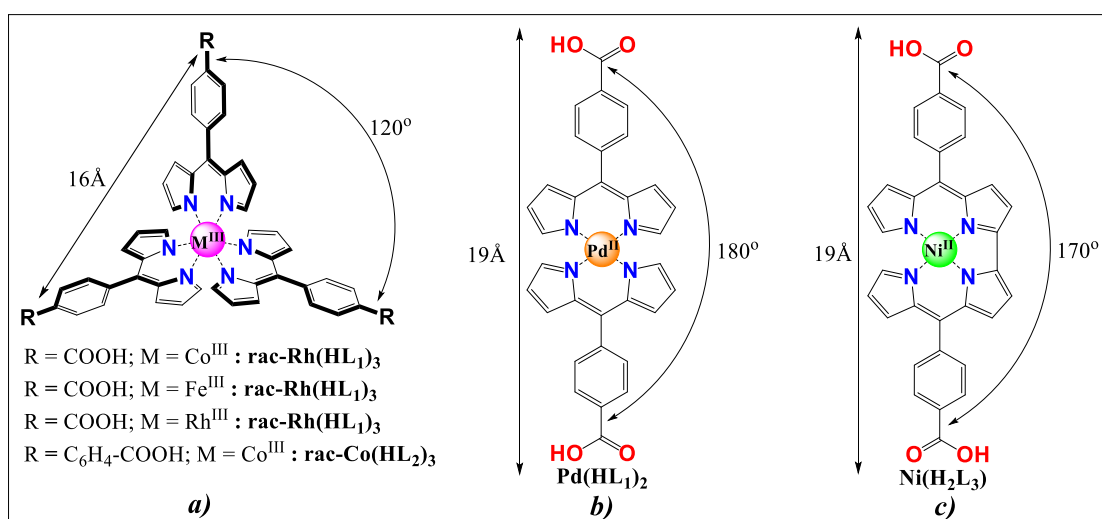


Figure 40 Structure of the targeted triangular tris(dipyrrin) connectors **rac-Co(HL₁)₃**, **rac-Fe(HL₁)₃**, **rac-Rh(HL₁)₃**, **rac-Co(HL₂)₃** (a); Structure of the targeted linear bis(dipyrrin) connectors **Pd(HL₁)₂** (b) and **Ni(H₂L₃)** (c)

In conclusion, the connectors based on tris(dipyrrin) and bis(dipyrrin) complexes are promising candidates for the formation of new large neutral face-panelled and edge-panelled MOCs with potential optical, redox, and chiral properties.

II.2. Synthesis of racemic triangular tris(dipyrrin) connectors ($\text{rac-M}(\text{HL}_1)_3$, $\text{rac-Co}(\text{HL}_2)_3$)

The synthesis of tris(dipyrrin) connectors $\text{rac-Co}(\text{HL}_1)_3$, $\text{rac-Fe}(\text{HL}_1)_3$ and $\text{rac-Rh}(\text{HL}_1)_3$ has been already reported and includes 4 steps with an overall yield of 20%, 15%, 22% respectively (Figure 41).^{111,112}

These low yields can be explained by multiple factors. First, the synthesis of 5-(4-Carboxymethylphenyl)dipyrromethane (first step) is a reaction with multiple possible side products, for instance, formation of oligomeric species. Furthermore, 5-(4-Carboxymethylphenyl)dipyrromethane is an easy oxidizing species and it requires to be extracted carefully and stored under the light protection at low temperature in the fridge.

The formation of dipyrrin MeL_1 using DDQ as an oxidizing agent also generates multiple side products, for instance, oligomeric and cyclic (porphyrins, corroles) species.

The yields of the metallation steps are in correspondence with the reported ones.^{111,112}

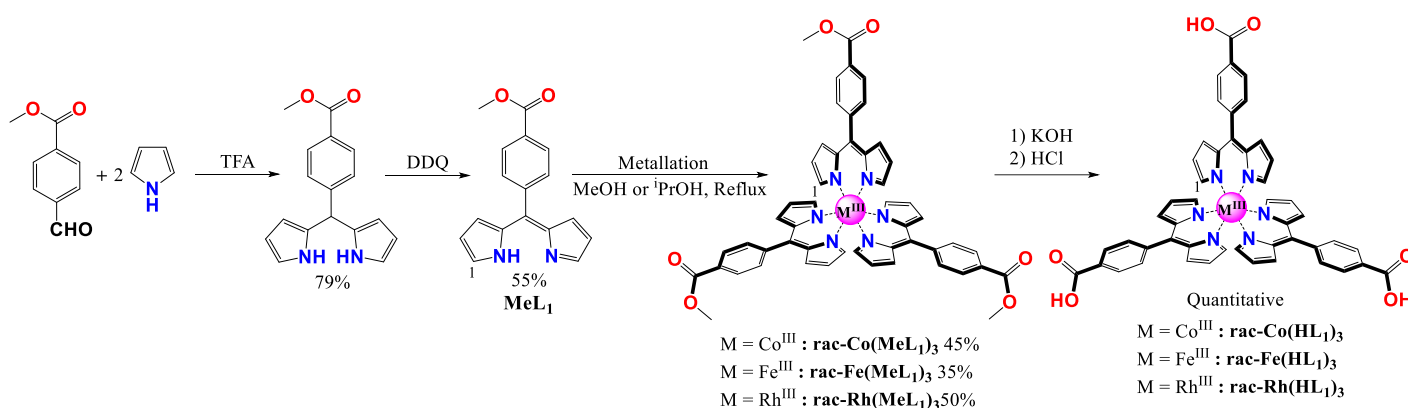


Figure 41 The synthetic pathway for the connectors $\text{rac-Co}(\text{HL}_1)_3$, $\text{rac-Fe}(\text{HL}_1)_3$ and $\text{rac-Rh}(\text{HL}_1)_3$

The synthetic pathway illustrated Figure 41 begins with the coupling of pyrrole and 4-(carboxymethyl)benzaldehyde. We modified the reported synthesis¹²³ by precipitation of 5-(4-Carboxymethylphenyl)dipyrromethane instead of a purification via a column chromatography. This procedure leads to 5-(4-Carboxymethylphenyl)dipyrromethane with an acceptable purity. Traces of pyrrole may still be presented but it does not impact the following step. Excluding the column chromatography purification does not impact on the yield of 5-(4-Carboxymethylphenyl)dipyrromethane.

The next step is the oxidation with DDQ, which was performed without any alterations from the previously reported procedure.¹¹⁶



The following step is the metallation of **MeL₁**, which was performed using different metal salts. It was experimentally observed that sodium hexanitrocobaltate(III) (Na₃[Co(NO₂)₆]) is the most preferable salt for obtaining **rac-Co(MeL₁)₃**, while iron (III) chloride hexahydrate (FeCl₃•6H₂O) is preferred for **rac-Fe(MeL₁)₃**, and rhodium (III) chloride hydrate (RhCl₃•xH₂O) is the preferred salt for **rac-Rh(MeL₁)₃**. The conditions of the metallation step differ, reflux in methanol have been used for **rac-Co(MeL₁)₃** and **rac-Fe(MeL₁)₃** and reflux in isopropanol have been used for **rac-Rh(MeL₁)₃** due to a higher energy activation required for the formation of **rac-Rh(MeL₁)₃**. We modified the reported synthesis¹¹¹ by excluding the column chromatography purification step by using filtration and washing of the suspension of the reaction mixture residue after solvent evaporation in cold methanol. The success of the metallation process is clearly visible in the ¹H-NMR spectra of metallated and non-metallated ligand by significant upfield shift of α-pyrrolic proton (**H₁**). The shift is explained by the interactions between **H₁** protons of the opposite pyrrolic rings that leads to a shift from **7.68** ppm for the non-metallated ligand, to **6.41** ppm for **rac-Co(MeL₁)₃**, and **6.66** ppm for **rac-Rh(MeL₁)₃** (see experimental part). Due to the paramagnetic nature of **rac-Fe(MeL₁)₃** related to the presence of Fe³⁺ ion in the structure, the ¹H-NMR spectrum is not informative (Figure 42).

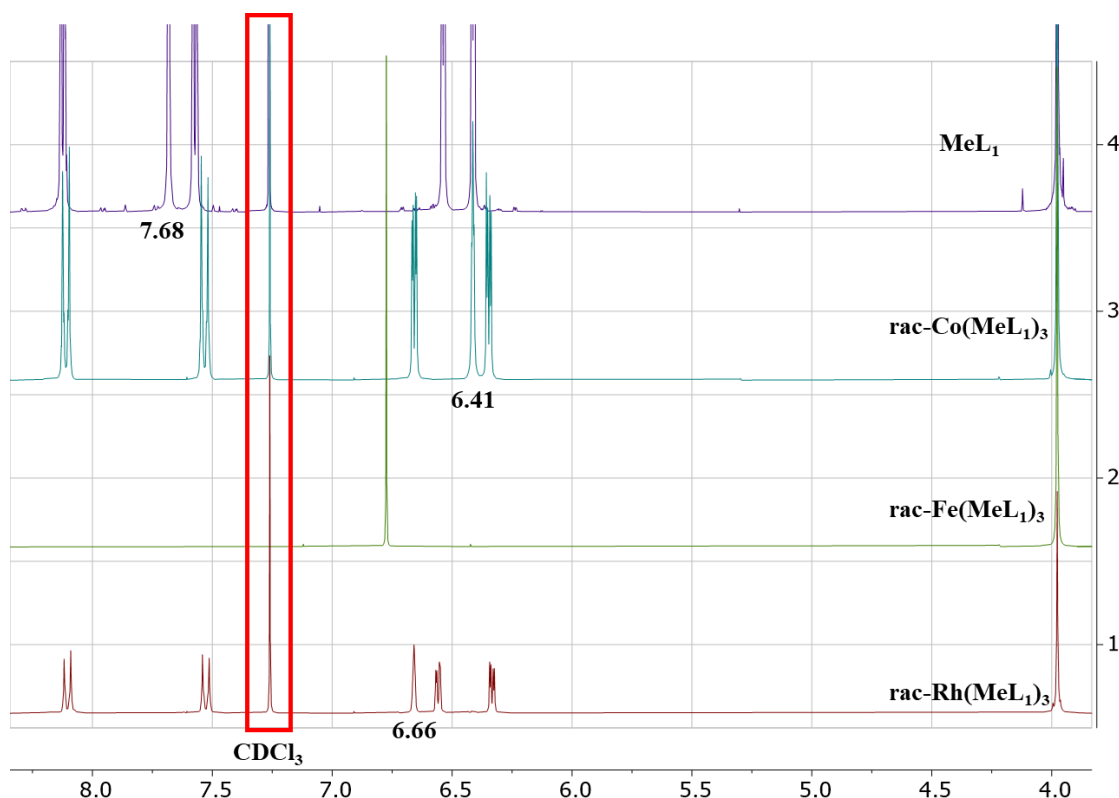


Figure 42 *NMR spectra of tris(dipyrin) connectors **rac-Co(HL₁)₃**, **rac-Fe(HL₁)₃** and **rac-Rh(HL₁)₃***

The final step of the synthesis of **rac-Co(HL₁)₃**, **rac-Fe(HL₁)₃** and **rac-Rh(HL₁)₃** is hydrolysis of the three ester groups which was performed in quantitative yield according to the reported procedure without modifications.¹¹⁶ The ¹H-NMR spectra of the obtained connectors are in perfect accordance with the literature data (see experimental part).^{111,112} Moreover, the MS spectra demonstrate peaks of mass 849.19 [M]⁺ for **rac-Co(HL₁)₃**, 844.15 [M]⁺ for **rac-Fe(HL₁)₃** and 893.16 [M]⁺ for **rac-Rh(HL₁)₃** which is in perfect accordance with the expected values.^{111,112}

The obtained **rac-M(HL₁)₃** (M = Co^{III}, Fe^{III}, Rh^{III}) demonstrated a good stability in the solid state and in the solution (DMSO) with no modification of the ¹H-NMR spectra of **rac-Co(HL₁)₃**, **rac-Fe(HL₁)₃** and **rac-Rh(HL₁)₃** after a week.

The synthesis of enlarged connector **rac-Co(HL₂)₃** was not reported, however, we took inspiration from the synthesis of **rac-M(HL₁)₃** (Figure 41). **Rac-Co(HL₂)₃** was obtained in a 5 steps procedure with an overall yield of 13.5% (Figure 43).

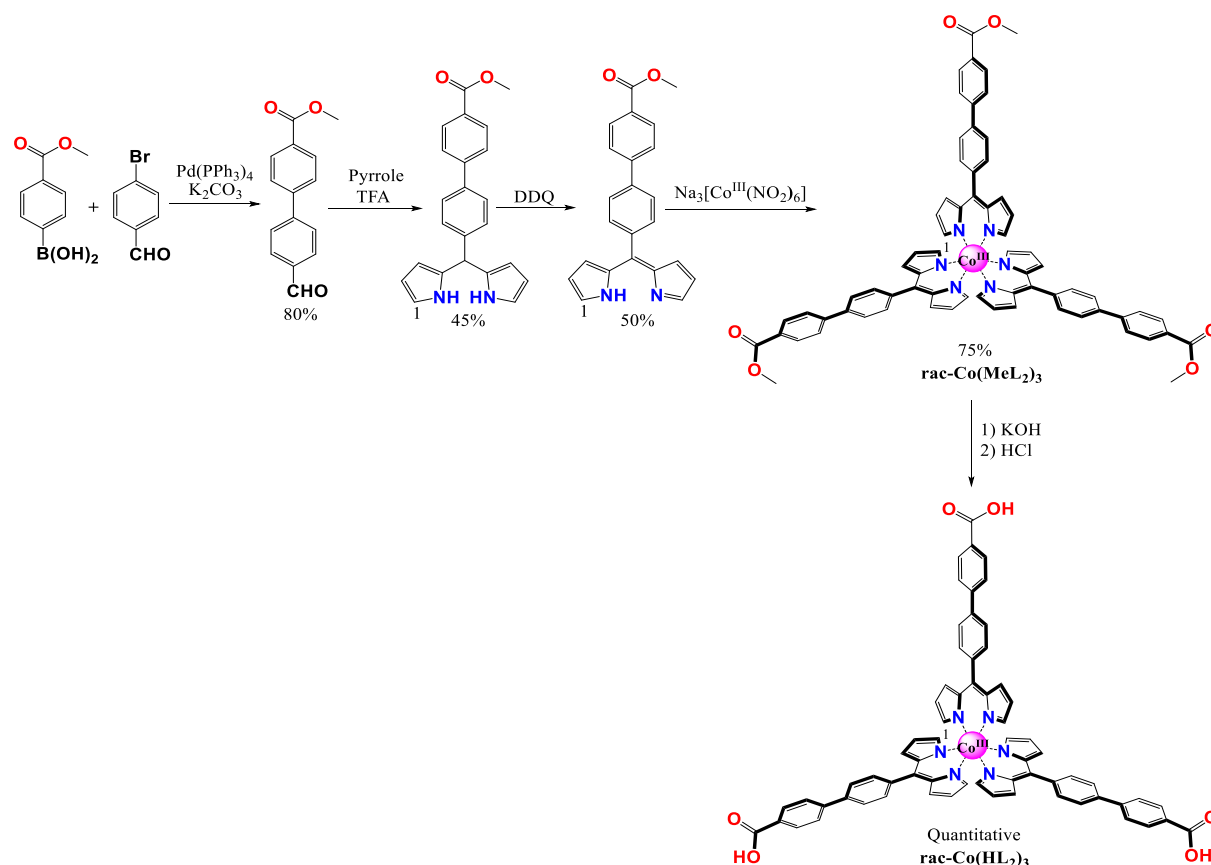


Figure 43 The synthetic pathway for the connector **rac-Co(HL₂)₃**

The first step is a classical Suzuki coupling that was performed according to the already reported procedure.¹²⁴ The following steps were performed analogously to the procedure for **rac-M(HL₁)₃**. Particular interest however is the metallation step. This step was performed by reflux in MeOH and it was possible to achieve a yield 75% yield of the desired complex that is much higher than the yield of 45% in the metallation step for **rac-Co(MeL₁)₃**.



The formation of **rac-Co(MeL₂)₃** was evidenced by ¹H-NMR with a significant upfield shift of **H₁** of 1.2 ppm (from 7.67 to 6.45 ppm) compared to the starting tris(dipyrin) (Figure 44).

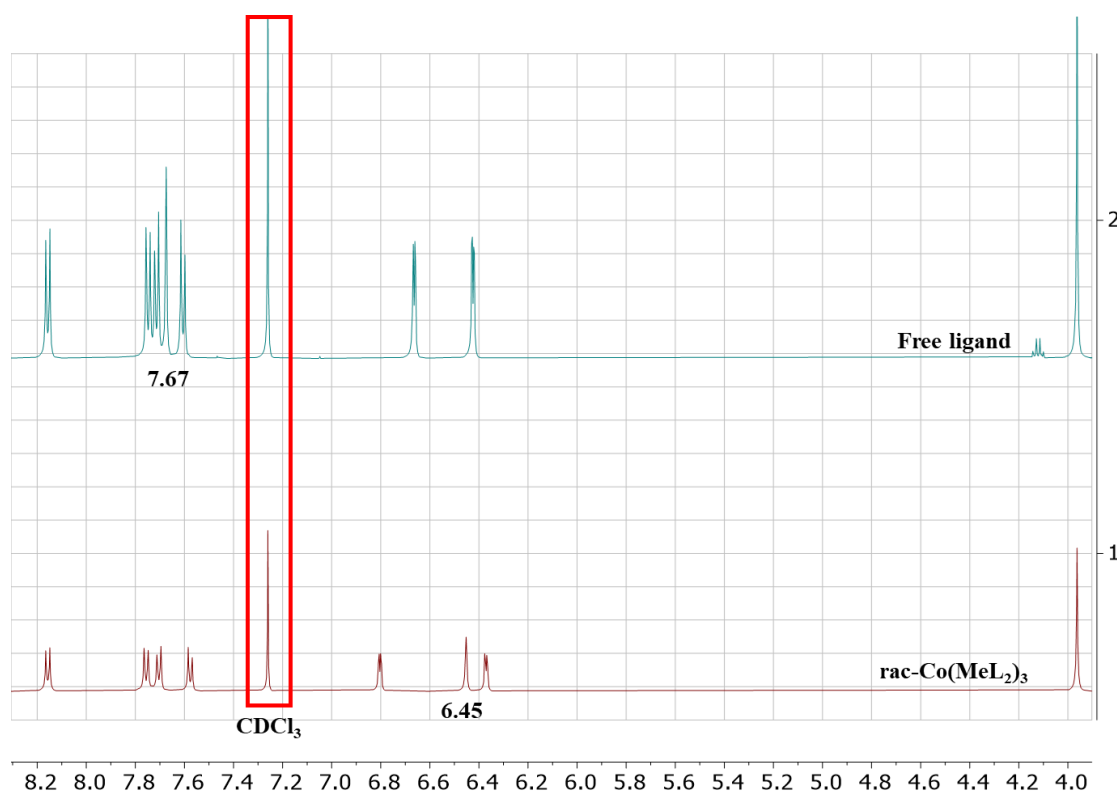


Figure 44 NMR spectra of long dipyrin ligand and **rac-Co(MeL₂)₃**

The final step of the synthesis of **rac-Co(HL₂)₃** is hydrolysis of the three ester groups which was performed in quantitative yield in the same manner as for the connectors **rac-M(HL₁)₃** (M = Co^{III}, Fe^{III}, Rh^{III})

MS demonstrated a peak of mass 1077.28 [M]⁺ for **rac-Co(HL₂)₃** which is in perfect accordance with expected mass of the connector.

The connector **rac-Co(HL₂)₃** demonstrated a good stability in the solid state and in the solution (DMSO) with no modification of the ¹H-NMR spectra of **rac-Co(HL₂)₃** after a week.

II.3. Chiral resolution of the triangular connector $\text{rac-M}(\text{HL}_1)_3$ (Λ - $\text{M}(\text{HL}_1)_3$ and Δ - $\text{M}(\text{HL}_1)_3$)

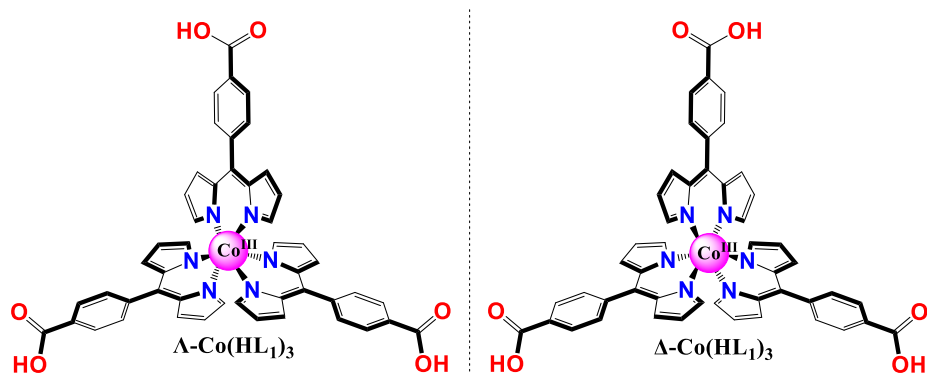


Figure 45 Chiral dipyrrin connectors Λ - $\text{Co}(\text{HL}_1)_3$ and Δ - $\text{Co}(\text{HL}_1)_3$

As it was mentioned before in §II.1, tris(dipyrrin) complexes are chiral and, thus, exist in two enantiomeric forms (Λ and Δ) due to the orientation of dipyrrin ligands in a chiral, propeller-like arrangement (Figure 45). The separation of enantiomers of the connectors $\text{rac-Co}(\text{HL}_1)_3$, $\text{rac-Fe}(\text{HL}_1)_3$ and $\text{rac-Rh}(\text{HL}_1)_3$ is appealing challenge due to the possibility of chiral cages formation.

The procedure of enantiomers separation of $\text{rac-Co}(\text{HL}_1)_3$ has been already reported.¹²⁵ The enantiomers separation is based on the formation of diastereomeric complexes of $\text{rac-Co}(\text{HL}_1)_3$ with (-)-cinchonidine and their solubility difference in THF. We applied the same methodology in order to separate enantiomers of connectors $\text{rac-Co}(\text{HL}_1)_3$, $\text{rac-Fe}(\text{HL}_1)_3$ and $\text{rac-Rh}(\text{HL}_1)_3$.

We managed to obtain chiral connectors Λ - $\text{Co}(\text{HL}_1)_3$ and Δ - $\text{Co}(\text{HL}_1)_3$ with enantiomeric excess up to 92% that was proven by methods of CD and chiral HPLC.

The CD spectra of chiral connectors in THF solution display peaks at $\lambda = 515$ and 465 nm that are almost perfect mirror images, providing an evidence of the large enantiomeric excess (Figure 46).

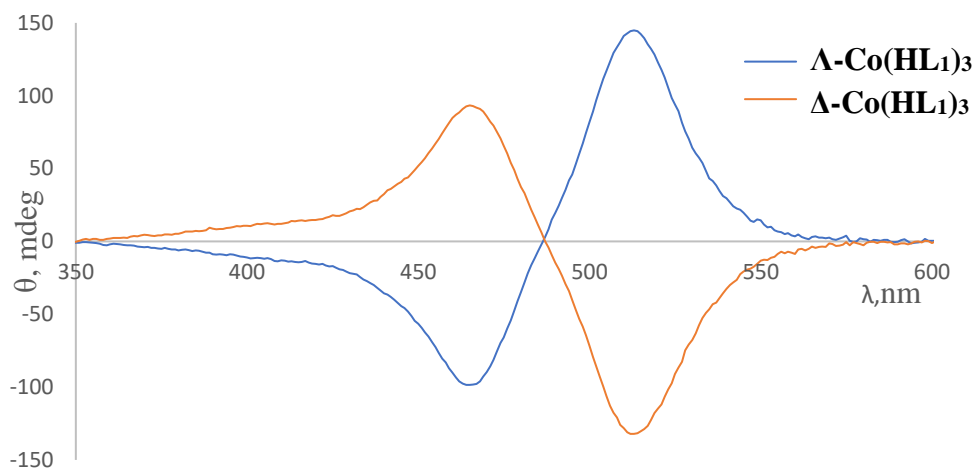


Figure 46 CD spectra of Λ -Co(HL₁)₃ and Δ -Co(HL₁)₃ (RT, $5 \cdot 10^{-5} M$, THF, 2 mm)

The observed position of the peaks corresponds with the data previously reported in the literature.¹²⁵ However, HPLC measurements were also performed in order to estimate accurate values of enantiomeric excess (*ee*). The chiral HPLC demonstrated the retention time of 16.7 min for Λ -Co(HL₁)₃ and 14.8 min for Δ -Co(HL₁)₃. According to the integration of peaks, the value of *ee* excess was calculated, 92% for Λ -Co(HL₁)₃ and 85% for Δ -Co(HL₁)₃ (Figure 47).

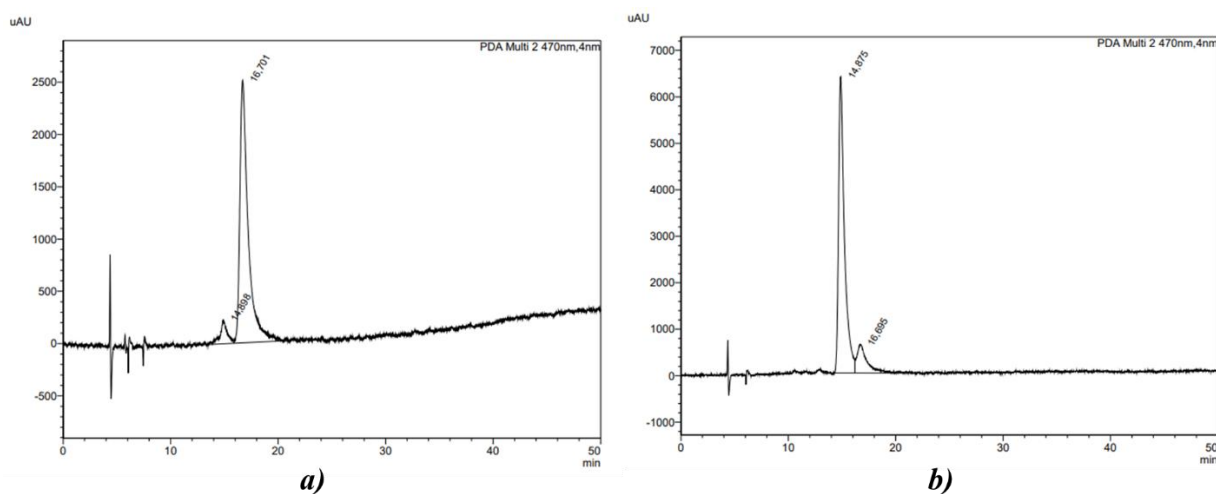


Figure 47 HPLC chromatograms of Λ -Co(HL₁)₃ (a); Δ -Co(HL₁)₃ (b)

(ChiralPak 1A, Hexane/THF/TFA = 80/20/0.1, flow rate = 0.8 ml/min, 470 nm)

The obtained Λ -Co(HL₁)₃ and Δ -Co(HL₁)₃ appeared to be stable in the THF. No changes were observed in the CD spectra after 48 hours showing that no racemisation occurs during the observation time (48 hours).

The same methodology was applied for the chiral resolution of **rac-Fe(HL₁)₃** and **rac-Rh(HL₁)₃**. Although **rac-Fe(HL₁)₃** is structurally similar to **rac-Co(HL₁)₃**, enantiomers separation was not successful for the iron analogue, possibly due to its lower stability.

For **rac-Rh(HL₁)₃**, it was more positive since it was possible to isolate a solid phase that contains one of the enantiomers as a major product. CD spectrum of this solid dissolved in THF (Figure 48) demonstrates a signature similar to one of **Λ-Co(HL₁)₃** (Figure 46, blue line).

However, it was not possible to isolate another phase containing the other enantiomer as the major product.

Nevertheless, we can make the hypothesis that having in hand chiral **Λ-Co(HL₁)₃** and **Δ-Co(HL₁)₃** gives us the possibility to synthesize chiral MOCs based on them with the perspective to extend eventually these procedures to MOCs based on enantiomers of **rac-Rh(HL₁)₃**.

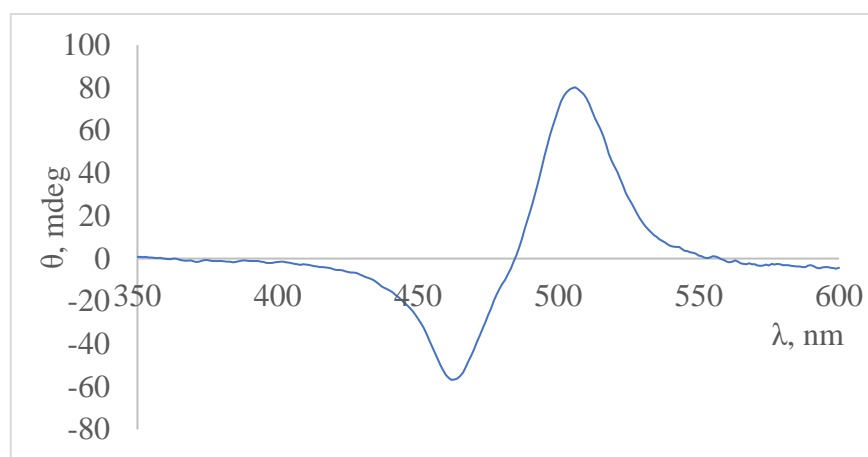


Figure 48 CD spectrum of the phase containing one enantiomer of **rac-Rh(HL₁)₃** as the major product (RT, $5 \cdot 10^{-5} M$, THF, cuvette length = 2 mm)



II.4. The synthesis of linear dipyrin connectors ($\text{Pd}(\text{HL}_1)_2$, $\text{Ni}(\text{H}_2\text{L}_3)$)

The synthesis of $\text{Pd}(\text{HL}_1)_2$ connector was performed according to the already reported procedure.¹¹² It is similar to synthesis of $\text{rac-Co}(\text{HL}_1)_3$, $\text{rac-Fe}(\text{HL}_1)_3$ and $\text{rac-Rh}(\text{HL}_1)_3$ and it was obtained with overall yield 36.5% (Figure 49).

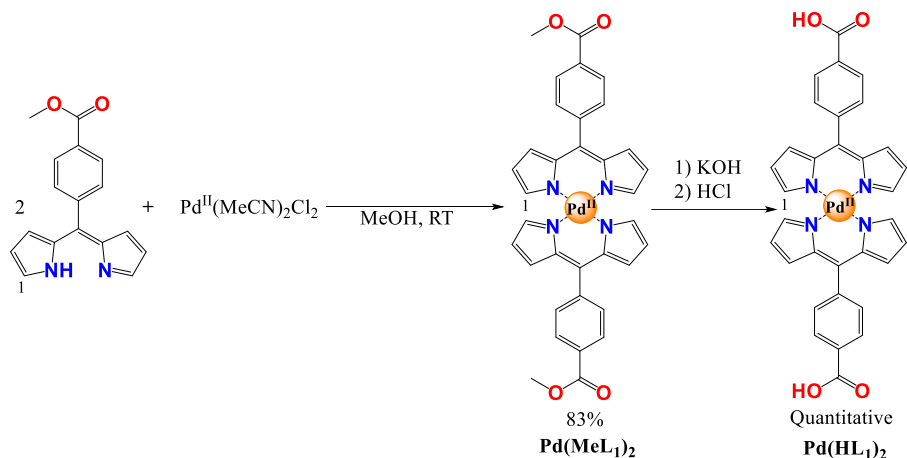


Figure 49 The synthetic pathway of the connector $\text{Pd}(\text{HL}_1)_2$

Apart from the stoichiometry used in the metallation, one of the notable differences in the synthesis of $\text{Pd}(\text{HL}_1)_2$ compare to tris(dipyrin) complexes $\text{rac-M}(\text{HL}_1)_3$ ($\text{M} = \text{Co}^{\text{III}}$, Fe^{III} , Rh^{III}) is that the metallation occurs at room temperature in methanol that could be an evidence of the smaller activation energy of the reaction. The metallation step presents a yield of 83% which is one of the best among all of the dipyrin-based connectors.

The $^1\text{H-NMR}$ spectrum of $\text{Pd}(\text{HL}_1)_2$ is in a perfect accordance with the literature data.¹¹² As it was discussed for $\text{rac-M}(\text{HL}_1)_3$ in §II.2, it is possible to track the formation of dipyrin complexes by the significant shift of H_1 after metallation. For $\text{Pd}(\text{MeL}_1)_2$, the chemical shift for H_1 is 7.41, and the upfield shift is, as expected, much smaller (*ca* 0.3 ppm) compare to the ones observed for the much more constrained tris(dipyrin) $\text{rac-M}(\text{HL}_1)_3$ analogues (Figure 52).

The formation of the connector $\text{Pd}(\text{HL}_1)_2$ was also proven by Mass-spectrometry that demonstrates a peak of mass 632.97 $[\text{M}]^+$ for $\text{Pd}(\text{HL}_1)_2$ that is in a perfect accordance the expected mass.¹¹²

It is worth mentioning that we succeeded to grow single-crystals of $\text{Pd}(\text{HL}_1)_2$ and characterized it for the first time by X-Ray diffraction. (Figure 50). As expected, Pd^{II} adopts a square-planar N4 coordination geometry (see crystallographic data in annexes §I.3.) and the angle between opposite coordinating sites equal to 180° . Two dipyrin ligands are parallel but not coplanar, the distance between the two planes of the dipyrin ligands is equal to 1.95Å. Additionally, dipyrin ligands are not perfectly planar but slightly curved (the angle between planes of pyrrolic rings of one dipyrin is equal to 29°).

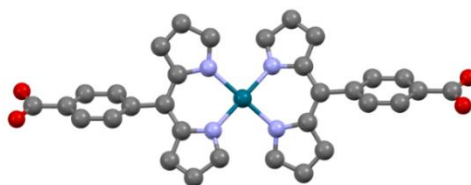


Figure 50 Crystal structure of $\text{Pd}(\text{HL}_1)_2$

The obtained connector $\text{Pd}(\text{HL}_1)_2$ demonstrated a good stability in the solid state. The ^1H -NMR spectrum of freshly obtained $\text{Pd}(\text{HL}_1)_2$ and the ^1H -NMR spectrum of $\text{Pd}(\text{HL}_1)_2$ stored for a week as powder are identical. However, the stability of $\text{Pd}(\text{HL}_1)_2$ in the solutions was not investigated.

Despite the visible similarities with $\text{Pd}(\text{HL}_1)_2$, connector $\text{Ni}(\text{H}_2\text{L}_3)$ is significantly different due to the presence of the σ -bond that connects two dipyrin ligands forming a “semi-opened” cavity. Thus, $\text{Ni}(\text{H}_2\text{L}_3)$ is much more rigid when compared with $\text{Pd}(\text{HL}_1)_2$ and closer in terms of properties to corroles. The consequence is the low solubility, and difficulties for the full characterisation.

The synthesis of the connector $\text{Ni}(\text{H}_2\text{L}_3)$ is an already reported procedure¹²¹ and similar to the one of $\text{Pd}(\text{HL}_1)_2$ but includes one additional step with DDQ oxidation of $\text{Ni}(\text{MeL}_1)_2$ with overall yield 16.2% (Figure 51).

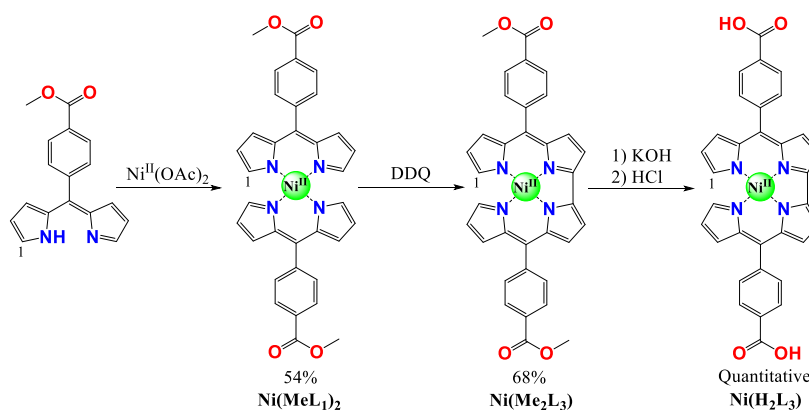


Figure 51 The synthetic pathway for the connector $\text{Ni}(\text{H}_2\text{L}_3)$

As it was noticed for all dipyrin complexes there is a significant shift of H_1 after the metallation step. It is interesting to notice the huge difference of the chemical shift of H_1 in $\text{Ni}(\text{MeL}_1)_2$ and $\text{Ni}(\text{Me}_2\text{L}_3)$ that only differs from the presence of the additional sigma bond. First, in comparison with complexes $\text{rac-M}(\text{Me}_2\text{L}_1)_3$ ($\text{M} = \text{Co}^{\text{III}}, \text{Fe}^{\text{III}}, \text{Rh}^{\text{III}}$) and $\text{Pd}(\text{MeL}_1)_2$, complex $\text{Ni}(\text{MeL}_1)_2$ exhibits large H_1 downfield shift at 10.38 ppm (see experimental part). This distinctive shift of the signal is related to the distorted geometry of the Ni complex. As it was discussed earlier in this section, two protons H_1 of the opposite pyrrolic rings in the complexes have the steric



hindrances. For the complex $\text{Pd}(\text{MeL}_1)_2$ it is possible to avoid these hindrances with remaining of square planar geometry due to the length 2.01 Å of the Pd-N bond and especially due to the non-coplanarity of the two dipyrrin ligands, as mentioned previously. In comparison with Pd-N, Ni-N bond is shorter¹²² and has the length 1.96 Å and the geometry for Ni^{II} is close to tetrahedral (Figure 53a). Due to that fact, the distance between protons H_1 of opposite pyrrolic rings significantly increases while decreasing the steric hindrance, thus leading to the significant downfield shift compared to the Pd-analogue $\text{Pd}(\text{MeL}_1)_2$ (Figure 52).

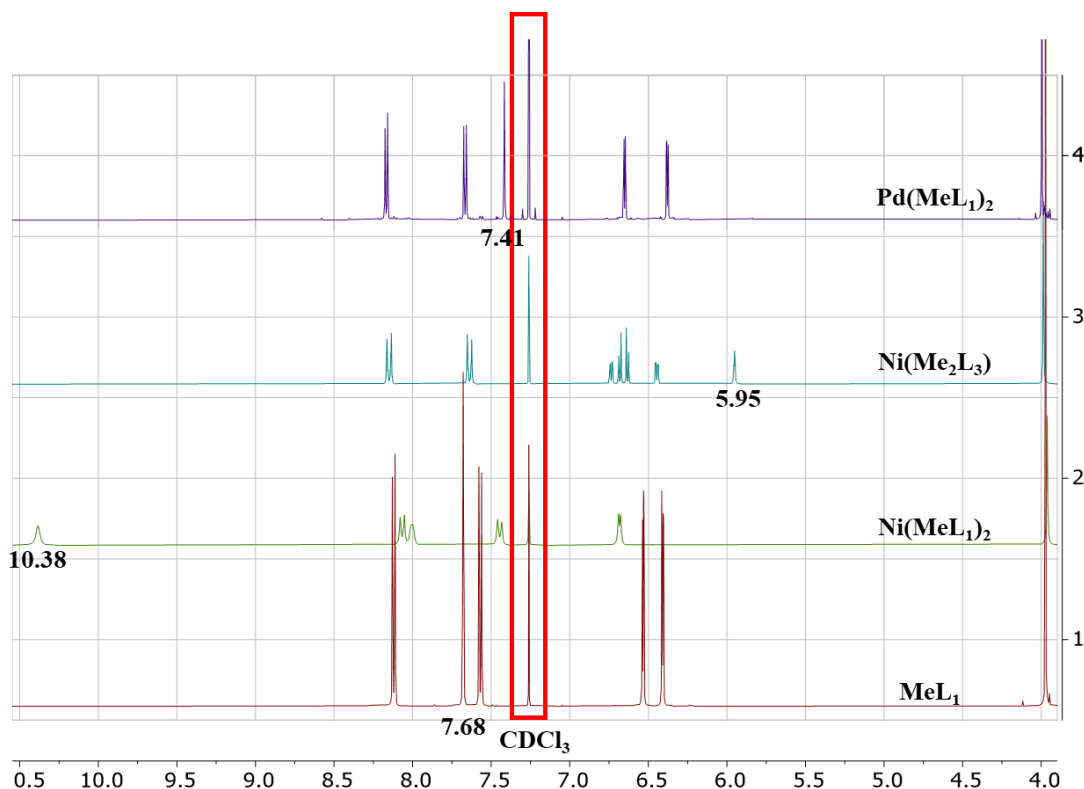


Figure 52 NMR spectra of bis(dipyrrin) connectors

The formation of the σ -bond between two ligands leads to $\text{Ni}(\text{Me}_2\text{L}_3)$ and a significant upfield shift of H_1 from 10.38 ppm for $\text{Ni}(\text{MeL}_1)_2$ to 5.95 ppm for related $\text{Ni}(\text{Me}_2\text{L}_3)$ (Figure 52) due to the drastic change in the environment of H_1 and coordination geometry of Ni^{II} from almost tetrahedral geometry in $\text{Ni}(\text{MeL}_1)_2$ to almost square planar geometry in the more rigid complex $\text{Ni}(\text{Me}_2\text{L}_3)$ (Figure 53b).¹²²

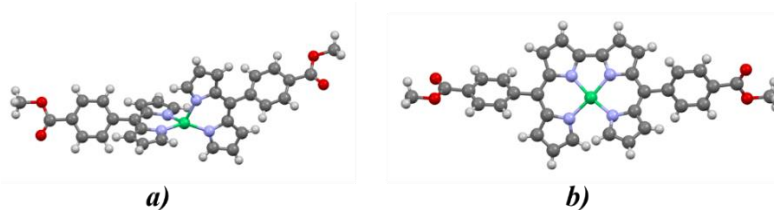


Figure 53 Crystal structures of $\text{Ni}(\text{MeL}_1)_2$ (a) and $\text{Ni}(\text{Me}_2\text{L}_3)$ (b)¹²²



The hydrolysis of the two ester groups in **Ni(Me₂L₃)** leads to the connector **Ni(H₂L₃)**. The formation of **Ni(H₂L₃)** was proven by Mass-spectrometry with a peak at 583.23 [M]⁺ that is in accordance with the expected mass.¹²¹

Due to the poor solubility of **Ni(H₂L₃)** it is difficult to analyse the stability of this connector. However, the circumstantial evidence of the **Ni(H₂L₃)** stability is the stability of the complex **Ni(Me₂L₃)** in the solid state. It was noticed that there are no changes in the ¹H-NMR spectrum of **Ni(Me₂L₃)** after 1 week if the sample was stored as a powder.



III. Phenanthroline-based metal-organic connector

III.1. Complexes of phenanthroline: a review

Phenanthroline is a rigid bidentate ligand that can form highly stable complexes with various metal ions. These complexes are widely used in analytical chemistry, biochemistry, and material science due to their inherent properties. Phenanthroline complexes typically consist of a central metal ion that coordinates phenanthroline ligands, forming a chelate bis(phenanthroline) complex (Figure 54a) or tris(phenanthroline) complex (Figure 54b). The metal ions commonly presented in phenanthroline complexes are transition metals such as copper(I)¹²⁶, ruthenium(II)¹²⁷, iron(II), cobalt(II) and nickel(II).¹²⁸

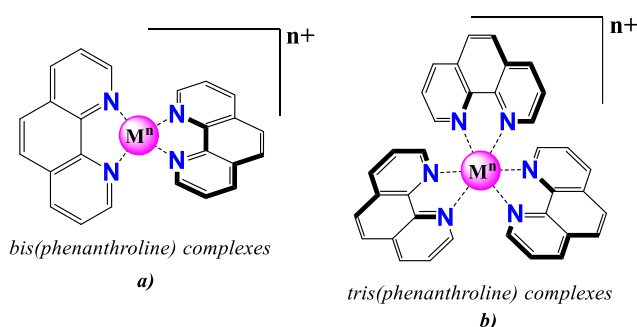


Figure 54 Two types of encountered phenanthroline complexes

Phenanthroline complexes exhibit a range of distinctive properties, depending on the metal ion and the ligand's substituents. For example, they can exhibit interesting photophysical properties,⁵ making them useful in the design of sensors and imaging agents. They can also display catalytic properties.^{129,130} Additionally, some phenanthroline complexes can undergo redox reactions, making them useful in electrochemistry and as redox-active materials.¹³¹

Phenanthroline complexes have been already used in the field of the supramolecular chemistry for the formation of phenanthroline-based MOFs presenting interesting properties. For example, MOFs exhibit luminescent properties had been reported in several publications.^{132,133} Furthermore, phenanthroline-based MOFs were studied in the field of catalysis.¹³⁴ It is worth mentioning that there are reported MOCs based on phenanthroline derivatives that demonstrated excellent fluorescent behaviour with the ability to design chemosensors for detection of many species starting with Fe^{III} ions and finishing with antibiotics (Figure 55).¹³⁵ However, to the best of our knowledge, there are no reported calixarene-based MOCs with phenanthroline complexes in the structure.

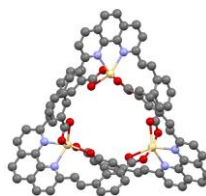


Figure 55 The structure of phenanthroline-based MOC (from ref. ¹³⁵)

Among all of the phenanthroline complexes we focused on tris(phenanthroline) complexes due to their geometrical characteristics suitable for the MOCs formation (Figure 54b). Structure of tris(phenanthroline) complexes allows to arrange coordinating positions (carboxyl groups) at an angle close to 120° which is suitable for the formation of new calixarene-based MOCs. Furthermore, chiral propeller-like arrangement of tris(phenanthroline) complexes allows the formation of new chiral MOCs which is also a perspective field.

III.1. Phenanthroline connector: size, geometry and properties

Tris[2-(4-Carboxyphenyl)imidazo[4,5-f][1,10]phenanthroline]Fe(II) hexafluorophosphate (**[rac-Fe(HL₄)₃][PF₆]₂**) is suitable for our goals (Figure 56) due its trigonal geometry together with to the presence of carboxyl groups. Similarly to the triangular tris(dipyrrin) connectors (**rac-M(HL₁)₃**, M = Co^{III}, Fe^{III}, Rh^{III}) discussed in §II.2, phenanthroline ligands in the structure of **[rac-Fe(HL₄)₃][PF₆]₂** are also orientated in propeller-like arrangement and thus **[rac-Fe(HL₄)₃][PF₆]₂** exists in two enantiomeric forms¹²⁷ Δ and Λ , which could lead to the formation of the MOCs with chiral properties. However, to the best of our knowledge there is no reported procedure for the enantiomers separation of the connector **[rac-Fe(HL₄)₃][PF₆]₂**.

In addition, iron(II) complexes of phenanthroline demonstrated high stability and distinct catalytic properties.¹²⁹ As a result, by choosing **[rac-Fe(HL₄)₃][PF₆]₂** complex as a connector, we could expect formation of the highly stable calixarene-based MOCs displaying catalytic and optical properties. Furthermore, it is worth noting that chiral MOCs could in principle be obtained using enantiomerically-pure **[Δ -Fe(HL₄)₃][PF₆]₂** and **[Λ -Fe(HL₄)₃][PF₆]₂** complexes, however enantiomers separation is a synthetic challenge.

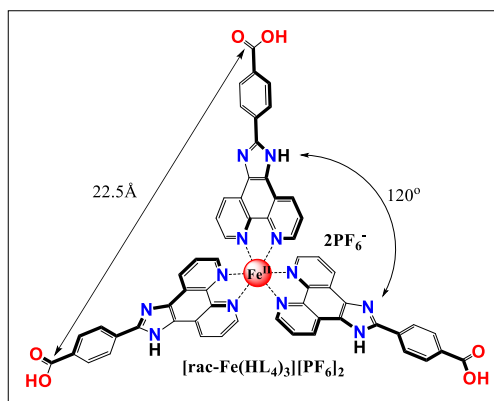


Figure 56 Structure of the triangular connector $[\text{rac-Fe}(\text{HL}_4)_3][\text{PF}_6]_2$

In terms of metrics, based on the structure of the ruthenium(II) analogue¹²⁷ the length of the connector $[\text{rac-Fe}(\text{HL}_4)_3][\text{PF}_6]_2$ is approximately 22.5 Å, and this is much larger than the corresponding tris(dipyrrin) complexes discussed in §II.1. of this chapter. Another major difference from the tris(dipyrrin) complexes is the charge, tris(phenanthroline) complexes are ionic species. Thus, $[\text{rac-Fe}(\text{HL}_4)_3][\text{PF}_6]_2$ is an ionic species with a 2+ cationic moiety, which will influence its solubility as well as the solubility of the MOCs in which it will be included.

III.2. The synthesis of triangular phenanthroline connector ($[\text{rac-Fe}(\text{HL}_4)_3][\text{PF}_6]_2$)

The exact targeted phenanthroline-based connector $[\text{rac-Fe}(\text{HL}_4)_3][\text{PF}_6]_2$ bearing two PF_6^- counterions is not reported in the literature. However, a similar complex with another counterion (SO_4^{2-}) is reported.¹³⁶

The synthesis of $[\text{rac-Fe}(\text{HL}_4)_3][\text{PF}_6]_2$ includes 4 steps (Figure 57) that was performed with an overall yield 52%.

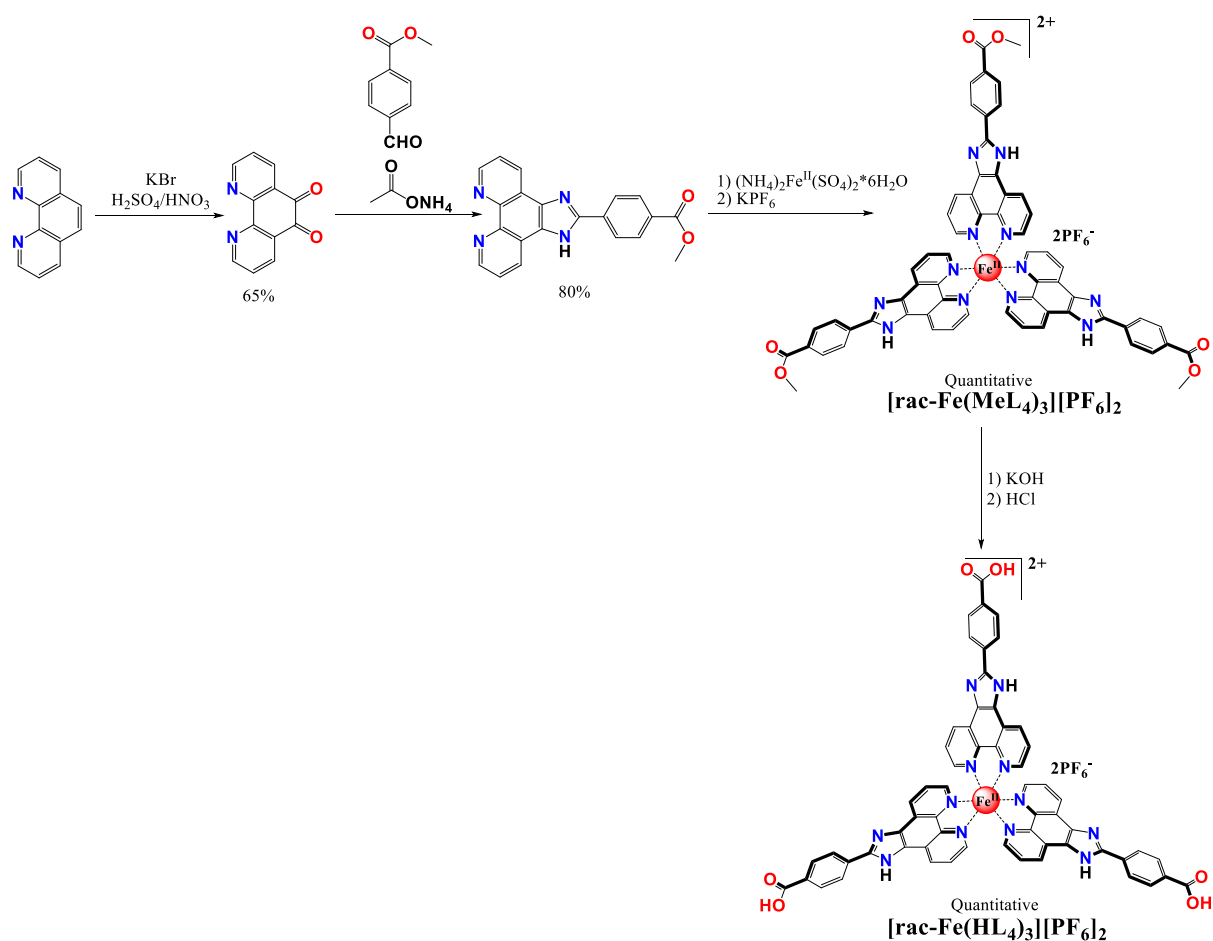


Figure 57 The synthetic pathway for the connector $[\text{rac-Fe}(\text{HL}_4)_3][\text{PF}_6]_2$

The first two steps of the $[\text{rac-Fe}(\text{HL}_4)_3][\text{PF}_6]_2$ synthesis are well-known reported procedures.¹³⁷ For the metallation step, it was experimentally demonstrated that Mohr salt $(\text{NH}_4)_2\text{Fe}(\text{SO}_4)_2 \cdot 6\text{H}_2\text{O}$ is more preferable for the metallation among other Fe^{II} salts due to its stability. Moreover, we choose hexafluorophosphate as a counter anion in order to precipitate the desired complex from the solution, as frequently exploited for such charged complexes.

Both $[\text{rac-Fe}(\text{MeL}_4)_3][\text{PF}_6]_2$ and $[\text{rac-Fe}(\text{HL}_4)_3][\text{PF}_6]_2$ complexes present a low solubility in a variety of solvents, furthermore structure of $[\text{rac-Fe}(\text{HL}_4)_3][\text{PF}_6]_2$ has multiple exchangeable protons, which results in non-informative NMR spectra. However, it is possible to observe the formation of the complex by Mass-spectrometry. The MS spectra demonstrated a peak of mass 559.14 $[\text{M}-2\text{PF}_6]^{2+}$ for $[\text{rac-Fe}(\text{MeL}_4)_3][\text{PF}_6]_2$ and peak of mass 538.44 $[\text{M}-2\text{PF}_6]^{2+}$ for $[\text{rac-Fe}(\text{HL}_4)_3][\text{PF}_6]_2$ that are in perfect accordance with the expected mass of these species. Moreover, the purity of $[\text{rac-Fe}(\text{HL}_4)_3][\text{PF}_6]_2$ was confirmed by elemental analysis.



IV. Terpyridine-based metal-organic connectors family

IV.1. Terpyridine complexes: review

The family of terpyridine complexes comprises a variety of metal-organic structures with various metal ions together with various substituents integrated in the organic part. In general, terpyridine family consist of mono(terpyridine) and bis(terpyridine) species. (Figure 58). Prior to metal coordination, the nitrogens on the 2-pyridine cycles are arranged in a *trans-trans* geometry to minimize the repulsion between the lone-pairs of the nitrogen. However, upon coordination with a metal cation, a *cis-cis* geometry is established after chelation leading to the formation of stable complexes.¹³⁸

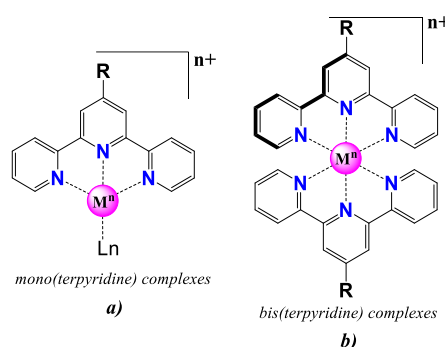


Figure 58 Two types of encountered terpyridine complexes

Family of terpyridine complexes represented by complexes with the variety of metal ions. There are reported terpyridine complexes with iron(II), cobalt(II), manganese(II), zinc(II), ruthenium(II), osmium (II) and etc.¹³⁹⁻¹⁴³ Terpyridine complexes are interesting complexes for the MOCs formation due to their unique inherent properties. For instance, terpyridine complexes of Ru^{II} demonstrated redox activity¹⁴⁴, terpyridine complexes of Zn^{II} demonstrated optical properties¹⁴². Furthermore, Ru^{II}-terpyridine complexes demonstrated great photochemical activity that was observed in the reactions of proton reduction from water⁷ or water oxidation.¹⁴⁵ Mono(terpyridine) complexes of Fe^{II} and Co^{II} demonstrated catalytic activity in different reactions including Suzuki–Miyaura Cross-Coupling Reactions.^{139,140}

Some of the terpyridine complexes were already applied in the field of supramolecular chemistry for the formation of MOFs, for example, MOF based on Zn^{II}-terpyridine with adsorption and luminescent properties has been reported.¹⁴⁶ Furthermore, it was possible to obtain Cu^{II} terpyridine-based MOFs with catalytic properties¹⁴⁷ and Ho^{III} terpyridine-based MOFs with ion separation properties.¹⁴⁸ It is worth mentioning that terpyridine molecules were also used for the formation of MOCs. For example, giant terpyridine-based MOC was reported in 2018.¹⁴⁹ This

MOC was formed by terpyridine ligands that self-assembled with Zn^{II} ions in the cage like structure (Figure 59).

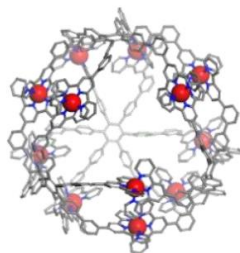


Figure 59 Terpyridine-based MOC (red spheres represent Zn^{II} cations) (from ref. ¹⁴⁹)

Among all of the terpyridine complexes, we focused on bis(terpyridine) complexes due to their geometrical characteristic suitable for the edge-panelled MOCs formation (Figure 58b). To the best of our knowledge there are no reported MOCs where bis(terpyridine) complexes played a role of metal-organic connector, as well as, there is no reported calixarene-based MOCs with terpyridine moieties.

IV.2. Linear terpyridine connectors: properties, size and geometry

Bis(terpyridine) complexes suitable for the formation of targeted calixarene-based MOCs must present in their structure coordinating groups. Thus, we focused on [4'-(4-Carboxyphenyl)-2,2':6',2''-terpyridinato] M(II) complexes (Figure 60).

Among all the variety of metal ions suitable for the formation of bis(terpyridine) complexes we focused on complexes with iron(II), cobalt(II) and ruthenium (II): Bis[4'-(4-Carboxyphenyl)-2,2':6',2''-terpyridine] Fe(II) hexafluorophosphate ($[Fe(HL_5)_2][PF_6]_2$), Bis[4'-(4-Carboxyphenyl)-2,2':6',2''-terpyridine] Co(II) hexafluorophosphate ($[Co(HL_5)_2][PF_6]_2$) and Bis[4'-(4-Carboxyphenyl)-2,2':6',2''-terpyridine] Ru(II) hexafluorophosphate ($[Ru(HL_5)_2][PF_6]_2$). These three bis(terpyridine) complexes form *the family of terpyridine connectors* that will be used in the synthesis of new calixarene-based MOCs (Figure 60).

The terpyridine connectors family was limited by $[M(HL_5)_2][PF_6]_2$ ($M = Fe^{II}, Co^{II}, Ru^{II}$) compounds due to several reasons: first of all, bis(terpyridine) complexes of Ru^{II} , Co^{II} and Fe^{II} are relatively stable when compared to other terpyridine complexes.¹⁴³ Also, we expect that calixarene-based MOCs based on $[Ru(HL_5)_2][PF_6]_2$ to exhibit great photocatalytic activity due to predisposition of Ru^{II} -terpyridine complexes to electron transfer from the excited state. This activity was well-demonstrated in the reactions of hydrogen evolution where electron from excited state of bis(terpyridine) complex of Ru^{II} was transferred to protons, which caused protons reduction.¹⁵⁰

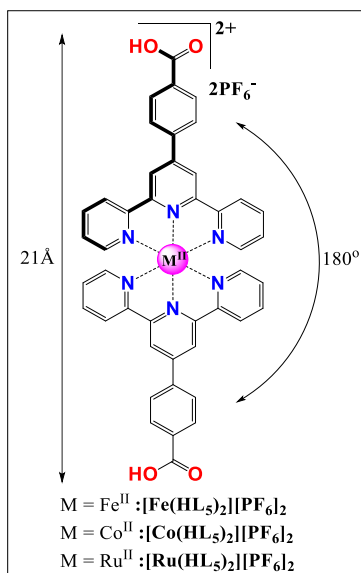


Figure 60 Structure of the linear connectors $[\text{Fe}(\text{HL}_5)_2][\text{PF}_6]_2$, $[\text{Co}(\text{HL}_5)_2][\text{PF}_6]_2$ and $[\text{Ru}(\text{HL}_5)_2][\text{PF}_6]_2$

In terms of size, XRD data of similar bis(terpyridine) complex of Ru^{II} allowed to estimate the length of the connectors $[\text{M}(\text{HL}_5)_2][\text{PF}_6]_2$ ($M = \text{Fe}^{\text{II}}, \text{Co}^{\text{II}}, \text{Ru}^{\text{II}}$) to approximately 21 Å, the angle between coordinating sites is 180° which is perfect for the formation of edge-panelled MOCs (Figure 60).¹⁵¹ Additionally, similarly to the phenanthroline connector $[\text{rac-Fe}(\text{HL}_4)_3][\text{PF}_6]_2$, terpyridine connectors $[\text{M}(\text{HL}_5)_2][\text{PF}_6]_2$ ($M = \text{Fe}^{\text{II}}, \text{Co}^{\text{II}}, \text{Ru}^{\text{II}}$) are ionic species.

IV.3. The synthesis of linear terpyridine connectors ($[\text{M}(\text{HL}_5)_2][\text{PF}_6]_2$)

$[\text{Fe}(\text{HL}_5)_2][\text{PF}_6]_2$, $[\text{Co}(\text{HL}_5)_2][\text{PF}_6]_2$ and $[\text{Ru}(\text{HL}_5)_2][\text{PF}_6]_2$ complexes are already reported species.^{152–154}

The three connectors are obtained in a 2 steps synthesis. The first step is the synthesis of the HL_5 in 60% yield via a Kröhnke reaction starting from 2-acetylpyridine and 4-carboxybenzaldehyde. The metallation occurs in a second step leading to $[\text{Fe}(\text{HL}_5)_2][\text{PF}_6]_2$, $[\text{Co}(\text{HL}_5)_2][\text{PF}_6]_2$ and $[\text{Ru}(\text{HL}_5)_2][\text{PF}_6]_2$ with overall yield of 57% for $[\text{Fe}(\text{HL}_5)_2][\text{PF}_6]_2$, 48% for $[\text{Co}(\text{HL}_5)_2][\text{PF}_6]_2$ and 60% for $[\text{Ru}(\text{HL}_5)_2][\text{PF}_6]_2$.¹⁵¹ It is worth mentioning that the best results in the metallation process were obtained using the corresponding chloride salts (see details in experimental part).

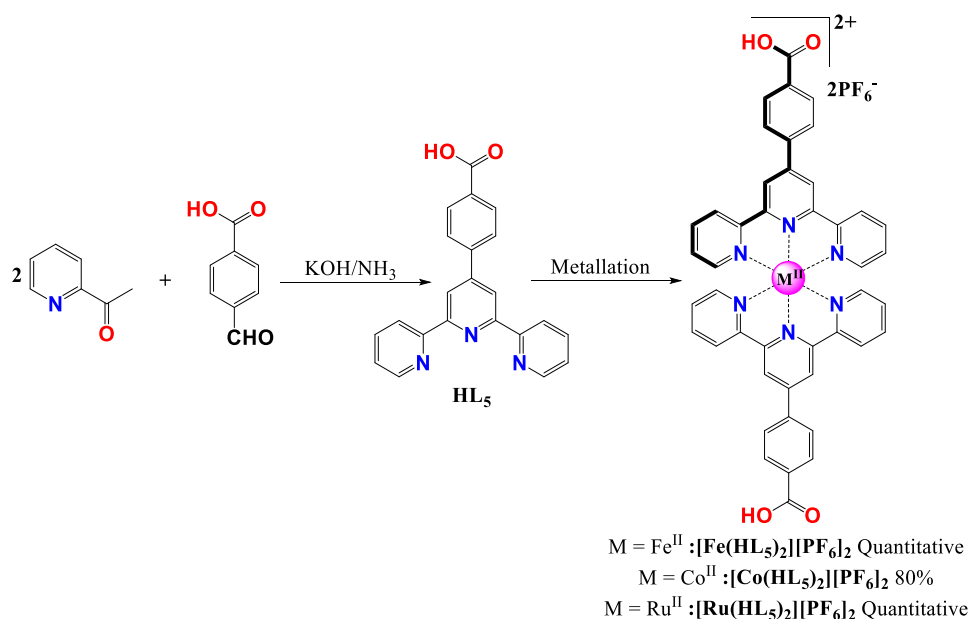


Figure 61 The synthetic pathway for the connectors $[\text{Fe}(\text{HL}_5)_2][\text{PF}_6]_2$, $[\text{Co}(\text{HL}_5)_2][\text{PF}_6]_2$ and $[\text{Ru}(\text{HL}_5)_2][\text{PF}_6]_2$

In addition, the use of N-ethylmorpholine as a reducing agent is crucial to obtain the connector $[\text{Ru}(\text{HL}_5)_2][\text{PF}_6]_2$.

The $^1\text{H-NMR}$ spectrum of $[\text{Ru}(\text{HL}_5)_2][\text{PF}_6]_2$ is in accordance with the published data.¹⁵¹ The $^1\text{H-NMR}$ spectrum of $[\text{Fe}(\text{HL}_5)_2][\text{PF}_6]_2$ revealed the formation of the desired complex, however, due to the poor solubility, the observed peaks are broad (see experimental part). The $^1\text{H-NMR}$ spectrum of $[\text{Co}(\text{HL}_5)_2][\text{PF}_6]_2$ is not informative due to paramagnetic nature of Co^{II} ions.

The MS experiments demonstrated the formation of the desired species with peaks of mass at 381.10 $[\text{M}-2\text{PF}_6]^{2+}$, 382.58 $[\text{M}-2\text{PF}_6]^{2+}$, 404.07 $[\text{M}-2\text{PF}_6]^{2+}$ for $[\text{Fe}(\text{HL}_5)_2][\text{PF}_6]_2$, $[\text{Co}(\text{HL}_5)_2][\text{PF}_6]_2$ and $[\text{Ru}(\text{HL}_5)_2][\text{PF}_6]_2$ respectively, which are in perfect accordance with the expected values.

The obtained connectors $[\text{M}(\text{HL}_5)_2][\text{PF}_6]_2$ ($M = \text{Fe}^{\text{II}}, \text{Co}^{\text{II}}, \text{Ru}^{\text{II}}$) appeared to be stable in the solid state and in solution (DMSO). The $^1\text{H-NMR}$ spectra did not demonstrate changes after one week of observations for powders and solutions.



V. Porphyrin-based metal-organic connector

V.1. Porphyrin macrocycles: review

Porphyrins are composed of four pyrrole rings, which are linked by methine bridges to form a macrocycle (Figure 62). The distinctive properties of porphyrins arise from their conjugated system of double bonds, which give them a characteristic absorption spectrum in the visible range widely used in sensors¹⁵⁵.

Porphyrin family includes derivatives with substituents in *meso*- and β -pyrrolic positions, as shown on Figure 62. In this work we focused on *meso*-substituted porphyrin derivatives due to their characteristics appropriate for our goals. There is a great variety of *meso*-substituted porphyrin derivatives, distinct from each other by the number, the type, and the position of the substituents (Figure 62).

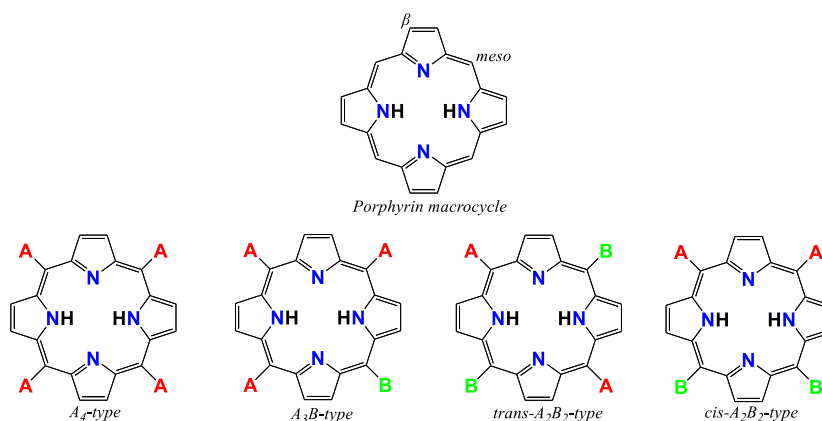


Figure 62 Representation of the porphyrin macrocycle and the different types of *meso*-substituted porphyrin derivatives

The porphyrin macrocycle presents a large central cavity with diameter close to 4Å that can bind a variety of metal ions to form metalloporphyrins that display unique physical and chemical properties. This coordination can affect the electronic properties of the macrocycle, leading to changes in its optical properties,¹⁵⁶ appearance of new electrochemical¹⁵⁷ and photocatalytic^{158,159} properties achieved due to the highly photosensitive porphyrin macrocycle and the presence of the metal ion in the cavity of the porphyrin. In addition, the presence of one or two additional ligands in the axial positions of the metallic cations in the cavity depends on the nature and the oxidation number of the metal ion.

Metalloporphyrins exhibit a range of interesting and distinguishable properties, depending on the nature of the metal ion coordinated to the porphyrin macrocycle. For example, Fe^{III}-porphyrins exhibit distinct magnetic properties, related with magnetic coupling between metalloporphyrin and ferromagnetic surfaces.^{160,161} Ni^{II}-porphyrins demonstrate excellent

photocatalytic activity.¹⁶² Furthermore, all of the metalloporphyrins exhibit distinct optical properties due to the porphyrin macrocycle.

The potential of metalloporphyrins in the field of supramolecular chemistry has been demonstrated by the synthesis of numerous porphyrin-based MOFs and MOCs. Metalloporphyrins have been used for the synthesis of MOFs with fluorescent¹⁶³ and catalytic properties,¹⁵⁸ and there is a great manifold of synthesized porphyrin-based MOCs, for example multimetallic Zn/Ru porphyrin based cage (Figure 63).¹⁶⁴ Furthermore, MOCs that include both metalloporphyrin and calixarene moieties have been reported in the literature, for example, MOC that included a zinc(II)-porphyrin covalently connected to ionophoric calixarene was reported in 2001.¹⁶⁵ However, to the best of our knowledge there are no reported structure of MOCs based on calixarenes and porphyrins connected to each other through coordination bonds.

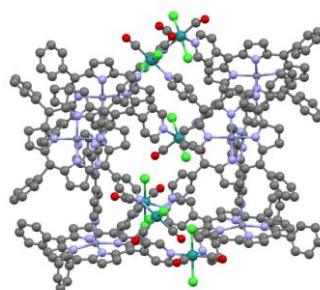


Figure 63 The representation of a multimetallic Zn/Ru porphyrin-based MOC (from ref. ¹⁶⁴)

Metalloporphyrin-based MOCs with calixarenes would be particularly interesting for biomedical applications, as metalloporphyrins have demonstrated anticancer¹⁶⁶ and antibacterial¹⁶⁷ properties, while the use of calixarenes in drug delivery systems is gaining increasing attention due to their ability to encapsulate guest molecules.¹⁶⁸ The combination of metalloporphyrins and calixarenes in MOCs can provide a new platform for drug delivery and biomedical imaging applications.

V.2. Porphyrin connector: size, geometry and properties

Among all of the variety of metalloporphyrin derivatives we focused on *trans*-A₂B₂-metalloporphyrins (Figure 62) due to their linear geometry allowing angle 180° between the coordinating positions that is suitable for the formation of edge-panelled calixarene-based MOCs. Other derivatives are less favourable due to the potential steric hindrances between porphyrin connectors and shuttlecock calixarene-nodes that might occur. For instance, in A₃B-metalloporphyrins the angle between coordinating positions is 90° that is not acceptable for the octahedral cage formation. A₄-metalloporphyrin are also expected to have an angle 90° between



coordinating positions with possibility to obtain cubic MOCs, however, steric hindrances might also occur between shuttlecock calixarene units and A₄-metalloporphyrin connector.

As it was discussed in the §I. of this chapter, carboxyl groups are required for the formation of calixarene-based MOCs, so we focused on a *trans*-A₂B₂-metalloporphyrin with carboxyl groups located in two opposite *meso*-positions (Figure 62) making it suitable for the formation of edge-panelled calixarene-based MOCs.

Concerning the metal ion present in the cavity we first targeted *trans*-A₂B₂-metalloporphyrin with Ni^{II} due to its high stability and excellent photocatalytic properties.¹⁶² It is worth mentioning that Ni^{II} ion perfectly fits into the cavity of the porphyrin macrocycle when compared to larger ions (for example, lanthanides) that are located above porphyrin macrocycle.¹⁶⁹

Usually, Ni^{II} ion in a porphyrin cavity adopts a square planar coordination geometry with no axial ligand. However, it has been demonstrated that under certain conditions, Ni^{II}-porphyrins can coordinate certain additional ligand, making it potentially useful for catalysis^{170,171} especially in the confined space of MOCs.

Based on the aforementioned constraints, the neutral complex [5,15-bis(4-carboxyphenyl)-10,20-diphenylporphyrinato] Ni(II) (**Ni(H₂L₆)**) was chosen as targeted metal-organic connector for synthesis of novel calixarene-based MOCs (Figure 64).

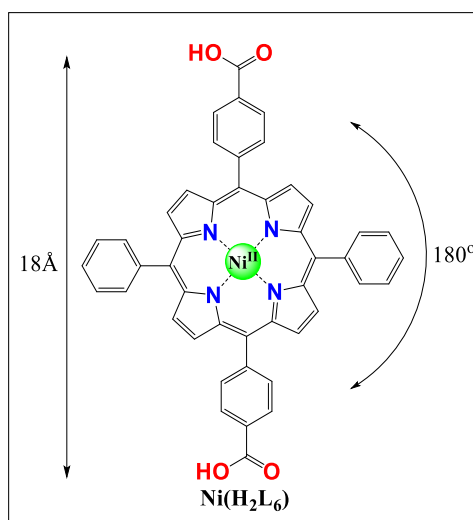


Figure 64 Structure of the linear connector **Ni(H₂L₆)**

The linear size of **Ni(H₂L₆)** is estimated approximately to 18 Å from the crystal data of the similar species¹⁵⁸ which exceeds the size of the linear connectors previously used for the formation of edge-panelled octahedral calixarene-based MOCs.

V.3. The synthesis of the linear porphyrin connector (Ni(H₂L₆))

The synthetic pathway was followed according to the already reported procedures.^{172,159}

The synthesis of Ni(H₂L₆) is a 3 steps procedure with an overall yield of 8.3% (Figure 65). This low yield can be explained mainly by the first step that lead to the formation of many different oligomeric and cyclic products from numerous side reaction. The optimized conditions used leads to the formation of Me₂L₆ in 15%, which is acceptable for such a reaction.

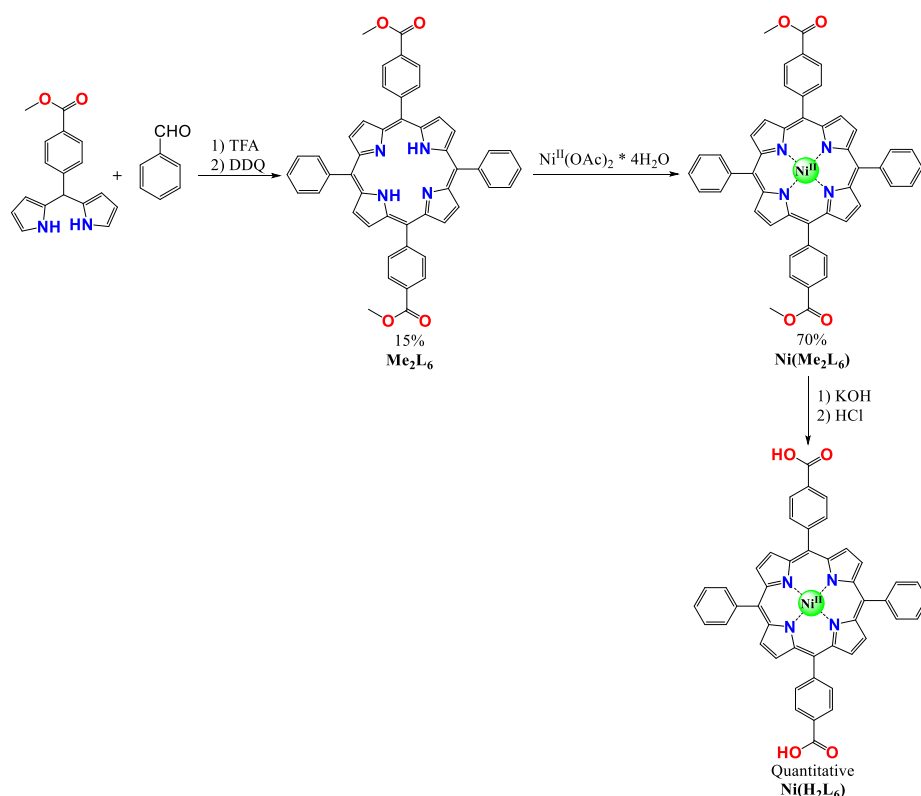


Figure 65 The synthetic pathway for the connector Ni(H₂L₆)

Me₂L₆ is easily tracked by ¹H-NMR spectroscopy due to characteristic upfield shifted peak of NH-protons close to -2.7 ppm.¹⁷² Moreover, the A₂B₂-nature of the porphyrin is proven by the presence of two methyl groups per porphyrin while the trans-A₂B₂ symmetry of the compound is confirmed by the presence of two doublets for the 8 β-pyrrolic protons (Figure 66).

The second step is the metallation with the use of salt Ni(OAc)₂ · 4H₂O. The completeness of this step is also easily tracked due to disappearance of the signals in ¹H-NMR related to the NH-protons (Figure 66).

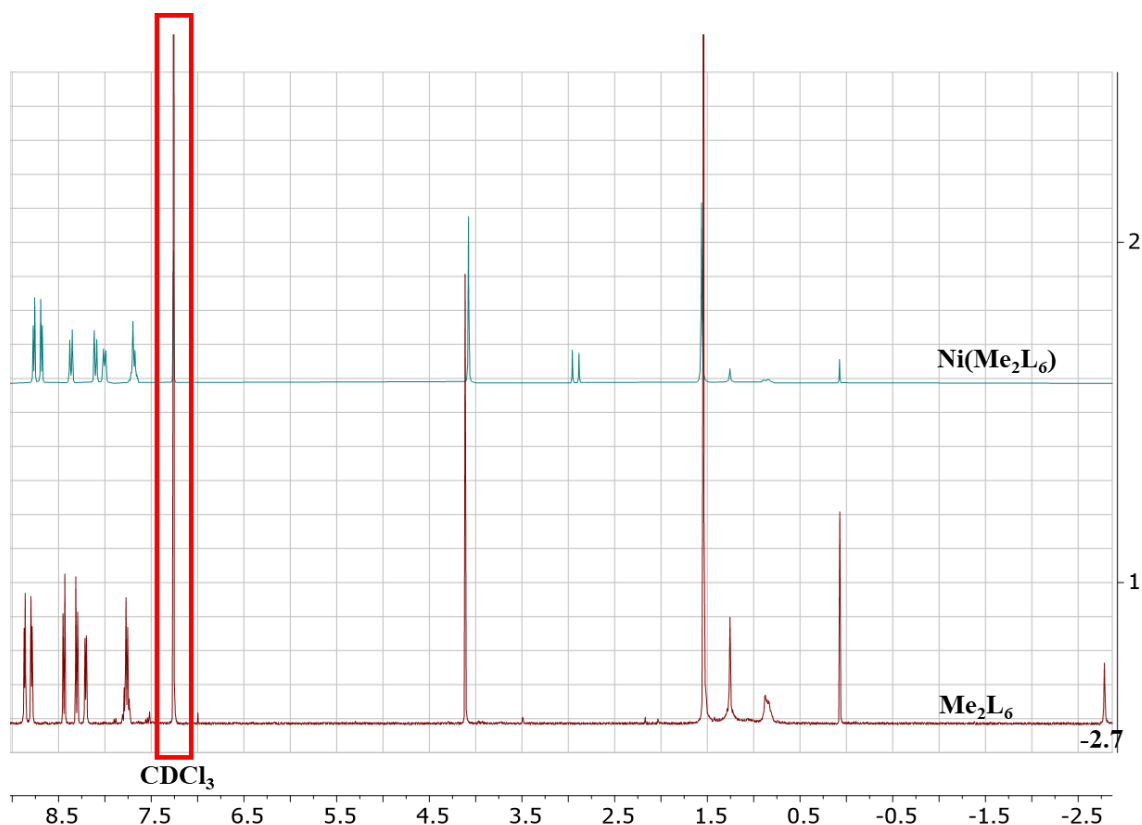


Figure 66 *NMR spectra of Me_2L_6 and $\text{Ni}(\text{Me}_2\text{L}_6)$*

The final step is the hydrolysis of $\text{Ni}(\text{Me}_2\text{L}_6)$ that was performed in the similar way to hydrolysis of the connectors from dipyrin family. The formation of $\text{Ni}(\text{H}_2\text{L}_6)$ connector was proved by $^1\text{H-NMR}$ with the disappearance of methyl groups. Mass-spectrometry demonstrated the formation of species with peak of mass 758.15 $[\text{M}]^+$ that is in a perfect accordance with the expected value of the metalloconnector $\text{Ni}(\text{H}_2\text{L}_6)$.

The connector $\text{Ni}(\text{H}_2\text{L}_6)$ demonstrates a good stability in the solid state and in solution (DMSO). However, due to photosensitivity it is recommended to keep this connector protected from light. $\text{Ni}(\text{H}_2\text{L}_6)$ does not demonstrate decomposition processes if stored as a powder. The $^1\text{H-NMR}$ spectrum of freshly obtained $\text{Ni}(\text{H}_2\text{L}_6)$ and the $^1\text{H-NMR}$ spectrum of $\text{Ni}(\text{H}_2\text{L}_6)$ stored for a week as a powder under light protection are identical.

Another similar macrocycle chosen as a metal-organic connector for the formation of calixarene-based MOCs is a corrole macrocycle.

VI. Corrole-based metal-organic connector

VI.1. Corrole macrocycle: review

Corroles belong to a class of tetrapyrrolic macrocycles that is similar to the porphyrin family, but with a direct connection between two pyrroles. These molecules are characterized by a macrocyclic structure with a central cavity (diameter 3.7 Å) that can bind numerous metal ions, forming metal complexes (metallocorroles) with a variety of interesting properties (Figure 67). A major difference between corrole and porphyrin is the presence of three inner NH group instead of two for the porphyrin. Many metallocorroles with different metals are reported. For example, metallocorroles with Co^{III} , Mn^{III} , Fe^{III} , Pt^{IV} , Ta^{V} etc.¹⁷³ As well as metalloporphyrins, metallocorroles exhibit excellent catalytic,¹⁷⁴ electrochemical¹⁷⁵ and optical¹⁷⁶ properties due to highly photosensitive corrole macrocycle and the presence of the metal ion with possible available axial coordination positions.



Figure 67 Structure of the metallocorrole core

Metallocorroles were used for example for the formation of MOFs with large surface areas.^{6,177} That means that corrole molecules are able to form periodic and highly symmetric structures. However, to the best of our knowledge, there are no examples of the MOCs with corrole moieties.

VI.2. Corrole connector: size, geometry and properties

Among all the variety of corrole derivatives we focused on species having carboxylate coordinating groups, in particular, tricarboxylate derivatives. Trans-dicarboxylate derivatives could have been of interest, but the synthesis of these corroles appears more than tedious, thus, we focused first on the synthesis of the more symmetrical corrole having the same substituents in the 3 *meso*-positions. For the same reason, we chose $\text{Co}(\text{III})$ that is stable and fits perfectly in the corrole cavity.¹⁷⁸

As a result, complex [5,10,15-Tris(4-carboxyphenyl)corrolato] $\text{Co}(\text{III})$ ($\text{Co}(\text{H}_3\text{L}_7)$) was chosen as a metal-organic neutral connector according to the aforementioned restraints (Figure 68). Connector $\text{Co}(\text{H}_3\text{L}_7)$ is expected to exhibit great optical properties due to presence of corrole core and catalytic properties due to availability of axial coordination positions of Co^{III} ions as it was demonstrated for the similar species.¹⁷⁴

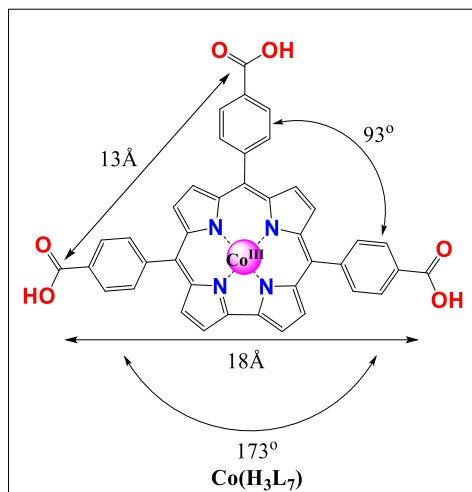


Figure 68 Structure of the triangular connector $\text{Co}(\text{H}_3\text{L}_7)$

The $\text{Co}(\text{H}_3\text{L}_7)$ connector possesses a unique structure and geometry, distinguishing it from other selected connectors. It is triangular tridentate connector, with the Co^{III} in the planar environment situated within the corrole cavity. It worth mentioning that normally Co^{III} coordinates other molecules (molecules of solvent) in the axial positions in order to fill free coordination positions, which leads to the octahedral environment.¹⁷³ However, it is possible to decoordinate these molecules or substitute them in order to achieve desired properties.

The shape of the connector is *ca* T geometry with two different angles between coordinating positions, namely 93° and 173° (Figure 68)¹⁷⁹ that should in principle not be appropriate to be used as a trigonal tridentate connector for the obtaining face-panelled MOCs. However this, corrole complexes have a certain degree of flexibility, as demonstrated in the structure of one related MOF, where the angles adapt values of approximately 101° and 157° .⁶ Consequently, we can anticipate a certain degree of flexibility in the $\text{Co}(\text{H}_3\text{L}_7)$ connector, and its adaptability to be included in a distorted octahedral face-panelled MOCs.

According to aforesaid, the formation of corrole-based MOCs is a perspective field. The formed cages are expected to be face-panelled with excellent optical, catalytic and electrochemical properties due to the presence of metallocorrole $\text{Co}(\text{H}_3\text{L}_7)$ in the structure of the cage.

VI.3. The synthesis of triangular corrole connector ($\text{Co}(\text{H}_3\text{L}_7)$)

The synthetic pathway of $\text{Co}(\text{H}_3\text{L}_7)$ is based on the already reported procedures^{6,178,180} and includes 3 steps starting from dipyrromethane with an overall yield 31% (Figure 69).

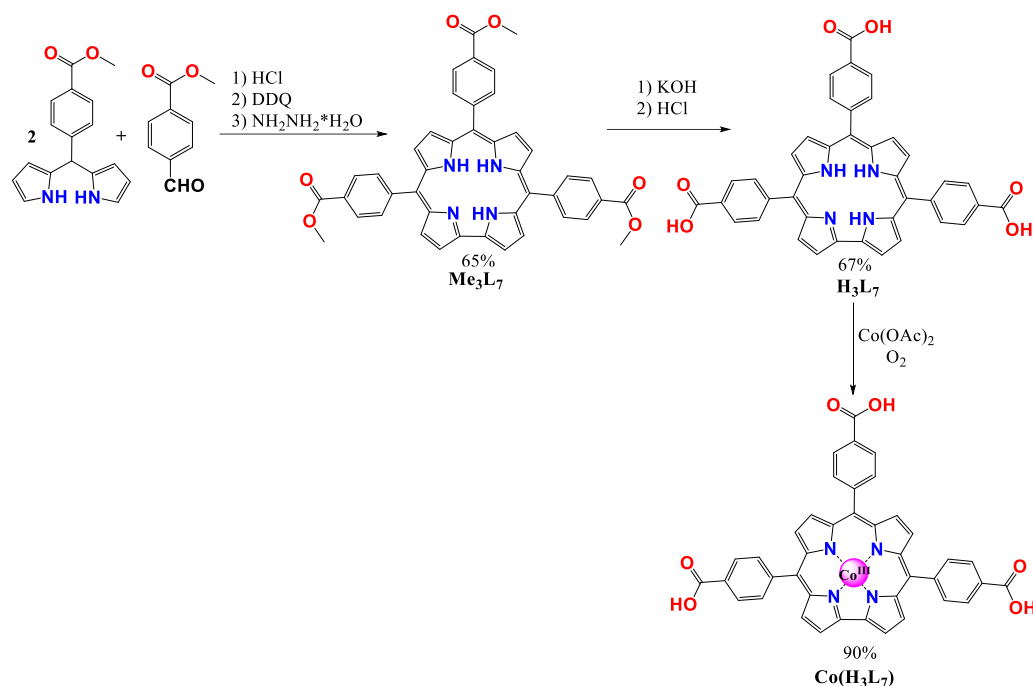


Figure 69 The synthetic pathway for the connector $\text{Co}(\text{H}_3\text{L}_7)$

The corrole macrocycle formation looks similar to the formation of porphyrins, however, in order to favour the formation of corrole it is important to add DDQ before bilane is converted to porphyrinogen (Figure 70). In addition, a quenching with hydrazine hydrate demonstrated increasing of the reaction yield.¹⁸¹

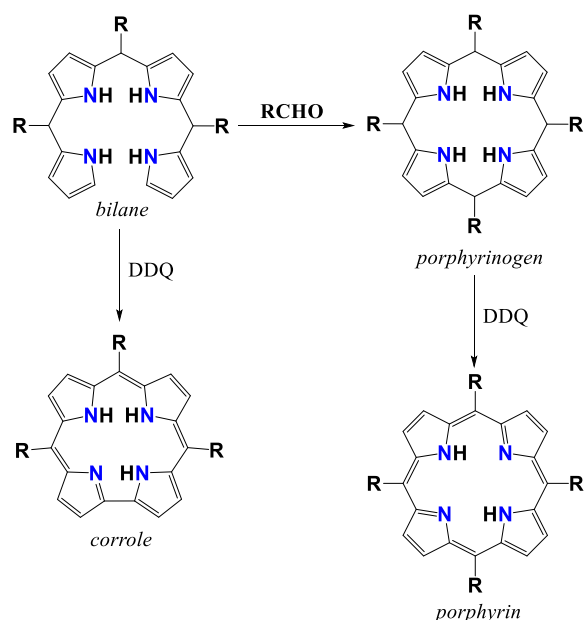


Figure 70 Differences in the synthesis of porphyrin and corrole macrocycles

The first step is the well-known reaction of 5-(4-Carboxymethylphenyl)dipyrromethene and 4-(carboxymethyl)benzaldehyde coupling that was reported by Gryko *et al.*¹⁸⁰ However, it was possible to significantly improve the reported procedure, and to skip the step of purification



with the column chromatography and achieve the yield of the desired corrole **Me₃L₇** up to 65% (see experimental part).

It is important to run the hydrolysis of the ester functions prior to the metallation because complex **Co(Me₃L₇)** is not stable upon the hydrolysis conditions. Saponification of **Me₃L₇** leads to the tri-carboxylate corrole **H₃L₇** in 67% yield.

The last step of the procedure is metallation with $\text{Co}(\text{OAc})_2$. It is important to perform this reaction with an access to oxygen in order to oxidize [**Co^{II}H₃L₇**] to [**Co^{III}H₃L₇**]. It is important to say, that Co^{III} has free coordination positions and coordinates molecules of DMSO from the reaction mixture (see experimental part). It was demonstrated that in order to obtain better NMR spectra it is necessary to substitute DMSO molecules with NH_3 molecules. As a result, it is important to perform NMR experiments under NH_3 atmosphere. Nevertheless, the connector **Co(H₃L₇)** has poor solubility in many of the most common solvents so it is hard to obtain descent ¹H-NMR and usually peaks appeared broad. The MS experiment demonstrated a peak at 714.10 [M]⁺ that is in perfect accordance with the expected mass of **Co(H₃L₇)**.

The stability investigations were not performed for the connector **Co(H₃L₇)** due to its poor solubility in the variety of solvents. Furthermore, the black colour of **Co(H₃L₇)** creates obstacles for the observations of colour change if the decomposition occurs.

The connectors discussed in all the previous sections of this chapter are metal-organic molecules and the field of MOCs based on them is rather underexplored. However, we have also focused on a family of purely organic connectors, whose role in calixarene-based MOCs synthesis is also poorly explored. This family is discussed in detail in the following section.

VII. Organic connectors

Despite the wide variety of triangular organic connectors that have been used for the construction of calixarene-based MOCs, there are still many species that have not been explored for these purposes. Many organic connectors with carboxyl groups were used for the formation of calixarene-based MOCs lack groups that provide specific interactions, such as π -interactions (Figure 71).^{78,182} Reported calixarene-based MOCs typically vary the size and the geometry of the connectors to modify the size of the cavity to adapt them to the shape needed for the trapping of targeted species. Our objective is rather the introduction of connectors with specific properties in the cage structure in order to build cages with interesting and useful properties.

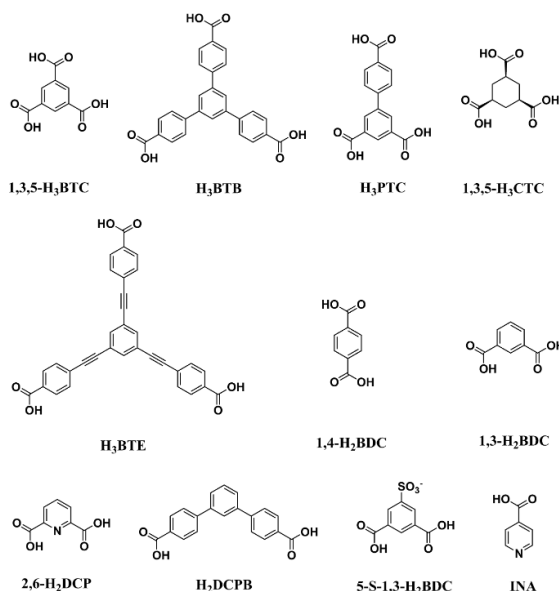


Figure 71 Some of the organic connectors with carboxyl groups used for the formation of calixarene-based MOCs (from ref. ⁷⁸)

One of the species that could be of interest is derivatives of 1,3,5-triazine that exhibits intriguing properties that could be exploited for the formation of large calixarene-based MOCs capable for anion- π recognition. These properties are discussed in detail in the following section.

VII.1. Triazine core: review

Anion- π recognition refers to the ability of a molecule to selectively bind and recognize anions due to non-covalent interaction between anions and the π -system of the molecule. The 1,3,5-triazine ring has a positive charge area that is widely-used for the design of anion- π recognition systems⁸ arising from their electron-deficient nature (Figure 72). Thus, applying of 1,3,5-triazine core in the structure of connectors could lead to MOCs with anion recognition properties.

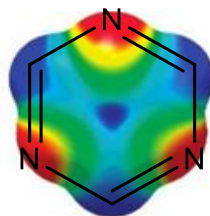


Figure 72 Calculated 6-31+G*/6-31+G* electrostatic potential surfaces for 1,3,5-triazine. Electrostatic potential surface energies range from -15 (red) to +15 (blue) kcal mol⁻¹ (from ref. ⁸)

1,3,5-triazine derivatives have already been used for the formation of MOFs: there is an example of MOF based on 4,4',4''-(1,3,5-triazine-2,4,6-triyl)tribenzoic acid that demonstrated a



great porosity with the pore width of 35Å and with BET surface area 2008 m²/g.¹⁸³ Additionally, there are examples of triazine-based MOCs¹⁸⁴ that demonstrated outstanding host-guest properties.¹⁸⁵ One particular example that demonstrates perspectives of the 1,3,5-triazine species usefulness for the formation of MOCs with anion- π recognition properties is triazine-based MOC with the ability to interact with Cl⁻ anions.¹⁸⁶ This MOC demonstrates chloride-triazine recognition in the solid state with distances of 3.19Å between 1,3,5-triazine ring and Cl⁻, and 3.13Å between 1,3,5-triazine ring and [CuCl₄]²⁻. These parameters are almost exactly the same as those predicted for the complex 1,3,5-triazine with Cl⁻ anions (Figure 73). It is worth noting that octahedral calixarene-based MOC with 1,3,5-triazine connector has been already reported in the literature.¹⁸⁷ However, anion- π recognition properties of this cage were not studied. The structure of this cage will be discussed in detail in §V.1. of Chapter III.

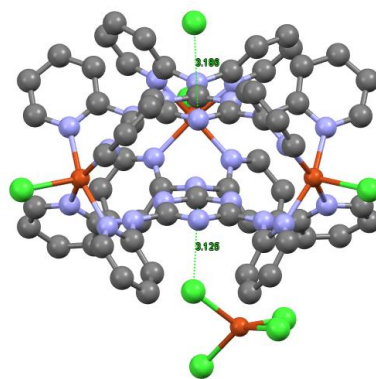


Figure 73 Triazine-based MOC with anion- π recognition properties (from ref. ¹⁸⁶)

Based on the analysis, the incorporation of the 1,3,5-triazine moiety into the structure of calixarene-based MOCs represents a promising avenue due to the positive charge distribution in the central region of the 1,3,5-triazine core. This strategy has the potential to generate novel calixarene-based MOCs with distinct anion- π recognition properties. In addition, the 1,3,5-triazine moiety offers the possibility of functionalization and the formation of diverse derivatives, enabling the production of MOCs with the desired size and properties.

VII.2. Triazine connectors: size, geometry and properties

The inherent structure of 1,3,5-triazine core favours triangular geometry. Consequently, the targeted connectors are expected to be triangular tridentate species. Three neutral connectors bearing carboxyl groups were selected to form *triazine connectors family* (Figure 74): 4,4',4''-(1,3,5-triazine-2,4,6-triyl)tribenzoic acid (**H₃L₈**), 2,2',2''-((1,3,5-triazine-2,4,6-triyl)tris(azanediyl))triacetic acid (**H₃L₉**) and 4,4',4''-(((1,3,5-triazine-2,4,6-triyl)tris(azanediyl))tris(methylene))tribenzoic acid (**H₃L₁₀**). They differ by the nature of the

junction between carboxyl groups and 1,3,5-triazine core and, as a result, they also differ in the flexibility and the size.

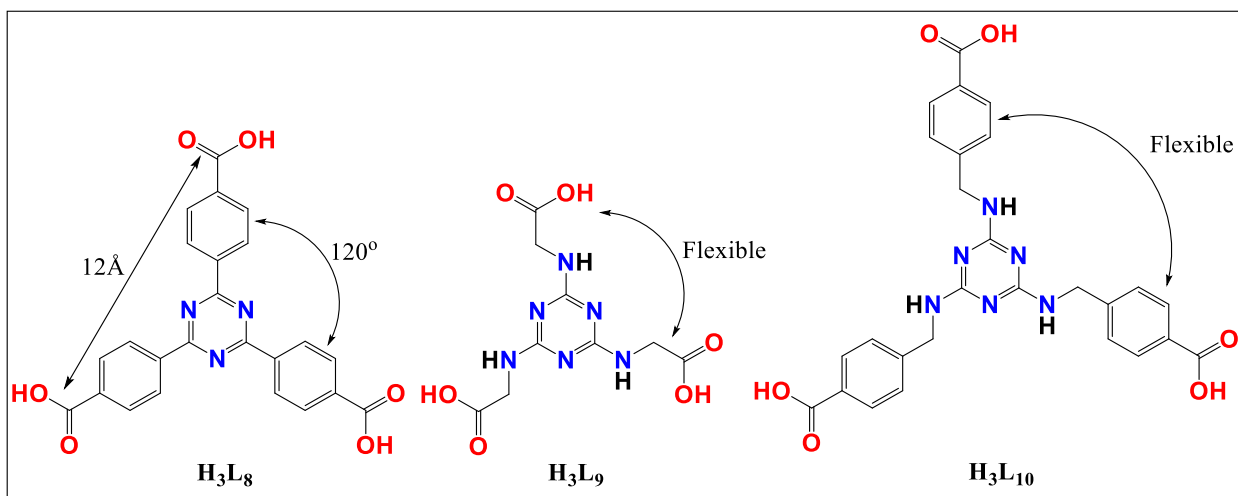


Figure 74 Structure of the triangular organic connectors **H₃L₈**, **H₃L₉**, **H₃L₁₀**

Connectors from triazine family are the great candidates for the formation of MOCs, particularly in terms of geometry. XRD data¹⁸⁸ demonstrates that **H₃L₈** connector has a moderate size (12 Å) similar to the size of the most frequently used connectors in the MOCs synthesis while the angle between coordinating sites (120°) is perfect for the formation of face-panelled MOCs. Connectors **H₃L₉** and **H₃L₁₀** are much more flexible than connector **H₃L₈**. As a result, we expect that these connectors are able to adapt to the geometry required for the formation of the MOCs (Figure 74).

VII.3. The synthesis of triangular 1,3,5-triazine connectors (**H₃L₈**, **H₃L₉**, **H₃L₁₀**)

Connectors **H₃L₈**, **H₃L₉**, **H₃L₁₀** have been already reported and the synthesis was adapted from the literature procedures.^{189,190}

The synthesis of 1,3,5-triazine connectors is a two-steps procedure for the connector **H₃L₈** and one-step procedure for the connectors **H₃L₉** and **H₃L₁₀** (Figure 75).

The synthesis of the **H₃L₈** is a procedure that was performed without significant modifications from the reported one.¹⁸⁹ The first step of the **H₃L₈** synthesis is the Friedel-Crafts reaction where cyanuric chloride plays a role of the electrophile after activation by AlCl₃. The crude product is obtained with a yield of 75% and used without purification in the following step. The second step is a reaction of oxidation of the 3 methyl groups directly to the carboxylic acid with a yield of 75%. The overall yield of the **H₃L₈** synthesis is 68%, which is in accordance with the literature.



The synthesis of **H3L9** and **H3L10** are also reported procedures that were performed without significant modifications with yields 75% for **H3L9** and 80% for **H3L10**, which corresponds with the reported yields.^{190,191}

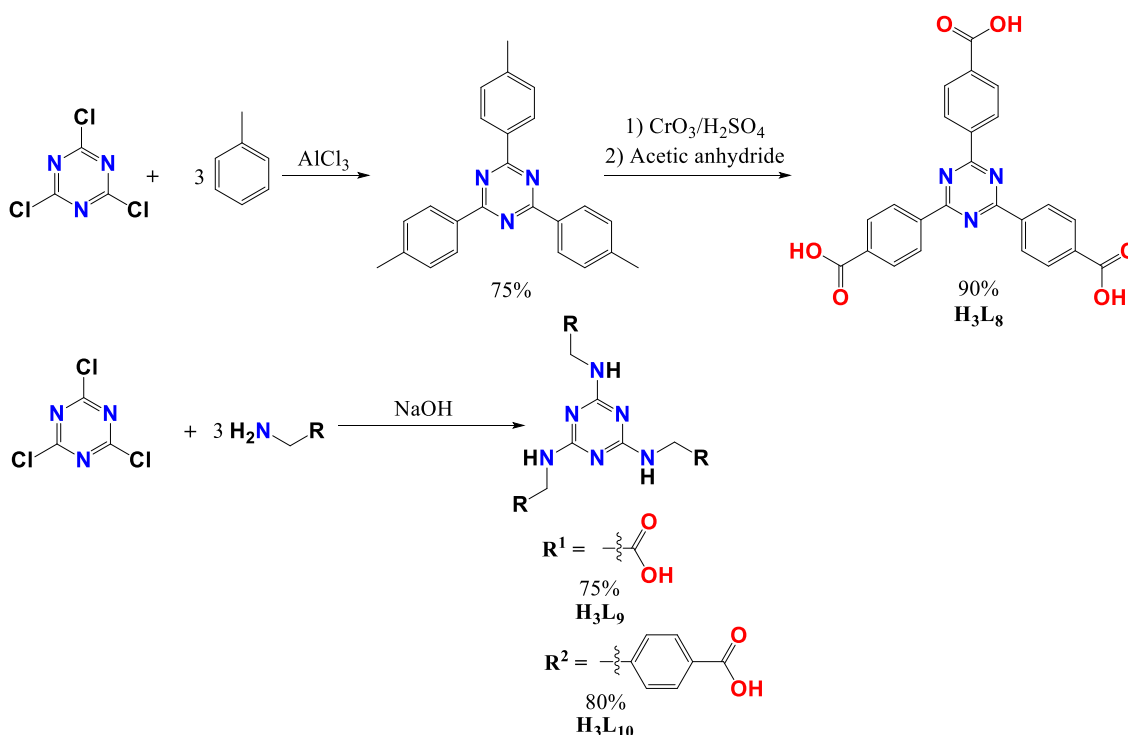


Figure 75 The synthetic pathway for the connectors **H3L8**, **H3L9**, **H3L10**

The $^1\text{H-NMR}$ revealed the formation of the desired connectors and the spectra are in accordance with the literature data (see experimental part).^{189,190}

The formation of the desired connectors was also proved by Mass-spectrometry. The MS experiments demonstrated the formation of species with the peaks of mass 442.11 $[\text{M}]^+$, 301.09 $[\text{M}]^+$ and 529.18 $[\text{M}]^+$ that are in perfect accordance with the expected mass of the connectors **H3L8**, **H3L9** and **H3L10**.

The connectors **H3L8**, **H3L9** and **H3L10** appeared to be stable in the solid state. The $^1\text{H-NMR}$ spectra of the freshly obtained connectors and the $^1\text{H-NMR}$ spectra of these connectors stored for a week as powders are identical.

VII.4. 1,3,5-trifluorobenzene connector: size, geometry and properties

As well as 1,3,5-triazine moiety that was described in the previous section, 1,3,5-trifluorobenzene has an area of a positive charge in the middle of the benzene ring leading to the anion recognition properties of this molecule as well.¹⁹² As a consequence we could expect the same property from the connector 4,4',4''-((2,4,6-trifluorobenzene-1,3,5-triyl)tris(ethyne-2,1-

diyl)tribenzoic acid (**H₃L₁₁**) and, thus, the MOCs formed with it should also possess such properties (Figure 76). To the best of our knowledge, the connector **H₃L₁₁** has never been reported.

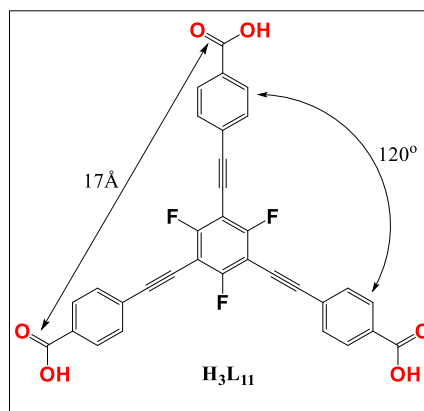


Figure 76 Structure of the triangular organic connector **H₃L₁₁**

The connector **H₃L₁₁** is a neutral purely organic triangular tridentate connector, perfectly suited for the formation of face-panelled MOCs. (Figure 76). The size of the connector was estimated from XRD analysis of similar species to be close to 17Å.²⁷ This size is similar to the largest organic connector used for the formation of octahedral calixarene-based MOCs. (Table 3).

1,3,5-trifluorobenzene moiety has been already reported for the synthesis of MOCs. For example, MOC with 1,3,5-trifluorobenzene derivative was reported in 2015. That MOC is octahedral with the internal cavity diameter approximately equal to 15Å. Furthermore, it demonstrated optical properties.²⁷

Therefore, based on the abovementioned facts, the formation of new MOCs based on 1,3,5-trifluorobenzene connectors is a promising field, as it offers the possibility of obtaining face-panelled MOCs adapted for anion recognition.

VII.5. The synthesis of triangular 1,3,5-trifluorobenzene connector (**H₃L₁₁**)

The synthetic pathway was adapted from the already reported procedure.²⁷

The synthesis of the connector **H₃L₁₁** is a two-steps procedure with an overall yield of 81% (Figure 77).

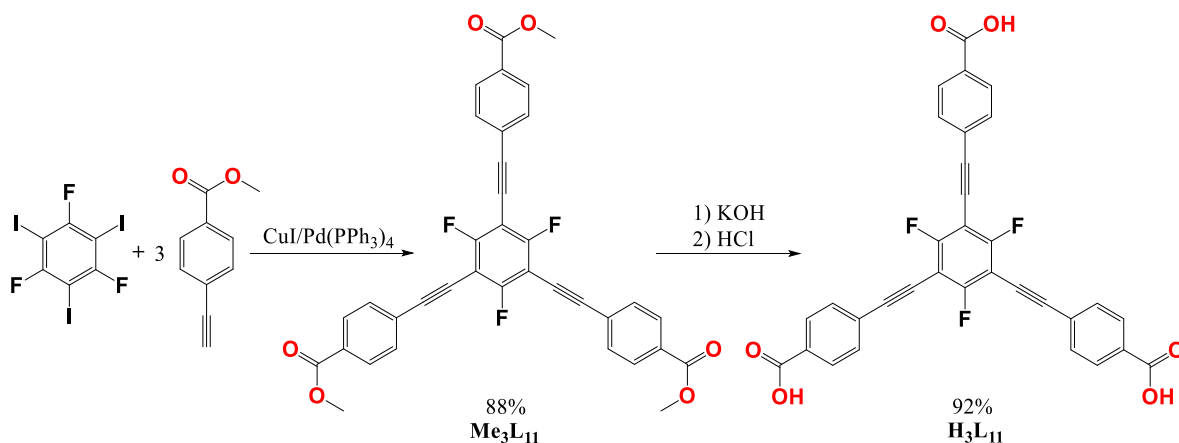


Figure 77 The synthetic pathway for the connector **H₃L₁₁**

The first step involves a Sonogashira coupling. The formation of **Me₃L₁₁** is proved by ¹H-NMR with the appearance of two doublets of equal integration at **8.01** ppm and **7.59** ppm corresponding to the aromatic protons **Me₃L₁₁**; a singlet at **3.93** ppm corresponds to methyl group of the ester function (Figure 78). Moreover, only one peak is observed at **-68.90** ppm in the ¹⁹F-NMR confirming the presence of the equivalent fluorine in the obtained structure.

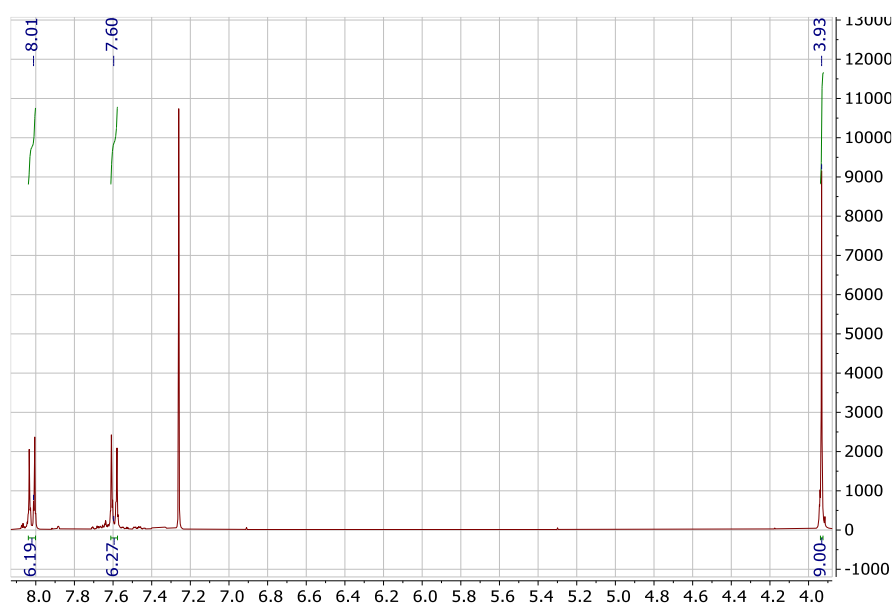


Figure 78 NMR spectra of **MeL₁₁**

The second step is the hydrolysis of the ester groups that was performed in the similar way discussed for previous connectors. The formation of the desired **H₃L₁₁** connector is confirmed by methods of NMR and Mass-spectrometry. In the ¹H-NMR spectrum there are two doublets peaks at **7.98** and **7.75** ppm which correspond to the aromatic protons while the ¹⁹F-NMR spectrum shows only one peak with the shift **-68.34** ppm. The MS experiment demonstrated a peak of mass **565.09 [M]⁺** that corresponds to the expected mass for **H₃L₁₁**.



The connector **H₃L₁₁** appeared to be unstable. The ¹H-NMR spectrum of freshly obtained **H₃L₁₁** and the ¹H-NMR spectrum of **H₃L₁₁** stored for a week demonstrate significant differences with the drastic decrease of the desired connector amount. Furthermore, **H₃L₁₁** has a distinct white colour and during 1 week of observation, significant darkening was noticed.

VIII. Conclusion

The present chapter reports the synthesis of metal-organic and purely organic connectors families, which were characterized by various analytical techniques. The synthetic procedure was optimized for many of these connectors to increase yields and/or decrease the number of synthetic steps. The suitability of these connectors for their use in the formation of MOCs was assessed based on their geometrical (linear and triangular) and chemical characteristics, which revealed a range of properties, including redox activity, unique optical, and chiral properties.

It is possible to use these connectors to obtain different types of octahedral calixarene-based MOCs, such as both face-panelled and edge-panelled structures. Based on the selected connectors, the formation of moderate to extra-large octahedral calixarene-based MOCs are expected. The resulting MOCs are also expected to exhibit enhanced properties, leading to a wide range of applications.

All of the obtained connectors, which will be used for the synthesis of calixarene-based MOCs, are summarized Table 4. A total of 18 connectors were obtained, which includes:

- 14 metal-organic,
- 4 purely organic,
- 12 triangular tridentate,
- 6 linear bidentate.
- 14 neutral
- 4 ionic



	Connector name	Structure	Connector name	Structure
Triangular metal-organic connectors	rac-M(HL ₁) ₃ (neutral)	<p>M = Co^{III} : rac-Co(HL₁)₃ M = Fe^{III} : rac-Fe(HL₁)₃ M = Rh^{III} : rac-Rh(HL₁)₃</p>	rac-Co(HL ₂) ₃ (neutral)	<p>rac-Co(HL₂)₃</p>
	Δ-Co(HL ₁) ₃ Δ-Co(HL ₁) ₃ (neutral)	<p>Δ-Co(HL₁)₃</p>	Co(H ₃ L ₇) (neutral)	<p>Co(H₃L₇)</p>
	[rac-Fe(HL ₄) ₃][PF ₆] ₂ (charged)	<p>[rac-Fe(HL₄)₃][PF₆]₂</p>		
Linear metal-organic connectors	Pd(HL ₁) ₂ , Ni(H ₂ L ₃) (neutral)	<p>Pd(HL₁)₂ Ni(H₂L₃)</p>	Ni(H ₂ L ₆) (neutral)	<p>Ni(H₂L₆)</p>
	[M(HL ₅) ₂][PF ₆] ₂ (charged)	<p>M = Fe^{II} : [Fe(HL₅)₂][PF₆]₂ M = Co^{II} : [Co(HL₅)₂][PF₆]₂ M = Ru^{II} : [Ru(HL₅)₂][PF₆]₂</p>		
Triangular organic connectors	H ₃ L ₈ , H ₃ L ₉ , H ₃ L ₁₀ (neutral)	<p>H₃L₈ H₃L₉ H₃L₁₀</p>	H ₃ L ₁₁ (neutral)	<p>H₃L₁₁</p>

Table 4 Structure of the targeted connector

Chapter III.

Formation and structural investigations of MOCs

Table of contents

<u>I. Synthesis of crystalline molecular cages</u>	105
<u>I.1. Determination of the synthetic conditions</u>	106
<u>I.2. Synthesis of crystalline cages using metal-organic connectors</u>	111
<u>I.3. Synthesis of crystalline cages using organic connectors (H₃L₈-H₃L₁₁)</u>	115
<u>II. Structural investigation of racemic dipyrin-based MOCs: XRD analysis</u>	116
<u>II.1. Crystalline data</u>	116
<u>II.2. Metal environment</u>	118
<u>II.3. Cages metrics</u>	119
<u>II.4. Packing of the dipyrin-based MOCs in the unit cell</u>	122
<u>III. Structural investigation of chiral dipyrin-based MOCs: XRD analysis</u>	124
<u>IV. Additional characterizations techniques for dipyrin-based MOCs</u>	125
<u>IV.1. CD and chiral HPLC of enantiomerically pure cages</u>	126
<u>IV.2. MS characterization in solution</u>	127
<u>IV.3. XRPD in the solid state for racemic cages</u>	129
<u>IV.4. TGA measurements and IR analysis of the racemic cages</u>	130
<u>IV.5. Conclusion</u>	131
<u>V. Structural investigation of MOCs based on organic connectors</u>	133
<u>V.1. Crystalline data for [M₄SO₂TCA(μ₄-OH₂)]₆[L₈]₈ (M = Co^{II}, Ni^{II})</u>	133
<u>V.2. Cages metrics</u>	134
<u>V.3. Packing of the Cages</u>	135
<u>V.4. TGA and IR for triazine-based MOCs</u>	136



I. Synthesis of crystalline molecular cages

All of the connectors described in the **Chapter II** were subsequently used for the synthesis of octahedral calixarene-based MOCs. In order to do that, a one-pot three-component approach was performed: metal-organic or organic connectors (linear or triangular) were mixed with *p*-tert-butylsulfonylcalix[4]arene (H_4SO_2TCA) and metal salts, and the conditions suitable for the self-assembling process (solvents, temperature, base, stoichiometry, time) were provided. Depending on the type of connector used for the synthesis of MOCs, we expected the formation of two different types of MOCs (Figure 79):

- face-panelled MOCs with the formula $[M_4SO_2TCA(\mu_4-OH_2)]_6(TC)_8 \cdot nS$ (S – quantity of solvents) if triangular connectors (TC) are used.
- edge-panelled MOCs with the formula $[M_4SO_2TCA(\mu_4-OH_2)]_6(LC)_{12} \cdot nS$ (S – quantity of solvents) if linear connectors (LC) are used.

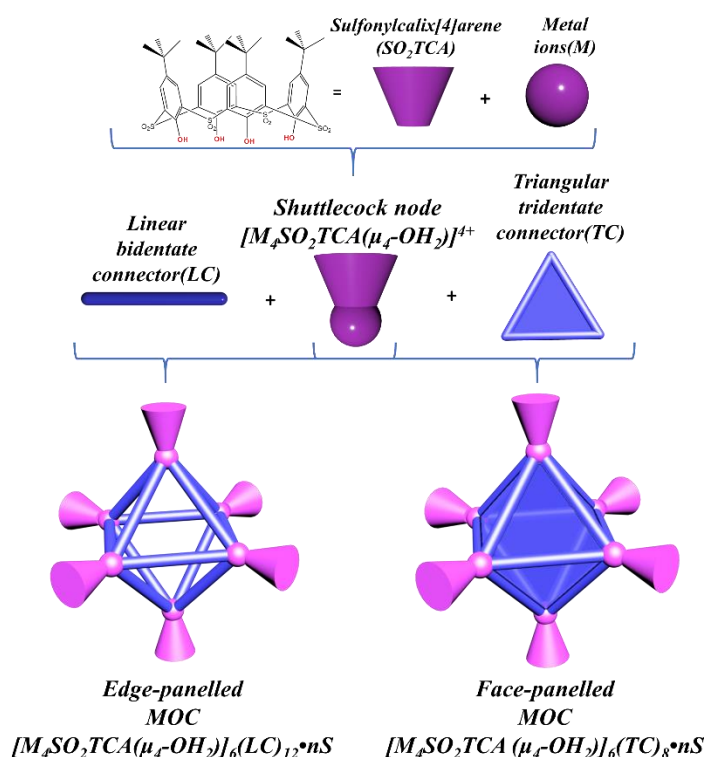


Figure 79 The schematic representation of the self-assembly reaction for the formation of MOCs

The obtained MOCs need to be characterised from the structural point of view. It is possible to investigate MOCs structure in solid state by different techniques:

- Single-crystal X-ray diffraction analysis (XRD)
- X-ray diffraction analysis of powdered samples (XRPD)
- Extended X-ray absorption Fine Structure (EXAFS) of amorphous compounds



- Thermogravimetric analysis (TGA) of powdered compounds
- IR-spectroscopy of powdered compounds

In addition, MOCs can be characterised in solution by some other techniques:

- Mass-spectroscopy (ESI-MS, IM-MS)
- UV-vis spectroscopy
- Circular dichroism (CD) for chiral MOCs
- Chiral HPLC of chiral MOCs

However, for such big assemblies, single-crystal XRD is the most appropriate characterisation technique that unambiguously determines the scaffold of the desired assemblies (geometry, stoichiometry, and metal environment). For this reason, we focused on the one-pot three-component synthesis due to its ability to generate single-crystals suitable for the XRD analysis.

I.1. Determination of the synthetic conditions

In order to obtain the desired MOCs, it is necessary to provide suitable synthetic conditions that promote the self-assembly process leading to the MOCs formation in a crystalline form. In this regard, it is important to examine and analyse the methods reported for such systems. Detailed explanations of each aspect of the synthetic techniques are discussed here below.

I.1.1. Choice of the synthetic method

The self-assembly process was conducted using two different synthetic techniques that are commonly used for the formation of MOCs and MOFs:

- Solvothermal technique that involves a reaction between reactants in appropriate solvents at high temperatures and pressures in a sealed vial.^{98,193} The temperatures typically used in this technique range from 60°C to 120°C (in this work the temperature of 80°C was used). The quality of the resulting crystals usually depends on the crystal formation rate while slower formation usually leads to higher quality crystals. Gradual heating and cooling (at a rate of approximately 2-4 °C/h) are commonly employed to slow down the crystal formation. For the same reasons, diluted solutions with concentrations up to 20 mM are commonly used to achieve slow and controlled crystal growth (in this work concentrations up to 10 mM were used). The reaction time in this technique is not strictly defined and depends on the nature of the reactants and the rate of heating and cooling. However, it typically takes at least one week to achieve completeness (see detail in the experimental part).
- Liquid-liquid diffusion technique involves the diffusion at room temperature (RT) of a solution containing some of the components into a solution containing the other



components, resulting in the formation of MOCs crystals at the interface of the two solvents due to the self-assembly reaction on this interface.¹⁹³ In this technique, similarly to the solvothermal approach, diluted solutions up to 10 mM are commonly used to facilitate the formation of high-quality crystals. When compared to the solvothermal technique, the reaction time in the liquid-liquid diffusion technique depends on the nature of the used solvents (see detail in §I.1.3. of this chapter), their relative density and their degree of miscibility. However, this technique is typically slow, and it could take weeks to months to achieve complete reaction. Nevertheless, it is possible to observe the formation of the first crystals after a few hours of the reaction.

I.1.2. Choice of the metal salt for the formation of shuttlecock calixarene nodes

The selection of metal ions for the synthesis of MOCs was based on their ability to form tetranuclearsulfonylcalix[4]arene shuttlecock nodes $[\text{M}_4\text{SO}_2\text{TCA}(\mu_4\text{-OH}_2)]^{4+}$ or similar tetranuclear complexes that were previously reported in the literature. The formation of calixarene-based MOCs is achieved using 3d metal salts as chlorides,^{72,98} acetates^{4,81} and less commonly nitrates.⁹⁶ The selection of these anions is based on their solubility in a variety of solvents:

- Cobalt (II) chloride hexahydrate ($\text{CoCl}_2 \cdot 6\text{H}_2\text{O}$)⁹⁸
- Nickel (II) chloride hexahydrate ($\text{NiCl}_2 \cdot 6\text{H}_2\text{O}$)¹⁰⁴
- Iron (II) chloride tetrahydrate ($\text{FeCl}_2 \cdot 4\text{H}_2\text{O}$)¹⁹⁴
- Zinc (II) chloride hydrate ($\text{ZnCl}_2 \cdot x\text{H}_2\text{O}$)⁴
- Copper (II) chloride dihydrate ($\text{CuCl}_2 \cdot 2\text{H}_2\text{O}$)¹⁹⁵

I.1.3. Choice of bases and solvents

The reaction rate of MOCs formation can be enhanced by the deprotonation of the carboxyl groups of the connectors and the hydroxy groups of the sulfonylcalix[4]arene, as they are functional groups that participate in the metal ion coordination. Accordingly, it is necessary to introduce a base into the reaction system. The choice of a particular base is determined by the technique used and should be considered in conjunction with the choice of solvent for the reaction, as certain techniques and solvents do not require an additional base to be added to the reaction mixture.

In the solvothermal technique, choice of a solvent is determined by the solubility of all components involved in the reaction. In the formation of MOFs and MOCs, N,N-dimethylformamide (DMF), dimethylsulfoxide (DMSO), and N,N-dimethylacetamide (DMA) are commonly used solvents due to their ability to dissolve both organic (ligands) and inorganic (metal salts) species and also to their high boiling points (153°C, 189°C and 165°C respectively). Other solvents are used less frequently. In this study, we selected N,N-dimethylformamide (DMF) as a



solvent in the solvothermal synthetic technique based on two factors: firstly, DMF is able to solubilize all of the participants of one-pot three-component reaction (connector, metal salt and sulfonycalix[4]arene); additionally, DMF is known to degrade under heat, leading to the formation of small amounts of dimethylamine, which can serve as a base which initiates the reaction.

In the liquid-liquid diffusion technique, the choice of the solvents is obviously also determined by the solubility of the components of the reaction mixture. However, the main difference between the liquid-liquid diffusion technique and the solvothermal technique, besides the reaction temperature, is the use of at least two different solvents that are necessarily miscible. Moreover, these solvents must have different densities to form two separate layers initially. Consequently, the number of appropriate solvent combinations is limited. The most common combinations include DMF/alcohol, DMSO/alcohol, DMA/alcohol, and chloroform/alcohol. In this work, the solvents combination of DMF/methanol was chosen for the liquid-liquid diffusion technique due to their miscibility and their relative density (0.944 g/ml and 0.792 g/ml, respectively) but also because the three components can be dissolved in DMF while the base (triethylamine) is added to MeOH, allowing a low amount of base to be present at the interface of DMF/MeOH and thus the metallation to slowly occurred.

In comparison with the solvothermal technique where the *in-situ* formation of small amounts of dimethylamine eliminates the need to add bases for deprotonation, the liquid-liquid diffusion technique requires the addition of bases to initiate the reaction of MOCs formation. For this purpose, triethylamine was chosen as a base due to its stability and convenience. Furthermore, triethylamine ($pK_a = 10.75$) has been commonly used as a non-coordinating base in the reported procedures for MOCs synthesis.⁹⁸

I.1.4. Influence of the used stoichiometry

Stoichiometry is a crucial factor in the formation of MOCs and, thus, must be carefully calculated. The stoichiometry of metal ions/calixarenes/connectors used in the synthesis determines the nature of the formed products. If the stoichiometry is not well balanced, it may result in the formation of undesired products, or powders. For instance, the excess of sulfonycalix[4]arene may lead to the formation of polynuclear complexes with different calixarene/metal stoichiometries. On the other hand, the excess of a connector may lead to the formation of coordination polymers or MOFs. Furthermore, it was observed that the use of an



excess of metal salts may lead to the crystallization of used salts instead of desired MOCs under the selected reaction conditions.

For both techniques (solvothermal and liquid-liquid diffusion) the stoichiometry used in the self-assembly process was selected based on the stoichiometry of the expected MOCs and was in accordance with stoichiometries already reported in the literature for the formation of calixarene-based MOCs.^{4,72}

- While using linear bidentate connectors (LC) for the formation of MOCs, the chosen stoichiometry is 12/6/24 for connector/sulfonylcalix[4]arene/metal salt, respectively. This stoichiometry favours the formation of edge-panelled MOCs.
- While using triangular tridentate connectors (TC) for the formation of MOCs, the chosen stoichiometry is 8/6/24 for connector/sulfonylcalix[4]arene/metal salt, respectively. This stoichiometry favours the formation of face-panelled MOCs.

Additionally, when using the liquid-liquid diffusion technique, a total of 60 equivalents of triethylamine were added in MeOH. This amount is compatible with the requirement to deprotonate all carboxyl groups of the connectors (two groups for each linear bidentate connector and three groups for each triangular tridentate connector) and all hydroxy groups of sulfonylcalix[4]arenes (four groups for each calixarene).

The results of the reactions conducted using both solvothermal and liquid-liquid diffusion techniques are summarized in the following Table 5 (see details in the experimental part).

	Connectors	Liquid-liquid diffusion approach					Solvothermal approach				
		Co ²⁺	Ni ²⁺	Zn ²⁺	Fe ²⁺	Cu ²⁺	Co ²⁺	Ni ²⁺	Zn ²⁺	Fe ²⁺	Cu ²⁺
Metal-organic	Triangular	rac-Co(HL ₁) ₃	[Co ₄ SO ₂ TCA] ₆ [rac-Co(L ₁) ₃] ₈	[Ni ₄ SO ₂ TCA] ₆ [rac-Co(L ₁) ₃] ₈							
		Λ-Co(HL ₁) ₃	[Co ₄ SO ₂ TCA] ₆ [Λ-Co(L ₁) ₃] ₈	[Ni ₄ SO ₂ TCA] ₆ [Λ-Co(L ₁) ₃] ₈							
		Δ-Co(HL ₁) ₃	[Co ₄ SO ₂ TCA] ₆ [Δ-Co(L ₁) ₃] ₈	[Ni ₄ SO ₂ TCA] ₆ [Δ-Co(L ₁) ₃] ₈							
		rac-Fe(HL ₁) ₃	[Co ₄ SO ₂ TCA] ₆ [rac-Fe(L ₁) ₃] ₈	[Ni ₄ SO ₂ TCA] ₆ [rac-Fe(L ₁) ₃] ₈							[Cu ₂ SO ₂ TCA]
		rac-Rh(HL ₁) ₃	[Co ₄ SO ₂ TCA] ₆ [rac-Rh(L ₁) ₃] ₈	[Ni ₄ SO ₂ TCA] ₆ [rac-Rh(L ₁) ₃] ₈							
		rac-Co(HL ₂) ₃									
		[rac-Fe(HL ₄) ₃][PF ₆] ₂						[Co ₂ SO ₂ TCA]			
	Co(H ₃ L ₇)	[CoSO ₂ TCA]									
	Linear	Pd(HL ₁) ₂	Pd(HL ₁) ₂	Pd(HL ₁) ₂							
		Ni(H ₂ L ₃)						[Ni ₄ SO ₂ TCA]			
		Ni(H ₂ L ₆)									[Cu ₂ SO ₂ TCA]
		[Fe(HL ₅) ₂][PF ₆] ₂						[Ni ₄ SO ₂ TCA]		[Fe ₂ SO ₂ TCA]Cl ₂	
[Co(HL ₅) ₂][PF ₆] ₂									[Fe ₄ SO ₂ TCA]	[CuHL ₅]Cl ₂	
[Ru(HL ₅) ₂][PF ₆] ₂											
Organic	Triangular	H ₃ L ₈	[Co ₄ SO ₂ TCA] ₆ [L ₈] ₈					[Ni ₄ SO ₂ TCA] ₆ [L ₈] ₈			
		H ₃ L ₉									
		H ₃ L ₁₀									
		H ₃ L ₁₁									

The precipitation of crystals suitable for XRD analysis that were analysed and the structure of the desired MOCs was proven

The formation of amorphous precipitate

The formation of crystalline structures unsuitable for XRD analysis (bad shape, twins, small size)

The formation of crystals suitable for XRD that were not analysed

The formation of crystals suitable for XRD analysis that were analysed and demonstrated other structures

Table 5 Summary of the reactions performed to obtain MOCs in the crystalline form



During this work, a total of 180 reactions were performed to synthesize the desired calixarene-based MOCs in a crystalline form. In every case, the precipitation of crystals or powders was observed. Based on the data represented in Table 5, several conclusions can be drawn.

I.2. Synthesis of crystalline cages using metal-organic connectors

None of the chosen large metal-organic connectors (**rac-Co(HL₂)₃**, [**rac-Fe(HL₄)₃][PF₆]₂**, **Pd(HL₁)₂**, **Ni(H₂L₃)**, [**Fe(HL₅)₂][PF₆]₂**, [**Co(HL₅)₂][PF₆]₂**, [**Ru(HL₅)₂][PF₆]₂) have so far led to the crystal formation of the desired MOCs under the chosen conditions, possibly due to their inappropriate size (more than 16 Å, see detail in corresponding sections of **Chapter II**), which may result in the instability of the desired MOCs. Instead, it was observed that these connectors preferentially result in the formation of undesired two component crystalline structures or powdered precipitates, which are unsuitable for single-crystal XRD analysis. This assumption is supported by a fact that, to the best of our knowledge, there is no reported octahedral calixarene-based MOCs with connectors larger than 19.5 Å (see details in **§I. Chapter II**). Additionally, the lack of the stability of larger calixarene-based MOCs is supported by the observation that the enlarged triangular tris(dipyrrin) connector **rac-Co(HL₂)₃** also did not produce the desired MOCs despite the fact that all other smaller triangular tris(dipyrrin) connectors (**rac-M(HL₁)₃**, **Δ-Co(HL₁)₃**, **Λ-Co(HL₁)₃**) demonstrated the formation of the desired dipyrrin-based MOCs. The structure of the obtained dipyrrin-based MOCs will be discussed in the following sections.**

I.2.1. Analysis of the obtained results: solvothermal reactions

Under the solvothermal conditions, most of the tests give either amorphous precipitate or with Ni(II) and Co(II) complexes of **rac-M(HL₁)₃** (M = Co^{III}, Fe^{III}, Rh) and **Δ,Λ-Co(HL₁)₃** crystalline structure not suitable for single-crystals XRD (Table 5). Besides that, crystalline structures of non-desired calixarene complexes were frequently formed instead of the desired three-components MOCs. The structure of these single-crystals was investigated by XRD which revealed the formation of five different complexes between sulfonylcalix[4]arene and metal ions used in the synthesis (see details in crystallographic annexes **§I.2.**):

- [Co₂SO₂TCA]•4DMF
- [Cu₂SO₂TCA]•4DMF
- [Fe₂SO₂TCA]Cl₂•4DMF
- [M₄(SO₂TCA)₂]•4DMF (M = Ni^{II}, Fe^{II})



The structure of these complexes will be briefly discussed in this section. A huge amount of similar complexes between calixarenes and metal ions have been already reported in the literature and it is possible to compare them with the obtained ones.¹⁹⁴

In the obtained five metalocalixarene complexes, the conformations of calixarenes in 1,2-alternate or cone (see §III.1 Chapter I), and different ratios Metal/Calixarene were observed (Figure 80):

- ratio Metal/Calixarene = 2/1 is observed for complexes $[M_2SO_2TCA] \cdot 4DMF$ ($M = Co^{II}, Cu^{II}$) and $[Fe_2SO_2TCA]Cl_2 \cdot 4DMF$
- ratio Metal/Calixarene = 4/2 is observed for complexes $[M_4(SO_2TCA)_2] \cdot 4DMF$ ($M = Ni^{II}, Fe^{II}$)

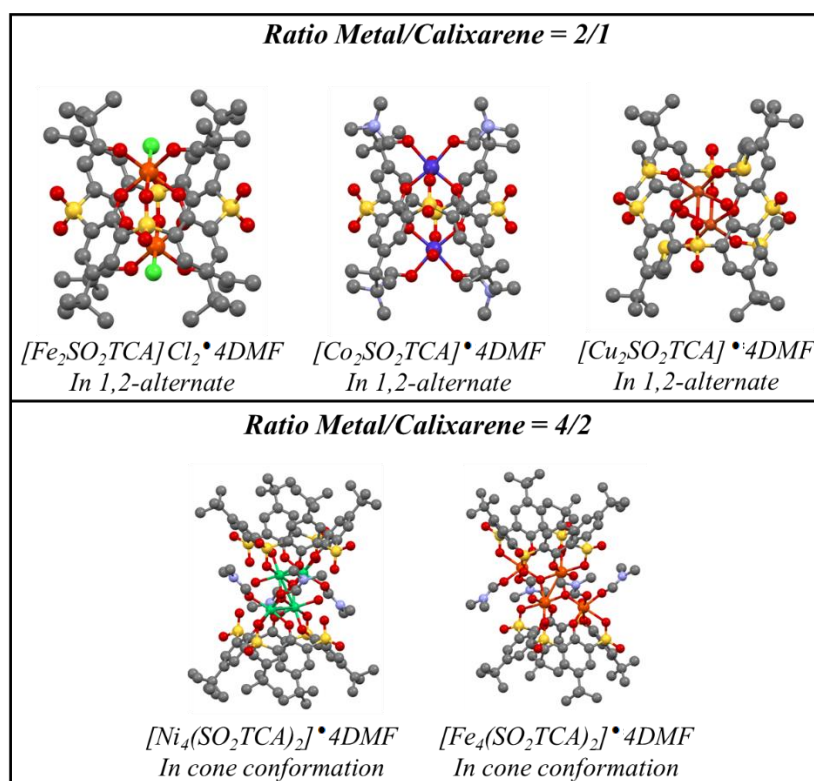


Figure 80 Crystal structures of the obtained side products while using solvothermal technique - metalocalixarene complexes with different stoichiometries Metal/Calixarene

In these 5 metalocalixarene complexes, the geometry around metal ions is the following:

- In the complex $[Co_2SO_2TCA] \cdot 4DMF$, each Co^{II} present an O6 octahedral environment, with 2 oxygen atoms from calixarene phenolates, 1 oxygen atom from μ -H₂O, 1 oxygen atom from sulfonyl group of calixarene and 2 oxygen atoms from coordinated DMF molecules. This compound has already been reported in the literature.¹⁹⁶



- In the complex $[\text{Cu}_2\text{SO}_2\text{TCA}]\cdot 4\text{DMF}$, each Cu^{II} present an O5 square pyramidal environment, with 2 oxygen atoms from calixarene phenolates, 1 oxygen atom from a sulfonyl group of calixarene and 2 oxygen atoms from coordinated DMF molecules. This structure is not reported in the literature, however, the similar structure $[\text{Cu}_2\text{SO}_2\text{TCA}]\cdot \text{MeOH}$ has been reported.¹⁹⁷
- In the complex $[\text{Fe}_2\text{SO}_2\text{TCA}]\text{Cl}_2\cdot 4\text{DMF}$, each Fe^{III} presents an O5Cl octahedral environment, with 2 oxygen atoms from calixarene phenolates, 1 oxygen atom from sulfonyl group of calixarene, 2 oxygen atoms from coordinated DMF molecules and 1 coordinated chloride-anion. This compound has been already reported in the literature.¹⁹⁸
- In the complexes $[\text{M}_4(\text{SO}_2\text{TCA})_2]\cdot 4\text{DMF}$ ($\text{M} = \text{Ni}^{\text{II}}, \text{Fe}^{\text{II}}$), the metal ions present two different environments: (i) 2 Metal ions with an O6 octahedral environment with 2 oxygen atoms from calixarene phenolates, 3 oxygen atoms from $\mu\text{-H}_2\text{O}$, 1 oxygen atom from sulfonyl group of calixarene; (ii) 2 metal ions ions with a different O6 octahedral environment with 2 oxygen atoms from phenolates, 1 oxygen atom from $\mu\text{-H}_2\text{O}$, 1 oxygen atom from sulfonyl group of calixarene and 2 oxygen atoms from coordinated DMF molecules. To the best of our knowledge, these compounds are not reported in the literature.

It is worth noting that the complexes $[\text{M}_4(\text{SO}_2\text{TCA})_2]\cdot 4\text{DMF}$ ($\text{M} = \text{Ni}^{\text{II}}, \text{Fe}^{\text{II}}$) display a structure with two sulfonylcalix[4]arenes in cone conformation connected to each other through four metal ions with the formation of a sandwich-like structure similar to the structure of expected for the shuttlecock-like calixarene units $[\text{M}_4\text{SO}_2\text{TCA}(\mu_4\text{-OH}_2)]^{4+}$. These observations suggest that during the self-assembly process shuttlecock unit $[\text{M}_4\text{SO}_2\text{TCA}(\mu_4\text{-OH}_2)]^{4+}$ forms firstly as an intermediate and then capped by other components of the reaction. If the shuttlecock unit $[\text{M}_4\text{SO}_2\text{TCA}(\mu_4\text{-OH}_2)]^{4+}$ is capped by the connector molecules it results in the formation of calixarene-based MOC. If the shuttlecock unit $[\text{M}_4\text{SO}_2\text{TCA}(\mu_4\text{-OH}_2)]^{4+}$ is capped by the other calixarene molecule, it results in the formation of the complexes $[\text{M}_4(\text{SO}_2\text{TCA})_2]\cdot 4\text{DMF}$.

Additionally, among all the non-desired obtained compounds, single-crystals of a compound obtained due to transmetallation process were observed under solvothermal conditions, in which the metal ion (Co^{II}) in the structure of the metal-organic connector was replaced by the metal ion (Cu^{II}) from the salt used in the reaction with the obtaining of new mono(terpyridine) complex of Cu^{II} instead of desired MOC (Figure 81). Furthermore, to the best of our knowledge, the structure of this complex was not reported in the literature (see crystallographic annexes §I.2.), however, similar structure has been reported.¹⁹⁹

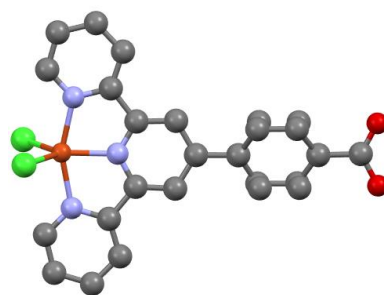


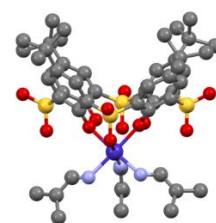
Figure 81 The structure of transmetallated complex Bis[4'-(4-Carboxyphenyl)-2,2':6',2''-terpyridinato] Cu(II) dichloride ($[CuHL_5]Cl_2$)

I.2.2. Analysis of the obtained results : Liquid-liquid diffusion

In the case of liquid-liquid diffusion technique, the results were more promising especially with tris(dipyrrin) complexes $rac\text{-}M(HL_1)_3$ ($M = Co^{III}, Fe^{III}, Rh$) and $\Delta, \Lambda\text{-}Co(HL_1)_3$ in the presence of Co(II) and Ni(II).

However, a side product different from solvothermal technique was observed. This is a complex of formula $[CoSO_2TCA] \cdot 3DMF$ (Figure 82), with a 1/1 ratio Co(II)/Calixarene consisting of one sulfonylcalix[4]arene in cone conformation and a Co^{II} ion is in O6 octahedral coordination geometry where three oxygen atoms from coordinated molecules of DMF, two oxygen atoms from two alcoholate groups of calixarene and one oxygen atom from sulfonyl group of calixarene (see crystallographic annexes §I.2.). This complex has an interesting structure due to three coordinated DMF molecules. To the best of our knowledge such type of metalocalixarene has never been reported earlier.

Furthermore, it was observed that in a few cases liquid-liquid approach favours the crystal formation of the connector $Pd(HL_1)_2$ (see crystallographic annexes §I.2.). To the best of our knowledge the structure of $Pd(HL_1)_2$ was not reported in the literature.



$[CoSO_2TCA] \cdot 3DMF$
In cone conformation

Figure 82 The structure of the obtained side product $[CoSO_2TCA] \cdot 3DMF$

Beside these side products, the use of metal ions Co^{II} and Ni^{II} were found to be the most favourable for the formation of desired calixarene-based MOCs using the liquid-liquid diffusion technique, likely due to their strong affinity for the other reaction participants (both



sulfonylcalix[4]arene and connectors) and the resulting stability of O6 octahedral coordination geometry in the structure of MOCs. The stability of shuttlecock units $[\text{M}_4\text{TCA}(\mu_4\text{-OH}_2)]^{4+}$ ($\text{M} = \text{Co}^{\text{II}}, \text{Ni}^{\text{II}}$) is confirmed by the fact that there is a manifold of calixarene-based MOCs with the same shuttlecock units.^{72,96,98} Furthermore, shuttlecock-like units $[\text{M}_4\text{TCA}(\mu_4\text{-OH}_2)]^{4+}$ ($\text{M} = \text{Co}^{\text{II}}, \text{Ni}^{\text{II}}$) are observed in other structures, for instance, discrete tetranuclearsulfonylcalix[4]arene clusters.⁷¹ The use of these ions with triangular dipyrin connectors (**rac-M(HL₁)₃** $\text{M} = \text{Co}^{\text{III}}, \text{Fe}^{\text{III}}, \text{Rh}^{\text{III}}$, **Δ-Co(HL₁)₃**, **Λ-Co(HL₁)₃**) in the liquid-liquid diffusion technique led to the formation of the greatest variety of desired calixarene-based MOCs, including ten new compounds, four of which are chiral (MOCs based on **Δ-Co(HL₁)₃**, **Λ-Co(HL₁)₃**):

- $[\text{M}_4\text{SO}_2\text{TCA}(\mu_4\text{-OH}_2)]_6[\text{rac-Co}(\text{L}_1)_3]_8$, ($\text{M} = \text{Co}^{\text{II}}, \text{Ni}^{\text{II}}$)
- $[\text{M}_4\text{SO}_2\text{TCA}(\mu_4\text{-OH}_2)]_6[\text{rac-Fe}(\text{L}_1)_3]_8$, ($\text{M} = \text{Co}^{\text{II}}, \text{Ni}^{\text{II}}$)
- $[\text{M}_4\text{SO}_2\text{TCA}(\mu_4\text{-OH}_2)]_6[\text{rac-Rh}(\text{L}_1)_3]_8$, ($\text{M} = \text{Co}^{\text{II}}, \text{Ni}^{\text{II}}$)
- Chiral MOCs $[\text{M}_4\text{SO}_2\text{TCA}(\mu_4\text{-OH}_2)]_6[\Delta\text{-Co}(\text{L}_1)_3]_8$ and $[\text{M}_4\text{SO}_2\text{TCA}(\mu_4\text{-OH}_2)]_6[\Lambda\text{-Co}(\text{L}_1)_3]_8$ ($\text{M} = \text{Co}^{\text{II}}, \text{Ni}^{\text{II}}$)

The structures of these new calixarene-based MOCs will be discussed in §II. of this chapter.

I.3. Synthesis of crystalline cages using organic connectors (**H₃L₈**-**H₃L₁₁**)

Among the variety of the purely organic connectors used for the MOCs synthesis, only one rigid triangular connector (**H₃L₈**) demonstrated good results for growing single-crystals, indicating that the flexible connectors (**H₃L₉**, **H₃L₁₀**) are not the best for the formation of crystalline calixarene-based MOCs. **H₃L₈** led to the formation of MOCs with the formula $[\text{M}_4\text{SO}_2\text{TCA}(\mu_4\text{-OH}_2)]_6[\text{L}_8]_8$, ($\text{M} = \text{Co}^{\text{II}}, \text{Ni}^{\text{II}}$). Additionally, the use of **H₃L₁₁** connectors also led to the formation of crystals, however, these crystals could not be analysed because of their low stability.

MOCs based on **H₃L₈** was formed using different conditions. Single-crystals of $[\text{Co}_4\text{SO}_2\text{TCA}(\mu_4\text{-OH}_2)]_6[\text{L}_8]_8$ were obtained during liquid-liquid diffusion while the Ni(II) analog, $[\text{Ni}_4\text{SO}_2\text{TCA}(\mu_4\text{-OH}_2)]_6[\text{L}_8]_8$ was obtained in the solvothermal conditions. Nevertheless, both MOCs based on organic connector **H₃L₈** appeared to be isostructural (see details in §V. of this chapter).



II. Structural investigation of racemic dipyrin-based MOCs: XRD analysis

The obtained crystals of calixarene-based MOCs with triangular racemic tris(dipyrin) metal-organic connectors (**rac-M(HL₁)₃**, M = Co^{III}, Fe^{III}, Rh^{III}) were investigated in depth by different techniques in order to prove the formation of the desired structures.

First of all, crystals of MOCs were investigated by methods of single-crystal XRD. It is important to mention that, due to large internal and external voids which are filled with a large amount of solvent molecules, the structures demonstrate a great disorder. Additionally, these MOCs included racemate tris(dipyrin) complexes demonstrate disorder in the N₆ environment around metal cations of the connectors due to the presence of both Λ- and Δ-enantiomers. These facts lead to the poor diffracting power of the obtained MOCs crystals. As a result, it was hard to achieve a satisfactory diffracting pattern with an acceptable quality and peak intensities, which leads to the increasing of the single-crystal XRD recordings time up to 1 week. However, by using a powerful diffractometer, the group of Pr. K. RISSANEN (Jyväskylä University, Finland) was able to achieve the appropriate diffracting pattern allowing the fully resolution of the structures (see experimental part).

The following four compounds have been fully analysed with refinement of the structure using single-crystal XRD methods (see crystallographic annexes §I.1.):

- [M₄SO₂TCA(μ₄-OH₂)]₆[**rac-Co(L₁)₃**]₈ (M = Co^{II}, Ni^{II})
- [Ni₄SO₂TCA(μ₄-OH₂)]₆[**rac-Fe(L₁)₃**]₈
- [Ni₄SO₂TCA(μ₄-OH₂)]₆[**rac-Rh(L₁)₃**]₈

For two additional MOCs [Co₄SO₂TCA(μ₄-OH₂)]₆[**rac-Fe(L₁)₃**]₈, [Co₄SO₂TCA(μ₄-OH₂)]₆[**rac-Rh(L₁)₃**]₈ only unit cells parameters have been measured (Table 6), proven clearly that they are both isostructural to the 4 MOCs based on connectors **rac-M(HL₁)₃**. This results in a total of 6 new MOCs based on the metal-organic connectors **rac-M(HL₁)₃** (M = Co^{III}, Fe^{III}, Rh^{III}).

The crystalline data of these MOCs along with distinctive structural characteristics are discussed in detail in the following section.

II.1. Crystalline data

Single-crystal XRD analysis clearly demonstrated the formation of neutral isostructural octahedral cages with formula [M₄SO₂TCA(μ₄-OH₂)]₆[**rac-M'(L₁)₃**]₈•nDMF•mH₂O (M = Co^{II}, Ni^{II}; M' = Co^{III}, Fe^{III}, Rh^{III}). This series of MOCs crystallize in the centrosymmetric *R3c* trigonal space group (see crystallographic annexes §I.1.). The obtained dipyrin-based MOCs crystals



demonstrated enormous unit cell parameters and corresponding volumes (Table 6). For example, the cage $[\text{Co}_4\text{SO}_2\text{TCA}(\mu_4\text{-OH}_2)]_6[\text{rac-Co}(\text{L}_1)_3]_8$ demonstrated parameters: $a = 37.1152(8)\text{\AA}$; $b = 37.1152(8)\text{\AA}$, $c = 191.198(3)\text{\AA}$ with a unit cell volume of about 228095\AA^3 .

The unit cell parameters of the MOCs based on the connectors $\text{rac-M}(\text{HL}_1)_3$ ($M = \text{Co}^{\text{III}}$, Fe^{III} , Rh^{III}) are summarised in the following Table 6.

It is worth noting that the solvent molecules presented in the structure could not be modelled and were accounted for using a Solvent Mask generated by the BYPASS module within Olex2 which defined 21797.0 electrons per unit cell accounted for solvent molecules for $[\text{Co}_4\text{SO}_2\text{TCA}(\mu_4\text{-OH}_2)]_6[\text{rac-Co}(\text{L}_1)_3]_8$ and 39847.0 electrons per unit cell for $[\text{Ni}_4\text{SO}_2\text{TCA}(\mu_4\text{-OH}_2)]_6[\text{rac-Co}(\text{L}_1)_3]_8$.²⁰⁰

$[\text{M}_4\text{SO}_2\text{TCA}(\mu_4\text{-OH}_2)]_6[\text{rac-M}'(\text{L}_1)_3]_8 \cdot n\text{DMF} \cdot m\text{H}_2\text{O}$ ($M = \text{Co}^{\text{II}}$, Ni^{II} ; $M' = \text{Co}^{\text{III}}$, Fe^{III} , Rh^{III})			
Trigonal R-3c			
	Cell lengths, \AA	Volume, \AA^3	Cell angles
$M' = \text{Co}^{\text{III}}$ $M = \text{Co}^{\text{II}}$	$a = b = 37.1152(8)$ $c = 191.198(3)$	228 095 (11)	$\alpha = 90^\circ$ $\beta = 90^\circ$ $\gamma = 120^\circ$
$M' = \text{Co}^{\text{III}}$ $M = \text{Ni}^{\text{II}}$	$a = b = 36.9039(4)$ $c = 190.7619(15)$	224 992 (5)	
$M' = \text{Fe}^{\text{III}}$ $M = \text{Co}^{\text{II}}$	$a = b = 36.9$ $c = 191.2$	226 077	
$M' = \text{Fe}^{\text{III}}$ $M = \text{Ni}^{\text{II}}$	$a = b = 37.2723(3)$ $c = 190.9387(9)$	229 719 (4)	
$M' = \text{Rh}^{\text{III}}$ $M = \text{Co}^{\text{II}}$	$a = b = 37.4$ $c = 191.4$	232 307	
$M' = \text{Rh}^{\text{III}}$ $M = \text{Ni}^{\text{II}}$	$a = b = 37.2759(3)$ $c = 191.3281(13)$	230 232 (4)	

Table 6 The unit cell parameters of the six obtained MOCs based on $\text{rac-M}(\text{HL}_1)_3$ connectors (MOCs with only unit cell parameters measurements are highlighted yellow)

As expected, the cages are formed by eight $\text{rac-Co}(\text{L}_1)_3^{3-}$ connectors located on the eight faces of the formed octahedron and six $[\text{M}_4\text{SO}_2\text{TCA}(\mu_4\text{-OH}_2)]^{4+}$ shuttlecock-like nodes located in the vertices of the octahedron. The observed ratio shuttlecock node/connector is thus = 6/8 is in a perfect accordance with the expected value for the face-panelled MOCs (Figure 83).

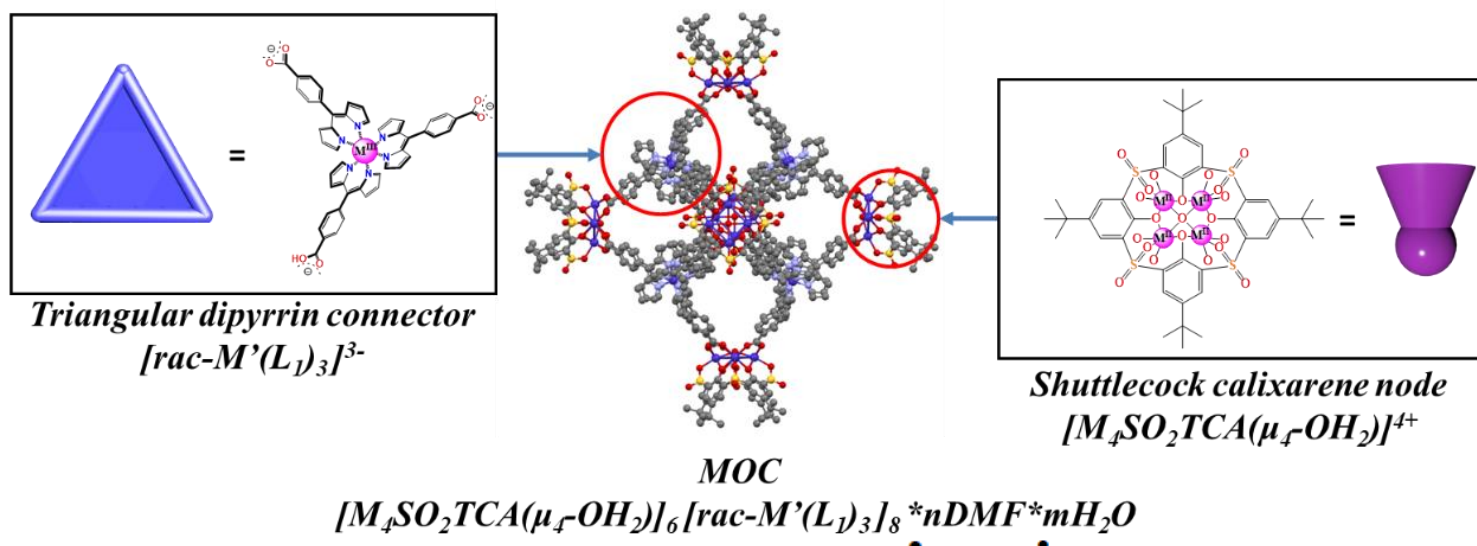


Figure 83 The structure of the obtained dipyrin-based MOCs of formula $[M_4SO_2TCA(\mu_4-OH_2)]_6[rac-M'(L_1)_3]_8 \cdot nDMF \cdot mH_2O$ ($M = Co^{II}, Ni^{II}; M' = Co^{III}, Fe^{III}, Rh^{III}$)

II.2. Metal environment

In the $[M_4TCA(\mu_4-OH_2)]^{4+}$ shuttlecock-like nodes, located at the vertices of the octahedron, each metal ion is in an octahedral O6 environment, coordinated to one oxygen atom from sulfonyl group, two oxygen atoms from deprotonated hydroxy groups of sulfonylcalix[4]arene, two oxygens atoms from two carboxylate-groups of two different $rac-M(HL_1)_3$ connectors and one oxygen atom from μ_4-OH_2 , which source is the water from the hydrate of the metal salt (Figure 84a). The structure of the shuttlecock-like nodes is common for calixarene-based MOCs, as already mentioned in §I.2.1 of this chapter. The shuttlecock-like calixarene nodes presented in the obtained MOCs demonstrate the same metrics of the metal ions as ones in shuttlecock-like calixarene nodes in the structure of previously reported calixarene-based MOCs.^{98,109} A comparison of M-O and M-M distances in shuttlecock-like nodes of the obtained MOCs with the ones in the reported structures along with the comparison of M-N distances in the structure of connectors forming MOCs are presented in Table 7.

$[M_4SO_2TCA(\mu_4-OH_2)]_6[rac-M'(L_1)_3]_8 \cdot nDMF \cdot mH_2O$ ($M = Co^{II}, Ni^{II}; M' = Co^{III}, Fe^{III}, Rh^{III}$)					
	M-O(phenolate), Å	M-O(H ₂ O), Å	M-O(SO ₂), Å	M-M, Å	M-N, Å
$[Co_4SO_2TCA]_6[rac-Co(L_1)_3]_8$	2.08	2.21	2.12	3.01	1.90
$[Ni_4SO_2TCA]_6[rac-Co(L_1)_3]_8$	2.05	2.18	2.06	2.96	1.92
$[Ni_4SO_2TCA]_6[rac-Fe(L_1)_3]_8$	2.05	2.18	2.06	2.96	1.95
$[Ni_4SO_2TCA]_6[rac-Rh(L_1)_3]_8$	2.05	2.18	2.06	2.96	2.02
Reported structures					
$[Co_4SO_2TCA]_6$ in the reported structure ⁹⁸	2.08	2.22	2.12	3.01	-
$[Ni_4SO_2TCA]_6$ in the reported structure ¹⁰⁹	2.06	2.14	2.04	2.96	-

Table 7 Metal ions metrics in the obtained MOCs with the ones reported in the literature



As shown Table 7, the observed distances $M-O_{(\text{phenolate})}$ are in the 2.05-2.08 Å range, depending on the nature of the metal ion in the structure of shuttlecock-like moiety, which is in accordance with observations for related MOCs. The observed distances $M-O_{(\text{H}_2\text{O})}$ are also in the already observed range. The observed distances $M-M$ are in a good correspondence with the radii of metal ions in the structure of the shuttlecock node (0.89 Å for Co^{II} and 0.83 Å for Ni^{II}).

The metal ions of the connectors $\text{rac-M}(\text{HL}_1)_3$ ($M = \text{Co}^{\text{III}}, \text{Fe}^{\text{III}}, \text{Rh}^{\text{III}}$) demonstrate a N6 octahedral environment which is typical for tris(dipyrin) complexes (Figure 84b).¹¹² The observed $M-N$ distances are in a good correspondence with the radii of metal ions in the structure of the connector (0.69 Å for Co^{III} , 0.69 Å for Fe^{III} , 0.81 Å for Rh^{III}).

The connectors $\text{rac-M}(\text{HL}_1)_3$ ($M = \text{Co}^{\text{III}}, \text{Fe}^{\text{III}}, \text{Rh}^{\text{III}}$) are present as a racemic mixture, displaying an equal amount of both $\Delta\text{-M}(\text{HL}_1)_3$ and $\Lambda\text{-M}(\text{HL}_1)_3$ enantiomers. The presence of both enantiomers in the structure of the obtained MOCs leads to the observation of the disorder in the N6 environment of M^{III} ions.

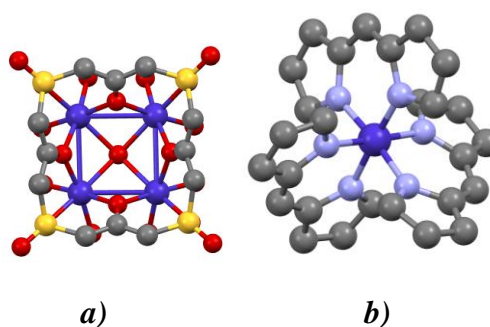


Figure 84 The structure of $[\text{M}_4\text{TCA}(\mu_4\text{-OH}_2)]^{4+}$ shuttlecock-like node (a); the metal ions environment of the connectors $\text{rac-M}(\text{L}_1)_3^{3-}$ in the MOCs of formula $[\text{M}_4\text{SO}_2\text{TCA}(\mu_4\text{-OH}_2)]_6[\text{rac-M}'(\text{L}_1)_3]_8 \cdot n\text{DMF} \cdot m\text{H}_2\text{O}$ ($M = \text{Co}^{\text{II}}, \text{Ni}^{\text{II}}$; $M' = \text{Co}^{\text{III}}, \text{Fe}^{\text{III}}, \text{Rh}^{\text{III}}$)

II.3. Cages metrics

The size of the obtained MOCs and the cavity diameter were measured. The cage size is the distance between the most remote centres of carbon atoms of methyl groups in opposite shuttlecock-like nodes, measured in the Mercury software (Figure 85). The cavity diameter is the diameter of a sphere that can be inscribed inside MOCs without crossing bonds or atoms (including hydrogen atoms) of the cage (Figure 85).

The dimensions of the obtained octahedral tris(dipyrin)-based MOCs are approximately 46 x 46 x 46 Å³ and the internal cavity has a diameter of 19 Å (Table 8).

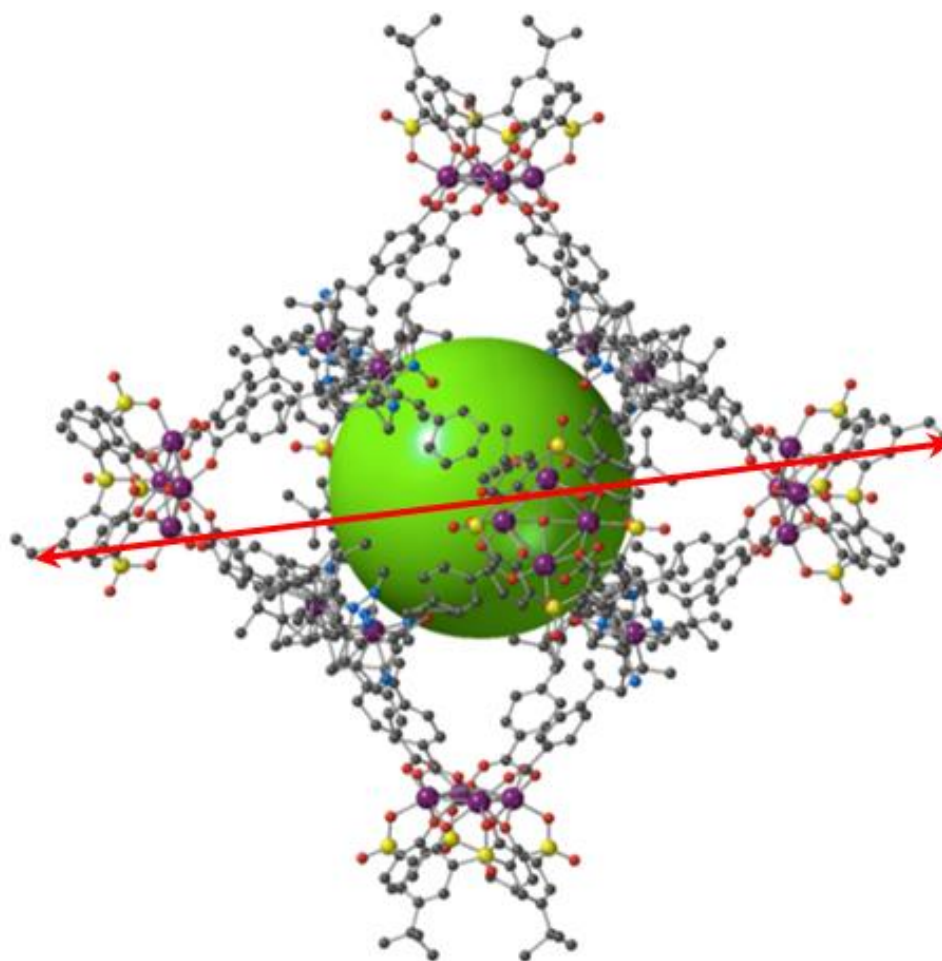


Figure 85 The representation of the MOCs of formula $[M_4SO_2TCA(\mu_4-OH_2)]_6[rac-M'(L_1)_3]_8 \cdot nDMF \cdot mH_2O$ ($M = Co^{II}, Ni^{II}; M' = Co^{III}, Fe^{III}, Rh^{III}$); red arrow represents the MOCs size; green sphere represents internal cavity

$[M_4SO_2TCA(\mu_4-OH_2)]_6[rac-M'(L_1)_3]_8 \cdot nDMF \cdot mH_2O$ ($M = Co^{II}, Ni^{II}; M' = Co^{III}, Fe^{III}, Rh^{III}$)	Cage size, Å ³	Cavity diameter, Å
$[Co_4SO_2TCA]_6[rac-Co(L_1)_3]_8$	46 x 46 x 46	19
$[Ni_4SO_2TCA]_6[rac-Co(L_1)_3]_8$		
$[Co_4SO_2TCA]_6[rac-Fe(L_1)_3]_8$		
$[Ni_4SO_2TCA]_6[rac-Fe(L_1)_3]_8$		
$[Co_4SO_2TCA]_6[rac-Rh(L_1)_3]_8$		
$[Ni_4SO_2TCA]_6[rac-Rh(L_1)_3]_8$		

Table 8 The linear size of the MOCs and the size of their internal cavity

The size of MOCs of formula $[M_4SO_2TCA(\mu_4-OH_2)]_6[rac-M'(L_1)_3]_8 \cdot nDMF \cdot mH_2O$ ($M = Co^{II}, Ni^{II}; M' = Co^{III}, Fe^{III}, Rh^{III}$) appear to be independent on the nature of metal ions (both in the shuttlecock node and in the connector). This is in accordance with the certain degree of “flexibility” (adaptation of the distances) of the observed components in such assemblies.



Dipyrin-based MOCs demonstrate cavities of a moderate size and inferior to the largest reported calixarene-based MOC - CIAC-114, which displays an internal cavity diameter of approximately 27 Å (see §III.5.1. Chapter I).⁹⁸ However, the cavity size of dipyrin-based MOCs exceeds the one of earlier reported calixarene-based MOCs, for instance, CIAC-106 (see §III.5.1. Chapter I).⁷³ These observations are in accordance with the lengths of the connectors used for MOCs synthesis. Thus, MOC CIAC-114 is based on a connector with a length 19.5 Å, MOC CIAC-106 is based on a connector with a length 12 Å and $[M_4SO_2TCA(\mu_4-OH_2)]_6[rac-M'(L_1)_3]_8 \cdot nDMF \cdot mH_2O$ ($M = Co^{II}, Ni^{II}, M' = Co^{III}, Fe^{III}, Rh^{III}$) are based on connectors with a length of 16 Å (see details in §II.1. Chapter II). In addition, it is important to compare the geometrical characteristics of the obtained dipyrin-based MOCs with the MOC based on $Mn^{II}(salen)$ metal-organic connector⁴ that was discussed in detail in the §III.6. Chapter I. The crystal structure of that MOC demonstrated internal cavity of approximately 18 Å. As a result, the cavity of the obtained dipyrin-based MOCs is slightly larger than the cavity of calixarene-based MOC with $Mn^{II}(salen)$ metal-organic connector.

The portals allowing the molecular species to get inside and outside the cavity are estimated to have a diameter of approximately 6 Å (Figure 86), that also was measured as a sphere that could be inscribed in the portal without crossing any bonds or atoms including hydrogen. The internal cavity demonstrates a mostly non-polar hydrophobic nature due to the absence of polar groups (for example, hydroxy-groups) orientated inside the cavity.

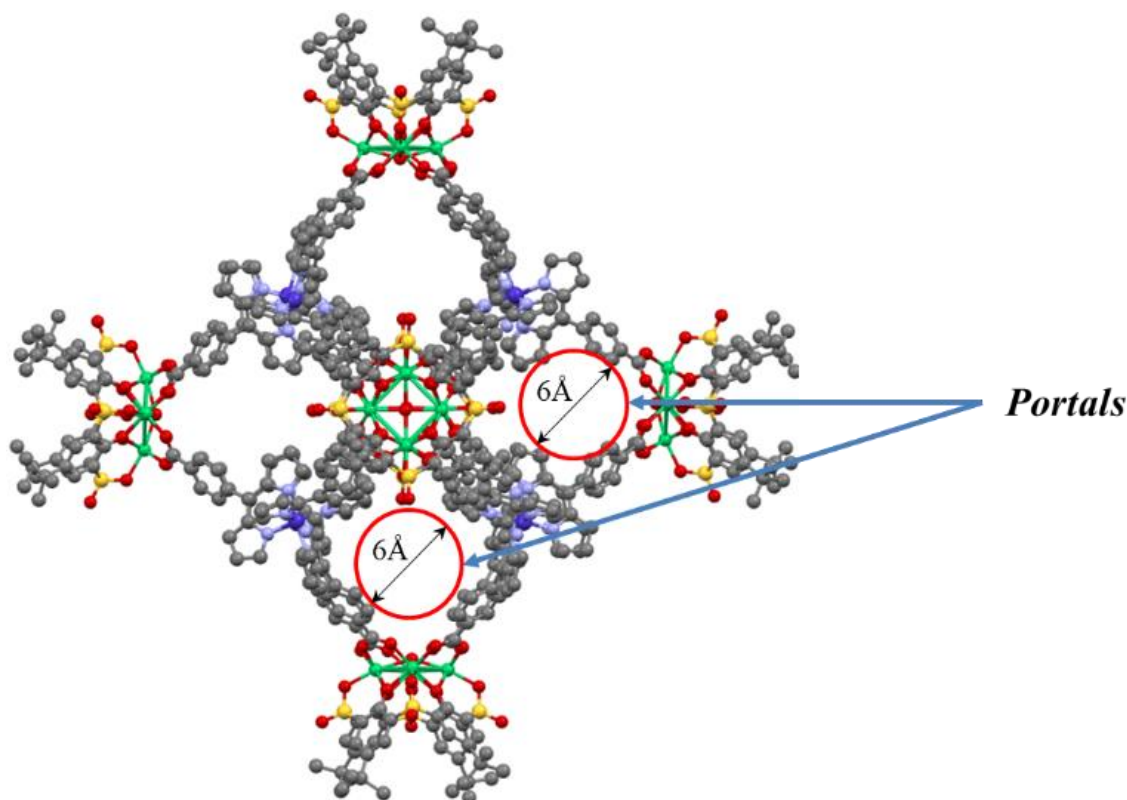


Figure 86 Portals of $[M_4SO_2TCA(\mu_4-OH_2)]_6[rac-M'(L_1)_3]_8 \cdot nDMF \cdot mH_2O$ ($M = Co^{II}, Ni^{II};$
 $M' = Co^{III}, Fe^{III}, Rh^{III}$); accessibility of guest molecules

Due to the large internal cavity along with the packing of the cages in the crystal, MOCs of formula $[M_4SO_2TCA(\mu_4-OH_2)]_6[rac-M'(L_1)_3]_8 \cdot nDMF \cdot mH_2O$ ($M = Co^{II}, Ni^{II}; M' = Co^{III}, Fe^{III}, Rh^{III}$) demonstrate a great porosity. It was calculated by PLATON²⁰¹ that obtained crystalline MOCs have approximately 67-68% of the crystal total volume available for gas adsorption that might occur inside (internal porosity) and outside of the cavity (external porosity) (Table 9).

$[M_4SO_2TCA(\mu_4-OH_2)]_6[rac-M'(L_1)_3]_8 \cdot nDMF \cdot mH_2O$ ($M = Co^{II}, Ni^{II}; M' = Co^{III}, Fe^{III}, Rh^{III}$)	
	Porosity, %
$[Co_4SO_2TCA]_6[rac-Co(L_1)_3]_8$	67.7
$[Ni_4SO_2TCA]_6[rac-Co(L_1)_3]_8$	67.4
$[Ni_4SO_2TCA]_6[rac-Fe(L_1)_3]_8$	67.4
$[Ni_4SO_2TCA]_6[rac-Rh(L_1)_3]_8$	67.1

Table 9 The porosity of the obtained and refined MOCs based on connectors $rac-M(HL_1)_3$ calculated by PLATON

II.4. Packing of the dipyrin-based MOCs in the unit cell

In the unit cell, these MOCs are packed in a hexagonal fashion in the xOy plane and aligned parallelly along the b axis. Along the c axis, they display a rotation, so they are not superimposable (Figure 87).

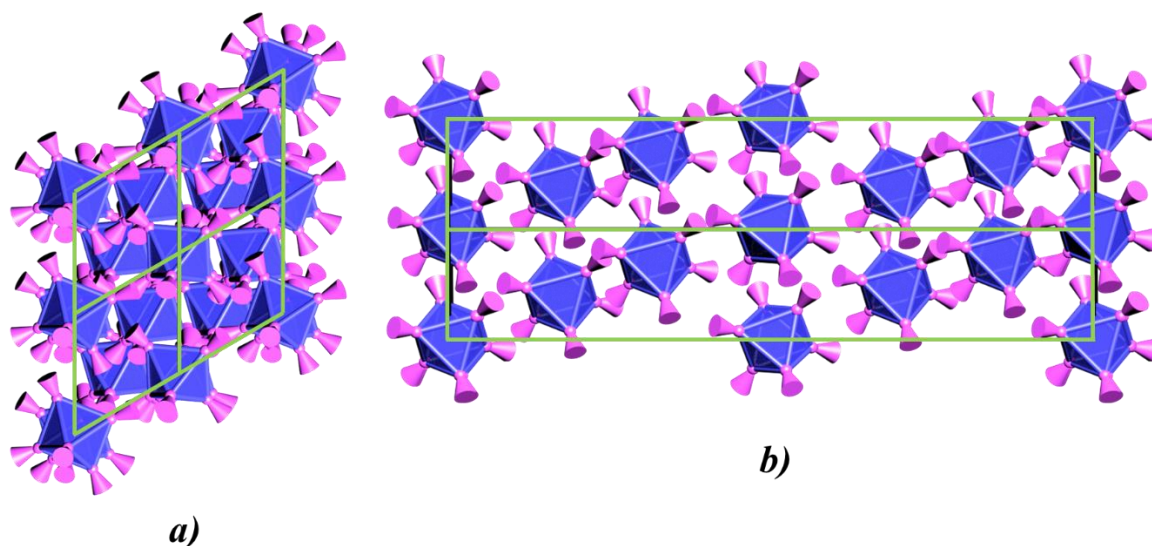


Figure 87 The schematic representation for the packing of $[M_4SO_2TCA(\mu_4-OH_2)]_6[rac-M'(L_1)_3]_8 \cdot nDMF \cdot mH_2O$ ($M = Co^{II}, Ni^{II}$; $M' = Co^{III}, Fe^{III}, Rh^{III}$) in the crystal, in the xOy plane (a), in the yOz plane (b). Octahedra represent calixarene-based MOCs, green lines represent unit cell

These results were published in *Chem. Comm.* in 2022.²⁰²



III. Structural investigation of chiral dipyrin-based MOCs: XRD analysis

It was possible to fully solve the structure of chiral MOCs based on the chiral connectors Δ -Co(HL₁)₃ and Λ -Co(HL₁)₃ (see details in crystallographic annexes §I.1.). The four obtained compounds present the formulas [M₄SO₂TCA(μ₄-OH₂)]₆[Δ , Λ -Co(L₁)₃]₈•nDMF•mH₂O and [M₄SO₂TCA(μ₄-OH₂)]₆[Δ -Co(L₁)₃]₈•nDMF•mH₂O (M = Co^{II}, Ni^{II}). These chiral MOCs crystallize in the chiral R32 trigonal space group and their crystallographic parameters are similar to the MOCs based on rac-M(HL₁)₃ connectors (M = Co^{III}, Fe^{III}, Rh^{III}) (Table 10).

	[M ₄ SO ₂ TCA(μ ₄ -OH ₂)] ₆ [Δ , Λ -Co(L ₁) ₃] ₈ •nDMF•mH ₂ O (M = Co ^{II} , Ni ^{II})				
	Trigonal R32				
	Cell length, Å	Cell angles	Volume, Å ³	Flack parameter	Porosity, %
[Co ₄ SO ₂ TCA] ₆ [Δ -Co(L ₁) ₃] ₈	a = b = 37.0736(6)Å c = 190.622(3)	α = 90° β = 90° γ = 120°	226898(8)	0.422(4)	70.5
[Co ₄ SO ₂ TCA] ₆ [Λ -Co(L ₁) ₃] ₈	a = b = 37.9778(10) c = 190.170(4)		237538(13)	0.242(5)	72.4
[Ni ₄ SO ₂ TCA] ₆ [Δ -Co(L ₁) ₃] ₈	a = b = 37.0388(3) c = 190.1726(19)		225939(5)	0.215(5)	70.6
[Ni ₄ SO ₂ TCA] ₆ [Λ -Co(L ₁) ₃] ₈	a = b = 36.9578(6) c = 190.122(2)		224892(8)	0.181(4)	70.7

Table 10 Crystallographic parameters for MOCs based on chiral dipyrin connectors Δ -Co(HL₁)₃ and Λ -Co(HL₁)₃

The presence of numerous disordered molecules in the unit cells leads to the same difficulties that the ones faced for the racemate analogues based on rac-M(HL₁)₃ (M = Co^{III}, Fe^{III}, Rh^{III}) (see details in §II. of this chapter).

The obtained chiral MOCs demonstrated almost the same range of porosity as MOCs based on rac-M(HL₁)₃ (M = Co^{III}, Fe^{III}, Rh^{III}) connectors, however, a small increase of the porosity is observed (Table 10). This fact can be explained by the absence of the disorder in the N6 metal ion environment of the connector in the chiral version compare to cages obtained with the rac-M(HL₁)₃ (M = Co^{III}, Fe^{III}, Rh^{III}) connectors.

One of the most important parameters for chiral space groups in XRD analysis is the so-called Flack-parameter (Table 10). The Flack-parameter is related to the absolute configuration of stereogenic centres. It takes values from 0 to 1 and the Flack-parameter value of 0.5 indicates that the absolute configuration cannot be determined from the available data. In contrast, a Flack-parameter value close to 0 indicates that the absolute configuration has been determined with the high confidence. On the other hand, the values close to 1 mean that inverted structure is likely correct.²⁰³ In the case of chiral MOCs presented in the Table 10 only one compound [Ni₄SO₂TCA]₆[Δ -Co(L₁)₃]₈ demonstrated a nearly acceptable Flack-parameter. These high values



can be explained by either low enantiomeric excess (*ee*) or due to poor diffracting power of crystals because of the large number of disordered solvent molecules that fill the voids in the structure, which is perfectly acceptable in our case considering that the high porosity (more than 70%) of the formed MOCs.

The M-O_(phenolate), M-O_(H₂O), M-O_(SO₂), M-M and M-N distances are given Table 11. As expected, they are similar to the one observed in the corresponding racemate MOCs based on **rac-M(HL₁)₃** (M = Co^{III}, Fe^{III}, Rh^{III}) (Table 11).

[M₄SO₂TCA(μ₄-OH₂)]₆[Δ,Λ-Co(L₁)₃]₈•nDMF•mH₂O (M = Co^{II}, Ni^{II})					
	M-O_(phenolate), Å	M-O_(H₂O), Å	M-O_(SO₂), Å	M-M, Å	M-N, Å
[Co₄SO₂TCA]₆[Λ-Co(L₁)₃]₈	2.09	2.22	2.09	3.01	1.93
[Co₄SO₂TCA]₆[Δ-Co(L₁)₃]₈	2.09	2.21	2.10	3.00	1.93
[Ni₄SO₂TCA]₆[Λ-Co(L₁)₃]₈	2.05	2.20	2.08	2.97	1.91
[Ni₄SO₂TCA]₆[Δ-Co(L₁)₃]₈	2.05	2.20	2.06	2.96	1.90

Table 11 The metrics of the metal ions in the structure of MOCs based on the chiral dipyrin connectors **Δ-Co(HL₁)₃** and **Λ-Co(HL₁)₃**

The obtained MOCs based on the connectors **rac-M(HL₁)₃** (M = Co^{III}, Fe^{III}, Rh^{III}), **Δ-Co(HL₁)₃** and **Λ-Co(HL₁)₃** were further investigated with other techniques in order to evaluate the enantiomeric excess of the chiral species, thermal stability and stability in solution. These techniques along with the experiments results are discussed in the following section.

IV. Additional characterizations techniques for dipyrin-based MOCs

The obtained MOCs based on the connectors **rac-M(HL₁)₃** (M = Co^{III}, Fe^{III}, Rh^{III}), **Δ-Co(HL₁)₃** and **Λ-Co(HL₁)₃** were further investigated with other techniques in order to evaluate the enantiomeric excess of the chiral species, and to analyse their thermal stability together with their stability in solution.

- The obtained vacuum dried MOCs **[M₄SO₂TCA(μ₄-OH₂)]₆[**rac-Co(L₁)₃]**₈, **[M₄SO₂TCA(μ₄-OH₂)]₆[**Δ-Co(L₁)₃]**₈ and **[M₄SO₂TCA(μ₄-OH₂)]₆[**Λ-Co(L₁)₃]**₈ (M = Co^{II}, Ni^{II}) have very limited solubility in DMSO, DCM and acetonitrile.******
- The obtained chiral MOCs **[M₄SO₂TCA(μ₄-OH₂)]₆[**Δ-Co(L₁)₃]**₈ and **[M₄SO₂TCA(μ₄-OH₂)]₆[**Λ-Co(L₁)₃]**₈ (M = Co^{II}, Ni^{II}) were investigated in solutions by Circular Dichroism (CD) and chiral HPLC in order to exclude any racemisation during the crystallisation process and to estimate the enantiomeric excess (*ee*) of the chiral MOCs.****
- MOCs based on connectors **rac-M(HL₁)₃** (M = Co^{III}, Fe^{III}, Rh^{III}), **Δ-Co(HL₁)₃** and **Λ-Co(HL₁)₃** were also investigated by different methods of mass-spectroscopy (ESI-MS, IM-MS) to provide additional evidence concerning structure of the obtained compounds.



- Concerning MOCs $[\text{M}_4\text{SO}_2\text{TCA}(\mu_4\text{-OH}_2)]_6[\text{rac-Co}(\text{L}_1)_3]_8$ ($\text{M} = \text{Co}^{\text{II}}, \text{Ni}^{\text{II}}$): they were analysed by XRPD in order to check the integrity of the crystalline phase. We also performed TGA measurements to provide valuable information concerning the amount of solvent molecules present in the structure along with thermal stability of the compounds. Furthermore, IR-spectroscopy methods were applied as an auxiliary method providing additional information concerning the structure of MOCs.
- NMR-spectra of the obtained MOCs are not informative due to limited solubility and to presence of paramagnetic ions ($\text{Co}^{\text{II}}, \text{Ni}^{\text{II}}$) in the structure.

IV.1. CD and chiral HPLC of enantiomerically pure cages

In order to prove the chirality and clearly estimate the *ee* of the obtained chiral cages $[\text{M}_4\text{SO}_2\text{TCA}(\mu_4\text{-OH}_2)]_6[\Delta\text{-Co}(\text{L}_1)_3]_8$ and $[\text{M}_4\text{SO}_2\text{TCA}(\mu_4\text{-OH}_2)]_6[\Lambda\text{-Co}(\text{L}_1)_3]_8$ ($\text{M} = \text{Co}^{\text{II}}, \text{Ni}^{\text{II}}$) circular dichroism (CD) and chiral HPLC experiments in solution were conducted.

IV.1.1. CD of enantiomerically pure cages

The CD spectra of the chiral cages $[\text{Ni}_4\text{SO}_2\text{TCA}(\mu_4\text{-OH}_2)]_6[\Lambda\text{-Co}(\text{L}_1)_3]_8$ and $[\text{Ni}_4\text{SO}_2\text{TCA}(\mu_4\text{-OH}_2)]_6[\Delta\text{-Co}(\text{L}_1)_3]_8$ in DCM solution display curves with peaks at 515 nm and 465 nm, which are almost perfect mirror images providing an evidence of a high enantiomeric excess (*ee*) (Figure 88) in both cases. The obtained values of ellipticity for $[\text{Ni}_4\text{SO}_2\text{TCA}(\mu_4\text{-OH}_2)]_6[\Lambda\text{-Co}(\text{L}_1)_3]_8$ are 421.29 and -479.56 mdeg; for $[\text{Ni}_4\text{SO}_2\text{TCA}(\mu_4\text{-OH}_2)]_6[\Delta\text{-Co}(\text{L}_1)_3]_8$ are -395.16 and 452.06 mdeg.

The CD spectra of $[\text{Co}_4\text{SO}_2\text{TCA}(\mu_4\text{-OH}_2)]_6[\Lambda\text{-Co}(\text{L}_1)_3]_8$ and $[\text{Co}_4\text{SO}_2\text{TCA}(\mu_4\text{-OH}_2)]_6[\Delta\text{-Co}(\text{L}_1)_3]_8$ demonstrated the same patterns (see experimental part).

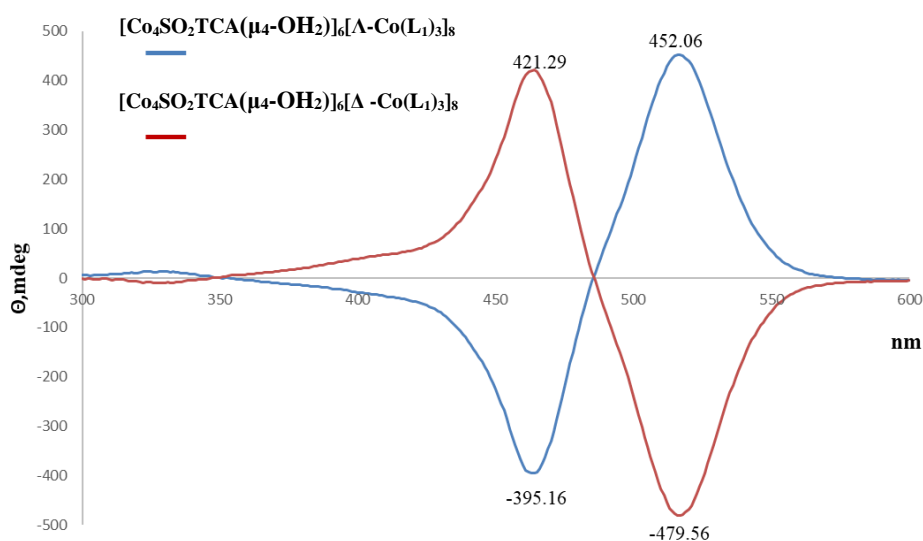


Figure 88 CD spectra of $[\text{Ni}_4\text{SO}_2\text{TCA}(\mu_4\text{-OH}_2)]_6[\Lambda\text{-Co}(\text{L}_1)_3]_8$ and $[\text{Ni}_4\text{SO}_2\text{TCA}(\mu_4\text{-OH}_2)]_6[\Delta\text{-Co}(\text{L}_1)_3]_8$ (RT, $5 \times 10^{-5} \text{M}$, DCM, cuvette length = 2 mm)

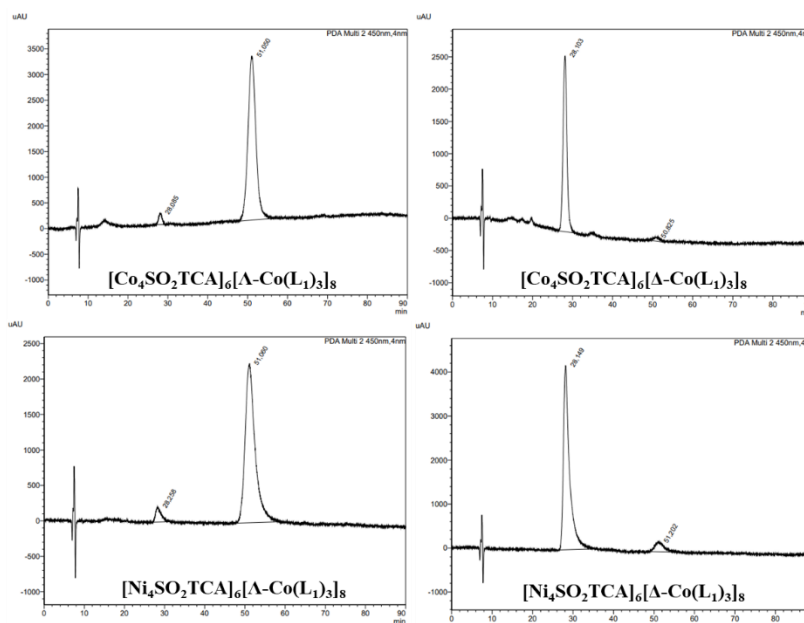


The values of ellipticity of the analysed chiral MOCs are much larger than the values of ellipticity for connectors alone: Λ -Co(HL₁)₃ (-98.47 and 144.44 mdeg) and Δ -Co(HL₁)₃ (91.9 and -131.7 mdeg) (§II.3. chapter II) using the same concentrations.

However, the CD data provide only circumstantial evidence about high *ee* of the obtained species, thus, we decided to run chiral HPLC measurements.

IV.1.2. Chiral HPLC measurements for enantiomerically pure cages

The strong evidences about large *ee* was provided using chiral HPLC measurements. The chiral HPLC experiments demonstrated the formation of chiral MOCs with *ee* up to 97%. The data of HPLC experiments is summarized in the following Table 12.



	Retention time, min	<i>ee</i>
[Co₄SO₂TCA(μ₄-OH₂)₆][Δ-Co(L₁)₃]₈	51.050	97%
[Co₄SO₂TCA(μ₄-OH₂)₆][Λ-Co(L₁)₃]₈	28.103	96%
[Ni₄SO₂TCA(μ₄-OH₂)₆][Δ-Co(L₁)₃]₈	51.060	95%
[Ni₄SO₂TCA(μ₄-OH₂)₆][Λ-Co(L₁)₃]₈	28.149	93%

Table 12 Chiral HPLC experiments data with the values of retention time and *ee* for the series of chiral MOCs $[M_4SO_2TCA(\mu_4-OH_2)]_6[\Delta, \Lambda-Co(HL_1)_3]_8 \cdot nDMF \cdot mH_2O$, ($M = Co^{II}, Ni^{II}$)

In conclusion, according to CD and chiral HPLC data in solution, we have the evidence that the desired chiral calixarene-based MOCs were successfully obtained with high level of enantiomeric excess up to 97%, even though high values of Flack-parameters were found during XRD measurements for-single crystals in the solid state.

IV.2. MS characterization in solution

MS experiments were performed for $[M_4SO_2TCA(\mu_4-OH_2)]_6[rac-Co(L_1)_3]_8$, and enantiomerically pure $[M_4SO_2TCA(\mu_4-OH_2)]_6[\Delta-Co(L_1)_3]_8$, $[M_4SO_2TCA(\mu_4-OH_2)]_6[\Lambda-Co(L_1)_3]_8$



$\text{Co}(\text{L}_1)_3\text{]}_8$ ($M = \text{Co}^{\text{II}}, \text{Ni}^{\text{II}}$). These measurements were performed in collaboration with Pr. K. Rissanen and Dr. Elina Kalenius (Jyväskylä University, Finland)

In order to perform these analysis the samples were dissolved in CH_2Cl_2 and the solutions were analysed on ESI-MS negative mode. These experiments demonstrated the presence of abundant single peak distribution for each dipyrin-based MOC on m/z range 2220-2230 which corresponds to intact MOCs with 6^- charge with some $n\text{H}_2\text{O}/m\text{DMF}$ adduct formation, which is common for such type of materials (Figure 89) (see experimental part). The 6^- charge can be related with the deprotonation of $\mu_4\text{-OH}_2$ in each shuttlecock moiety.

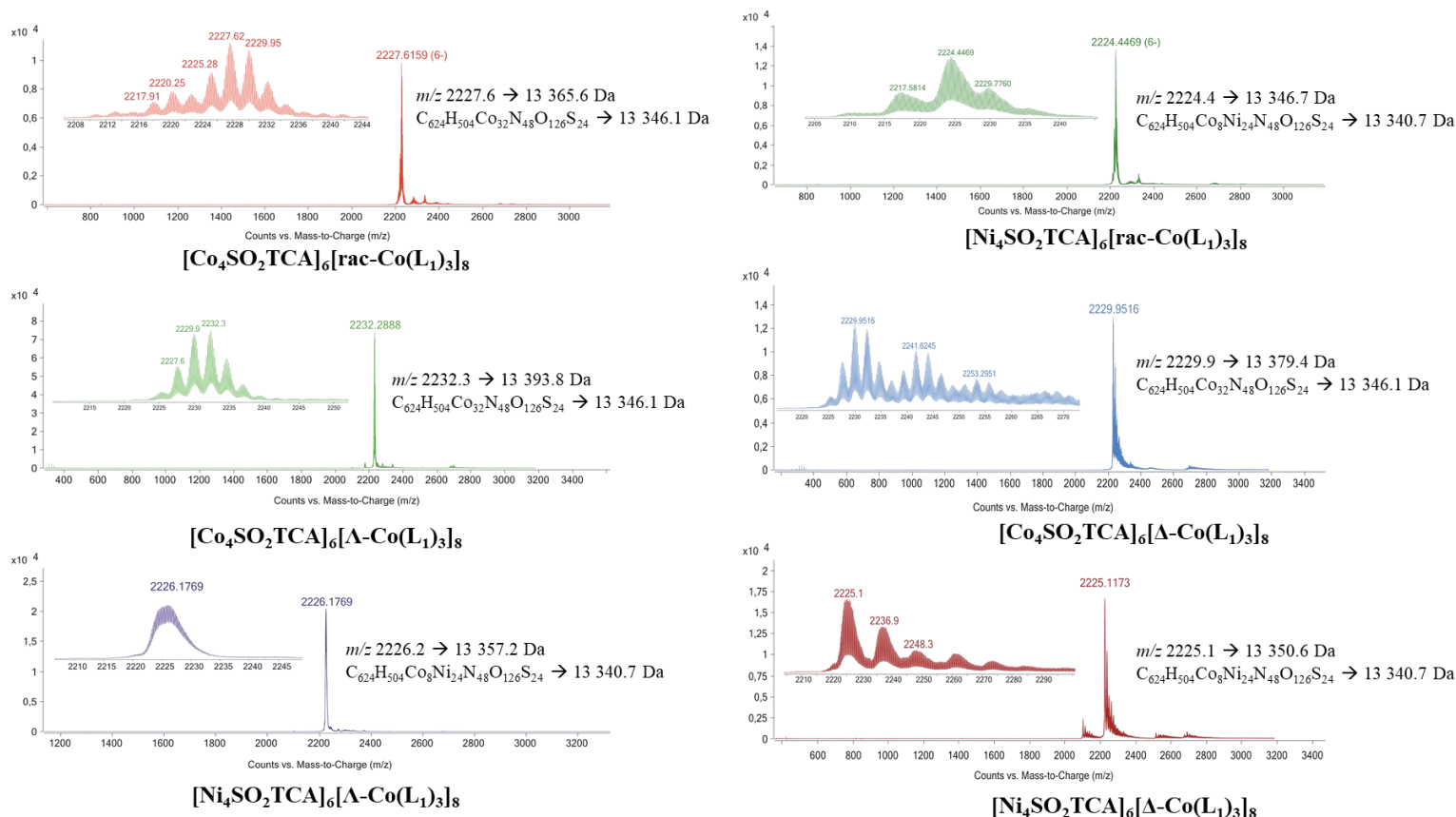


Figure 89 ESI-MS data for dipyrin-based MOCs $[\text{M}_4\text{SO}_2\text{TCA}(\mu_4\text{-OH}_2)]_6[\text{rac-Co}(\text{L}_1)_3]_8$, $[\text{M}_4\text{SO}_2\text{TCA}(\mu_4\text{-OH}_2)]_6[\text{A-Co}(\text{L}_1)_3]_8$ and $[\text{M}_4\text{SO}_2\text{TCA}(\mu_4\text{-OH}_2)]_6[\Delta\text{-Co}(\text{L}_1)_3]_8$ ($M = \text{Co}^{\text{II}}, \text{Ni}^{\text{II}}$)

In addition to ESI-MS, IM-MS measurements were performed. This technique refers to the separation and identification of molecules according to their mobility in a buffer gas.²⁰⁴ The most important values that can be extracted from these experiments are the arrival time and collision cross section ($^{\text{DT}}\text{CCS}_{\text{N}_2}$). Both values depend on the shape and the molecular mass of the particles while they move inside the drifting tube and collide with the molecules of the buffer gas (usually N_2).



IM-MS arrival time distributions demonstrated single drift peaks, with similar drift times for all cages except $[\text{Ni}_4\text{SO}_2\text{TCA}(\mu_4\text{-OH}_2)]_6[\Delta\text{-Co}(\text{L}_1)_3]_8$ cage, where it was not possible to resolve drift peak. Drift time for all cages resulted in the experimental $^{\text{DT}}\text{CCS}_{\text{N}_2}$ values, which are summarized Table 13.

	$^{\text{DT}}\text{CCS}_{\text{N}_2}, \text{\AA}^2$
$[\text{Co}_4\text{SO}_2\text{TCA}(\mu_4\text{-OH}_2)]_6[\text{rac-Co}(\text{L}_1)_3]_8$	1878.5
$[\text{Ni}_4\text{SO}_2\text{TCA}(\mu_4\text{-OH}_2)]_6[\text{rac-Co}(\text{L}_1)_3]_8$	1855.0
$[\text{Co}_4\text{SO}_2\text{TCA}(\mu_4\text{-OH}_2)]_6[\Delta\text{-Co}(\text{L}_1)_3]_8$	1830.0
$[\text{Co}_4\text{SO}_2\text{TCA}(\mu_4\text{-OH}_2)]_6[\Delta\text{-Co}(\text{L}_1)_3]_8$	1833.6
$[\text{Ni}_4\text{SO}_2\text{TCA}(\mu_4\text{-OH}_2)]_6[\Delta\text{-Co}(\text{L}_1)_3]_8$	Not resolved
$[\text{Ni}_4\text{SO}_2\text{TCA}(\mu_4\text{-OH}_2)]_6[\Delta\text{-Co}(\text{L}_1)_3]_8$	1846.1

Table 13 $^{\text{DT}}\text{CCS}_{\text{N}_2}$ values of the obtained dipyrin-based MOCs $[\text{M}_4\text{SO}_2\text{TCA}(\mu_4\text{-OH}_2)]_6[\text{rac-Co}(\text{L}_1)_3]_8$ and chiral $[\text{M}_4\text{SO}_2\text{TCA}(\mu_4\text{-OH}_2)]_6[\Delta, \Delta\text{-Co}(\text{L}_1)_3]_8$, ($M = \text{Co}^{\text{II}}, \text{Ni}^{\text{II}}$)

The theoretical values of $^{\text{T}}\text{CCS}_{\text{N}_2}$ can be calculated from the linear size of the obtained MOCs and the linear size of the buffer gas molecules (N_2). From the crystallographic data (Figure 83), it was possible to estimate the size of the cage, as a distance between two most remote methyl groups of the opposite shuttlecock moieties (approximately 45.6\AA), and Van der Waals radius of N_2 is approximately 1.55\AA , which results in the following equation:

$$^{\text{T}}\text{CCS}_{\text{N}_2} = \pi * (r(\text{cage}) + r(\text{N}_2))^2$$

$$^{\text{T}}\text{CCS}_{\text{N}_2} = \pi * (22.8 + 1.55)^2 = \underline{1862.72\text{\AA}^2}$$

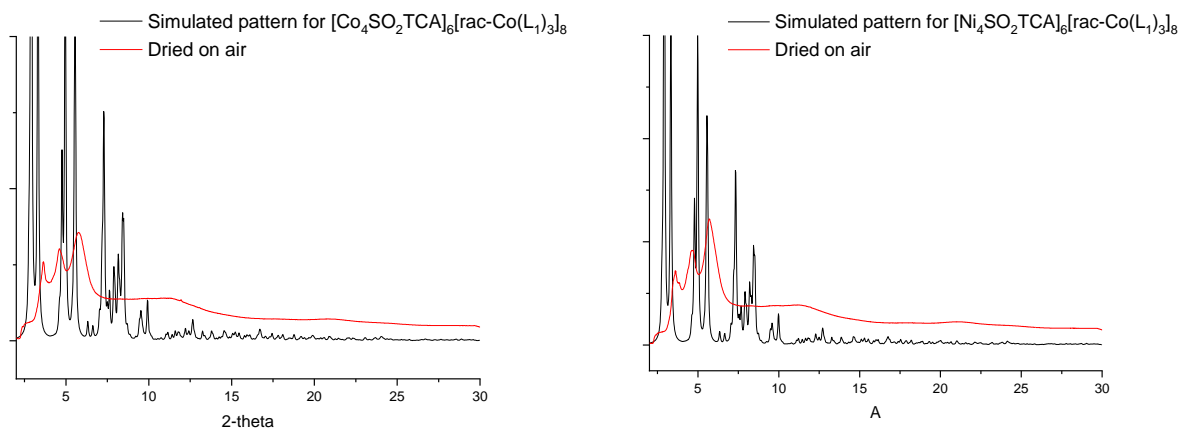
The obtained experimental values $^{\text{DT}}\text{CCS}_{\text{N}_2}$ have an excellent correlation with the calculated ones from single-crystal XRD structure. The small deviations in the experimental values might be explained by the minor deformations of the analysed MOCs during the collision processes. The obtained ESI-MS and IM-MS data consolidates structural similarity to the solid-state structure obtained by XRD techniques. It is worth mentioning, that the obtained MS data are also strong evidence of the MOCs high stability in solution. Thus, the presence of the particles with a mass corresponding with the expected values along with $^{\text{DT}}\text{CCS}_{\text{N}_2}$ values similar to $^{\text{T}}\text{CCS}_{\text{N}_2}$ proves that obtained MOCs retain structural integrity and do not degrade in solution during the experiment.

IV.3. XRPD in the solid state for racemic cages

XRPD measurement is a powerful tool to determine a crystalline phase in the solid state. However, for large molecular species like MOCs, this is not very informative. The disorder created by the presence of solvent molecules inside and outside the cage cavity generally does not lead to resolved diffraction patterns.



The polycrystalline samples of freshly prepared MOCs with formula $[\text{M}_4\text{SO}_2\text{TCA}(\mu_4\text{-OH}_2)]_6[\text{rac-Co}(\text{L}_1)_3]_8$ ($\text{M} = \text{Co}^{\text{II}}, \text{Ni}^{\text{II}}$) were analysed using the Kurchatov Synchrotron Radiation



Source (Moscow, Russia). The results of XRPD experiments are depicted Figure 90. Unfortunately, it was not possible to obtain XRPD data for other dipyrin-based MOCs due to the limited access to Kurchatov Synchrotron and XRPD measurements using a diffractometer power radiation were not successful.

Figure 90 XRPD traces for polycrystalline samples of $[\text{Co}_4\text{SO}_2\text{TCA}(\mu_4\text{-OH}_2)]_6[\text{rac-Co}(\text{L}_1)_3]_8$ (left); $[\text{Ni}_4\text{SO}_2\text{TCA}(\mu_4\text{-OH}_2)]_6[\text{rac-Co}(\text{L}_1)_3]_8$ (right)

The XRPD traces reveal very broad peaks, which is an evidence of a poor crystallinity of the powdered samples due to the decomposition of the crystal arrangement (amorphization) related with a partial release of the solvent molecules when exposed to the air. However, this behaviour is frequently observed for such porous structures.^{4,187}

IV.4. TGA measurements and IR analysis of the racemic cages

In order to estimate the quantity of solvents present in the structure of the obtained MOCs with the formula $[\text{M}_4\text{SO}_2\text{TCA}(\mu_4\text{-OH}_2)]_6[\text{rac-Co}(\text{L}_1)_3]_8$ ($\text{M} = \text{Co}^{\text{II}}, \text{Ni}^{\text{II}}$), TGA experiments on crystalline samples were performed. Additionally, these experiments provide valuable data concerning the thermal stability of the obtained MOCs. Unfortunately, it was not possible to obtain TGA data for other dipyrin-based MOCs due to the insufficient amount of compounds.

TGA experiments were performed with powdered samples obtained by filtration of crystals from the mother liquor. The TGA traces are demonstrated on Figure 91.

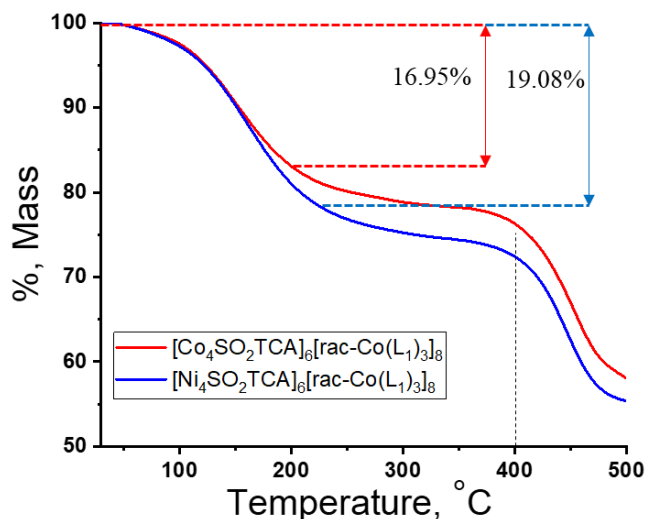


Figure 91 TGA traces for freshly obtained $[M_4SO_2TCA(\mu_4-OH_2)]_6[rac-Co(L_1)_3]_8$ ($M = Co^{II}$, Ni^{II})

As illustrated in Figure 91, the freshly obtained samples exhibit an initial mass loss (30-200°C) of around 20-25%, attributed to the solvents removal. The temperature range of solvent removal corresponds with the departing of DMF used during the synthesis. For both compounds, decomposition of the obtained MOCs begins at a temperature approximately 360°C. However, it is not possible to calculate the exact amount of the solvent molecules using TGA data due to different solvents (H_2O , DMF, MeOH) present in the unit cell. Nevertheless, these results will be used in the following Chapter IV in order to estimate the completeness of MOCs activation, with the following analysis of their gas adsorption properties.

IR characterisation was also performed for the obtained MOCs with formula $[M_4SO_2TCA(\mu_4-OH_2)]_6[rac-Co(L_1)_3]_8$ ($M = Co^{II}$, Ni^{II}). Due to the complexity of the obtained compounds, the complete assignment of the IR bands is difficult. However, IR characterisation will be used in the following Chapter IV, as an additional technique for the analysis of the MOCs structure under the activation process.

IV.5. Conclusion

In conclusion, a series of isostructural dipyrin-based MOCs was obtained. This series includes 6 new racemic MOCs based on the connectors $rac-M(HL_1)_3$ ($M = Co^{III}$, Fe^{III} , Rh^{III}) and 4 chiral MOCs based on chiral connectors $\Lambda-Co(HL_1)_3$ and $\Delta-Co(HL_1)_3$.

XRD analysis of single-crystals revealed the formation of large, porous, octahedral MOCs with an internal cavity diameter of approximately 19 Å, which is significant for this type of structures. Chiral MOCs based on chiral connectors $\Lambda-Co(HL_1)_3$ and $\Delta-Co(HL_1)_3$ were also



characterised and their chirality was supported by various techniques (CD, chiral HPLC). Furthermore, analysis by mass-spectrometry (ESI-MS and IM-MS) supported the formation of the desired structures and provided strong evidences of their stability in the solution and under ionization processes. Some of the obtained MOCs were also analysed by additional methods like XRPD but did not lead to conclusive results due to probably amorphization. Finally, TGA traces demonstrated that freshly obtained MOCs are stable until 360°C and contain 20-25% of solvent molecules (primally DMF).



V. Structural investigation of MOCs based on organic connectors

As it was discussed in the §VII. Chapter II. the chosen organic connectors are promising candidates for the formation of calixarene-based MOCs with anion- π recognition properties. The connectors **H₃L₈**-**H₃L₁₁** were used in the reaction of the MOCs formation. However, according to the Table 5 in §I.1 of this chapter, only rigid **H₃L₈** connector demonstrated the MOCs crystals formation of formula $[M_4SO_2TCA(\mu_4-OH_2)]_6[L_8]_8 \cdot nDMF \cdot mH_2O$ ($M = Co^{II}, Ni^{II}$) suitable for single-crystal XRD analysis.

V.1. Crystalline data for $[M_4SO_2TCA(\mu_4-OH_2)]_6[L_8]_8$ ($M = Co^{II}, Ni^{II}$)

A single-crystal XRD study demonstrated the formation of neutral isostructural octahedral cages with formula $[M_4SO_2TCA(\mu_4-OH_2)]_6[L_8]_8 \cdot nDMF \cdot mH_2O$ ($M = Co^{II}, Ni^{II}$) (Figure 92). These cages are formed by eight **L₈³⁻** connectors located on the eight faces of the formed octahedral cage and six shuttlecock-like building units $[M_4TCA(\mu_4-OH_2)]^{4+}$ located in the vertices of the octahedron. The observed ratio *shuttlecock calixarene node/triangular triazine connector* = 6/8 is in perfect accordance with the already reported face-panelled octahedral MOCs (Figure 92).⁹⁸ It is worth noting that the similar octahedral MOC of formula **(sc4a)Fe(tatb)** based on the connector **H₃L₈** has been already reported in the literature.¹⁸⁷ However, the reported in the literature MOC presents very different structure of shuttlecock-like moiety of formula $[Fe_4SO_2TCA(\mu_4-Cl)]^{3+}$ which leads to the formation of negatively charged structure. As a result, it is important to compare geometrical characteristics of the obtained MOCs $[M_4SO_2TCA(\mu_4-OH_2)]_6[L_8]_8$ with the ones of **(sc4a)Fe(tatb)** (see Table 16 in this chapter).

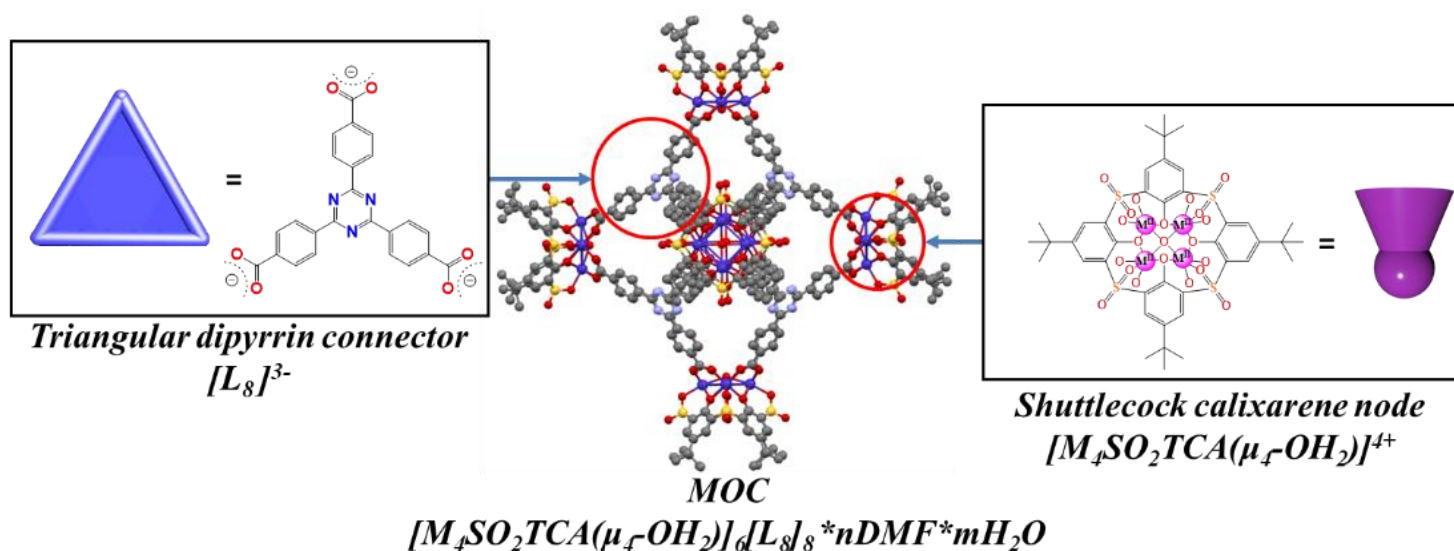


Figure 92 The structure of the obtained triazine-based MOCs $[M_4SO_2TCA(\mu_4-OH_2)]_6[L_8]_8 \cdot nDMF \cdot mH_2O$ ($M = Co^{II}, Ni^{II}$)



Both cages $[M_4SO_2TCA(\mu_4-OH_2)]_6[L_8]_8 \cdot nDMF \cdot mH_2O$ ($M = Co^{II}, Ni^{II}$) crystallize in the $I4/m$ tetragonal space group (see crystallographic annexes §I.1.). It is worth noting that the solvent molecules present in the structure could not be modelled and were accounted using a Solvent Mask generated by the PLATON SQUEEZE module within Olex2 which defined 13592.2 electrons per unit cell accounted for solvent molecules for $[Co_4SO_2TCA(\mu_4-OH_2)]_6[L_8]_8$ and 11567.3 electrons per unit cell for $[Ni_4SO_2TCA(\mu_4-OH_2)]_6[L_8]_8$.²⁰⁰

The demonstrated unit cell volumes (close to 58000 Å³) are almost the same as the ones of structurally similar CIAC-106 and (sc4a)Fe(tatb) calixarene-based MOCs.^{73,187}

	$[M_4SO_2TCA(\mu_4-OH_2)]_6[L_8]_8 \cdot nDMF \cdot mH_2O$ ($M = Co^{II}, Ni^{II}$)		
	I4/m tetragonal		
	Cell length, Å	Cell angles	Volume, Å ³
$[Co_4SO_2TCA]_6[L_8]_8$	a = b = 33.0404(10) c = 54.083(2)	$\alpha = \beta = \gamma = 90^\circ$	59041(4)
$[Ni_4SO_2TCA]_6[L_8]_8$	a = b = 32.5402(7) c = 53.8929(13)		57065(3)

Table 14 The unit cell parameters of the obtained MOCs based on H_3L_8 connector

V.2. Cages metrics

The obtained triazine-based MOCs demonstrate metrics and M-O distances similar to ones of dipyrin-based MOCs discussed earlier in §II.3 of this chapter. The dimensions of the obtained octahedral cages are smaller than ones reported for dipyrin-based MOCs and equal approximately to 40 x 40 x 40 Å³ (Table 15). In addition, the internal cavity diameter 18Å of $[M_4SO_2TCA(\mu_4-OH_2)]_6[L_8]_8$ ($M = Co^{II}, Ni^{II}$) is slightly inferior to ones of dipyrin-based MOCs (see §II.3. of this chapter) while almost identical to calixarene-based MOCs CIAC-106 and (sc4a)Fe(tatb).

$[M_4SO_2TCA(\mu_4-OH_2)]_6[L_8]_8 \cdot nDMF \cdot mH_2O$ ($M = Co^{II}, Ni^{II}$)							
	M-O _(phenolate) , Å	M-O _(H₂O) , Å	M-O _(SO₂) , Å	M-M, Å	Cavity diameter, Å	Dimension of the cages, Å ³	Porosity, %
$[Co_4SO_2TCA]_6[L_8]_8$	2.07	2.24	2.12	3.00	18	40 x 40 x 40	71.5
$[Ni_4SO_2TCA]_6[L_8]_8$	2.04	2.18	2.07	2.96			71.6

Table 15 The metrics of the metal ions environment, geometrical characteristics and porosity of MOCs of formula $[M_4SO_2TCA(\mu_4-OH_2)]_6[L_8]_8$ ($M = Co^{II}, Ni^{II}$),

It is important to mention, that despite the fact that the connector H_3L_8 is significantly smaller than the connector $rac-Co(HL_1)_3$ (12Å against 16Å), the formed triazine-based MOCs present a similar cavity size probably due to the totally planar nature of H_3L_8 in comparison with $rac-M(HL_1)_3$ ($M = Co^{III}, Fe^{III}, Rh^{III}$). The cavity demonstrates as well non-polar hydrophobic nature due to the absence of polar groups (such as hydroxy-groups) orientated inside the cavity. The portals of triazine-based MOCs allowing molecular species to get inside and outside the cavity, have a diameter of 8Å (Figure 93) which is larger than the portals of the dipyrin-based MOCs



discussed in §II.3 of this chapter. Consequently, the internal cavities of $[\text{Co}_4\text{SO}_2\text{TCA}(\mu_4\text{-OH}_2)]_6[\text{L}_8]_8$ and $[\text{Ni}_4\text{SO}_2\text{TCA}(\mu_4\text{-OH}_2)]_6[\text{L}_8]_8$ are expected to be more accessible than the internal cavities of dipyrin-based MOCs which may result in better gas adsorption properties of triazine-based MOCs.

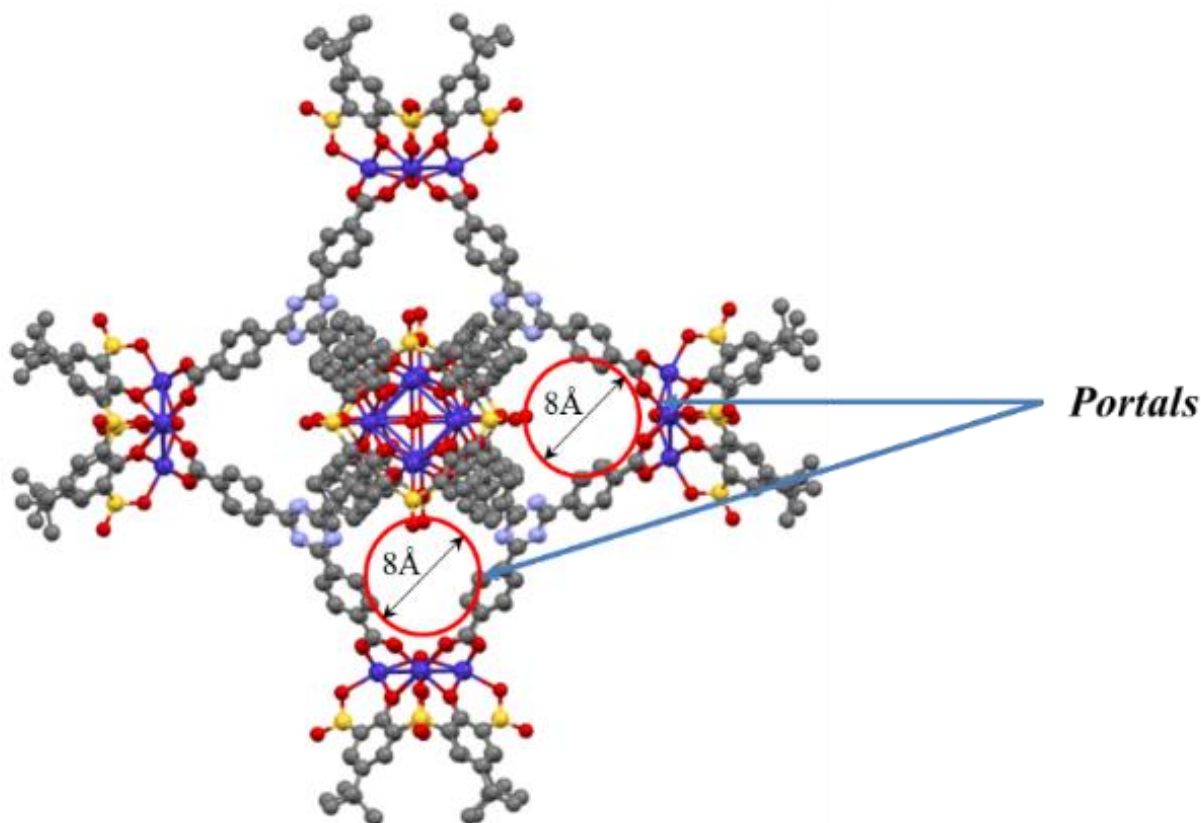


Figure 93 Portals of $[\text{M}_4\text{SO}_2\text{TCA}(\mu_4\text{-OH}_2)]_6[\text{L}_8]_8 \cdot n\text{DMF} \cdot m\text{H}_2\text{O}$ ($M = \text{Co}^{\text{II}}, \text{Ni}^{\text{II}}$)

It was calculated by PLATON²⁰¹ that the obtained MOCs have approximately 71.5% of the total volume available for gas adsorption that occurs inside and outside the cage cavity, which is similar to what is calculated for the structurally similar cage CIAC-106 (74.3%).⁷³

V.3. Packing of the Cages

In the unit cell, these triazine-based MOCs are packed in a cuboid fashion in the xOy plane and aligned parallelly along the b axis. Along the c axis they superimposable (Figure 94).

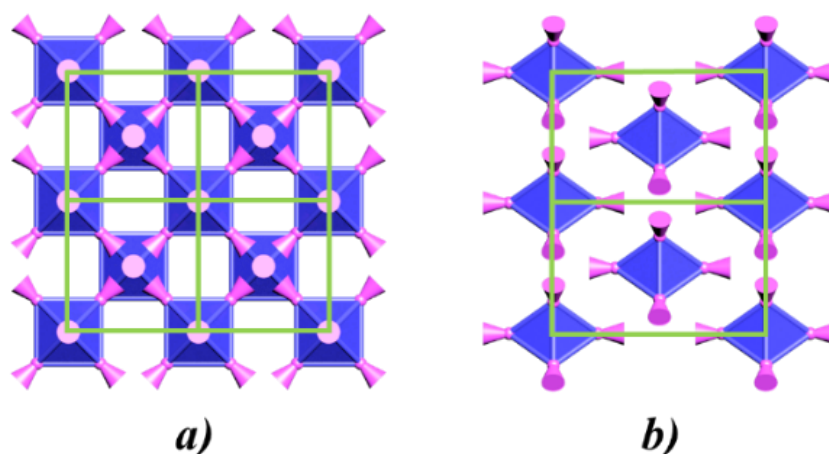


Figure 94 The schematic representation of the packing of $[M_4SO_2TCA(\mu_4-OH_2)]_6[L_8]_8$ ($M = Co^{II}, Ni^{II}$) in the crystal, in the xOy plane (a), in the yOz plane (b). Octahedra represent MOCs

In conclusion, XRD analysis revealed the formation of two isostructural octahedral triazine-based MOCs of formula $[M_4SO_2TCA(\mu_4-OH_2)]_6[L_8]_8$ ($M = Co^{II}, Ni^{II}$). XRD analysis of these MOCs demonstrates a great porosity up to 71.5% and, as a result, they are great candidates for the investigation of gas adsorption properties.

V.4. TGA and IR for triazine-based MOCs

Unfortunately, it was possible to obtain TGA and IR data only for a cage of formula $[Co_4SO_2TCA(\mu_4-OH_2)]_6[L_8]_8$ due to the small amount of the obtained compound $[Ni_4SO_2TCA(\mu_4-OH_2)]_6[L_8]_8$ (see details in experimental part).

The obtained MOC $[Co_4SO_2TCA(\mu_4-OH_2)]_6[L_8]_8$ was characterized by TGA in order to estimate the percentage of solvent molecules present in the structure. Additionally, TGA provides valuable data concerning the thermal stability of the obtained MOC.

TGA experiments were performed with a powdered sample obtained by filtration of crystals from the mother liquor. The TGA traces are demonstrated on Figure 95

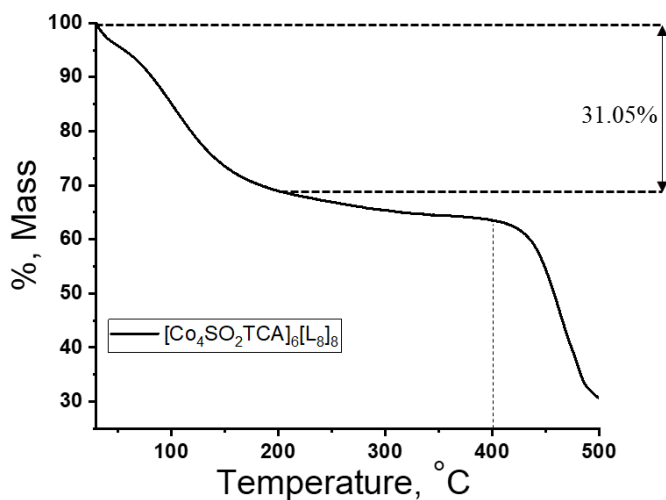


Figure 95 TGA data for freshly obtained $[\text{Co}_4\text{SO}_2\text{TCA}(\mu_4\text{-OH}_2)]_6[\text{L}_8]_8$

As illustrated Figure 95, the freshly obtained sample exhibits an initial mass loss of around 35%, attributed to solvent removal (30-200°C). The temperature range of solvent removal corresponds to the evaporation of methanol with subsequent evaporation of DMF. Both solvents were used during the synthesis (see experimental part). Decomposition of the obtained MOCs begins at a temperature of approximately 400°C. However, it is not possible to calculate the exact amount of the solvent molecules using TGA data due to different solvents (H_2O , DMF, MeOH) present in the unit cell.

IR characterisation was also performed for the obtained MOC of formula $[\text{Co}_4\text{SO}_2\text{TCA}(\mu_4\text{-OH}_2)]_6[\text{L}_8]_8$. Due to the complexity of these compound, the complete assignment of the observed IR bands is difficult.

However, IR characterisation will be used in the following Chapter IV, as an additional technique for the analysis of the MOC under the activation process.

The obtained vacuum dried MOCs $[\text{Co}_4\text{SO}_2\text{TCA}(\mu_4\text{-OH}_2)]_6[\text{L}_8]_8$ ($\text{M} = \text{Co}^{\text{II}}, \text{Ni}^{\text{II}}$) have very limited solubility in DMSO, DCM and acetonitrile. However, NMR-spectra of these cages is not informative due to presence of paramagnetic ions ($\text{Co}^{\text{II}}, \text{Ni}^{\text{II}}$) in the structure.



VI. Conclusion

In this work, we successfully synthesized a series of 12 novel MOCs using sulfonylcalix[4]arene, different connectors and different metal ions as building blocks. The structures of some MOCs obtained as single-crystals were thoroughly characterized using various analytical techniques, primarily X-ray diffraction (XRD). We have presented a summary of all the members of this series in Table 16, along with a comparison of their structural features with each other and some previously reported structures. The formulas of the solvate and μ_4 -OH₂ are omitted for clarity.

MOC/Characteristic	Cage size, Å ³	Cavity diameter, Å	Unit cell volume, Å ³	Molecular weight, Da
[Co ₄ SO ₂ TCA] ₆ [rac-Co(L ₁) ₃] ₈	46 x 46 x 46	19	228095(11)	13345
[Ni ₄ SO ₂ TCA] ₆ [rac-Co(L ₁) ₃] ₈	46 x 46 x 46	19	224992(5)	13321
[Co ₄ SO ₂ TCA] ₆ [Δ-Co(L ₁) ₃] ₈	46 x 46 x 46	19	226898(8)	13345
[Ni ₄ SO ₂ TCA] ₆ [Δ-Co(L ₁) ₃] ₈	46 x 46 x 46	19	225939(5)	13321
[Co ₄ SO ₂ TCA] ₆ [Δ-Co(L ₁) ₃] ₈	46 x 46 x 46	19	237538(13)	13345
[Ni ₄ SO ₂ TCA] ₆ [Δ-Co(L ₁) ₃] ₈	46 x 46 x 46	19	224892(8)	13321
[Co ₄ SO ₂ TCA] ₆ [rac-Fe(L ₁) ₃] ₈	46 x 46 x 46	19	226077	13321
[Ni ₄ SO ₂ TCA] ₆ [rac-Fe(L ₁) ₃] ₈	46 x 46 x 46	19	229719(4)	13316
[Co ₄ SO ₂ TCA] ₆ [rac-Rh(L ₁) ₃] ₈	46 x 46 x 46	19	232307	13698
[Ni ₄ SO ₂ TCA] ₆ [rac-Rh(L ₁) ₃] ₈	46 x 46 x 46	19	230232(4)	13692
[Co ₄ SO ₂ TCA] ₆ [L ₈] ₈	40 x 40 x 40	18	59041(4)	9992
[Ni ₄ SO ₂ TCA] ₆ [L ₈] ₈	40 x 40 x 40	18	57065(3)	9986
(sc4a)Fe(tatb) (ref. ¹⁸⁷)	40 x 40 x 40	18	60331(6)	10130
CIAC-106 (ref. ⁷³)	40 x 40 x 40	18	64116(4)	10069
CIAC-114 (ref. ¹⁰⁴)	51 x 51 x 51	27	106470(60)	11794
Mn ^{II} (salen) chiral MOC (ref. ⁴)	43 x 43 x 43	18	66343.4(14)	13367

Table 16 The comparison of the metrics and molecular weights of the obtained MOCs with the ones of MOCs reported in the literature (highlighted in yellow)

The synthesized MOCs exhibit large internal cavities and high porosity, with voids occupying of approximately 70% of the crystal volume. Consequently, these materials hold a significant potential for investigating their gas adsorption properties. The results of these investigations are presented in the following Chapter IV.

Chapter IV.

Gas adsorption properties of synthesized calixarene-based MOCs

Table of contents

<u>I. Generalities</u>	141
<u>I.1. Context of the study</u>	141
<u>I.2. The performed measurements on the synthesized MOCs</u>	142
<u>I.3. Activation of samples</u>	143
<u>II. Adsorption properties of triazine-based MOC</u>	144
<u>II.1. Behaviour of the sample after activation</u>	144
<u>II.2. N_{2(g)} adsorption and surface area evaluation</u>	146
<u>II.3. CO₂ adsorption</u>	148
<u>III. Adsorption properties of dipyrin-based MOCs</u>	149
<u>III.1. Behaviour of the samples after activation</u>	149
<u>III.2. N_{2(g)} adsorption and surface area investigation</u>	152
<u>III.3. Adsorption of other small molecules</u>	156
<u>III.4. Estimation of gas adsorption selectivity</u>	159
<u>IV. Conclusion</u>	162



I. Generalities

In the previous **Chapter III**, the structures of the synthesized calixarene-based MOCs were investigated in depth, that demonstrated an high calculated porosity up to 71.5%, which is related to rigid internal cavities of the cage (*internal porosity*) and packing of the cages in the unit cells of the crystals (*external porosity*). The latter porosity appears as “flexible” due to possible changes during the desolvation and, thus, amorphization processes of the powders. The high porosity of the obtained MOCs make them great candidates for gas storage and selective gas adsorption applications.

The porosity of such polycrystalline calixarene-based MOCs will be studied in this chapter through gas adsorption.

I.1. Context of the study

As it was discussed in **Chapter I**, MOCs generally exhibit good gas adsorption properties due to their internal and external porosity. Thus, many MOCs resulted gas adsorption and gas separation systems.⁷⁹

On the other hand, calixarene macrocycle itself exhibit good gas adsorption properties due to their distinct structure and versatility in the solid state.²⁰⁵ For example, calixarenes, mainly in cone conformation (see **§III.1. Chapter I**), display an internal cavity (7.2-7.8Å) suitable for the encapsulation of small molecules.^{101,102,206} Additionally, the recognition and encapsulation of small gaseous molecules can be tuned by the different calixarene conformations, the wide possibilities of chemical functionalization and the presence of the external porosity.

Application of calixarene moieties embedded in MOCs (calixarene-based MOCs) opens perspectives for gas adsorption studies due to the combination of inherent properties of MOCs and calixarenes. Gas adsorption properties of some calixarene-based MOCs have already been discussed in **§III.5.1. Chapter I**. In this section these properties will be discussed more in detail. Table 17 summarizes calixarene-based MOCs for which gas adsorption properties were investigated.

MOC	MOC shape, connector geometry	Investigated gases	BET N ₂ surface area, m ² /g
CIAC-114 ²⁰⁷	octahedral, triangular organic	N ₂	558
CIAC-106 ²⁰⁷	octahedral, triangular organic	N ₂	410
CIAC-103, CIAC-104 ⁷²	octahedral, triangular organic	N ₂ , H ₂	504, 477
[Co ^{II} ₂₄ (BTC _{4A}) ₆ (BDC) ₁₂] ⁸²	octahedral, linear organic	N ₂ , CO ₂ , H ₂	512
ImBDC-M (M = Co ^{II} , Ni ^{II}) ⁸³	octahedral, linear organic	CO ₂	n/a
(sc4a)Fe(btc), (tc4a)Fe(btc), (sc4a)Fe(tatb) ¹⁸⁷	octahedral, btc-linear organic tatb-triangular organic	Ar, N ₂ , CO ₂ , C ₃ H ₆ , C ₃ H ₈ , C ₂ H ₆ , C ₂ H ₄	368 (CO ₂), 217, 879
CIAC-112 ²⁰⁸	octahedral, angular organic	N ₂ , CO ₂	1211
CIAC-107 ⁷³	octahedral, triangular organic	N ₂	770
LSHU01 ¹⁰⁰	icosahedron, angular organic	N ₂ , CO ₂ , CH ₄ , C ₂ H ₄ , C ₂ H ₆ , C ₃ H ₈	803
CIAC-115 ⁹⁴	J ₁₇ hexadecahedron, triangular organic	N ₂ , CO ₂ , CH ₄ , C ₂ H ₆ , C ₃ H ₈	646
[M ₄ (TBSC)] ₆ [HL] ₈ (M = Co ^{II} , Ni ^{II}) ¹⁰³	octahedral, triangular organic	N ₂	1192, 1239
Mn ^{II} (salen)-based chiral MOC ⁴	octahedral, linear metal-organic	CO ₂	185 (CO ₂)

Table 17 Comparison of gas adsorption properties of the reported calixarene-based MOCs

To the best of our knowledge there are 17 reported calixarene-based MOCs for which gas adsorption properties were investigated (Table 17). It is worth noting, that some of the calixarene-based MOCs, for example, CIAC-112²⁰⁸ and [M₄(TBSC)]₆[HL]₈ (M = Co^{II}, Ni^{II})¹⁰³ demonstrate relatively large surface areas comparable to ones of some reported MOFs.^{209,210} Out of these MOCs listed Table 17, 15 have an octahedral shape, 7 included triangular organic connectors, and only one integrates a metal-organic connector. Moreover, there are only 3 publications dedicated to studying the gas adsorption properties of MOCs with light hydrocarbons, and only two of them provide data concerning IAST selective gas adsorption.^{94,100} From these observations, we can conclude that the gas adsorption properties of octahedral calixarene-based MOCs, especially their selective gas adsorption properties, are a relatively underexplored field of research.

As a result, in this work, we focused on the investigation of gas adsorption properties of some of the obtained octahedral calixarene-based MOCs. The studied gases will be N₂ (for estimation of surface area and pore size distribution), and CO₂, CH₄, C₂H₂, C₂H₄ and C₂H₆ (for estimation of gas adsorption selectivity).

I.2. The performed measurements on the synthesized MOCs

It was not possible to investigate the gas adsorption properties for all the obtained and characterised calixarene-based MOCs presented in **Chapter III** due to the insufficient amount of



the obtained polycrystalline pure material (minimum of 50 mg for each study is required). However, we performed a detailed study of the gas adsorption properties for two types of the obtained MOCs.

- one MOC with the organic connector **H₃L₈**, of formula **[Co₄SO₂TCA(μ₄-OH₂)₆L₈]₈**
- two isostructural MOCs based on the metal-organic tris(dipyrrin) connector **rac-Co(HL₁)₃**, of formula **[M₄SO₂TCA(μ₄-OH₂)₆rac-Co(L₁)₃]₈** (M = Co^{II}, Ni^{II})

Since the gas adsorption measurements are performed with the activated samples (see details in §I.3. of this Chapter), the formula of the MOCs solvates (**•nDMF•nH₂O**) is omitted.

One of the most important parameters related to the gas adsorption properties is the surface area (SA) accessible for the gas adsorption and pore size distribution. N_{2(g)} adsorption-desorption measurements are essentially used to determine these parameters. Consequently, experiments with N_{2(g)} were performed for the 3 aforementioned MOCs and the related surface areas along with the pore size distributions will be discussed in the light of the structural data.

Adsorption-desorption experiments of the obtained MOCs **[M₄SO₂TCA(μ₄-OH₂)₆rac-Co(L₁)₃]₈** (M = Co^{II}, Ni^{II}) with other gases (CO₂, CH₄, C₂H₂, C₂H₄ and C₂H₆) were also performed, however, these experiments were not performed for **[Co₄SO₂TCA(μ₄-OH₂)₆L₈]₈** due to the limited access to gas sorption analyser in A.V. Nikolaev Inorganic Chemistry Institute. These gases are important industrial compounds and their selective adsorption is a promising field for study and modelling of selective gas separation systems. Also, CO₂ and CH₄ are dangerous greenhouse gases and their capture is an important issue in ecology.

The measurements have been performed using BET apparatus (see details in experimental part) and for the measurements on MOCs of formula **[M₄SO₂TCA(μ₄-OH₂)₆rac-Co(L₁)₃]₈** (M = Co^{II}, Ni^{II}), they have been performed in collaboration with group of Pr. Fedin (A.V. Nikolaev Inorganic Chemistry Institute, Novosibirsk, Russia).

I.3. Activation of samples

As it was discussed in **Chapter III**, the pores of the obtained calixarene based MOCs are filled with molecules of solvents (mainly DMF, H₂O, MeOH) used during the synthesis of corresponding MOCs. As a result, the polycrystalline samples of MOCs must be “activated” by removing the solvents molecules before the investigation of the gas adsorption properties. The sample activation typically involves heating the sample under vacuum in order to remove any adsorbed gases and solvents that can interfere with the gas adsorption measurements. The temperature and duration of the activation process depend on the nature of the investigated compounds and the nature of the solvent molecules. The conditions of the activation procedure were chosen according to the thermal stability of the obtained MOCs. As it was demonstrated in

§IV.4 and §V.4 of Chapter III, the dipyrin-based MOCs of formula $[M_4SO_2TCA(\mu_4-OH_2)]_6[rac-Co(L_1)_3]_8$ ($M = Co^{II}, Ni^{II}$) demonstrate a thermal stability up to 360°C and triazine-based MOC of formula $[Co_4SO_2TCA(\mu_4-OH_2)]_6[L_8]_8$ demonstrates thermal stability up to 400°C. TGA traces demonstrated the mass loss related with the molecules of solvents in the range 30-200°C. As a result, the activation procedure was conducted at 180°C under a dynamic vacuum (vacuum level = 1.3 Pa) for 6h for all investigated MOCs.

II. Adsorption properties of triazine-based MOC

In this part we will focus on the investigation of gas adsorption properties of the polycrystalline MOC of formula $[Co_4SO_2TCA(\mu_4-OH_2)]_6[L_8]_8$. The isostructural MOC $[Ni_4SO_2TCA(\mu_4-OH_2)]_6[L_8]_8$ (see details in experimental part) was also obtained but in too small quantities to investigate its gas adsorption properties.

II.1. Behaviour of the sample after activation

As mentioned previously, activating of MOCs is necessary to fully unlock their potential by removing any residual solvents adsorbed in the solid state. The impact of this activation process on the structure of the MOCs is a prerequisite before performing adsorption measurements. Thus, the MOC of formula $[Co_4SO_2TCA(\mu_4-OH_2)]_6[L_8]_8$ was studied using IR and TGA techniques, since XRPD measurements not always provide a non-ambiguous answer.

II.1.1. IR data

Figure 96 gives the IR spectra of $[Co_4SO_2TCA(\mu_4-OH_2)]_6[L_8]_8$ after (orange curve) activation, of *p-tert*-butylsulfonylcalix[4]arene (H_4SO_2TCA) (blue) and connector H_3L_8 (grey).

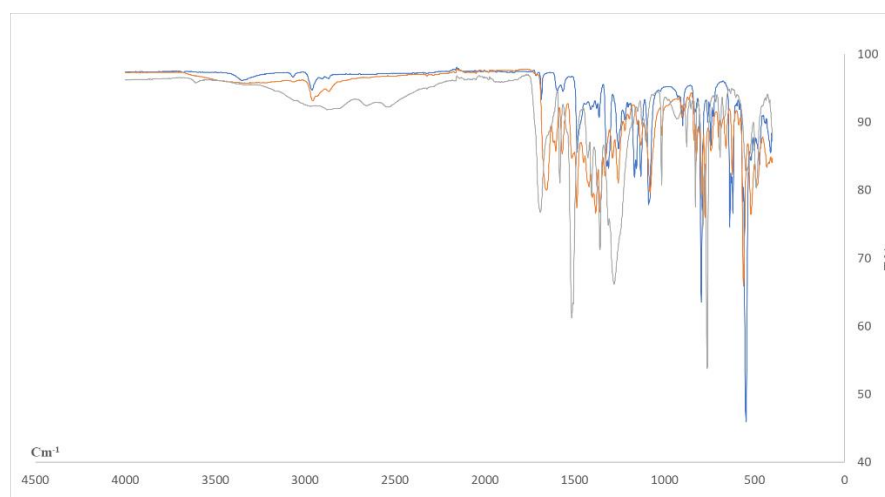


Figure 96 FTIR data for activated $[Co_4SO_2TCA(\mu_4-OH_2)]_6[L_8]_8$ (orange); for H_3L_8 (grey) and for H_4SO_2TCA (Blue)



The comparison of IR spectrum (Figure 96) of $[\text{Co}_4\text{SO}_2\text{TCA}(\mu_4\text{-OH}_2)]_6[\text{L}_8]_8$ with IR spectra of H_3L_8 and $\text{H}_4\text{SO}_2\text{TCA}$ demonstrates that the activated MOCs sample contains all the constituent components. However, in some cases there is a shift or broadening of signals, which may be due to interactions between components within the MOCs, the presence of metal cations (Co^{II}), and the disappearance of hydrogen bonds as a result of the deprotonation of the original components ($\text{H}_4\text{SO}_2\text{TCA}$ and H_3L_8). Nevertheless, the most intense signals are present and are corresponding with all components being present in the activated sample. XRPD measurements do not bring information.

II.1.2. TGA data

TGA analysis after activation of $[\text{Co}_4\text{SO}_2\text{TCA}(\mu_4\text{-OH}_2)]_6[\text{L}_8]_8$ was performed in order to prove the completeness of the activation (Figure 97).

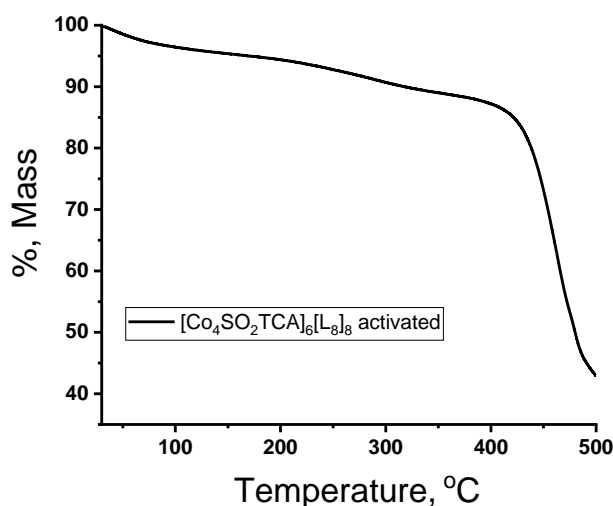


Figure 97 TGA trace of the activated $[\text{Co}_4\text{SO}_2\text{TCA}(\mu_4\text{-OH}_2)]_6[\text{L}_8]_8$

The TGA trace demonstrates that most of the molecules of solvent were removed from the sample during the activation process. However, it also indicates that a certain amount of solvent molecules is still present in the sample (up to 10%). This fact could be explained by the adsorption of water from the air due to air exposure between the activation and TGA analysis (the sample is highly hygroscopic). This fact is in accordance with the TGA of the freshly prepared samples (see §V.4. of Chapter III).

After the activation, gases adsorption experiments were performed (see details in experimental part).

II.2. N_{2(g)} adsorption and surface area evaluation

II.2.1. Measurements

The N_{2(g)} uptake was measured within the range of relative pressures from 10⁻⁶ to 0.999 P/P_0 at 77K (see details in experimental part). The N_{2(g)} adsorption-desorption experiment was performed one time in order to plot adsorption-desorption isotherm, to evaluate specific surface areas and calculate the pore size distribution. The obtained isotherm is presented in Figure 98.

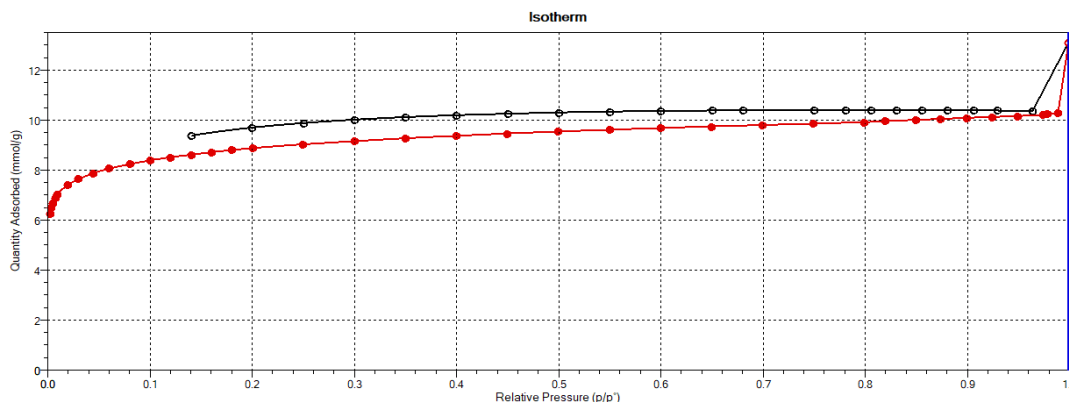


Figure 98 N_{2(g)} adsorption-desorption isotherm at 77K for [Co₄SO₂TCA(μ₄-OH₂)]₆[L₈]₈ (red curve – adsorption, black curve – desorption)

For [Co₄SO₂TCA(μ₄-OH₂)]₆[L₈]₈, the N_{2(g)} adsorption-desorption isotherm (Figure 98) revealed a type I isotherm indicating the behaviour of a microporous material. Its characteristic shape indicates that the adsorbent material has a limited number of adsorption sites available for gas molecules (pores), and that the adsorption process is primarily governed by physical interactions of one layer on the walls of the compound.

The N_{2(g)} adsorption-desorption isotherm for [Co₄SO₂TCA(μ₄-OH₂)]₆[L₈]₈ presents a sharp peak at the relative pressure close to 1, which is related to the condensation process among the material particles (“grains”) and not inside the pores. This behaviour is frequently observed for microporous materials.

From the obtained isotherm, the Langmuir and BET surface area were evaluated to be equal to 821.2 and 742.6 m²/g respectively, additionally the total pore volume (V_{pore}(DFT)) and total volume of adsorbed N_{2(g)} (V_{ads}(N_{2(g)})) were evaluated (Table 18). The comparison of these observed values with the ones reported in the literature for similar MOCs is presented in §III.2.2. of this chapter.



MOC	Specific surface area, m ² /g		V _{pore} (DFT) ^a , cm ³ /g	V _{ads} (N _{2(g)}) ^a , cm ³ (STP)/g
	Langmuir	BET		
[Co ₄ SO ₂ TCA] ₆ [L ₈] ₈ pristine	821.2	742.6	0.204	171.4

Table 18 Characteristic N_{2(g)} adsorption parameters for [Co₄SO₂TCA(μ₄-OH₂)₆][L₈]₈ (α - measured at P/P₀ = 0.95)

II.2.2. Pore size estimation

The pore size distribution was calculated from N_{2(g)} adsorption-desorption isotherm (Figure 98) using density functional theory (N₂-DFT) in the software MicroActive. The results of these calculations are presented Figure 99 and in Table 18.

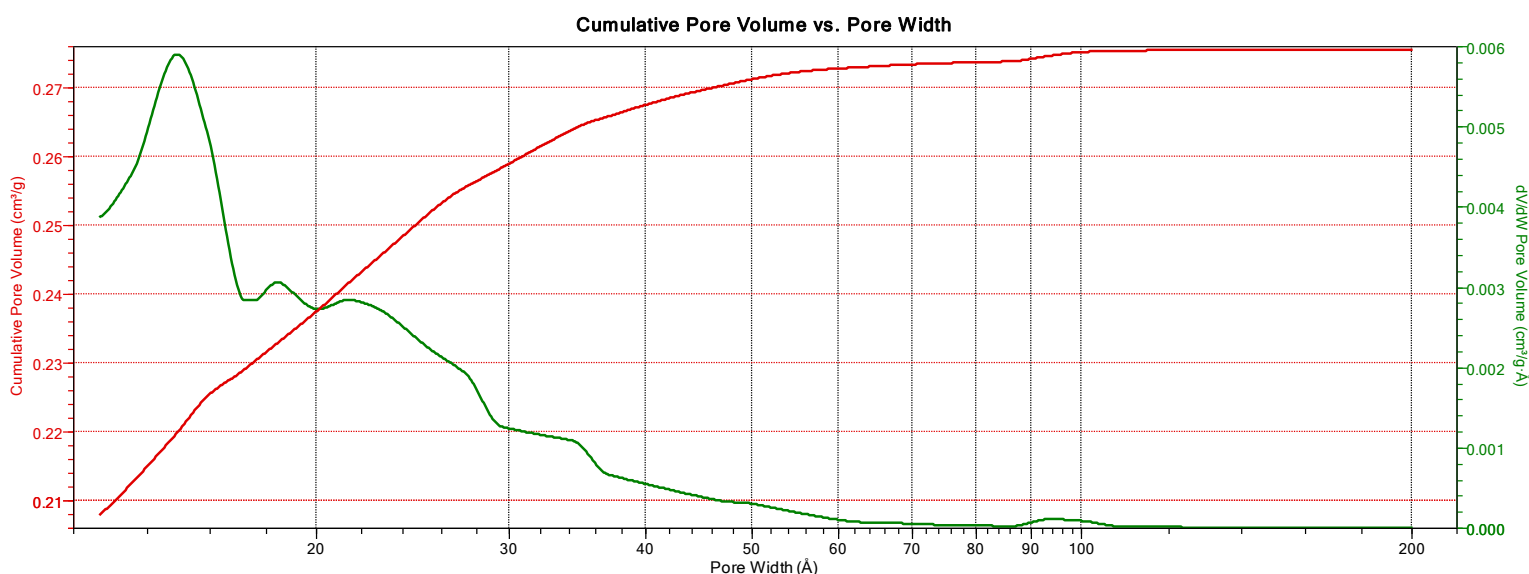


Figure 99 Pore size distribution (green line) and cumulative pore volumes (red line) for [Co₄SO₂TCA(μ₄-OH₂)₆][L₈]₈ calculated by N₂-DFT Model using MicroActive software

[Co₄SO₂TCA(μ₄-OH₂)₆][L₈]₈ exhibits a pore size width distribution in the interval 12-40 Å with a distinguishable peak at 15 Å related to the internal cavity of the MOC (Figure 99). The calculated pore size distribution is in a good accordance with the crystalline data that revealed the diameter of the internal cavity to be close to 18 Å (see §V.1. Chapter III). The difference between the observed and the estimated pore size might be explained by the fact the dimension of the internal cavity from the crystal structure was estimated as a diameter of a sphere, which could be inscribed inside the cavity of MOCs without crossing any bonds or atoms (including hydrogen), while gas adsorption measurements provide information about the accessible or effective pore size, additionally, gas adsorption measurements typically assume an idealized model of the porous material (slit), which may not accurately reflect the actual pore structure of the material. Other pores (width >15 Å) are related with external porosity, defects and dislocations in crystals leading to the mesostructuring of crystallites.

II.3. CO₂ adsorption

On the next step, the adsorption properties of [Co₄SO₂TCA(μ₄-OH₂)₆][L₈]₈ with CO_{2(g)} have been then investigated, since CO_{2(g)} is a common component in flue gas, the study of its adsorption and capture is an important field in ecology. These experiments will provide valuable data concerning the affinity of MOC towards gases with different properties (Table 19).

Gas/Characteristic	Molecular weight, g/mol	Kinetic diameter, Å	Density (STP), kg/m ³
N _{2(g)}	28	3.64	1.251
CO _{2(g)}	44	3.3	1.977

Table 19 Comparison of some physical characteristics of N_{2(g)} and CO_{2(g)} (ref. ²¹¹)

For [Co₄SO₂TCA(μ₄-OH₂)₆][L₈]₈, the CO_{2(g)} uptake was measured at 273K and within the range of relative pressures from 7*10⁻⁵ to 0.034. The CO_{2(g)} adsorption-desorption isotherm is presented on Figure 100.

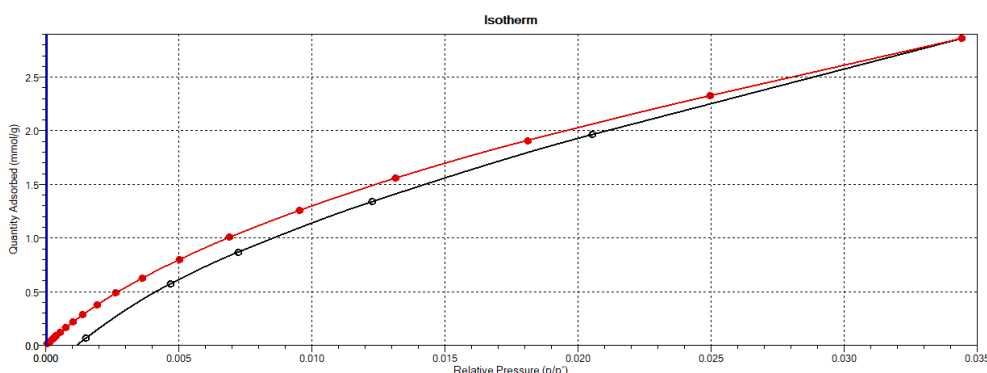


Figure 100 CO_{2(g)} adsorption-desorption isotherm at the temperature 273K for [Co₄SO₂TCA(μ₄-OH₂)₆][L₈]₈ (red curve - adsorption, black curve – desorption)

For [Co₄SO₂TCA(μ₄-OH₂)₆][L₈]₈, the CO_{2(g)} adsorption-desorption isotherm demonstrates that the saturation in the experimental range was not observed, contrary to what was observed for N_{2(g)}. It is important to compare the obtained values of specific surface areas with the ones already reported in the literature for structurally similar octahedral triazine-based MOC of formula (sc4a)Fe(tatb)¹⁸⁷ (Table 20). The structural features of this MOC were discussed in §V. of Chapter III.

MOC	N ₂ Specific surface area, m ² /g		CO ₂ Specific surface area, m ² /g		V _{pore} (DFT N ₂) cm ³ /g	V _{ads} (N _{2(g)}), cm ³ /g STP
	Langmuir	BET	Langmuir	BET		
[Co ₄ SO ₂ TCA] ₆ [L ₈] ₈	821.2	742.6	468.4	438.6	0.204	171.4
(sc4a)Fe(tatb) (ref. ¹⁸⁷)	1248	879	1082	652	-	-

Table 20 N_{2(g)} and CO_{2(g)} uptakes for [Co₄SO₂TCA(μ₄-OH₂)₆][L₈]₈

Even though CO₂ has a smaller kinetic diameter than N₂ (Table 19), [Co₄SO₂TCA(μ₄-OH₂)₆][L₈]₈ demonstrates a higher affinity towards N_{2(g)}. This observation might be explained by



the interaction energy between the gas molecules and the MOC surface. CO_{2(g)} interaction energy with the material may be weaker than one of N_{2(g)}. This means that N_{2(g)} may be more strongly adsorbed onto the material's surface. However, zero-coverage heats of adsorption were not obtained due to the lack of material for experiments under different temperature conditions.

The similar behaviour was observed for the reported triazine-based MOC of formula (sc4a)Fe(tatb).¹⁸⁷ However, despite the similar structure of these MOCs, generally surface areas of (sc4a)Fe(tatb) are larger than ones of [Co₄SO₂TCA(μ₄-OH₂)]₆[L₈]₈. These observations can be explained by the MOCs charge. As it was discussed in §V. of Chapter III, MOC (sc4a)Fe(tatb) is a negatively charged species in comparison with [Co₄SO₂TCA(μ₄-OH₂)]₆[L₈]₈, which is neutral. Charged substances have a higher polarising power than uncharged ones. As a result, there is greater affinity of gases to charged MOCs than to uncharged MOCs. This fact is also indirectly confirmed by the experiments carried out for dipyrin-based MOCs, where these MOCs demonstrated greater affinity to more lightly polarizable gases (see details in §III.4. of this chapter).

III. Adsorption properties of dipyrin-based MOCs

In this part, we will mainly focus on the investigation of gas adsorption properties of two polycrystalline MOCs of formula [M₄SO₂TCA(μ₄-OH₂)]₆[rac-Co(L₁)₃]₈ (M = Co^{II}, Ni^{II}), after some preliminary results concerning their structural behaviour when exposed to solvents and to the activation.

III.1. Behaviour of the samples after activation

As it was discussed, the activation of [M₄SO₂TCA(μ₄-OH₂)]₆[rac-Co(L₁)₃]₈ (M = Co^{II}, Ni^{II}) was performed. The effect of this activation process for [M₄SO₂TCA(μ₄-OH₂)]₆[rac-Co(L₁)₃]₈ (M = Co^{II}, Ni^{II}) was studied using XRPD, IR and TGA techniques. The aim of this section is to provide a comprehensive understanding of the activation process, including an estimation of its completeness (see activation conditions in §I.3. of this chapter).

III.1.1 Behaviour of the samples soaked in different solvents, XRPD measurements

As already mentioned, XRPD patterns for crystalline phases of large molecules (especially MOCs) frequently present broad peaks due to the huge amount of solvents present in the unit cell. When crystals are exposed to the air, they begin to desolvate. This leads usually to an amorphization of the crystalline phase.^{4,187} This amorphization affects the organization of the cages within the unit cell, and thus, the XRPD pattern.

As a result, when MOCs of formula $[M_4SO_2TCA(\mu_4-OH_2)]_6[rac-Co(L_1)_3]_8$ ($M = Co^{II}, Ni^{II}$) are dried in the air, amorphization is observed leading to the broadening of the peaks in XRPD diagram (Figure 101, red curve) (see details in §IV.3. of Chapter III).

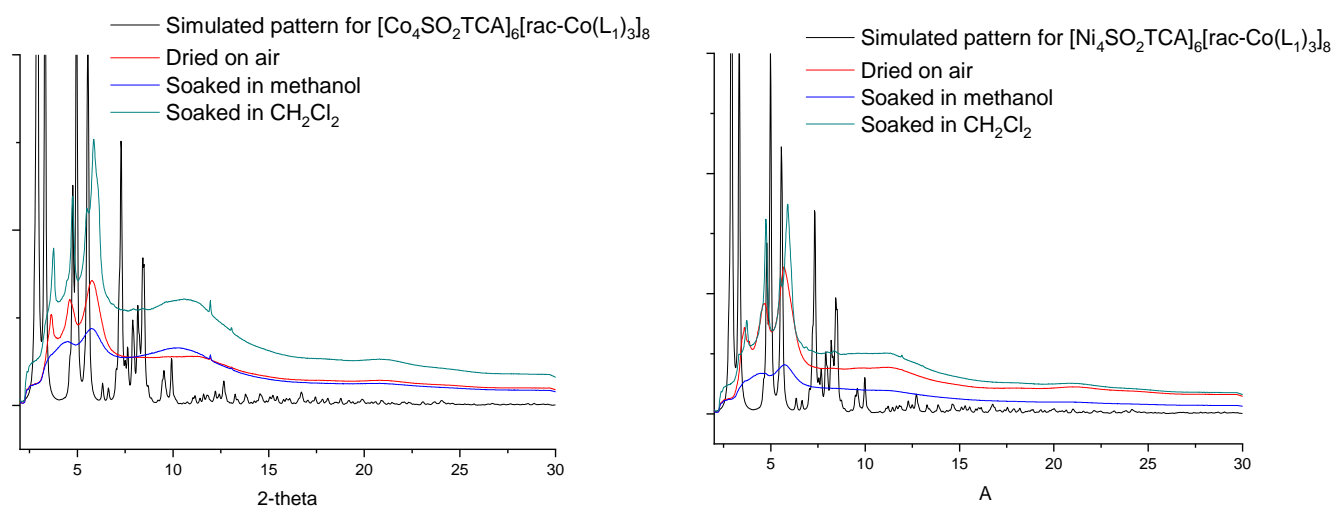


Figure 101 XRPD data of $[M_4SO_2TCA(\mu_4-H_2O)]_6[rac-Co(L_1)_3]_8$ soaked in different solvents

This phenomenon was also observed when non-activated crystals of $[M_4SO_2TCA(\mu_4-OH_2)]_6[rac-Co(L_1)_3]_8$ ($M = Co^{II}, Ni^{II}$) were soaked into a solution of MeOH or CH_2Cl_2 , while exchanging solvents with the crystals leading to a partial amorphization of the crystalline phase (Figure 101, blue and green curves). Compounds soaked in MeOH or dried in the air present an analogous pattern, while the soaking in CH_2Cl_2 leads to a more pronounced amorphization process.

Thus, the integrity of the MOCs scaffold when exposed to the air or when exposed to solvents has to be probed by other techniques, for example, IR that will be discussed in the next section.



III.1.2. IR analysis

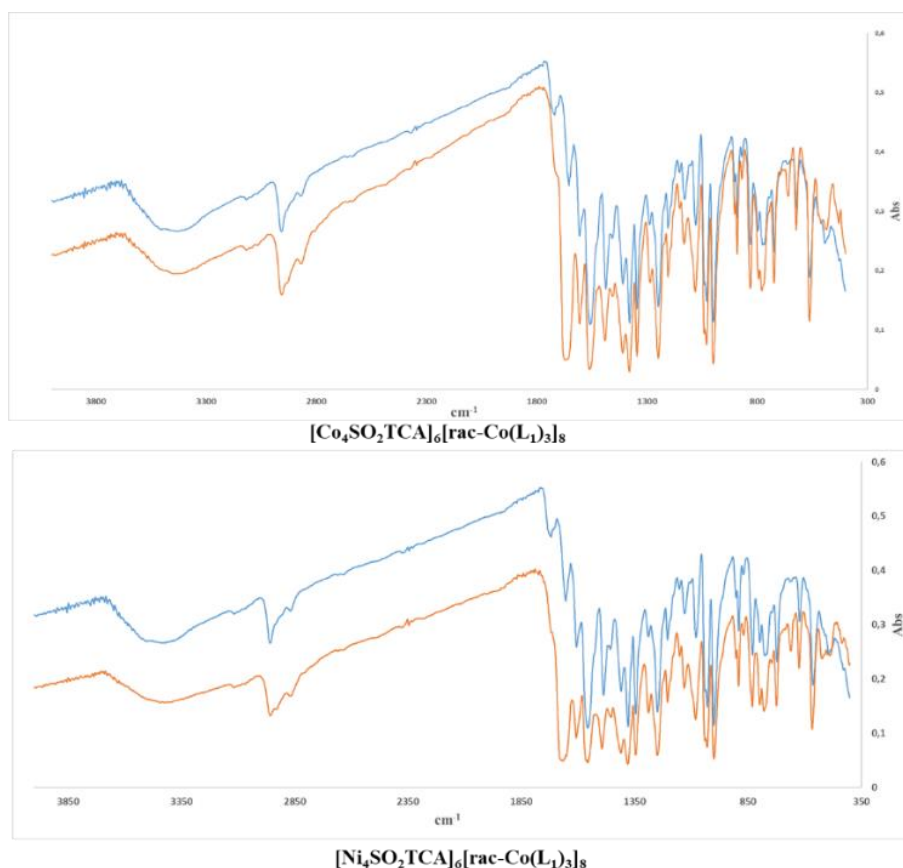


Figure 102 IR-spectra in KBr of freshly obtained and activated $[M_4SO_2TCA(\mu_4-OH_2)]_6[rac-Co(L_1)_3]_8$ ($M = Co^{II}, Ni^{II}$) (Blue lines – freshly obtained MOCs; orange lines - activated MOCs)

The spectra of the samples (freshly obtained and activated) were found to be relatively similar (Figure 102), despite changes of some peak's relative intensities, indicating for both activated compounds, the presence of all the components of $[M_4SO_2TCA(\mu_4-OH_2)]_6[rac-Co(L_1)_3]_8$ ($M = Co^{II}, Ni^{II}$) compounds.

III.1.3. TGA analysis

TGA analysis was performed for activated MOCs of formula $[M_4SO_2TCA(\mu_4-OH_2)]_6[rac-Co(L_1)_3]_8$ ($M = Co^{II}, Ni^{II}$) in order to estimate the completeness of the activation (Figure 103).

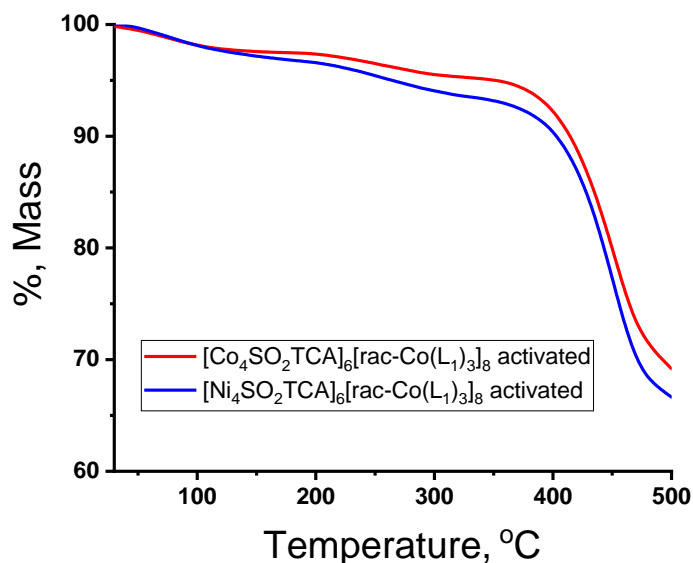


Figure 103 TGA traces for the activated MOCs $[M_4SO_2TCA(\mu_4-OH_2)]_6[rac-Co(L_1)_3]_8$ ($M = Co^{II}, Ni^{II}$)

The TGA analysis demonstrates that almost all the molecules of solvents were removed from the sample during the activation process. However, TGA curve exhibits a negligible number of volatile molecules still present in the samples (up to 5%). This fact could be explained by the adsorption of water from the air due to air exposure between the activation and TGA analysis (the samples are hygroscopic). This fact is in accordance with the TGA of the freshly prepared samples (see §IV.4. Chapter III).

After the activation gas adsorption experiments were conducted.

III.2. $N_{2(g)}$ adsorption and surface area investigation

These measurements have been performed in collaboration with the group of Pr. Fedin, A.V. Nikolaev Inorganic Chemistry Institute, Novosibirsk, Russia.

III.2.1. Measurements

Firstly, the $N_{2(g)}$ uptake of the activated samples of MOCs $[M_4SO_2TCA(\mu_4-OH_2)]_6[rac-Co(L_1)_3]_8$ ($M = Co^{II}, Ni^{II}$) was measured within the range of relative pressures from 10^{-6} to 0.995 P/P_0 at 77K (see details in experimental part). They were repeated two times with the same sample, without removing the sample from the apparatus and without additional activation. The results of these experiments are presented Figure 104.

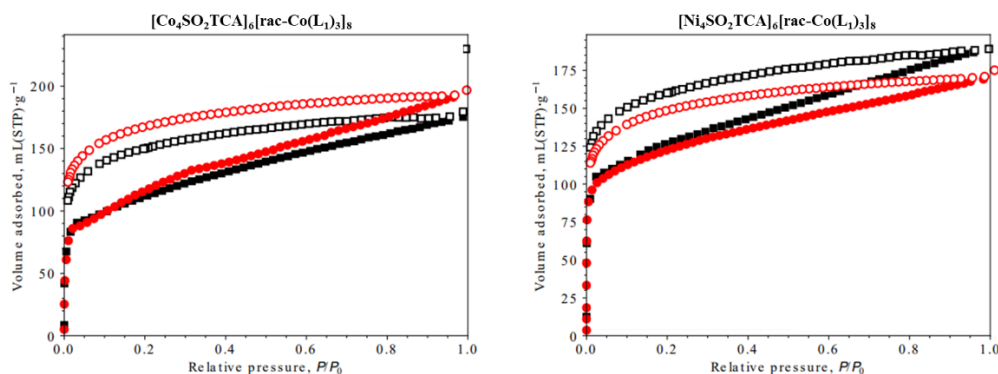


Figure 104 $N_{2(g)}$ adsorption-desorption isotherms at 77 K for $[M_4SO_2TCA(\mu_4-OH_2)]_6[rac-Co(L_1)_3]_8$ ($M = Co^{II}, Ni^{II}$) (filled symbols for adsorption, hollow ones for desorption; black symbols for pristine samples, red ones for the samples after the first cycle of $N_{2(g)}$ adsorption-desorption)

The $N_{2(g)}$ adsorption-desorption isotherms revealed a type I isotherms for both MOCs $[M_4SO_2TCA(\mu_4-OH_2)]_6[rac-Co(L_1)_3]_8$ ($M = Co^{II}, Ni^{II}$), indicating the behaviour of a microporous material. The obtained isotherms demonstrate an hysteresis (the amount of gas still adsorbed during desorption at a given pressure is more than the amount of gas adsorbed during adsorption at the same pressure) which is probably related to the effect of the external porosity of the MOCs.

The similar shape of the adsorption-desorption isotherms for the pristine samples and the samples after gas adsorption for both compounds $[M_4SO_2TCA(\mu_4-OH_2)]_6[rac-Co(L_1)_3]_8$ ($M = Co^{II}, Ni^{II}$) accounts for the stability of the obtained MOCs during adsorption-desorption processes. Small differences between adsorption-desorption isotherms of pristine samples and samples after one cycle of $N_{2(g)}$ adsorption-desorption can be explained by changing of the cage packing in the crystals during the first $N_{2(g)}$ adsorption-desorption cycle.

III.2.2. Analysis and comparison of the data

The obtained isotherms were used to estimate the specific surface area using different models (Langmuir and BET), the volume of pores and the volume of the adsorbed $N_{2(g)}$. These characteristic parameters along with the comparison with the triazine-based MOC $[Co_4SO_2TCA(\mu_4-OH_2)]_6[L_8]_8$ discussed in §II.2. of this chapter, and with the similar calixarene-based MOCs reported in the literature are presented in Table 21.

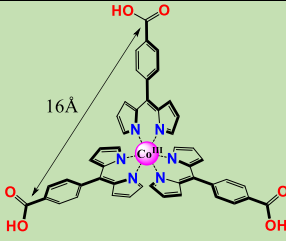
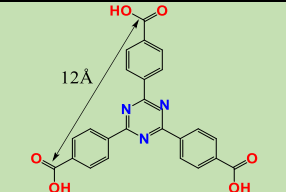
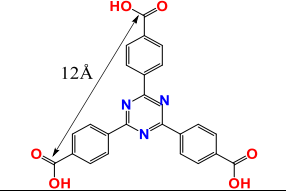
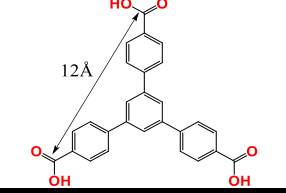
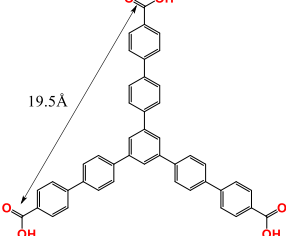
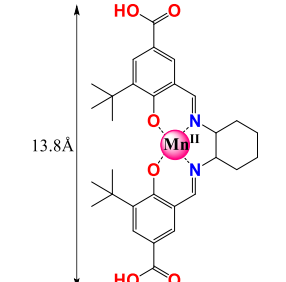
	Connector	Connector length	Cavity diameter (estimated from the crystal structure)	Observed N _{2(g)} BET SA m ² /g
[Co ₄ SO ₂ TCA(μ ₄ -OH ₂)] ₆ [rac-Co(L ₁) ₃] ₈ pristine		16 Å	19 Å	416.9
[Ni ₄ SO ₂ TCA(μ ₄ -OH ₂)] ₆ [rac-Co(L ₁) ₃] ₈ pristine				445.2
[Co ₄ SO ₂ TCA(μ ₄ -OH ₂)] ₆ [L ₈] ₈ pristine		12 Å	18 Å	742.6
(sc4a)Fe(tatb) (ref. ¹⁸⁷)		12 Å	18 Å	879
MOC CIAC-106 (ref. ²⁰⁷)		12 Å	18 Å	410
MOC CIAC-114 (ref. ²⁰⁷)		19.5 Å	27 Å	558
Mn ^{II} (salen)-based chiral MOC (ref. ⁴)		13.8 Å	18 Å	185.86 (CO ₂)

Table 21 Structure-adsorption properties relationships for activated [M₄SO₂TCA(μ₄-OH₂)]₆[rac-Co(L₁)₃]₈ (M = Co^{II}, Ni^{II}), [Co₄SO₂TCA(μ₄-OH₂)]₆[L₈]₈ and MOCs reported in the literature

According to Table 21, the obtained MOCs [M₄SO₂TCA(μ₄-OH₂)]₆[rac-Co(L₁)₃]₈ (M = Co^{II}, Ni^{II}) demonstrate moderate N_{2(g)} BET surface areas comparable to the ones reported in the literature for other octahedral calixarene-based cage like CIAC-106 and CIAC-114.²⁰⁷



BET surface areas of the obtained dipyrin-based MOCs are significantly larger than the one reported for the MOC based on Mn(II)salen metal-organic connector.⁴ This fact might be related with a better accessibility of the obtained MOCs internal cavities leading to better N_{2(g)} adsorption properties. Moreover, BET surface area is much larger (more than 1.5 times) for [Co₄SO₂TCA(μ₄-OH₂)]₆[L₈]₈ compare to [M₄SO₂TCA(μ₄-OH₂)]₆[rac-Co(L₁)₃]₈ (M = Co^{II}, Ni^{II}). Two factors account for these differences: (i) a better accessibility of the internal cavities of triazine-based MOCs due to a larger portal size compared to the one of tris(dipyrin) based MOCs (8Å and 6Å respectively) (see §II.3. and §V.2. of chapter III); (ii) a higher porosity (calculated by PLATON) for triazine-based MOCs (71.6%) compare to 67.7% for dipyrin-based MOCs (see §II.3. and §V.2 Chapter III).

III.2.3. Pore size estimation

For MOCs of formula [M₄SO₂TCA(μ₄-OH₂)]₆[rac-Co(L₁)₃]₈ (M = Co^{II}, Ni^{II}), the pores size distributions were estimated using QSDFT approach (Figure 105). QSDFT stands for "Quenched Solid Density Functional Theory" and is based on the principles of statistical mechanics and uses a mathematical model to relate the adsorption isotherm of a gas in a porous material to the pore size distribution of the material. In comparison with more classical DFT approach which only considers the interactions between the adsorbate molecules, QSDFT approach also takes into account the surface roughness and chemical heterogeneity.²¹²

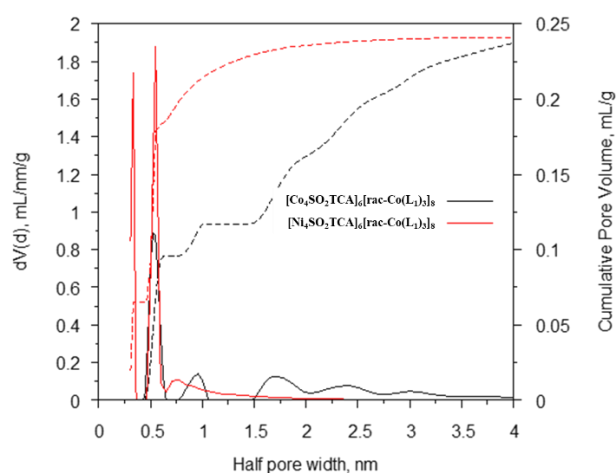


Figure 105 QSDFT calculated pore size distributions (solid lines) and cumulative pore volumes (dashed lines) for [M₄SO₂TCA(μ₄-OH₂)]₆[rac-Co(L₁)₃]₈ (M = Co^{II}, Ni^{II})

The pore size distributions demonstrated the presence of one type of narrow pores for [Co₄SO₂TCA(μ₄-OH₂)]₆[rac-Co(L₁)₃]₈ and two types of narrow pores for [Ni₄SO₂TCA(μ₄-OH₂)]₆[rac-Co(L₁)₃]₈.

For $[\text{Co}_4\text{SO}_2\text{TCA}(\mu_4\text{-OH}_2)]_6[\text{rac-Co}(\text{L}_1)_3]_8$, one type of narrow pores of width 10\AA may correspond with internal porosity of MOC. As it was discussed in §II.3. of Chapter III, we estimated that the internal cavity of this MOC has a diameter of *ca* samples 19\AA (XRD measurements). These different values obtained from the 2 methods might be explained by the fact that XRD method provides the crystallographic dimensions of the pores, while gas adsorption measurements provide the information on the accessible or effective pore size; additionally, gas adsorption measurements typically assume an idealized model of the porous material (slit), which may not accurately reflect the actual pore structure of the material. Other pores (width $> 10\text{\AA}$) are related with the external porosity, defects and dislocations in crystals leading to the mesostructuring of crystallites.

For $[\text{Ni}_4\text{SO}_2\text{TCA}(\mu_4\text{-OH}_2)]_6[\text{rac-Co}(\text{L}_1)_3]_8$, two types of narrow pores have been evidenced: (i) pores of width 10\AA which may correspond with internal porosity of MOC; (ii) the other pores with the width of 15\AA related with the external porosity. However, in comparison with $[\text{Co}_4\text{SO}_2\text{TCA}(\mu_4\text{-OH}_2)]_6[\text{rac-Co}(\text{L}_1)_3]_8$, $[\text{Ni}_4\text{SO}_2\text{TCA}(\mu_4\text{-OH}_2)]_6[\text{rac-Co}(\text{L}_1)_3]_8$ demonstrates much less mesostructuring of crystallites which might be related with the more stable cage packing in the unit cells of the crystals even after the activation process. In addition, pores of width 5\AA are observed, however, they are explained by anomalies during the measurements.

III.3. Adsorption of other small molecules

The adsorption properties of $[\text{M}_4\text{SO}_2\text{TCA}(\mu_4\text{-OH}_2)]_6[\text{rac-Co}(\text{L}_1)_3]_8$ ($\text{M} = \text{Co}^{\text{II}}, \text{Ni}^{\text{II}}$) were measured with 5 other different gases in order to investigate the affinity of such MOCs towards gases with different properties, sizes and shapes. Thus, we focused on the adsorption of $\text{CO}_{2(\text{g})}$, $\text{CH}_{4(\text{g})}$, $\text{C}_2\text{H}_{2(\text{g})}$, $\text{C}_2\text{H}_{4(\text{g})}$ and $\text{C}_2\text{H}_{6(\text{g})}$ molecules. As it was mentioned in §I.2. of this chapter, the adsorption of these gases is an important issue due to their significant role in industry and ecology. In addition, the estimation of the selective adsorption behaviour of gas mixtures by both MOCs has been initiated.

III.3.1. Isotherm measurements

Isotherms for these 5 gaseous molecules were measured at two different temperatures (273K and 298K , see explanation below §III.3.2. of this chapter) within the range of pressures from 1 to 800 torr. The results of these adsorption experiments are presented on Figure 106.

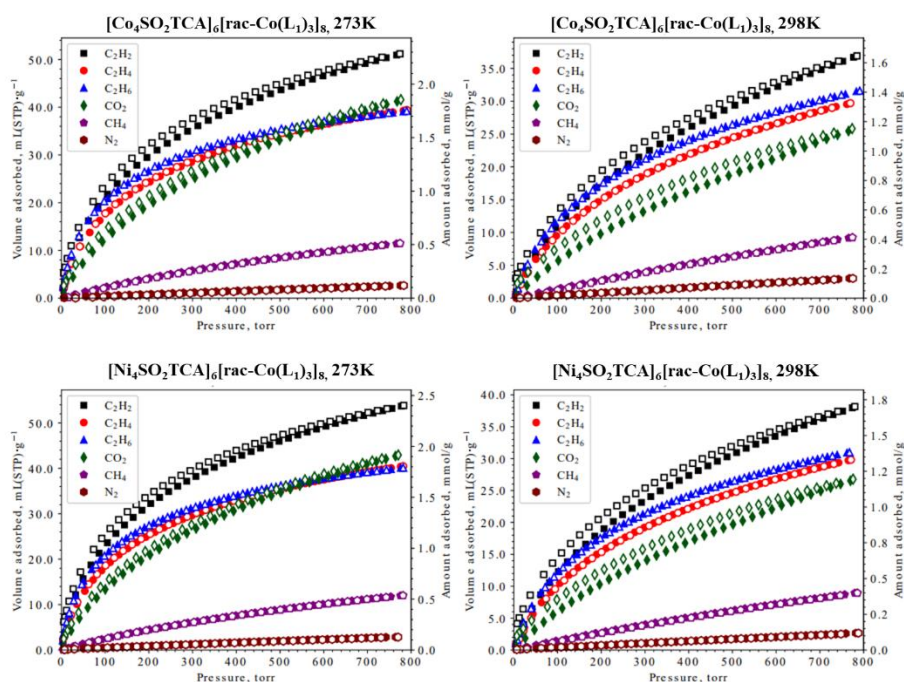


Figure 106 Gas ($CO_{2(g)}$, $CH_{4(g)}$, $C_2H_{2(g)}$, $C_2H_{4(g)}$ and $C_2H_{6(g)}$) adsorption-desorption isotherms for $[M_4SO_2TCA(\mu_4-OH_2)]_6[rac-Co(L_1)_3]_8$ ($M = Co^{II}$, Ni^{II}) (filled symbols for adsorption, hollow ones for desorption)

For all studied gases, the saturation in the experimental range was not observed. Both MOCs of formula $[M_4SO_2TCA(\mu_4-OH_2)]_6[rac-Co(L_1)_3]_8$ ($M = Co^{II}$, Ni^{II}) demonstrated very different affinity towards the different gases - the measurements clearly shown significant differences in the amount of adsorbed gases (lower values for N_2 , higher for C_2H_2).

The amount of gases uptakes (using different units) at 800 torr are summarized Table 22.

Gas	273K			298K		
	ml/g	mmol/g	wt., %	ml/g	mmol/g	wt., %
$[Co_4SO_2TCA(\mu_4-OH_2)]_6[rac-Co(L_1)_3]_8$						
C_2H_2	50.5	2.25	5.5	36.0	1.61	4.0
C_2H_4	38.8	1.73	4.6	29.4	1.31	3.5
C_2H_6	38.8	1.73	4.9	31.0	1.38	4.0
CO_2	40.8	1.92	7.4	25.1	1.12	4.7
CH_4	11.3	0.50	0.8	9.0	0.40	0.6
N_2	3.4	0.15	0.5	2.9	0.13	0.4
$[Ni_4SO_2TCA(\mu_4-OH_2)]_6[rac-Co(L_1)_3]_8$						
C_2H_2	53.1	2.37	5.8	37.4	1.67	4.2
C_2H_4	40.0	1.79	4.8	29.5	1.32	3.6
C_2H_6	39.8	1.77	5.1	30.8	1.37	4.0
CO_2	42.3	1.89	7.7	26.1	1.16	4.9
CH_4	11.7	0.52	0.8	8.6	0.39	0.6
N_2	2.8	0.13	0.4	2.5	0.11	0.3

Table 22 Gas ($N_{2(g)}$, $CO_{2(g)}$, $CH_{4(g)}$, $C_2H_{2(g)}$, $C_2H_{4(g)}$ and $C_2H_{6(g)}$) uptakes for $[M_4SO_2TCA(\mu_4-OH_2)]_6[rac-Co(L_1)_3]_8$ ($M = Co^{II}$, Ni^{II})

Both MOCs of formula $[M_4SO_2TCA(\mu_4-OH_2)]_6[rac-Co(L_1)_3]_8$ ($M = Co^{II}, Ni^{II}$) demonstrated almost the same behaviour towards studied gases, with gas uptakes decreasing with increasing of temperature (this is a standard observation in gas adsorption experiments due to the exothermic effect of gas adsorption). The observed differences in different gases uptakes for both MOCs can be explained by the polarizability of the gas molecules, related to the interactions towards the MOCs. The molecules with higher polarizability demonstrated better affinity towards dipyrin-based MOCs, which corresponds to stronger interactions with the MOCs during the physisorption phenomenon. The best affinity is found to be towards C_2H_2 (the molecule with the highest polarizability) whereas the worst affinity corresponds to $N_{2(g)}$ (the molecule with the worst polarizability).

III.3.2. Calculations of thermodynamic parameters

The adsorption-desorption isotherms are usually measured at two temperatures (in this work we measured at 273K and 298K) in order to calculate the zero-coverage heats of adsorption, Q°_{st} (energy released during adsorption of one mole of gas onto the surface of a material at constant temperature at the initial stages of the adsorption process) (see calculation with the use of virial equation in annexes §II.1. and §II.3.). This can provide a valuable information about the nature of the interactions between the gas molecules and the host compound (MOCs), as well as the effect of temperature on this interaction. Additionally, the zero-coverage heats of adsorption allow to more accurately estimate the affinity and selectivity of the host (MOCs) towards adsorbing gases.

The calculated values of zero-coverage heats of adsorption are summarized Table 23.

	$Q^{\circ}_{st}([Co_4SO_2TCA(\mu_4-OH_2)]_6[rac-Co(L_1)_3]_8)$ kJ/mol	$Q^{\circ}_{st}([Ni_4SO_2TCA(\mu_4-OH_2)]_6[rac-Co(L_1)_3]_8)$ kJ/mol
N_2	7.0	7.2
CH_4	11.7	14.8
CO_2	28.0	29.1
C_2H_6	27.4	29.4
C_2H_4	29.4	31.4
C_2H_2	29.4	31.4

Table 23 The values of zero-coverage heats of adsorption of different gases for $[M_4SO_2TCA(\mu_4-OH_2)]_6[rac-Co(L_1)_3]_8$ ($M = Co^{II}, Ni^{II}$)

$[M_4SO_2TCA(\mu_4-OH_2)]_6[rac-Co(L_1)_3]_8$ ($M = Co^{II}, Ni^{II}$) demonstrated similar behaviour concerning the zero-coverage heats of adsorption: they exhibit high values of zero-coverage heats of adsorption towards CO_2 , C_2H_2 , C_2H_4 and C_2H_6 and small values towards N_2 and CH_4 as observed on the corresponding isotherms.

Based on these observations, dipyrin-based MOCs of formula $[M_4SO_2TCA(\mu_4-OH_2)]_6[rac-Co(L_1)_3]_8$ ($M = Co^{II}, Ni^{II}$) appeared to demonstrate selective gas adsorption behaviour.



This behaviour can be used in order to estimate the selectivity coefficients towards different gas mixtures, from a modelling point of view.

III.4. Estimation of gas adsorption selectivity

The differences in the amounts of adsorbed gases allow in principle to estimate the gas adsorption selectivity towards different gas mixtures. In order to do that we applied several computational methods that will be discussed in detail in this section and also in annexes §II.

III.4.1. Calculations and modelling

Three different methods were applied in order to estimate the selectivity of gas adsorption mixtures based on the individual gas adsorption-desorption isotherms:

- Calculation of the ratio V_1/V_2 , where V_1 is the volume of gas 1 adsorbed at 800 torr by the MOC; V_2 is the volume of gas 2 adsorbed at 800 torr by the MOC
- Calculation of the ratio K_{H1}/K_{H2} , where K_{H1} is the Henry constant for gas 1, obtained from the virial coefficients of virial equation that fits adsorption-desorption isotherm; K_{H2} is the Henry constant for gas 2, obtained from the virial coefficients of virial equation that fits adsorption-desorption isotherm. In gas adsorption, Henry's constant is used to describe the equilibrium of gas uptake by a solid material at low pressures, where the amount of gas adsorbed is directly proportional to the partial pressure of the gas in contact with the solid (see calculations using virial equations in annexes §II.2.)
- Modelling with the Ideal Adsorbed Solution Theory (IAST).²¹³ IAST assumes that the adsorption of each gas component in a mixture is independent of the other components, and that the adsorbed gases do not interact with each other. These assumptions allow IAST to “predict” the adsorption behaviour of a mixture of gases based solely on the adsorption isotherms of the individual components, without requiring any additional experimental data on the mixture itself. In this work, we applied IAST method for calculation of selective gas adsorption for equimolar 1/1 gases mixtures (see detailed calculations in annexes §II.5).

The results concerning selective gas adsorption are presented in Table 24 .

Equimolar Mixture	273K			298K		
	Selectivity factor			Selectivity factor		
	V ₁ /V ₂	K _{H1} / K _{H2}	IAST	V ₁ /V ₂	K _{H1} / K _{H2}	IAST
[Co₄SO₂TCA(μ₄-OH₂)₆[rac-Co(L₁)₃]₈						
C ₂ H ₂ /C ₂ H ₄	1.3	1.1	1.8	1.2	1.0	1.3
C ₂ H ₂ /CO ₂	1.2	2.7	5.7	1.4	2.6	5.4
C ₂ H ₂ /CH ₄	4.5	21.6	18.3	4.0	11.3	11.9
C ₂ H ₆ /CH ₄	3.4	32.4	18.7	3.4	17.4	13.8
CO ₂ /CH ₄	3.6	7.9	8.9	2.8	4.3	2.7
CO ₂ /N ₂	12.0	31.1	19.3	8.7	14.7	12.5
[Ni₄SO₂TCA(μ₄-OH₂)₆[rac-Co(L₁)₃]₈						
C ₂ H ₂ /C ₂ H ₄	1.3	1.2	2.0	1.3	1.1	1.5
C ₂ H ₂ /CO ₂	1.3	2.9	6.1	1.4	2.7	5.7
C ₂ H ₂ /CH ₄	4.5	21.7	19.5	4.3	11.9	12.8
C ₂ H ₆ /CH ₄	3.4	30.0	18.5	3.6	16.5	13.6
CO ₂ /CH ₄	3.6	7.5	9.4	3.0	4.4	2.8
CO ₂ /N ₂	15.1	33.0	22.5	10.4	14.8	5.7

Table 24 Selectivity factors calculated for [M₄SO₂TCA(μ₄-OH₂)₆[rac-Co(L₁)₃]₈ (M = Co^{II}, Ni^{II}) for different equimolar gas mixtures

Despite the fact that all three methods demonstrated similar results, in this work we mostly relied on the factors calculated with the IAST model, allowing to more accurately compare the results with the literature data. However, IAST has limitations and they must be discussed in order to estimate the accuracy of the obtained data. One limitation of IAST is that it assumes that gas molecules adsorb independently and do not interact with each other. In the present case, the analysed gases do not have a tendency to react with each other, as a result, the deviations from this IAST limitation are not expected.

Another limitation of IAST is that it assumes that the adsorbent surface is uniform and homogeneous. However, according to the pore size distribution calculated by QSDFT approach (see §III.2.3. of this chapter), the obtained MOCs of formula [M₄SO₂TCA(μ₄-OH₂)₆[rac-Co(L₁)₃]₈ (M = Co^{II}, Ni^{II}) demonstrate highly homogeneous surface. As a result, the deviations from this IAST limitation are expected to be minor.

According to the analysis provided in the Table 24, the highest IAST selectivity was demonstrated for the binary gas mixtures of light hydrocarbons C₂H₆/CH₄ and C₂H₂/CH₄. It is worth mentioning that good IAST selectivity was also observed for C₂H₂/CO₂ mixture which is highly difficult to separate due to the almost the same kinetic diameter of these gases (3.3Å for both gases). Additionally, high IAST selectivity was observed for CO₂/CH₄ and CO₂/N₂ gas mixtures.

Concerning the effect of the temperature, the IAST selectivity of gas adsorption decreases with the increase of the temperature which appears reasonable because the physical adsorption is



usually an exothermic process. The second reason is a competitive adsorption: at high temperatures, the thermal energy of gas molecules increases, leading to a higher mobility. This can lead to lower IAST selectivity as different gas molecules compete for the same adsorption sites, reducing the IAST selectivity towards a specific gas.

III.4.2. Comparison with literature data

It is important to compare the obtained calculated values of IAST selectivity with the ones reported for known systems.

Thus, we compared the experimental C₂H₆ adsorption capacity and the calculated IAST selectivity towards C₂H₆/CH₄ equimolar binary mixture to some well-known porous MOFs and MOCs presenting selective gas adsorption properties, because this mixture is the most common mixture for investigation of selective gas adsorption properties of porous materials (Table 25). The formulas of μ₄-OH₂ are omitted for clarity.

Material	T, K	C ₂ H ₆ uptake, mmol/g	C ₂ H ₆ /CH ₄ IAST selectivity	BET surface area (N _{2(g)} , 77K) m ² /g
[Co ₄ SO ₂ TCA] ₆ [rac-Co(L ₁) ₃] ₈	273	1.73	18.7	417
	298	1.38	13.8	
[Ni ₄ SO ₂ TCA] ₆ [rac-Co(L ₁) ₃] ₈	273	1.77	18.5	445
	298	1.37	13.6	
Ni(tmbdc)(dabco) _{0.5} (ref. ²¹⁴)	298	5.81	29.0	940
Cu-MOF (ref. ²⁰⁹)	298	3.22	9.3	865
MFM-202a (ref. ²¹⁵)	293	4.21	10.0	2220
UTSA-35A (ref. ²¹⁶)	296	2.43	15.0	743
FIR-7a-ht (ref. ²¹⁰)	298	4.06	14.6	1366
JLU-Liu45 (ref. ²¹⁷)	298	3.78	20.1	9781
Zr-SDBA (ref. ¹⁰)	298	2.08	15.0	739
UPC-33 (ref. ²¹⁸)	273	1.56	6.64	934
FJI-H21 (ref. ⁹)	298	3.45	17.1	1583
UPC-100-In (ref. ²¹⁹)	298	5.32	17.9	1078
LIFM-26 (ref. ²²⁰)	273	4.6	11.0	1513
MOC LSHU01' (ref. ¹⁰⁰)	295	2.49	20.0	803
MOC CIAC-115 (ref. ⁹⁴)	298	1.1	8.3	646

Table 25 Comparison of C₂H₆ experimental adsorption capacity and estimated IAST selectivity towards mixture C₂H₆/CH₄ of the studied MOCs to some reported MOFs and MOCs

According to Table 25, excellent IAST selective gas adsorption properties are observed for MOCs of formula [M₄SO₂TCA(μ₄-OH₂)₆][rac-Co(L₁)₃]₈ (M = Co^{II}, Ni^{II}), which are superior to the ones reported for many MOFs. Only a few reported MOFs demonstrated higher estimated IAST gas adsorption selectivity.

As it was mentioned in §I.1. of this chapter, to the best of our knowledge there are only two reported MOCs for which IAST selective gas adsorption was calculated. Our MOCs of

formula $[\text{M}_4\text{SO}_2\text{TCA}(\mu_4\text{-OH}_2)]_6[\text{rac-Co}(\text{L}_1)_3]_8$ ($\text{M} = \text{Co}^{\text{II}}, \text{Ni}^{\text{II}}$) are superior to one of them (CIAC-115)⁹⁴ and slightly inferior to another one (LSHU01').¹⁰⁰

IV. Conclusion

In this work, adsorption properties of some synthesized octahedral calixarene-based MOCs were successfully investigated. The adsorption properties of two dipyrin-based MOCs of formula $[\text{M}_4\text{SO}_2\text{TCA}(\mu_4\text{-OH}_2)]_6[\text{rac-Co}(\text{L}_1)_3]_8$ ($\text{M} = \text{Co}^{\text{II}}, \text{Ni}^{\text{II}}$) and a triazine-based MOC of $[\text{Co}_4\text{SO}_2\text{TCA}(\mu_4\text{-OH}_2)]_6[\text{L}_8]_8$ were investigated in depth. All the studied compounds are porous and present a high surface area.

The triazine-based MOC $[\text{Co}_4\text{SO}_2\text{TCA}(\mu_4\text{-OH}_2)]_6[\text{L}_8]_8$ demonstrated a high porosity and significant $\text{N}_{2(\text{g})}$ adsorption capacity with pore size distribution in the interval 12-40 Å with a distinguishable peak at 15 Å corresponding with internal cavity of the MOC observed using XRD measurements.

The investigation of dipyrin-based MOCs of formula $[\text{M}_4\text{SO}_2\text{TCA}(\mu_4\text{-OH}_2)]_6[\text{rac-Co}(\text{L}_1)_3]_8$ ($\text{M} = \text{Co}^{\text{II}}, \text{Ni}^{\text{II}}$) revealed moderate porosity and lower surface areas, but in accordance with the ones reported for calixarene-based MOCs. The pore size distribution revealed the monomodal distribution and formation of microporous materials with the distinguished pore size approximately 10 Å which is in good agreement with the crystalline structure discussed in the previous **Chapter III**. These MOCs also demonstrate different affinity towards different small gases (CO_2 , CH_4 , C_2H_2 , C_2H_4 and C_2H_6). Furthermore, it was possible to estimate the selectivity of gas mixtures adsorption for $[\text{M}_4\text{SO}_2\text{TCA}(\mu_4\text{-OH}_2)]_6[\text{rac-Co}(\text{L}_1)_3]_8$ ($\text{M} = \text{Co}^{\text{II}}, \text{Ni}^{\text{II}}$), using the IAST model. The highest selectivity was observed towards $\text{C}_2\text{H}_6/\text{CH}_4$ and $\text{C}_2\text{H}_2/\text{CH}_4$ gas mixtures, which are important for natural gas upgrade. Additionally, high calculated IAST gas selectivity was observed towards CO_2/CH_4 and CO_2/N_2 gas mixtures which might be used in the design for the flue gas separation systems.

In conclusion, the presented compounds hold a great potential for further studies due to underexplored adsorption properties of other members of the obtained calixarene-based MOCs discussed in **Chapter II**.

General conclusion

I. Results of the work

This work is devoted to the synthesis of a new family of calixarene-based MOCs. We focused on the formation of face-panelled and edge-panelled octahedral calixarene-based MOCs using linear bidentate and triangular tridentate metal-organic and organic connectors.

A total of 18 different (nature, geometry and charge) connectors were synthesized for the obtention of new calixarene-based MOCs: among them 14 metal-organic and 4 purely organic connectors; 12 triangular tridentate and 6 linear bidentate connectors; 4 ionic and 14 neutral connectors.

All of the obtained connectors were used for the formation of MOCs as single-crystals for their structural studies, combined with *p-tert*-butylsulfonylcalix[4]arene ($\text{H}_4\text{SO}_2\text{TCA}$) and different metal ions (M^{II}). That resulted in 180 types of crystallizations performed during this work. The tricarboxylate connectors leded for the formation of calixarene-based MOCs as single-crystals are: racemic tris(dipyrrin) connectors **rac-M(HL₁)₃** ($\text{M} = \text{Co}^{\text{III}}, \text{Fe}^{\text{III}}, \text{Rh}^{\text{III}}$); chiral tris(dipyrrin) connectors **Λ -Co(HL₁)₃** **Δ -Co(HL₁)₃**; and triazine connector **H₃L₈**. These crystals were analysed, and the structures were solved which revealed the formation of 12 new large octahedral calixarene-based MOCs:

- 6 MOCs based on racemic tris(dipyrrin) connectors of formula **$[\text{M}_4\text{SO}_2\text{TCA}]_6[\text{rac-M}'(\text{L}_1)_3]_8$** ($\text{M} = \text{Co}^{\text{II}}, \text{Ni}^{\text{II}}$; $\text{M}' = \text{Co}^{\text{III}}, \text{Fe}^{\text{III}}, \text{Rh}^{\text{III}}$)
- 4 chiral MOCs based on chiral tris(dipyrrin) connectors of formula **$[\text{M}_4\text{SO}_2\text{TCA}(\mu_4\text{-OH}_2)]_6[\Delta, \Lambda\text{-Co}(\text{L}_1)_3]_8$** ($\text{M} = \text{Co}^{\text{II}}, \text{Ni}^{\text{II}}$)
- 2 MOCs based on purely organic connector **H₃L₈**: **$[\text{Co}_4\text{SO}_2\text{TCA}]_6[\text{L}_8]_8$** , **$[\text{Ni}_4\text{SO}_2\text{TCA}]_6[\text{L}_8]_8$** ,

The structures of these calixarene-based MOCs were studied in details first by single-crystals XRD, then confirmed by other techniques in solution and in the solid state. The formed MOCs are face-panelled octahedral cages consisting of 6 “shuttlecock-like” calixarene units of formula **$[\text{M}_4\text{SO}_2\text{TCA}(\mu_4\text{-OH}_2)]^{4+}$** in the vertices and 8 connectors covering the faces of the octahedra.

The obtained compounds appeared to be porous and it was calculated by PLATON software that these cages present a porosity about 70%, and consequently, gas adsorption properties of some of these cages were investigated in details.

$\text{N}_{2(\text{g})}$ and $\text{CO}_{2(\text{g})}$ adsorption was investigated for triazine-based MOC of formula **$[\text{Co}_4\text{SO}_2\text{TCA}]_6[\text{L}_8]_8$** .



$\text{N}_{2(\text{g})}$, $\text{CO}_{2(\text{g})}$, $\text{CH}_{4(\text{g})}$, $\text{C}_2\text{H}_2(\text{g})$, $\text{C}_2\text{H}_4(\text{g})$ and $\text{C}_2\text{H}_6(\text{g})$ adsorption was investigated for dipyrroin-based MOCs of formula $[\text{Co}_4\text{SO}_2\text{TCA}]_6[\text{rac-Co}(\text{L}_1)_3]_8$, $[\text{Ni}_4\text{SO}_2\text{TCA}]_6[\text{rac-Co}(\text{L}_1)_3]_8$ and different affinity towards these gases was observed that allowed us to estimate the gas adsorption selectivity towards different equimolar mixtures of these gases using IAST modelling

II. Perspectives for this work

II.1. Improvement of the synthesis for the formation of MOCs

The presented results deserve further investigation. As demonstrated in **Chapter II**, the synthesis of 18 compounds was presented that can serve as connectors for the synthesis of new calixarene-based MOCs. However, only 6 of them led to the desired products, obtained in the crystalline form under the discussed synthetic conditions. In other cases, a precipitate unsuitable for XRD analysis was obtained, however, an in-depth analysis is required for such precipitated compounds. Nevertheless, there is no direct evidence that the remaining 12 connectors cannot fundamentally form the desired MOCs. Perhaps, suitable synthetic conditions can be selected in order to obtain the desired structures in the crystalline form. For instance, the temperature conditions of solvothermal technique can be changed. In this study, solvothermal synthesis was performed at 80°C , but it can be carried out at higher or lower temperatures. Moreover, the use of more diluted solutions is possible, which may slow down the reaction rate and result in the formation of crystals. Additionally, it is possible to change the synthetic conditions in the liquid-liquid diffusion technique. For instance, other combinations of solvents (DMSO/Ethanol, DMA/Ethanol) that are more suitable for the formation of stable MOCs solvates, and therefore crystalline structures, can be used. In addition, other bases (diisopropylamine for example) can be used for the deprotonation of calixarenes and connectors. In the case of connectors with an ionic nature, other counterions (SO_4^{2-} , BF_4^-) can also be used to obtain the desired structures.

Another approach is to select conditions under which non-crystalline precipitates dissolve (DMSO, CH_2Cl_2 , acetonitrile in the ultrasonic bath) and then perform recrystallization using other methods, such as slow evaporation or gas diffusion with the use of various volatile solvents (for example, diethyl ether). Thus, there are many alternative techniques that have to be investigated in order to obtain new calixarene-based MOCs in the single-crystals form using the reported connectors.

Despite the fact that, the structure of the obtained MOCs was characterised by various techniques and gas adsorption properties of some of them were investigated in details, there are still many MOCs properties (both in solid state and in solution) that were not studied. Some of these properties are discussed below.

II.2. Further investigation of gas adsorption properties of the reported MOCs

As demonstrated in **Chapter IV**, only three of the obtained crystalline calixarene-based MOCs were investigated for gas adsorption. Therefore, further investigations in this area are required to fully understand the adsorption properties of the other obtained MOCs and their influence on the gas adsorption properties. Many parameters can be studied, for example, nature of the metal ion and length of the used connector.

MOCs with the formula $[\text{M}_4\text{SO}_2\text{TCA}(\mu_4\text{-OH}_2)]_6[\text{rac-Co}(\text{L}_1)_3]_8$ ($\text{M} = \text{Co}^{\text{II}}, \text{Ni}^{\text{II}}$) demonstrated good IAST predicted selectivity towards various equimolar gas mixtures ($\text{C}_2\text{H}_2/\text{C}_2\text{H}_4$; $\text{C}_2\text{H}_2/\text{CO}_2$; $\text{C}_2\text{H}_2/\text{CH}_4$; $\text{C}_2\text{H}_6/\text{CH}_4$; CO_2/CH_4 ; CO_2/N_2) (see details in **§III.4. Chapter IV**). However, experimental confirmation of these data is necessary to determine the potential application of these MOCs in natural gas upgrade and flue gas separation systems. Furthermore, not all the obtained crystalline MOCs were investigated for selective gas adsorption. Thus, additional experiments in gas adsorption, selective gas adsorption and selective gas separation are required for the reported MOCs.

II.3. Investigation of catalytic properties

Since MOCs of formula $[\text{M}_4\text{SO}_2\text{TCA}(\mu_4\text{-OH}_2)]_6[\text{rac-Co}(\text{L}_1)_3]_8$ ($\text{M} = \text{Co}^{\text{II}}, \text{Ni}^{\text{II}}$) exhibit remarkable gas uptake properties up to 2.37 mmol/g towards small gaseous molecules (CO_2 , CH_4 , C_2H_2 , C_2H_4 and C_2H_6) (see details in **§III.3. Chapter IV**) they can lead to the design of highly active catalytic systems for chemical alterations of these small molecules, when combined with the enclosed cavity of MOCs. For instance, the catalytic hydrogenation or polymerization of unsaturated hydrocarbons (C_2H_2 , C_2H_4), as well as the capture and oxidation of methane, can be studied.

Moreover, as discussed in **§III.5.4. of Chapter I**, metallic nanoparticles can be stabilized using the internal cavity of MOCs, enhancing their catalytic activity. Thus, these properties require further investigations.

MOCs of formula $[\text{M}_4\text{SO}_2\text{TCA}(\mu_4\text{-OH}_2)]_6[\text{rac-Rh}(\text{L}_1)_3]_8$ ($\text{M} = \text{Co}^{\text{II}}, \text{Ni}^{\text{II}}$) are highly interesting for the design of catalytic systems with an exceptional activity, due to the presence of Rh(III). Metal-organic complexes of Rh^{III} often possess photoactive properties (see details in **§II.1. of Chapter II**), so the obtained calixarene-based MOCs $[\text{M}_4\text{SO}_2\text{TCA}(\mu_4\text{-OH}_2)]_6[\text{rac-Rh}(\text{L}_1)_3]_8$ ($\text{M} = \text{Co}^{\text{II}}, \text{Ni}^{\text{II}}$) may have photocatalytic potential. Currently, we intend to investigate the heterogeneous catalytic properties of these MOCs for reactions of CO_2 reduction, as well as, hydrogen evolution reactions and water oxidation.



II.4. Investigation of the molecular recognition properties

In this work, many properties of the obtained MOCs related to their internal cavity and discrete structure were not investigated, except for their gas adsorption properties. Therefore, there are significant perspectives for exploring them. As discussed in §III.5. of **Chapter I**, many calixarene-based MOCs reported in the literature exhibit unique properties related to selective binding, recognition of certain substances, and other host-guest interactions. For example, the binding of the obtained calixarene-based MOCs with biologically active substances in solution can be studied to design targeted drug delivery systems. Additionally, the adsorption of various dyes (both in solution and in the solid state) by the obtained calixarene-based MOCs can lead to sensor and imaging systems. Initial experiments performed using methylene blue and MOCs with the formula $[\text{M}_4\text{SO}_2\text{TCA}(\mu_4\text{-OH}_2)]_6[\text{rac-Co}(\text{L}_1)_3]_8$ ($\text{M} = \text{Co}^{\text{II}}, \text{Ni}^{\text{II}}$), using UV-titration methods and observing the adsorption of methylene blue from an aqueous solution by MOCs in the solid state, demonstrated the potential for further investigations in this area.

Chiral calixarene-based MOCs with the formula $[\text{M}_4\text{SO}_2\text{TCA}(\mu_4\text{-OH}_2)]_6[\Lambda\text{-Co}(\text{L}_1)_3]_8$ and $[\text{M}_4\text{SO}_2\text{TCA}(\mu_4\text{-OH}_2)]_6[\Delta\text{-Co}(\text{L}_1)_3]_8$ ($\text{M} = \text{Co}^{\text{II}}, \text{Ni}^{\text{II}}$) are also of great interest for studying their chiral properties. We can analyse their chiral properties in the solid state through vapor adsorption of volatile chiral compounds, such as enantiomers of 2-butanol. The experiments in this direction have been already initiated in collaboration with Pr. Beata Nowicka (Jagiellonian University, Krakow, Poland) Furthermore, we can investigate the selective adsorption for MOCs in the solid state of certain enantiomers from racemic solutions. These calixarene-based MOCs also present a possibility to investigate their chiral properties in solutions by studying their selective recognition of enantiomers or the separation of racemic mixtures. Preliminary studies have been performed, but under the selected conditions, these chiral MOCs did not demonstrate chiral properties. Thus, more extensive research is required under carefully selected conditions.

The MOCs based on the organic connector H_3L_8 with the formula $[\text{Co}_4\text{SO}_2\text{TCA}(\mu_4\text{-OH}_2)]_6[\text{L}_8]_8$ have a potential for further investigation of anion- π recognition properties due to the significant number of triazine rings with positively charged areas in their structure (see §VII.1. of **Chapter II**). Because of the large number of triazine rings and the enclosed structure of the cavity, these MOCs might demonstrate unique anion- π recognition properties.

II.5. Other properties

In addition, properties of the obtained calixarene-based MOCs related with the structure and properties of the used connectors also hold a great perspective for the investigation.

For instance, MOCs of formula $[\text{M}_4\text{SO}_2\text{TCA}(\mu_4\text{-OH}_2)]_6[\text{rac-Fe}(\text{L}_1)_3]_8$ ($\text{M} = \text{Co}^{\text{II}}, \text{Ni}^{\text{II}}$) are expected to demonstrate electrochemical properties due to presence of Fe^{III} ions in their structure.

According to the aforesaid there are many properties and applications of the obtained MOCs that can be further studied. As a result, this work demonstrates a great potential for further investigations that can significantly develop the field of octahedral calixarene-based MOCs, which is rather underexplored, and, in general, field of supramolecular chemistry.

To the best of our knowledge, there is only one octahedral calixarene MOC based on metal-organic connector, except 10 new MOCs reported in this work. As a result, this work significantly contributes to the family of MOCs based on metal-organic connectors. Hopefully, this work will inspire other projects to contribute in this field and investigate the unique properties of calixarene-based MOCs that present in their structure metal-organic connectors.

Experimental part

- Rac-Co(HL₁)₃** Tris[5-(4-Carboxyphenyl)-4,6-dipyrinato] Co(III)
- Λ-Co(HL₁)₃** Λ-Tris[5-(4-Carboxyphenyl)-4,6-dipyrinato] Co(III)
- Δ-Co(HL₁)₃** Δ-Tris[5-(4-Carboxyphenyl)-4,6-dipyrinato] Co(III)
- Rac-Fe(HL₁)₃** Tris[5-(4-Carboxyphenyl)-4,6-dipyrinato] Fe(III)
- Rac-Rh(HL₁)₃** Tris[5-(4-Carboxyphenyl)-4,6-dipyrinato] Rh(III)
- Pd(HL₁)₂** Bis[5-(4-Carboxyphenyl)-4,6-dipyrinato] Pd(II)
- Rac-Co(HL₂)₃** Tris[5-(4-(4-Carboxyphenyl)phenyl)-4,6-dipyrinato] Co(III)
- Ni(H₂L₃)** Ni-BisdpmCOOH
- [Rac-Fe(HL₄)₃][PF₆]₂** Tris[2-(4-Carboxyphenyl)imidazo[4,5-f][1,10]phenanthroline] Fe(II)
hexafluorophosphate
- [Fe(HL₅)₂][PF₆]₂** Bis[4'-(4-Carboxyphenyl)-2,2':6',2''-terpyridine] Fe(II)
hexafluorophosphate
- [Co(HL₅)₂][PF₆]₂** Bis[4'-(4-Carboxyphenyl)-2,2':6',2''-terpyridine] Co(II)
hexafluorophosphate
- [Ru(HL₅)₂][PF₆]₂** Bis[4'-(4-Carboxyphenyl)-2,2':6',2''-terpyridine] Ru(II)
hexafluorophosphate
- Ni(H₂L₆)** [5,15-bis(4-carboxyphenyl)-10,20-diphenylporphyrinato] Ni(II)
- Co(H₃L₇)** [5,10,15-Tris(4-carboxyphenyl)corrolato] Co(III)
- H₃L₈** 4,4',4''-(1,3,5-triazine-2,4,6-triyl)tribenzoic acid
- H₃L₉** 2,2',2''-((1,3,5-triazine-2,4,6-triyl)tris(azanediyl))triacetic acid
- H₃L₁₀** 4,4',4''-(((1,3,5-triazine-2,4,6-triyl)tris(azanediyl))tris(methylene))tribenzoic acid
- H₃L₁₁** 4,4',4''-((2,4,6-trifluorobenzene-1,3,5-triyl)tris(ethyne-2,1-diyl))tribenzoic acid

Table 26 List of connectors

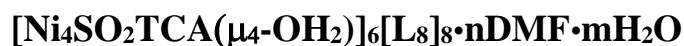
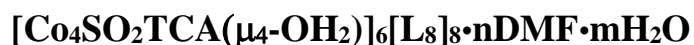


Table 27 List of the obtained calixarene-based MOCs

Solvents and reagents

The reactions sensitive to oxygen or moisture were realized under argon atmosphere. All commercially available reagents have been used without further purification.

Toluene, THF and DCM were dried, when needed on the solvents drying station under argon.

• Tetrahydrofuran	Fisher chemical	(≥99.8%)
• Ethanol	Carlo Erba	(≥99.8%)
• N,N-Dimethylformamide	Carlo Erba	(≥99.0%)
• Acetone	Carlo Erba	(≥99.0%)
• Propanol-2	Carlo Erba	(≥99.7%)
• Chloroform	Carlo Erba	(≥99.8%)
• Dichloromethane	Carlo Erba	(≥99.5%)
• Methanol	Carlo Erba	(≥99.9%)
• Diethyl Ether	Carlo Erba	(≥99.8%)
• Ethyl acetate (EA)	Carlo Erba	(≥99.8%)
• Petroleum ether	Carlo Erba	(35-65°C)
• Dimethyl sulfoxide	Carlo Erba	(≥99.9%)

Preparative column chromatography

- Silica gel Si 60 (0.040-0.063 mm) VWR chemicals 22E184126

Thin-layer chromatography

- TLC Silica gel 60 F254 on aluminium sheets, Merck HX17415654

Analyses and characterizations

NMR: ^1H - and ^{13}C -NMR spectra were recorded at room temperature on a Bruker AV 300 (300 MHz) and Bruker DRX-500 (500 MHz) spectrometers (Service commun de RMN de la Fédération de Recherche de Chimie de l'Université de Strasbourg). Chemical shifts were referenced to the residual proton or carbon peak of the solvent: 1) for ^1H -NMR: CDCl_3 : 7.26 ppm, $(\text{CD}_3)_2\text{SO}$: 2.50 ppm; 2) for ^{13}C -NMR: CDCl_3 : 77.36 ppm, $(\text{CD}_3)_2\text{SO}$: 39.52 ppm.

Spectral data are present as following:

- Chemical shift in ppm;
- Multiplicity of signal: bs = broad signal, s = singlet, d = doublet, t = triplet, dd = doublet



of doublets, m – multiplet;

- *J*-constants in Hz;
- Number of respective atoms;
- Nature of respective atoms.

IR spectra of the connectors were obtained on a Perkin Elmer FTIR 1600 spectrometer using ATR mode in a range of 4000-400 cm^{-1} . Spectral data are present as following: s - strong signal, m - medium signal, w - weak signal, b – broad signal, mb – medium broad signal, wb – weak broad signal.

IR spectra of milled crystalline samples in KBr of activated and non-activated MOCs were recorded on a Tensor 27 Fourier-transform spectrometer (Bruker) in a range of 4000-400 cm^{-1} .

Mass spectra (ESI-MS) of connectors were obtained on a MicroTOF(II) focus mass spectrometer (BRUKER, Germany) equipped with an Electrospray (ESI) source. (Service de spectrométrie de Masse, Fédération de Recherche de Chimie de l'Université de Strasbourg).

Mass spectra (ESI-MS and IM-MS) for MOCs were obtained on Agilent 6560 ESI-IM-QTOF mass spectrometer equipped with dual AJS ion source and Drift Gas Upgrade Kit (Agilent Technologies, USA) (The group of Dr. Elina Kalenius, University of Jyväskylä, Finland)

Circular Dichroism spectra were obtained on a Jasco “J-810” Circular Dichroism Spectrometer for circular dichroism measurements at wavelengths from 300 to 600 nm. Light source – Xe-lamp, 150W. (Service d'Analyses, de Mesures physiques et de Spectroscopie optique, Fédération de Recherche de Chimie de l'Université de Strasbourg)

Chiral HPLC. The analyses were realized on a Shimadzu Prominence HPLC with a LC-20AD Pump and SPD-M20A PDA detector, ChiralPak 1A. The data were analysed by Labsolution software. We acknowledge the LIMA UMR 7042 CNRS Université de Strasbourg for the access to the analytical equipment and expertise and especially Matthieu Chessé for recording the spectra.

X-ray analyses of MOCs were performed by the group of Pr. Kari Rissanen at University of Jyväskylä (Finland) on the following equipment:

Rigaku SuperNova dual-source Oxford diffractometer equipped with a HyPix-Arc 100 detector using mirror-monochromated $\text{Cu-K}\alpha$ ($\lambda = 1.54184 \text{ \AA}$) radiation was used for XRD analysis of $[\text{Ni}_4\text{SO}_2\text{TCA}]_6[\text{rac-Co}(\text{L}_1)_3]_8$, $[\text{Co}_4\text{SO}_2\text{TCA}]_6[\text{rac-Co}(\text{L}_1)_3]_8$, $[\text{Ni}_4\text{SO}_2\text{TCA}]_6[\Delta\text{-Co}(\text{L}_1)_3]_8$, $[\text{Co}_4\text{SO}_2\text{TCA}]_6[\Delta\text{-Co}(\text{L}_1)_3]_8$, $[\text{Ni}_4\text{SO}_2\text{TCA}]_6[\Lambda\text{-Co}(\text{L}_1)_3]_8$, $[\text{Co}_4\text{SO}_2\text{TCA}]_6[\Lambda\text{-Co}(\text{L}_1)_3]_8$

$\text{Co}(\text{L}_1)_3)_8$, $[\text{Ni}_4\text{SO}_2\text{TCA}]_6[\text{rac-Fe}(\text{L}_1)_3)_8$, $[\text{Co}_4\text{SO}_2\text{TCA}]_6[\text{rac-Fe}(\text{L}_1)_3)_8$, $[\text{Ni}_4\text{SO}_2\text{TCA}]_6[\text{L}_8)_8$, $[\text{Co}_4\text{SO}_2\text{TCA}]_6[\text{L}_8)_8$ (see details in crystallographic annexes §I.1.).

Rigaku XtaLAB Synergy-R diffractometer with a HyPix-Arc 100 detector using mirror-monochromated Cu-K α ($\lambda = 1.54184\text{\AA}$) radiation was used for XRD analysis of $[\text{Ni}_4\text{SO}_2\text{TCA}]_6[\text{rac-Rh}(\text{L}_1)_3)_8$, $[\text{Co}_4\text{SO}_2\text{TCA}]_6[\text{rac-Rh}(\text{L}_1)_3)_8$ (see details in crystallographic annexes §I.1.).

X-ray analyses of $[\text{M}_2\text{SO}_2\text{TCA}]\cdot 4\text{DMF}$ ($\text{M} = \text{Co}^{\text{II}}, \text{Cu}^{\text{II}}$), $[\text{Fe}_2\text{SO}_2\text{TCA}]\text{Cl}_2\cdot 4\text{DMF}$, $[\text{M}_4(\text{SO}_2\text{TCA})_2]\cdot 4\text{DMF}$ ($\text{M} = \text{Ni}^{\text{II}}, \text{Fe}^{\text{II}}$), $[\text{CoSO}_2\text{TCA}]\cdot 3\text{DMF}$, $\text{Pd}(\text{HL}_1)_2$ and $[\text{CuHL}_5]\text{Cl}_2$ were performed on a Bruker APEX8 CCD Diffractometer equipped with an Oxford Cryosystem liquid N₂ device at 173(2) K, using graphite-monochromated Mo-K α ($\lambda = 0.71073\text{\AA}$) radiation.

Elemental analysis. The data was obtained on a ThermoFisher Scientific "Flash 2000" apparatus for the simultaneous analysis of elements C, H and N. (Service d'Analyses, de Mesures physiques et de Spectroscopie optique, Fédération de Recherche de Chimie de l'Université de Strasbourg). Elemental analysis was performed with samples dried under vacuum during 48h without heating.

Gas adsorption properties. Nitrogen gas adsorption experiments with dipyrin-based MOCs of formula $[\text{M}_4\text{SO}_2\text{TCA}(\mu_4\text{-OH}_2)]_6[\text{rac-Co}(\text{L}_1)_3)_8$ ($\text{M} = \text{Co}^{\text{II}}, \text{Ni}^{\text{II}}$) have been performed in collaboration with group of Pr. Fedin (A.V. Nikolaev inorganic chemistry institute, Novosibirsk, Russia). Nitrogen adsorption was analysed using the nitrogen adsorption technique on a Quantchrome's Autosorb iQ gas sorption analyser at 77K.

Other gases adsorption experiments with dipyrin-based MOCs $[\text{M}_4\text{SO}_2\text{TCA}(\mu_4\text{-OH}_2)]_6[\text{rac-Co}(\text{L}_1)_3)_8$ ($\text{M} = \text{Co}^{\text{II}}, \text{Ni}^{\text{II}}$) were carried out volumetrically on Quantochrome's Autosorb iQ equipped with thermostat TERMEX Cryo-VT-12 to adjust temperature with 0.1 K accuracy. Adsorption-desorption isotherms were measured within the range of pressures of 1 to 800 torr The database of the National Institute of Standards and Technology [Thermophysical Properties of Fluid Systems, Database of National Institute of Standards and Technology, NIST. <http://webbook.nist.gov/chemistry/fluid/>] was used as a source of p-V-T relations at experimental pressures and temperatures.

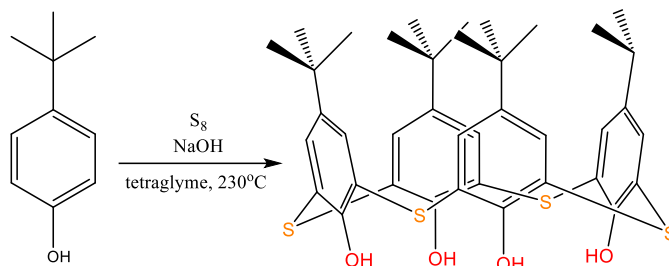
Nitrogen and CO₂ adsorption experiments with triazine-based MOC of formula $[\text{Co}_4\text{SO}_2\text{TCA}(\mu_4\text{-OH}_2)]_6[\text{L}_8)_8$ have been performed on ASAP 2020 gas sorption analyser. Nitrogen adsorption experiment was performed within the range of relative pressures from 10⁻⁶ to 0.999 P/P_0 at 77K. CO₂ adsorption experiment was performed within the range of relative pressures from 7*10⁻⁵ to 0.034 at 273K.



I. Synthesis of calixarenes

I.1. Synthesis of (5,26,27,28-tetrahydroxy-5,11,17,23-tetra-tert-butyl-2,8,14,20-tetrasulfonyl[4]arene (H₄SO₂TCA)

25,26,27,28-tetrahydroxy-5,11,17,23-tetra-tert-butyl-2,8,14,20-tetrathia[4]arene

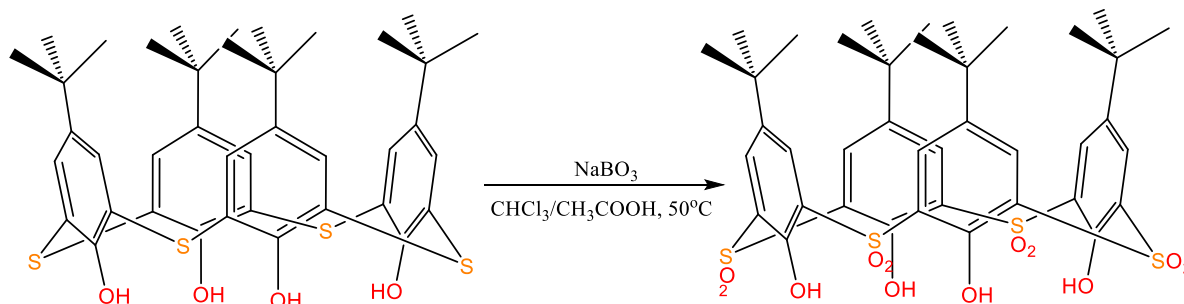


The product was synthesized according to the already published procedure.²²¹

The ¹H-NMR spectrum was in accordance with the already reported one.²²¹

¹H-NMR (CDCl₃, 300 MHz, 25 °C) δ ppm: 9.60 (s, 4H, OH), 7.64 (s, 8H, Ar-H), 1.23 (s, 36H, ^tBu)

(5,26,27,28-tetrahydroxy-5,11,17,23-tetra-tert-butyl-2,8,14,20-tetrasulfonyl[4]arene (H₄SO₂TCA)



The product was synthesized according to the already published procedure.²²²

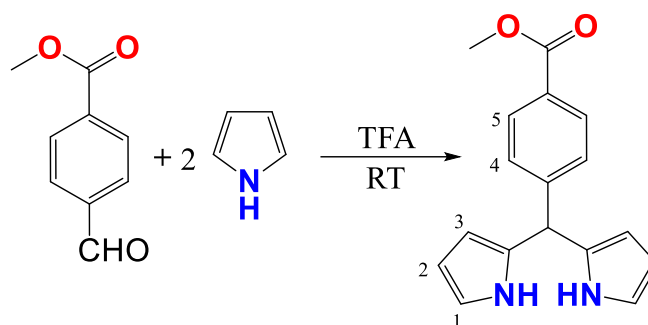
The ¹H-NMR spectrum was in accordance with the already reported one.²²²

¹H-NMR (CDCl₃, 300 MHz, 25 °C) δ ppm: 8.00 (s, 8H, Ar-H), 1.25 (s, 36H, ^tBu)

II. Synthesis of connectors

II.1. Synthesis of dipyrin connectors

5-(4-Carboxymethylphenyl)dipyrromethane



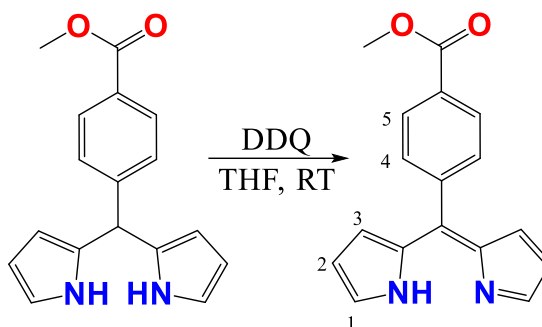
The product was synthesized based on the already reported procedure with modifications.¹²³

4-carboxymethylbenzaldehyde (5g, 0.03 mol) was dissolved in 70 ml of degassed pyrrole (1 mol) that was preliminary filtered through alumina to remove impurities. TFA (1 ml, 0.013 mol) was added subsequently and reaction mixture was stirred at RT for 24h under light protection and Ar-atmosphere. 5 ml of triethylamine was added to quench the reaction and unreacted pyrrole was removed under reduced pressure. The residue was suspended in 50 ml of cold diethyl ether. Suspension was filtered off and washed two times by cold diethyl ether; it afforded a white powder. Yield = 6.8g (79.6%).

The ¹H-NMR spectrum was in accordance with the already reported one.¹¹⁶

¹H-NMR (CDCl₃, 300 MHz, 25 °C) δ ppm: 7.98 (d, *J* = 8.4 Hz, 2H, H⁵), 7.30 (d, *J* = 8.4 Hz, 2H, H⁴), 6.72 (m, 2H, H¹), 6.16 (m, 2H, H³), 5.89 (m, 2H, H²), 5.54 (s, 1H, CH), 3.91 (s, 3H, CH₃)

5-(4-Carboxymethylphenyl)-4,6-dipyrrin

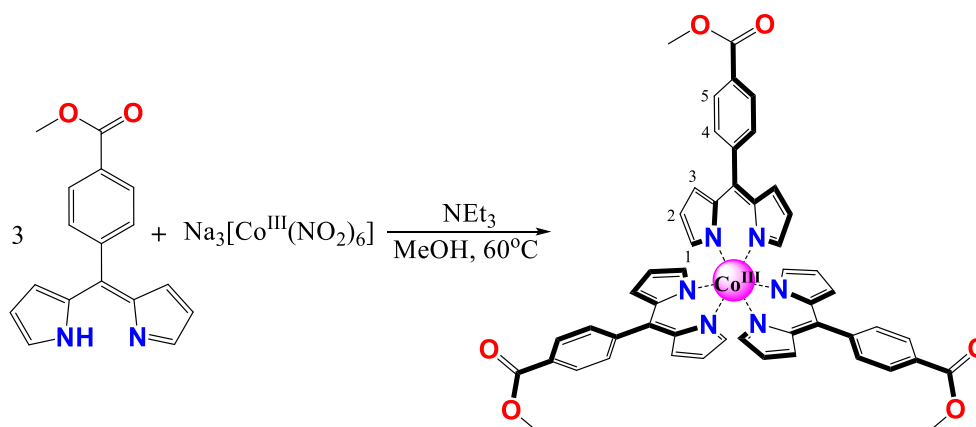


The product was synthesized according to the already published procedure.¹¹⁶

¹H-NMR (CDCl₃, 300 MHz, 25 °C) δ ppm: 8.12 (d, *J* = 8.5 Hz, 2H, H⁵), 7.68 (m, 2H, H¹), 7.57 (d, *J* = 8.4 Hz, 2H, H⁴), 6.53 (dd, *J* = 4.2, 1.2 Hz, 2H, H³), 6.41 (dd, *J* = 4.2, 1.5 Hz, 2H, H²), 3.97 (s, 3H, CH₃)

Tris[5-(4-Carboxyphenyl)-4,6-dipyrinato] Co(III) (rac-Co(HL₁)₃)

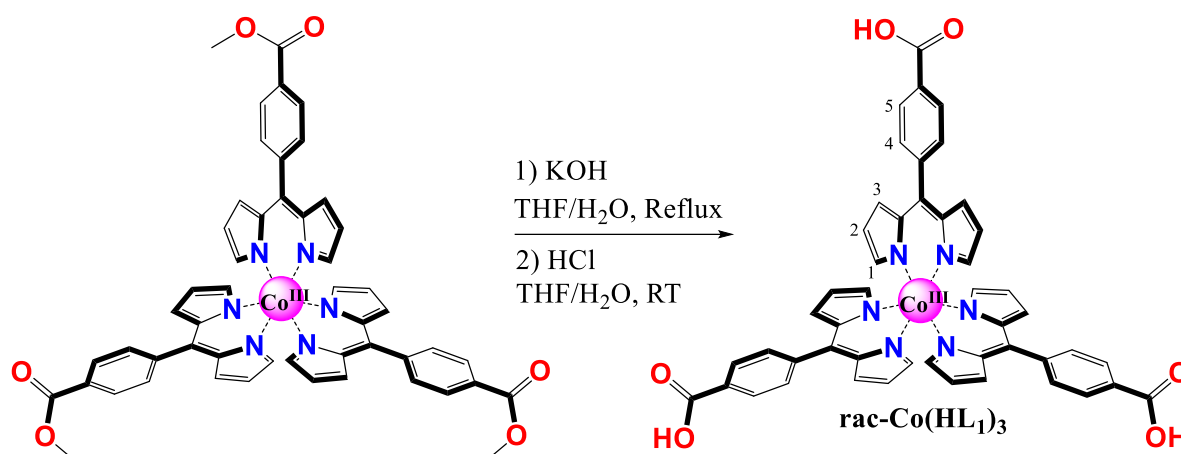
Tris[5-(4-Carboxymethylphenyl)-4,6-dipyrinato] Co(III)



The product was synthesized as a racemate based on the already reported procedure with modifications.¹¹⁶

5-(4-Carboxymethylphenyl)-4,6-dipyrrin (0.5g, 1.8 mmol) was dissolved in 35 ml of methanol, then 5 ml of triethylamine were added. Sodium hexanitrocobaltate(III) (0.2422g, 0.6 mmol) was dissolved in 5 ml of water. The solution was added to the 5-(4-Carboxymethylphenyl)-4,6-dipyrrin solution. The reaction mixture was stirred at 60°C for 19h. The solvents were evaporated under reduced pressure. The residue was suspended in 50 ml of methanol, filtered off and washed 2 times with methanol; it afforded a red-orange powder. Yield = 0.25g (46.8%).

¹H-NMR (CDCl₃, 300 MHz, 25 °C) δ ppm: 8.09 (d, *J* = 8.5 Hz, 6H, H⁵), 7.52 (d, *J* = 8.5 Hz, 6H, H⁴), 6.64 (dd, *J* = 4.3, 1.4 Hz, 6H, H³), 6.40 (m, 6H, H¹), 6.33 (dd, *J* = 4.4, 1.7 Hz, 6H, H²), 3.97 (s, 9H, CH₃)

Tris[5-(4-Carboxyphenyl)-4,6-dipyrinato] Co(III) (*rac*-Co(HL₁)₃)

The product was synthesized as a racemate according to the reported procedure.¹¹⁶

¹H-NMR (DMSO-*d*₆, 500 MHz, 25 °C) δ ppm: 8.08 (d, *J* = 7.8 Hz, 6H, H⁵), 7.56 (d, *J* = 7.8 Hz, 6H, H⁴), 6.64 (m, 6H, H³), 6.45 (m, 6H, H¹), 6.35 (m, 6H, H²)

¹³C-NMR (DMSO-*d*₆, 126 MHz, 25 °C) δ ppm: 167.45, 151.95, 145.46, 141.77, 135.17, 133.31, 131.59, 130.72, 129.12, 120.13

ESI-MS: expected *m/z* = 848.76 [M]⁺; found *m/z* = 849.19 [M]⁺;

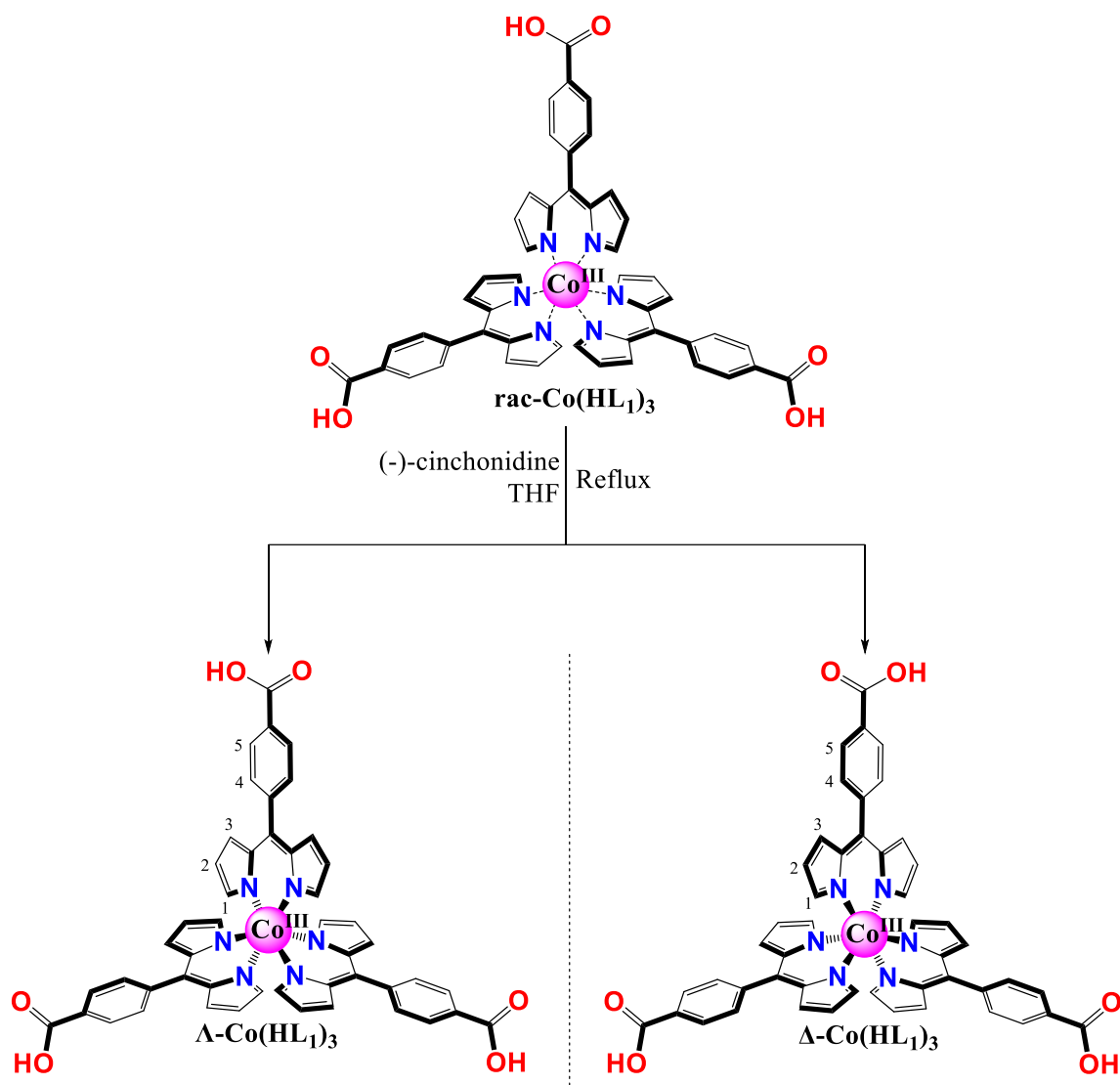
IR: 3111(wb), 1689(m), 1610(w), 1549(s), 1485(w), 1410(m), 1376(s), 1343(s), 1287(m), 1245(s), 1026(s), 993(s), 901(m), 891(s), 882(m), 826(s), 760(s), 719(s) cm⁻¹.

Elemental Analysis: % calculated: C, 67.93%; H, 3.92%; N, 7.65%

% found: C, 67.54%; H, 3.96%; N, 7.69%



Enantiomers separation of Tris[5-(4-Carboxyphenyl)-4,6-dipyrinato] Co(III) (Λ -Co(HL₁)₃, Δ -Co(HL₁)₃)



The two enantiomers $\Lambda\text{-Co(HL}_1\text{)}_3$ and $\Delta\text{-Co(HL}_1\text{)}_3$ were synthesized based on the already reported procedure with modifications.¹²⁵

Tris[5-(4-Carboxyphenyl)-4,6-dipyrinato] Co(III) (**rac-Co(HL₁)₃**) (0.350g, 0.4 mmol) and (-)-cinchonidine (0.2425g, 0.8 mmol) were dissolved in 20 ml of THF. The reaction mixture was refluxed overnight, then cooled in the fridge, filtered off and washed one time with cold THF; it afforded a red solid (Λ) and red filtrate (Δ).

Λ -Tris[5-(4-Carboxyphenyl)-4,6-dipyrinato] Co(III) ($\Lambda\text{-Co(HL}_1\text{)}_3$): Red solid was dissolved in a mixture of EA/TFA = 100/0.3 and then purified by column chromatography (SiO₂, eluent - EA/TFA = 100/0.3); it afforded a bright red solid (0.165g)

¹H-NMR (DMSO-d₆, 500 MHz, 25 °C) δ ppm: 8.08 (d, *J* = 7.8 Hz, 6H, H⁵), 7.56 (d, *J* = 7.8 Hz, 6H, H⁴), 6.64 (m, 6H, H³), 6.45 (m, 6H, H¹), 6.35 (m, 6H, H²)

CD (5*10⁻⁵M, THF, 2mm): 465 nm (θ = -98.47mdeg), 515 nm (θ =144.44 mdeg)

Chiral HPLC (ChiralPak 1A, Hexane/THF/TFA = 80/20/0.1, flow rate = 0.8 ml/min, 470 nm): 16.7 min, ee=92%

Δ-Tris[5-(4-Carboxyphenyl)-4,6-dipyrinato] Co(III) (Δ-Co(HL₁)₃): the obtained filtrate was evaporated and the dark red residue was dissolved in the mixture EA/TFA = 100/0.3 and then purified by column chromatography (SiO₂, eluent - EA/TFA = 100/0.3); it afforded a bright red solid (0.165g)

¹H-NMR (DMSO-d₆, 500 MHz, 25 °C) δ ppm: 8.08 (d, *J* = 7.8 Hz, 6H, H⁵), 7.56 (d, *J* = 7.8 Hz, 6H, H⁴), 6.64 (m, 6H, H³), 6.45 (m, 6H, H¹), 6.35 (m 6H, H²)

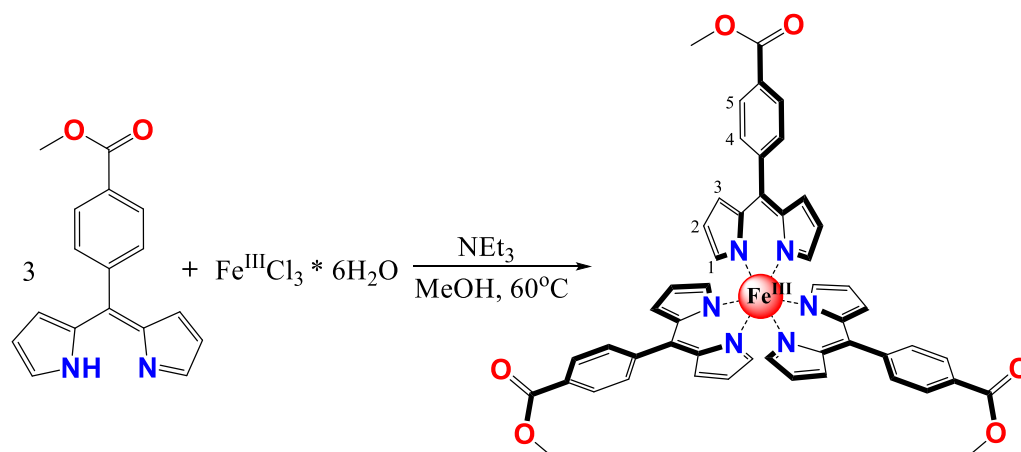
CD (5*10⁻⁵M, THF, 2mm): 465 nm (θ = 91.9 mdeg), 515 nm (θ =-131.7 mdeg)

Chiral HPLC (ChiralPak 1A, Hexane/THF/TFA = 80/20/0.1, flow rate = 0.8 ml/min, 470 nm): 14.8 min, ee=85%



Tris[5-(4-Carboxyphenyl)-4,6-dipyrrinato] Fe(III) (rac-Fe(HL₁)₃)

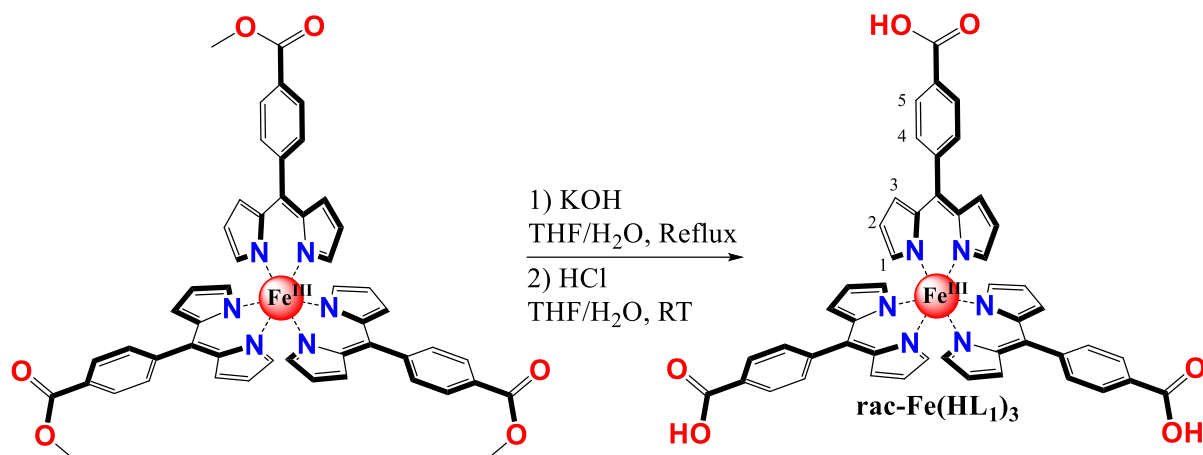
Tris[5-(4-Carboxymethylphenyl)-4,6-dipyrrinato] Fe(III)



The product was synthesized as a racemate based on the already reported procedure with modifications.¹¹¹

5-(4-Carboxymethylphenyl)-4,6-dipyrrin (0.5g, 1.8 mmol) was dissolved in 35 ml of methanol, then 5 ml of triethylamine were added. Iron(III) chloride hexahydrate (0.1619g, 0.6 mmol) was dissolved in 5 ml of water. The solution was added to the 5-(4-Carboxymethylphenyl)-4,6-dipyrrin solution. The reaction mixture was stirred at 60°C for 19h. The solvents were evaporated under reduced pressure. The residue was suspended in 50 ml of methanol, filtered off and washed 2 times with methanol; it afforded a red-orange powder. Yield = 0.189 (35.7%).

¹H-NMR (CDCl₃, 300 MHz, 25 °C) δ ppm: 11.27 (m, 6H), 9.47 (m, 6H), 4.46 (s, 9H, CH₃). Other peaks are not observed due to a presence of paramagnetic Fe^{III} ion in the obtained complex.

Tris[5-(4-Carboxyphenyl)-4,6-dipyrinato] Fe(III) (*rac*-Fe(HL₁)₃)

The product was synthesized as a racemate similar to the reported procedure for Tris[5-(4-Carboxyphenyl)-4,6-dipyrinato] Co(III) (**rac-Co(HL₁)₃**).¹¹⁶

Tris[5-(4-Carboxymethylphenyl)-4,6-dipyrinato] Fe(III) (0.189g, 0.22 mmol) was dissolved in 10 ml of THF. Subsequently, 10 ml of 4% KOH aqueous solution were added. The reaction mixture was refluxed for 5h and then was cooled to RT. The reaction mixture was acidified with 12% HCl solution until pH = 5-6, then filtered off and washed two times with water that afforded a dark brown powder. Yield = 0.153g (81%)

¹H-NMR (DMSO-*d*₆, 500 MHz, 25 °C) δ ppm: 11.23 (bs, 6H), 9.42 (bs, 6H). Other peaks are not observed due to a presence of paramagnetic Fe^{III} ion in the obtained complex.

¹³C-NMR (DMSO-*d*₆, 126 MHz, 25 °C) δ ppm: 168.57, 167.26, 144.86, 131.05, 129.82, 129.58, 119.22. Other peaks are not observed due to a presence of paramagnetic Fe^{III} ion in the obtained complex.

ESI-MS: expected $m/z = 845.67$ [M]⁺; found $m/z = 844.15$ [M]⁺

IR: 3113(wb), 1699(w), 1607(w), 1550(m), 1504(w), 1446(m), 1404(m), 1325(s), 1232(m), 1199(w), 1140(m), 1038(s), 998(m), 972(m), 892(m), 865(s), 822(s), 764(s), 719(s), 582(s), 513(s) cm⁻¹.

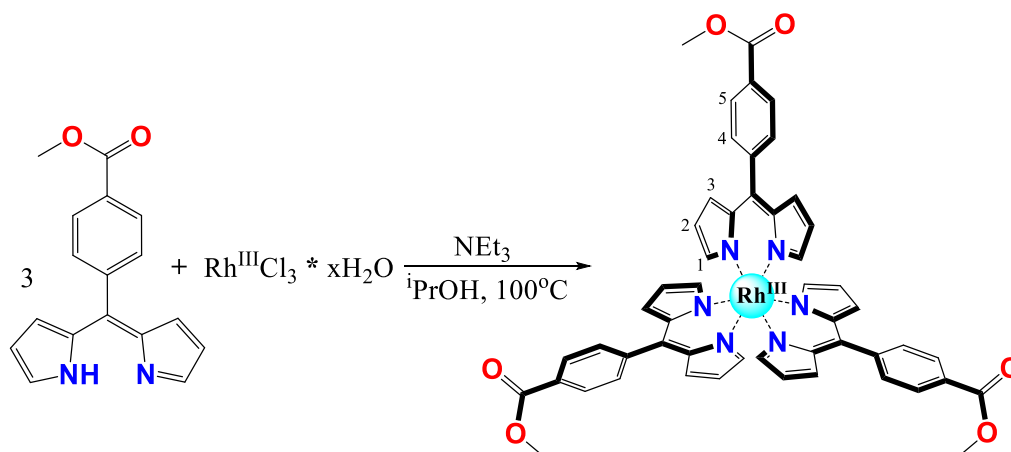
Elemental Analysis: % calculated: C, 67.93%; H, 4.28%; N, 9.90%

% found: C, 67.69%; H, 4.13%; N, 9.96%



Tris[5-(4-Carboxyphenyl)-4,6-dipyrinato] Rh(III) (rac-Rh(HL₁)₃)

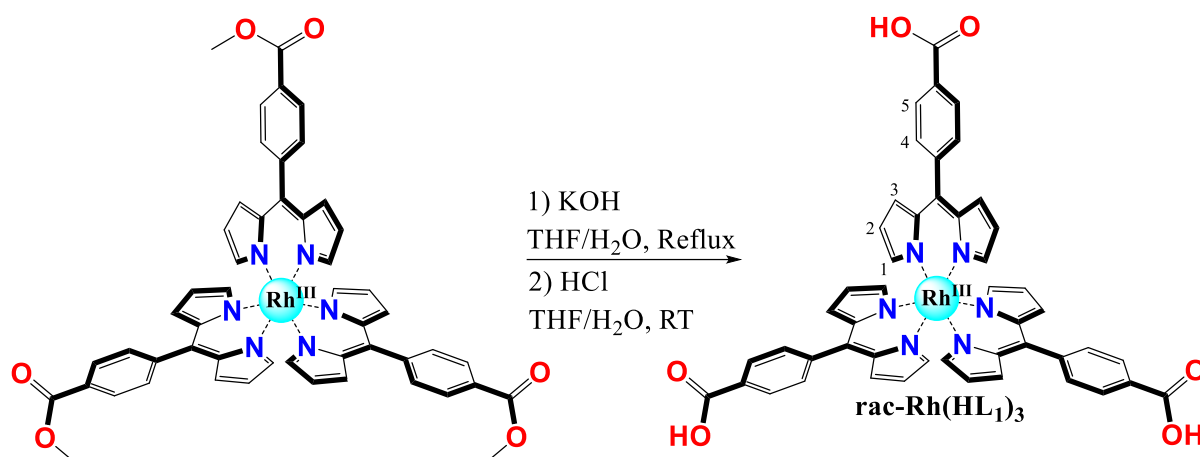
Tris[5-(4-Carboxymethylphenyl)-4,6-dipyrinato] Rh(III)



The product was synthesized as a racemate based on the already reported procedure with modifications.¹¹²

5-(4-Carboxymethylphenyl)-4,6-dipyrin (1 g, 3.6 mmol) was dissolved in 150 ml of isopropanol, then 5 ml of triethylamine were added. Rhodium(III) chloride hydrate (0.2637g, 1.2 mmol) was added subsequently. The reaction mixture was stirred at 100°C for 19h. The solvents were evaporated under reduced pressure. The residue was suspended in 50 ml of methanol, filtered off and washed 2 times with methanol; it afforded a red to brown powder. Yield = 0.585g (52.2%)

¹H-NMR (CDCl₃, 300 MHz, 25 °C) δ ppm: 8.10 (d, *J* = 8.6 Hz, 6H, H⁵), 7.52 (d, *J* = 8.6 Hz, 6H, H⁴), 6.66 (m, 6H, H¹), 6.56 (dd, *J* = 4.4, 1.5 Hz, 6H, H³), 6.33 (dd, *J* = 4.4, 1.5 Hz, 6H, H²), 3.98 (s, 9H, CH₃)

Tris[5-(4-Carboxyphenyl)-4,6-dipyrrinato] Rh(III) (*rac*-Rh(HL₁)₃)

The product was synthesized as a racemate according to the already reported procedure.¹¹²

¹H-NMR (DMSO-*d*₆, 500 MHz, 25 °C) δ ppm: 8.08 (d, *J* = 8.3 Hz, 6H, H⁵), 7.56 (d, *J* = 8.3 Hz, 6H, H⁴), 6.60 (m, 6H, H¹), 6.53 (dd, *J* = 4.4, 1.5 Hz, 6H, H³), 6.47 (dd, *J* = 4.4, 1.5 Hz, 6H, H²)

¹³C-NMR (DMSO-*d*₆, 126 MHz, 25 °C) δ ppm: 167.45, 150.49, 146.81, 142.14, 134.58, 132.05, 131.54, 130.70, 129.03, 119.34

ESI-MS: expected *m/z* = 892.73 [M]⁺; found *m/z* = 893.16 [M]⁺

IR: 2918(m), 2851(m), 1696(m), 1610(w), 1547(s), 1467(w), 1411(m), 1377(s), 1346(s), 1329(w), 1286(m), 1251(s), 1232(m), 1176(m), 1116(w), 1026(s), 994(s), 961(m), 893(m), 826(s), 773(s), 761(s), 719(s), 477(m), 418(m) cm⁻¹.

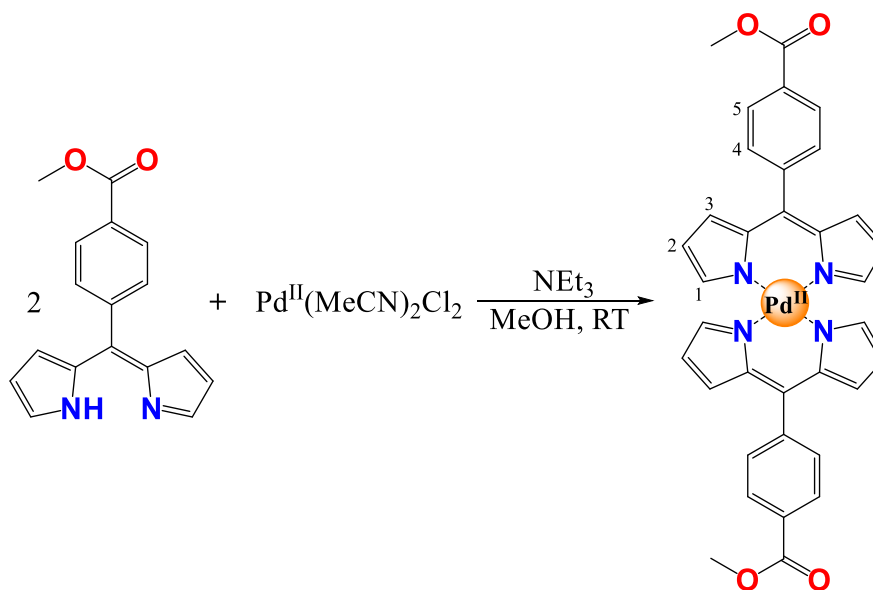
Elemental Analysis: % calculated: C, 64.58%; H, 3.73%; N, 9.41%

% found: C, 64.68%; H, 4.01%; N, 9.13%



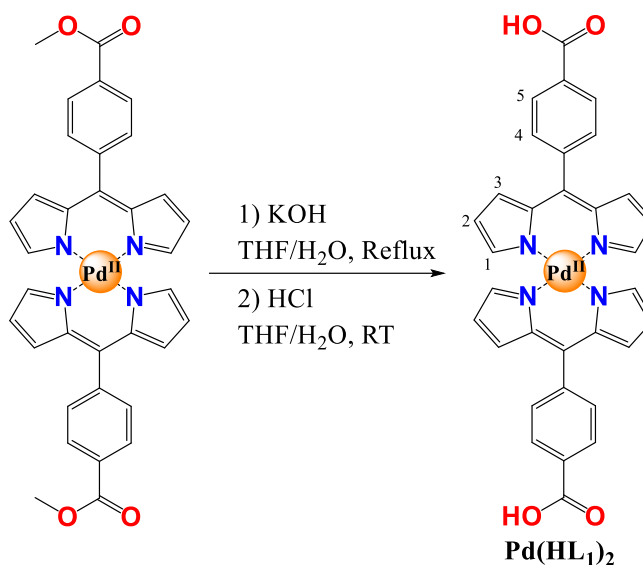
Bis[5-(4-Carboxyphenyl)-4,6-dipyrrinato] Pd(II) (Pd(HL₁)₂)

Bis[5-(4-Carboxymethylphenyl)-4,6-dipyrrinato] Pd(II)



The product was synthesized according to the already reported procedure.¹¹²

¹H-NMR (CDCl₃, 300 MHz, 25 °C) δ ppm: 8.17 (d, *J* = 8.2 Hz, 4H, H⁵), 7.67 (d, *J* = 8.2 Hz, 4H, H⁴), 7.41 (m, 4H, H¹), 6.65 (dd, *J* = 4.4, 1.4 Hz, 4H, H³), 6.38 (dd, *J* = 4.4, 1.5 Hz, 4H, H²), 4.00 (s, 6H, CH₃)

Bis[5-(4-Carboxyphenyl)-4,6-dipyrrinato] Pd(II) (Pd(HL₁)₂)

The product was synthesized according to the already reported procedure.¹¹²

¹H-NMR (DMSO-d₆, 500 MHz, 25 °C) δ ppm: 8.17 (bs, 4H, H⁵), 7.77 (bs, 4H, H⁴), 7.45 (bs, 4H, H¹), 6.70 (bs, 4H, H³), 6.56 (bs, 4H, H²)

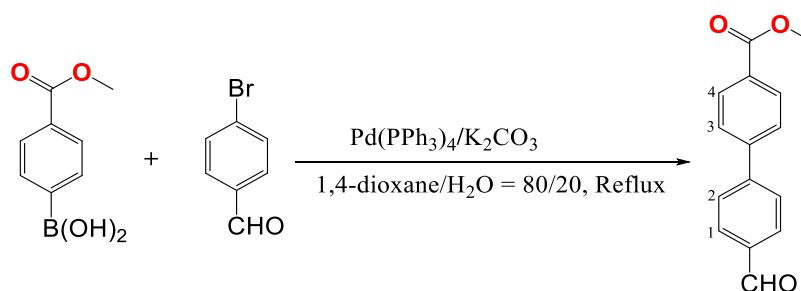
¹³C-NMR (DMSO-d₆, 126 MHz, 25 °C) δ ppm: 167.43, 152.46, 146.61, 141.32, 136.37, 131.73, 131.45, 130.85, 129.17, 118.45

ESI-MS: expected $m/z = 632.97$ [M]⁺; found $m/z = 633.08$ [M]⁺;

IR: 2873(wb), 1676(m), 1607(w), 1545(s), 1529(m), 1448(w), 1405(m), 1379(s), 1341(s), 1288(m), 1259(s), 1203(m), 1177(m), 1123(w), 1034(s), 993(s), 982(m), 898(m), 870(m), 830(s), 823(m), 760(s), 721(s), 607(m), 605(m), 541(m), 476(m), 413(m) cm⁻¹.

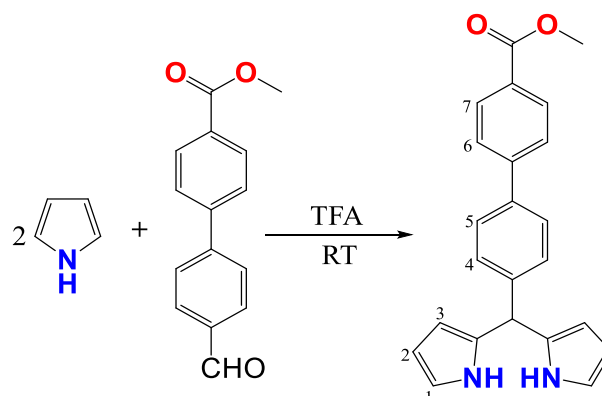
Elemental Analysis: % calculated: C, 60.72%; H, 3.50%; N, 8.85%

% found: C, 60.42%; H, 3.85%; N, 8.23%

**Tris[5-(4-(4-Carboxyphenyl)phenyl)-4,6-dipyrinato] Co(III) (rac-Co(HL₂)₃)***Methyl 4'-formyl-[1,1'-biphenyl]-4-carboxylate*

The product was synthesized according to the already reported procedure.¹²⁴

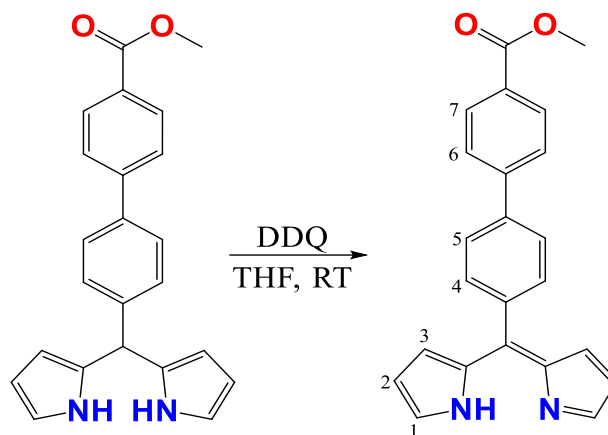
¹H-NMR (CDCl₃, 300 MHz, 25 °C) δ ppm: 10.08 (s, 1H, CHO), 8.14 (d, *J* = 8.4 Hz, 2H, H⁴), 7.98(d, *J* = 8.6 Hz, 2H, H¹), 7.78 (d, *J* = 8.4 Hz, 2H, H³), 7.71 (d, *J* = 8.7 Hz, 2H, H²), 3.96 (s, 3H, CH₃)

5-(4-(4-Carboxymethylphenyl)phenyl)dipyrromethane

Methyl 4'-formyl-[1,1'-biphenyl]-4-carboxylate (1.340g, 5.6 mmol) was dissolved in 14 ml of degassed pyrrole (190 mmol) that was filtered preliminary through alumina to remove impurities. TFA (0.2 ml, 2.6 mmol) was added subsequently and the reaction mixture was stirred at RT for 24h under light protection and Ar-atmosphere. 3 ml of triethylamine was added to quench the reaction and unreacted pyrrole was removed under reduced pressure. The residue was suspended in 50 ml of cold diethyl ether. Suspension was filtered off and washed two times with cold diethyl ether; it afforded a white powder. Yield = 0.861 (43.3%)

¹H-NMR (CDCl₃, 300 MHz, 25 °C) δ ppm: 8.07 (d, *J* = 8.7 Hz, 2H, H⁷), 7.61 (d, *J* = 8.7 Hz, 2H, H⁶), 7.55 (d, *J* = 8.3 Hz, 2H, H⁵), 7.30 (d, *J* = 8.3 Hz, 2H, H⁴), 6.71 (m, 2H, H¹), 6.16 (m, 2H, H³), 5.93 (m, 2H, H²), 5.51 (s, 1H, CH), 3.92 (s, 3H, CH₃)

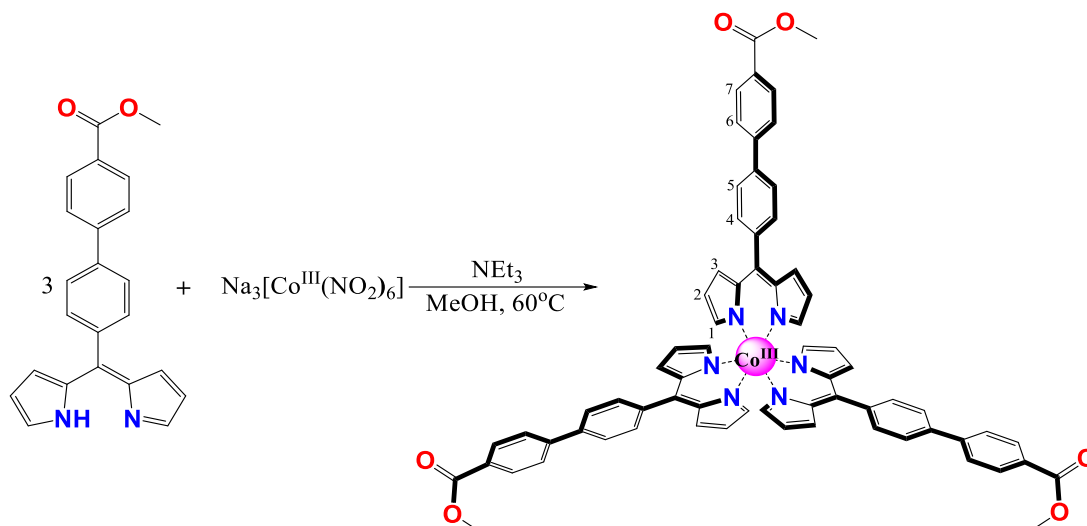
¹³C-NMR (CDCl₃, 126 MHz, 25 °C) δ ppm: 167.02, 145.15, 142.22, 138.67, 132.19, 130.15, 128.99, 128.89, 127.53, 126.93, 117.40, 108.56, 107.36, 52.18, 43.72

5-(4-(4-Carboxymethylphenyl)phenyl)phenyl)-4,6-dipyrrin

5-(4-(4-Carboxymethylphenyl)phenyl)dipyrromethene (0.861g, 2.4 mmol) was dissolved in 100 ml of THF. DDQ (0.737g, 2.7 mmol) was added subsequently. The reaction mixture was stirred during 24h at RT under light protection. The solvent was removed under reduced pressure. The residue was purified by column chromatography (SiO₂, eluent: DCM/NEt₃ = 100/1); it afforded a black-yellow powder. Yield = 0.431g (50.3%)

¹H-NMR (CDCl₃, 300 MHz, 25 °C) δ ppm: 8.14 (d, *J* = 8.7 Hz, 2H, H⁷), 7.74 (d, *J* = 8.7 Hz, 2H, H⁶), 7.71 (d, *J* = 8.5 Hz, 2H, H⁵), 7.67 (m, 2H, H¹), 7.60 (d, *J* = 8.5 Hz, 2H, H⁴), 6.66 (dd, *J* = 4.2, 1.4 Hz, 2H, H³), 6.42 (dd, *J* = 4.2, 1.4 Hz, 2H, H²), 3.96 (s, 3H, CH₃)

¹³C-NMR (CDCl₃, 126 MHz, 25 °C) δ ppm: 166.94, 144.78, 143.80, 141.41, 140.71, 140.56, 137.18, 131.49, 130.26, 129.31, 128.85, 127.10, 126.50, 117.76, 52.23

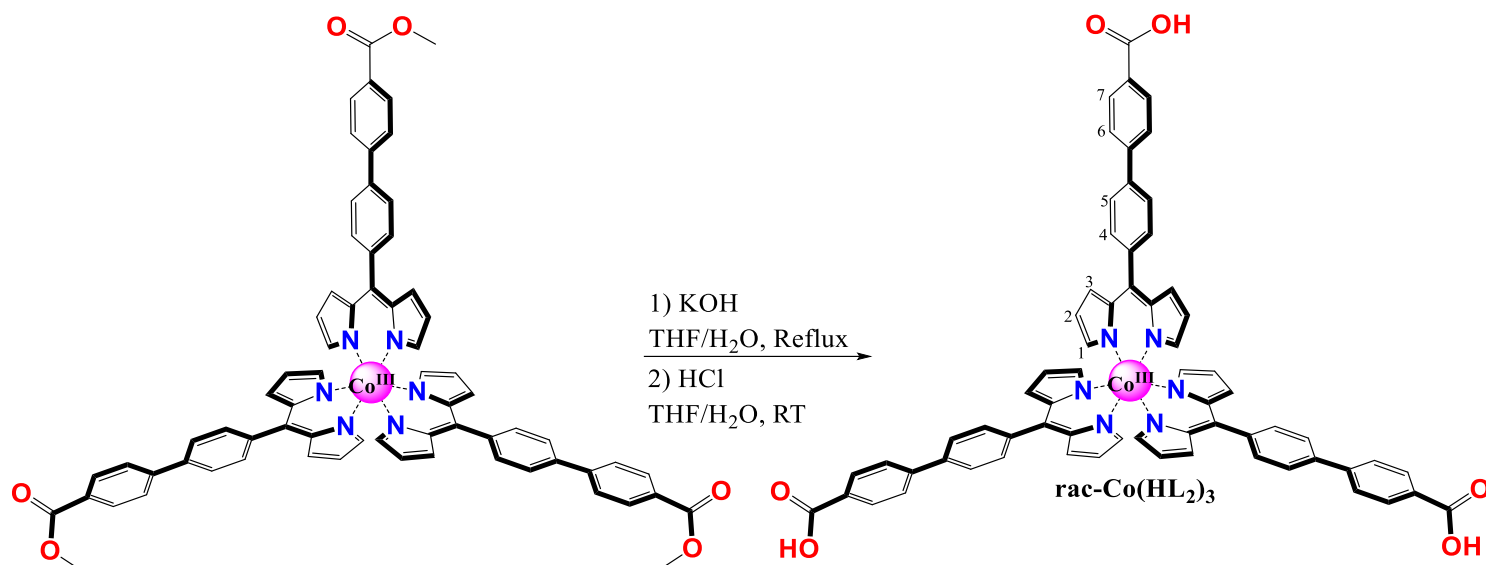
*Tris[5-(4-(4-Carboxymethylphenyl)phenyl)-4,6-dipyrrinato] Co(III)*

The product was synthesized as a racemate similar to the reported procedure for Tris[5-(4-Carboxyphenyl)-4,6-dipyrrinato] Co(III) (**rac-Co(HL₁)₃**).¹¹⁶

5-(4-(4-Carboxymethylphenyl)phenyl)-4,6-dipyrrin (0.431 g, 1.2 mmol) was dissolved in 35 ml of methanol, then 5 ml of triethylamine were added. Sodium hexanitrocobaltate(III) (0.164 g, 0.4 mmol) was dissolved in 5 ml of water. The solution was added to the 5-(4-(4-Carboxymethylphenyl)phenyl)-4,6-dipyrrin solution. The reaction mixture was stirred at 60°C for 19h. The solvents were evaporated under reduced pressure. The residue was suspended in 50 ml of methanol and filtered off and washed two times with methanol; it afforded a red-orange powder. Yield = 0.34 (76.5%).

¹H-NMR (CDCl₃, 300 MHz, 25 °C) δ ppm: 8.15 (d, *J* = 8.5 Hz, 6H, H⁷), 7.75 (d, *J* = 8.5 Hz, 6H, H⁶), 7.71 (d, *J* = 8.5 Hz, 6H, H⁵), 7.57 (d, *J* = 8.4 Hz, 6H, H⁴), 6.79 (dd, *J* = 4.3, 1.6 Hz, 6H, H³), 6.45 (m, 6H, H¹), 6.37 (dd, *J* = 4.3, 1.6 Hz, 6H, H²), 3.96 (s, 9H, CH₃)

¹³C-NMR (CDCl₃, 126 MHz, 25 °C) δ ppm: 166.99, 151.92, 145.68, 144.92, 140.10, 139.97, 135.61, 133.01, 131.08, 130.25, 129.22, 127.11, 126.16, 118.86, 52.23

Tris[5-(4-(4-Carboxyphenyl)phenyl)-4,6-dipyrinato] Co(III) (*rac*-Co(HL₂)₃)

The product was synthesized as a racemate.

Tris[5-(4-(4-Carboxymethylphenyl)phenyl)-4,6-dipyrinato] Co(III) (0.34g, 0.30 mmol) was dissolved in 20 ml THF and 20 ml of 4% KOH was added subsequently. The reaction mixture was refluxed for 5h and then cooled to RT. The reaction mixture was acidified with 12% HCl solution until pH = 5-6, then filtered off and washed two times with water; it afforded a dark red powder. Yield = 0.309g (94.4%).

¹H-NMR (DMSO-*d*₆, 500 MHz, 25 °C) δ ppm: 8.08 (d, *J* = 8.1 Hz, 6H, H⁷), 7.92 (m, 12H, H⁶, H⁵), 7.56 (d, *J* = 7.9 Hz, 6H, H⁴), 6.73 (dd, *J* = 4.4, 1.5 Hz, 6H, H³), 6.45 (m, 6H, H¹), 6.37 (dd, *J* = 4.3, 1.6 Hz, 6H, H²).

¹³C-NMR (DMSO-*d*₆, 126 MHz, 25 °C) δ ppm: 167.60, 151.76, 146.08, 143.51, 139.83, 137.54, 135.51, 133.33, 131.33, 130.55, 127.42, 126.67, 119.91, 67.49

ESI-MS: expected *m/z* = 1077.06 [M]⁺; found *m/z* = 1077.28 [M]⁺

IR: 2993(wb), 1691(m), 1607(w), 1558(m), 1508(w), 1410(m), 1379(s), 1344(s), 1328(m), 1243(s), 1229(s), 1200(s), 1114(m), 1029(s), 996(s), 888(s), 815(s), 769(s), 716(s), 499(s), 448(s) cm⁻¹.

Elemental Analysis:

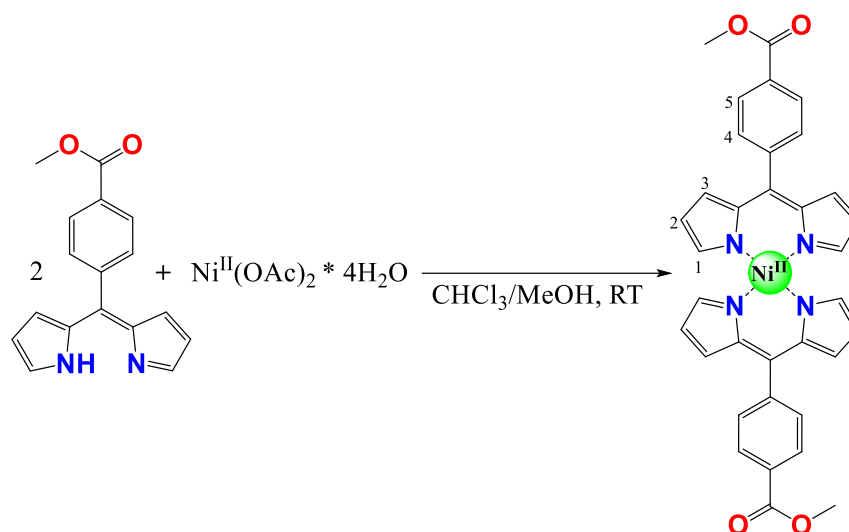
% calculated: C, 69.90%; H, 4.80%; N, 7.41% for **rac-Co(HL₂)₃•3H₂O**

% found: C, 70.09%; H, 4.54%; N, 7.43%



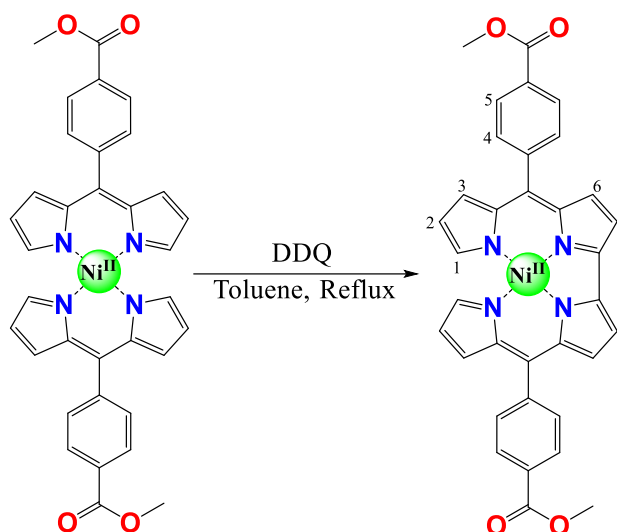
Ni-BisdpmCOOH (Ni(H₂L₃))

Bis[5-(4-(4-Carboxymethylphenyl)phenyl)-4,6-dipyrrinato] Ni(II)



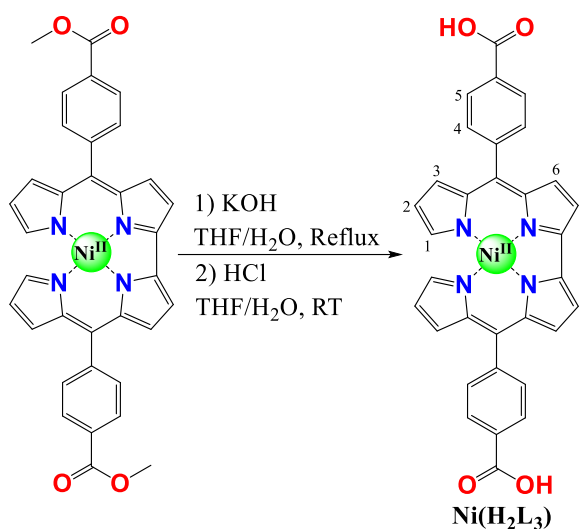
The product was synthesized according to the already reported procedure.¹²¹

¹H-NMR (CDCl₃, 300 MHz, 25 °C) δ ppm: 10.38 (bs, 4H, H¹), 8.06 (d, *J* = 8.0 Hz, 4H, H⁵), 8.00 (d, *J* = 4.1 Hz, 4H, H³), 7.45 (d, *J* = 8.0 Hz, 4H, H⁴), 6.68 (d, *J* = 4.1 Hz, 4H, H²), 3.96 (s, 6H, CH₃)

Ni-BisdpmCOOMe

The product was synthesized according to the already reported procedure.¹²¹

¹H-NMR (CDCl₃, 300 MHz, 25 °C) δ ppm: 8.14 (d, $J = 8.6$ Hz, 4H, H⁵), 7.64 (d, $J = 8.6$ Hz, 4H, H⁴), 6.73 (dd, $J = 4.4, 1.4$ Hz, 2H, H²), 6.68 (d, $J = 4.3$ Hz, 2H, H⁷), 6.63 (d, $J = 4.4$ Hz, 2H, H⁶), 6.44 (dd, $J = 4.4, 1.5$ Hz, 2H, H³), 5.95 (m, 2H, H¹), 3.98 (s, 6H, CH₃)

*Ni-BisdpmCOOH (Ni(H₂L₃))*

The product was synthesized according to the reported procedure.¹²¹

¹H-NMR (THF-d₈, 500 MHz, 25 °C) δ ppm: 8.13 (bs, 4H, H⁵), 7.52 (bs, 4H, H⁴), 6.81 (bs, 4H, H⁶, H⁷), 6.72 (bs, 2H, H²), 6.52 (bs, 2H, H³), 5.95 (bs, 2H, H¹)

ESI-MS: expected $m/z = 583.23$ [M]⁺; found $m/z = 582.09$ [M]⁺

IR: 3337(wb), 1592(m), 1547(m), 1523(m), 1395(m), 1381(m), 1353(w), 1306(s), 1296(m), 1249(m), 1229(m), 1183(m), 1101(w), 1041(s), 1016(m), 984(s), 900(w), 838(m), 787(m), 762(m), 717(s), 656(m), 602(m), 574(m), 476(m), 444(m) cm⁻¹.

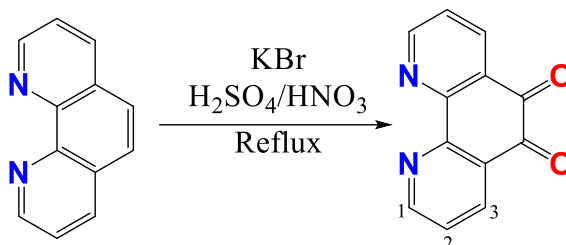
Elemental Analysis: % calculated: C, 63.71%; H, 4.01%; N, 9.29% for **Ni(H₂L₃)•H₂O**

% found: C, 63.91%; H, 3.67%; N, 9.32%.

II.2. Synthesis of phenanthroline connector

Tris[2-(4-Carboxyphenyl)imidazo[4,5-f][1,10]phenanthroline] Fe(II) hexafluorophosphate ([rac-Fe(HL₄)₃][PF₆]₂)

1,10-phenanthroline-5,6-dione

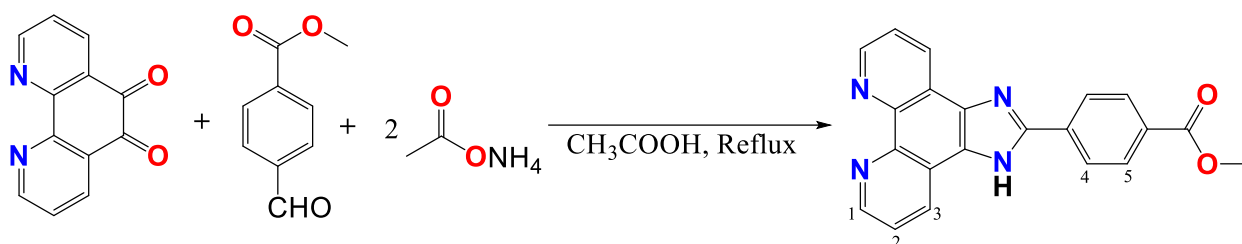


The product was synthesized according to the already reported procedure.²²³

The ¹H-NMR spectrum was in accordance with the already reported one.²²³

¹H-NMR (CDCl₃, 300 MHz, 25 °C) δ ppm: 9.12 (dd, *J* = 4.7, 1.8 Hz, 2H, H³), 8.51 (dd, *J* = 7.9, 1.8 Hz, 2H, H¹), 7.59 (dd, *J* = 7.9, 4.7 Hz, 2H, H²)

2-(4-Carboxymethylphenyl)imidazo[4,5-f][1,10]phenanthroline



The product was synthesized based on the already reported procedure with modifications.⁵

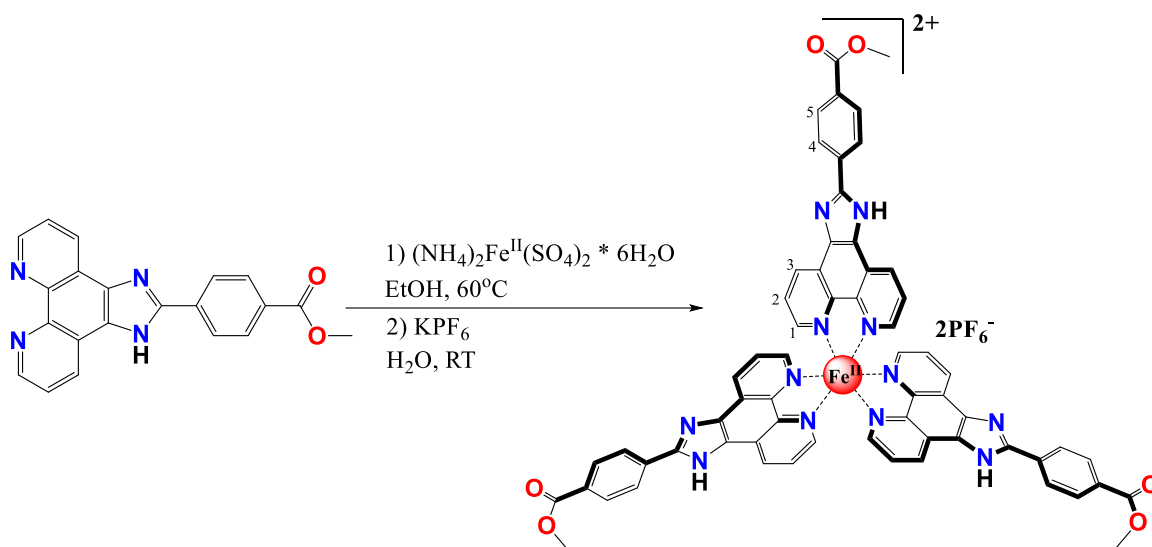
1,10-phenanthroline-5,6-dione (0.4g, 1.8 mmol) 4-carboxymethylbenzaldehyde (0.4686g, 2.7 mmol) and ammonium acetate (2.9334g, 36 mmol) were dissolved in 10 ml of glacial acetic acid. The reaction mixture was refluxed for 3h and then cooled to RT. Subsequently, the mixture was acidified with a 28% ammonia solution to pH=7 and filtered off; it afforded an orange solid. The compound was purified by recrystallization from methanol; it afforded a bright-yellow powder. Yield = 0.53g (78.6%)

The ¹H-NMR spectrum was in accordance with the already reported one.⁵

¹H-NMR (DMSO-d₆, 500 MHz, 25 °C) δ ppm: 9.03 (m, 2H, H³), 8.91 (m, 2H, H¹), 8.39 (d, *J* = 8.0 Hz, 2H, H⁵), 8.14 (d, *J* = 8.0 Hz, 2H, H⁴), 7.83 (dd, *J* = 8.0, 4.3 Hz, 2H, H²), 3.89 (s, 3H, CH₃)



*Tris[2-(4-Carboxymethylphenyl)imidazo[4,5-f][1,10]phenanthroline] Fe(II)
hexafluorophosphate*



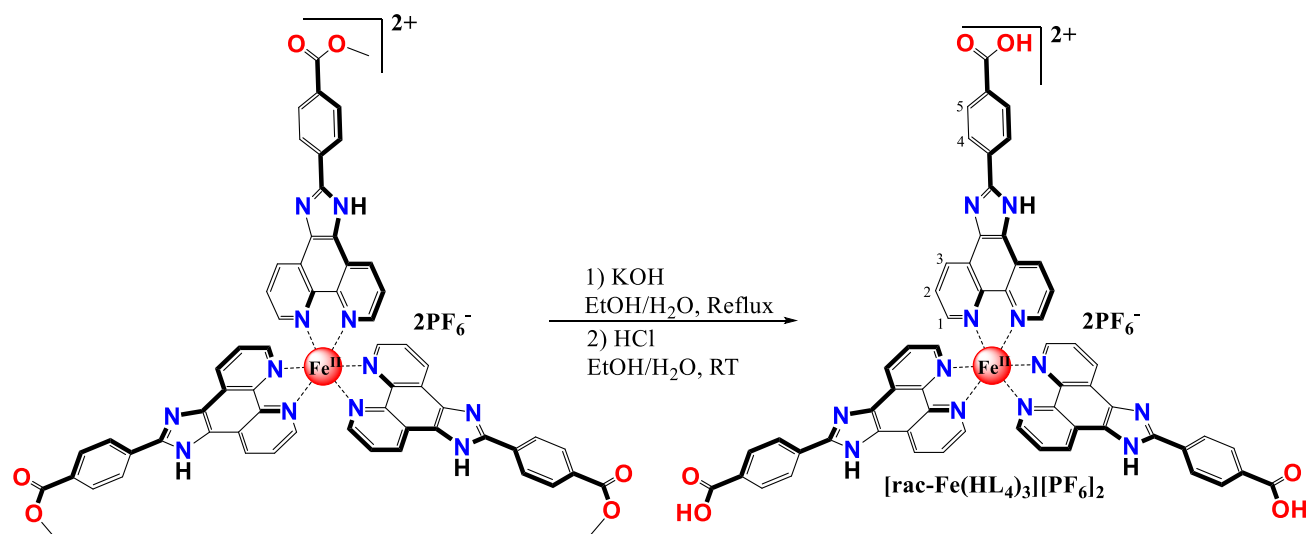
The product was synthesized as a racemate.

2-(4-Carboxymethylphenyl)imidazo[4,5-f][1,10]phenanthroline (0.36g, 1 mmol) was dissolved in 40 ml of ethanol. $(\text{NH}_4)_2\text{Fe}(\text{SO}_4)_2 \cdot 6\text{H}_2\text{O}$ (0.1383g, 0.35 mmol) was dissolved in 10 ml of water. The solution was added to the phenanthroline solution and was heated at 60°C for 24h. The reaction mixture was cooled to RT and the solvents were evaporated under reduced pressure. Subsequently, 30 ml of a KPF_6 aqueous solution (0.5g, 2.7 mmol of KPF_6) were added to the residue, the mixture was suspended in ultrasonic bath, filtered off and washed two times with cold water that afforded a dark red powder. Yield = 0.33g (88.7%).

$^1\text{H-NMR}$ (DMSO- d_6 , 500 MHz, 25 °C) δ ppm: 9.13 (bs, 6H, H^3), 8.48 (bs, 6H, H^1), 8.26 (bs, 6H, H^5), 7.82-7.73 (m, 12H, H^2 , H^4), 3.94 (bs, 9H, CH_3)

ESI-MS: expected $m/z = 559.48$ $[\text{M}-2\text{PF}_6]^{2+}$; found $m/z = 559.14$ $[\text{M}-2\text{PF}_6]^{2+}$

**Tris[2-(4-Carboxyphenyl)imidazo[4,5-f][1,10]phenanthroline] Fe(II)
hexafluorophosphate ([rac-Fe(HL₄)₃][PF₆]₂)**



The product was synthesized as a racemate.

Tris[2-(4-Carboxymethylphenyl)imidazo[4,5-f][1,10]phenanthroline] Fe(II) hexafluorophosphate (0.33g, 0.2 mmol) was dissolved in 50 ml of EtOH. Subsequently, 15 ml of 4% KOH aqueous solution were added. The reaction mixture was refluxed for 5h, then cooled to RT and acidified with HCl to pH = 5-6. The reaction mixture was filtered off, washed one time with 30 ml a KPF₆ aqueous solution (0.5g, 2.7 mmol of KPF₆) and two times with water that afforded a bright red solid. Yield = 0.279g (91.5%)

¹H-NMR (D₂O, 500 MHz, 25 °C, 1 mg KOH) δ ppm: 8.51 (bs, 6H, H³), 8.06 (bs, 6H, H¹), 7.87 (bs, 6H, H⁵), 7.38 (bs, 6H, H²), 7.05 (bs, 6H, H⁴)

ESI-MS: expected $m/z = 538.44$ [M-2PF₆]²⁺; found $m/z = 538.11$ [M-2PF₆]²⁺

IR: 3084(bm), 1707(m), 1615(m), 1555(m), 1481(m), 1447(w), 1365(s), 1321(m), 1303(m), 1267(m), 1198(m), 1075(s), 1016(m), 962(m), 864(m), 808(s), 712(s), 673(s), 619(s), 519(s), 466(s) cm⁻¹.

Elemental Analysis:

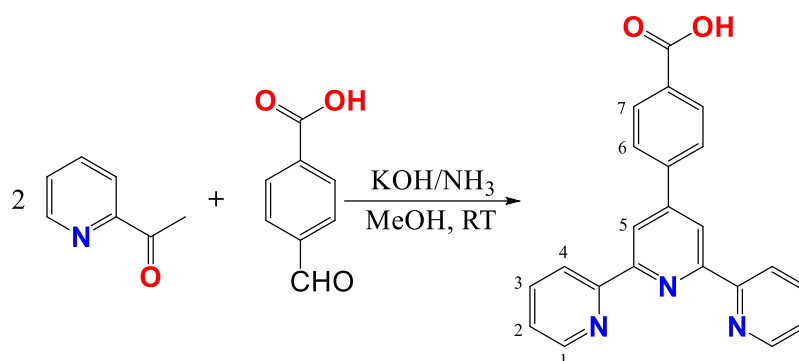
% calculated: C, 51.37%; H, 2.87%; N, 11.98% for [rac-Fe(HL₄)₃][PF₆]₂•2H₂O

% found: C, 51.35%; H, 2.87%; N, 11.99%



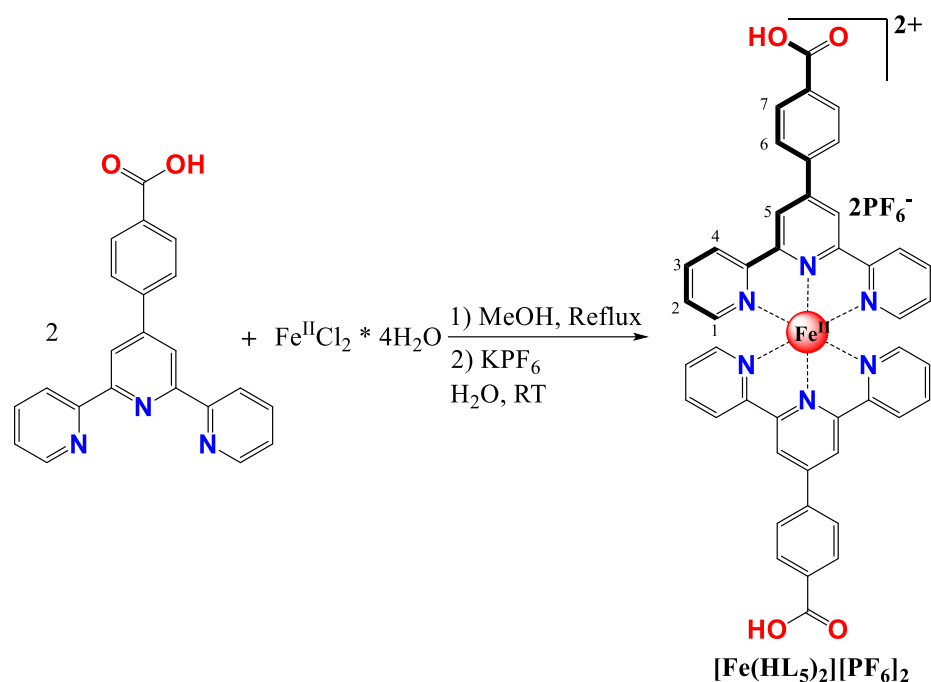
II.3. Synthesis of terpyridine connectors

4'-(4-Carboxyphenyl)-2,2':6',2''-terpyridine



The product was synthesized according to the already reported procedure.²²⁴

¹H-NMR (DMSO-d₆, 500 MHz, 25 °C) δ ppm: 9.02 (d, $J = 8.0$ Hz, 2H, H¹), 8.86 (s, 2H, H⁵), 8.93 (d, $J = 5.3$ Hz, 2H, H⁴), 8.39 (m, 2H, H³), 8.21 (d, $J = 8.6$ Hz, 2H, H⁷), 8.17 (d, $J = 8.6$ Hz, 2H, H⁶), 7.84 (m, 2H, H²)

Bis[4'-(4-Carboxyphenyl)-2,2':6',2''-terpyridine] Fe(II) hexafluorophosphate**([Fe(HL₅)₂][PF₆]₂)**

4'-(4-Carboxyphenyl)-2,2':6',2''-terpyridine (0.3g, 0.8 mmol) was dissolved in 150 ml of methanol. Iron(II) chloride tetrahydrate (0.083g, 0.4 mmol) was added subsequently. The reaction mixture was refluxed for 24h and then allowed to cool to RT. The solvents were removed under reduced pressure. 30 ml of a KPF₆ aqueous solution (0.5g, 2.7 mmol of KPF₆) were added to the residue and the mixture was suspended in the ultrasonic bath and then filtered off; it afforded a dark purple solid. Yield = 0.41g (94.6%).

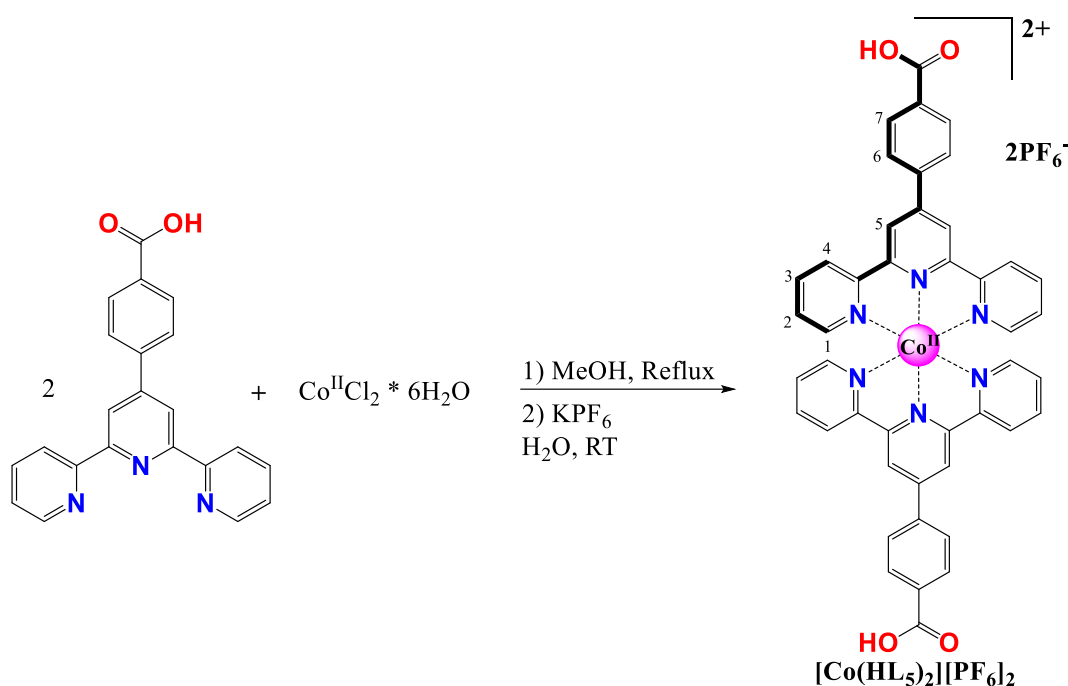
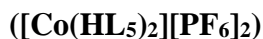
¹H-NMR (DMSO-d₆, 500 MHz, 25 °C) δ ppm: 9.76 (bs, 4H, H⁵), 9.10 (bs, 4H, H¹), 8.68 (bs, 4H, H⁴), 8.35 (bs, 4H, H³), 8.05 (bs, 4H, H⁷), 8.05 (bs, 4H, H²), 7.20 (bs, 4H, H⁶)

ESI-MS: expected $m/z = 381.31$ [M-2PF₆]²⁺; found $m/z = 381.10$ [M-2PF₆]²⁺

IR: 1716(s), 1611(m), 1543(w), 1486(w), 1472(w), 1435(w), 1418(w), 1401(m), 1367(w), 1283(s), 1252(s), 1192(m), 1154(s), 1112(s), 1064(m), 1055(s), 1046(m), 965(w), 900(w), 834(s), 791(m), 772(s), 760(m), 736(m), 705(m), 688(w), 656(w), 618(m), 605(m), 588(s), 557(s), 515(w), 462(m), 424(w) cm⁻¹.

Elemental Analysis: % calculated: C, 50.21%; H, 2.77%; N, 7.98%

% found: C, 50.83%; H, 3.60%; N, 7.62%

**Bis[4'-(4-Carboxyphenyl)-2,2':6',2''-terpyridine] Co(II) hexafluorophosphate**

4'-(4-Carboxyphenyl)-2,2':6',2''-terpyridine (0,3g, 0.8 mmol) was dissolved in 150 ml of methanol. Cobalt(II) chloride hexahydrate (0.053g, 0.4 mmol) was added subsequently. The reaction mixture was refluxed for 24h and then allowed to cool to RT. The solvents were removed under reduced pressure. 30 ml of KPF_6 aqueous solution (0.5g, 2.7 mmol of KPF_6) were added to the residue and the mixture was suspended in the ultrasonic bath and then filtered off; it afforded a dark red solid. Yield = 0.36g (79.5%).

$^1\text{H-NMR}$ (DMSO- d_6 , 500 MHz, 25 °C) δ ppm: 13.2 (bs), 10.41 (bs), 9.10 (bs)

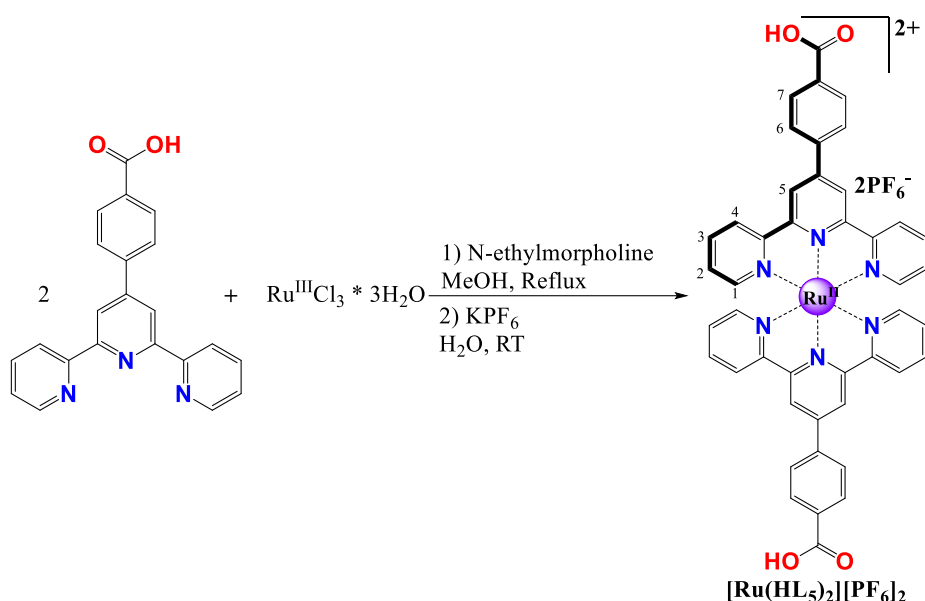
ESI-MS: expected $m/z = 1055.62$ $[\text{M}]^+$, 382.85 $[\text{M}-2\text{PF}_6]^{2+}$; found $m/z = 1055.10$ $[\text{M}]^+$, 382.58 $[\text{M}-2\text{PF}_6]^{2+}$

IR: 1716(s), 1623(m), 1529(w), 1503(w), 1481(w), 1445(w), 1423(w), 1412(m), 1291(s), 1267(s), 1203(m), 1157(s), 1132(s), 1096(m), 1066(s), 1046(m), 983(m), 913(m), 825(s), 801(m), 779(s), 763(m), 751(m), 723(m), 659(m), 628(m), 613(m), 590(s), 562(s), 523(w), 479(m), 431(w) cm^{-1} .

Elemental Analysis: % calculated: C, 50.06%; H, 2.86%; N, 7.96%

% found: C, 49.78%; H, 2.93%; N, 7.91%

Bis[4'-(4-Carboxyphenyl)-2,2':6',2''-terpyridine] Ru(II) hexafluorophosphate
([Ru(HL₅)₂][PF₆]₂)



The product was synthesized based on the already reported procedure with modifications.²²⁴

4'-(4-Carboxyphenyl)-2,2':6',2''-terpyridine (0.3g, 0.85 mmol) was dissolved in 200 ml of methanol. Ruthenium(III) chloride trihydrate (0.15g, 0.64 mmol) was added subsequently. N-ethylmorpholine (0.15ml, 1.19 mmol) was added to the reaction mixture. The reaction mixture was refluxed overnight. The solvents were removed under reduced pressure. 30 ml of KPF₆ aqueous solution (0.5g, 2.7 mmol of KPF₆) were added to the residue and the mixture was suspended in the ultrasonic bath and then filtered off; it afforded a dark red solid. Yield = 0.45g (97.3%)

The ¹H-NMR spectrum was in accordance with the already reported one.²²⁴

¹H-NMR (DMSO-d₆, 500 MHz, 25 °C) δ ppm: 9.56 (s, 4H, H⁵), 9.14 (d, *J* = 8.1 Hz, 4H, H¹), 8.57 (d, *J* = 8.5 Hz, 4H, H⁴), 8.30 (m, 4H, H³), 8.06 (m, 4H, H²), 7.57 (d, *J* = 5.5 Hz, 4H, H⁷), 7.28 (m, 4H, H⁶)

ESI-MS: expected *m/z* = 403.92 [M-2PF₆]²⁺; found *m/z* = 404.07 [M-2KPF₆]²⁺

IR: 3502(wb), 1716(s), 1604(s), 1547(w), 1470(m), 1430 (m), 1398(m), 1327(w), 1247(s), 1190(m), 1184(w), 1116(m), 1015(m), 892(m), 833(s), 790(s), 771(s), 764(m), 745(m), 692(m), 655(m), 620(w), 557(s), 500(m), 475(s), 439(s) cm⁻¹.

Elemental Analysis:

% calculated: C, 46.61%; H, 3.02%; N, 7.41% for [Ru(HL₅)₂][PF₆]₂•2H₂O

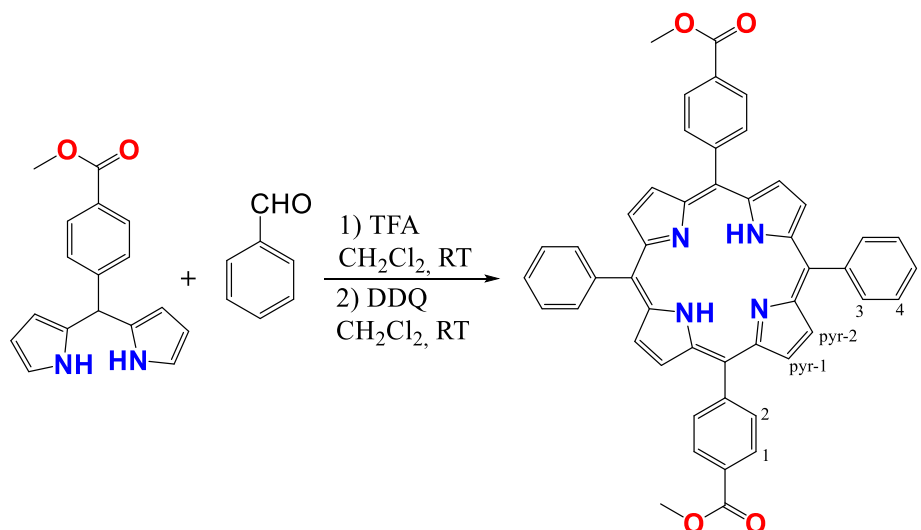
% found: C, 46.46%; H, 3.22%; N, 7.35%.



II.4. Synthesis of porphyrin connector

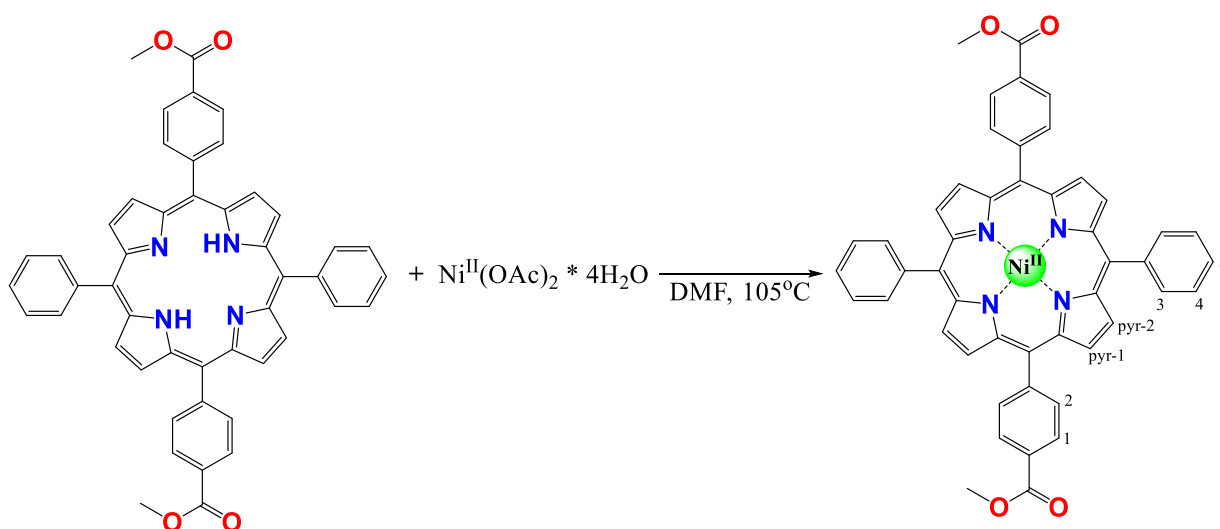
[5,15-bis(4-carboxyphenyl)-10,20-diphenylporphyrinato] Ni(II) (Ni(H₂L₆))

5,15-bis(4-carboxymethylphenyl)-10,20-diphenylporphyrin



The product was synthesized according to the already reported procedure.¹⁷²

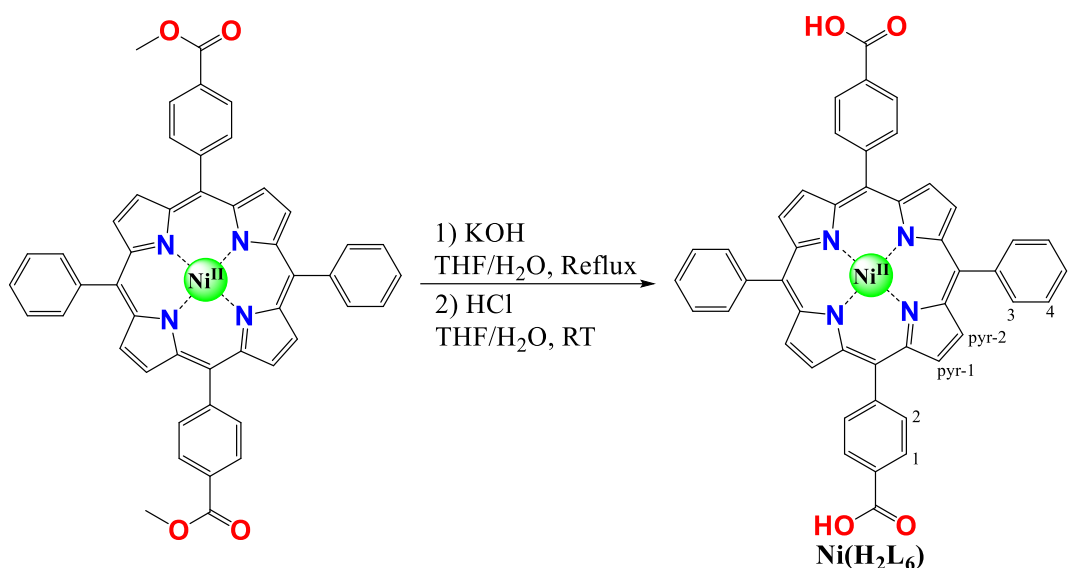
¹H-NMR (CDCl₃, 300 MHz, 25 °C) δ ppm: 8.87 (d, *J* = 4.9 Hz, 4H, pyr-H¹), 8.79 (d, *J* = 4.9 Hz, 4H, pyr-H²), 8.44 (d, *J* = 8.5 Hz, 4H, H¹), 8.31 (d, *J* = 8.5 Hz, 4H, H²), 8.21 (m, 4H, H⁴), 7.77 (m, 6H, H³, H⁵), 4.11 (s, 6H, CH₃), -2.79 (bs, 2H, NH)

[5,15-bis(4-carboxymethylphenyl)-10,20-diphenylporphyrinato] Ni(II)

The product was synthesized based on the already reported procedure with modifications.¹⁵⁹

5,15-bis(4-carboxymethylphenyl)-10,20-diphenylporphyrin (0.260g, 0.4 mmol) and nickel(II) acetate tetrahydrate (0.450g, 1.8 mmol) were dissolved in 30 ml of DMF. The reaction mixture was heated at 105°C for 24h. The solvent was evaporated under reduced pressure. The residue was suspended in 50 ml of methanol and the suspension was filtered off; it afforded a dark purple powder. Yield = 0.191g (68.1%)

¹H-NMR (CDCl₃, 300 MHz, 25 °C) δ ppm: 8.76 (d, *J* = 5.0 Hz, 4H, pyr-H¹), 8.68 (d, *J* = 5.0 Hz, 4H, pyr-H²), 8.37 (d, *J* = 8.2 Hz, 4H, H¹), 8.10 (d, *J* = 8.2 Hz, 4H, H²), 8.00 (m, 4H, H⁴), 7.69 (m, 6H, H³, H⁵), 3.99 (s, 6H, CH₃)

**[5,15-bis(4-carboxyphenyl)-10,20-diphenylporphyrinato] Ni(II) (Ni(H₂L₆))**

[5,15-bis(4-carboxymethylphenyl)-10,20-diphenylporphyrinato] Ni(II) (0.191g, 0.24 mmol) was dissolved in 20 ml of THF. Subsequently, 20 ml of 4% KOH aqueous solution were added. The reaction mixture was refluxed for 5h and allowed to cool to RT. The reaction mixture was acidified with a 12% HCl solution until pH = 5-6, then filtered off and washed two times with water to afford a dark red powder. Yield = 0.173g (93.9%)

¹H-NMR (DMSO-d₆, 500 MHz, 25 °C) δ ppm: 8.74 (bs, 8H, pyr-H¹, pyr-H²), 8.31 (d, *J* = 8.4 Hz, 4H, H¹), 8.14 (d, *J* = 8.4 Hz, 4H, H²), 8.01 (m, 4H, H⁴), 7.77 (m, 6H, H³, H⁵)

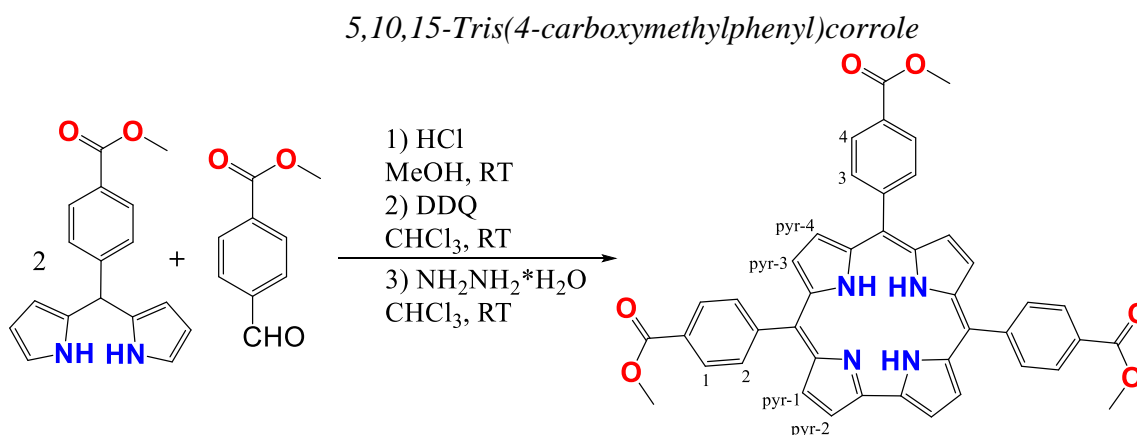
¹³C-NMR (DMSO-d₆, 126 MHz, 25 °C) δ ppm: 167.83, 144.82, 142.82, 142.28, 140.31, 134.14, 133.90, 133.35, 132.99, 130.98, 128.68, 128.55, 127.69, 119.75

ESI-MS: expected *m/z* = 759.45 [M]⁺; found *m/z* = 758.15 [M]⁺;

IR: 3284(wb), 1725(s), 1608(m), 1585(m), 1542(w), 1508(w), 1465(w), 1436(w), 1387(m), 1351(s), 1318(w), 1271(s), 1248(m), 1206(w), 1175(w), 1111(m), 1073(m), 1003(s), 975(m), 919(w), 823(m), 799(s), 757(s), 748(m), 712(s), 703(s), 667(m), 655(m), 530(w), 496(m), 468(m), 420(w) cm⁻¹.

Elemental Analysis: % calculated: C, 70.88%; H, 4.14%; N, 7.19% for Ni(H₂L₆)•H₂O

% found: C, 71.07%; H, 3.89%; N, 7.23%

II.5. Synthesis of corrole connector**[5,10,15-Tris(4-carboxyphenyl)corrolato] Co(III) (Co(H₃L₇))**

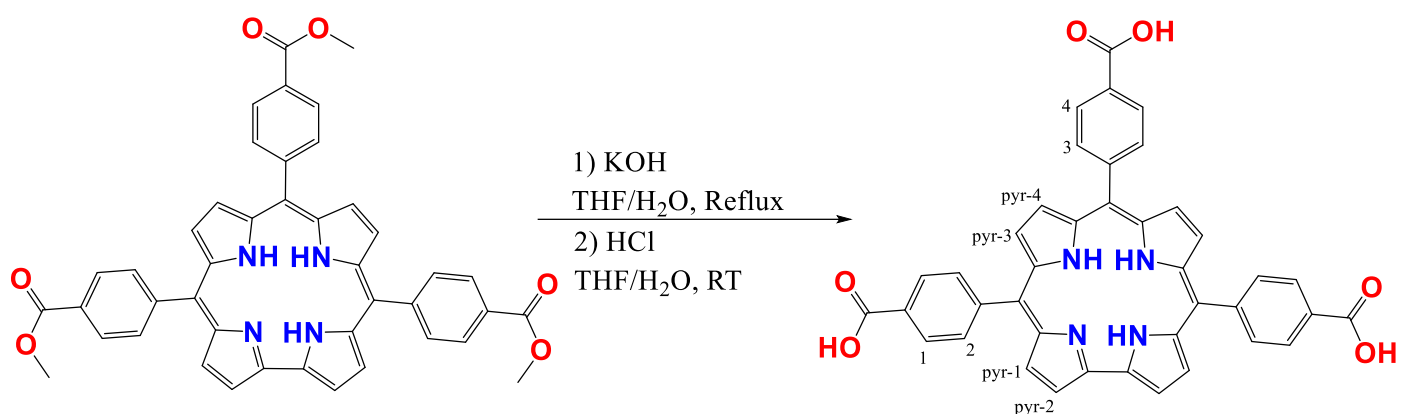
The product was synthesized based on the already reported procedure with modifications.¹⁸⁰

5-(4-Carboxymethylphenyl)dipyrromethane (0.5g, 1.8 mmol) and 4-carboxymethylbenzaldehyde (0.1464g, 0.9 mmol) were dissolved in 100 ml of degassed methanol. Subsequently, 100 ml of 3.5% HCl aqueous solution were added dropwise under vigorous stirring for 30 minutes. The reaction mixture was stirred for 2.5h at RT under light protection. The mixture was then added to a mixture of 100 ml of CHCl₃ and 100 ml of saturated NaHCO₃ solution. The chloroform phase was separated, dried over MgSO₄ and filtered off. The volume of the mixture was increased to 200 ml of CHCl₃ and degassed. DDQ (0.4057g, 1.8 mmol) was added. The reaction mixture was stirred overnight at RT. Hydrazine (0.2 ml, 4.5 mmol) was added and the mixture was stirred additionally 10 minutes. The reaction mixture was filtered off and the filtrate was evaporated to afford the crude product. The final product was obtained by recrystallization process from DCM/methanol as a dark purple solid. Yield = 0.405g (64.8%)

¹H-NMR (CDCl₃, 300 MHz, 25 °C) δ ppm: 8.90 (d, *J* = 4.3 Hz, 2H, Pyr-H³), 8.79 (d, *J* = 4.8 Hz, 2H, Pyr-H¹), 8.51 (d, *J* = 4.3 Hz, 2H, Pyr-H⁴), 8.47 (d, *J* = 4.8 Hz, 2H, Pyr-H²), 8.44-8.32 (m, 10H, H^{1,2,4}), 8.18 (d, *J* = 8.0 Hz, 2H, H³), 4.02 (s, 9H, CH₃)



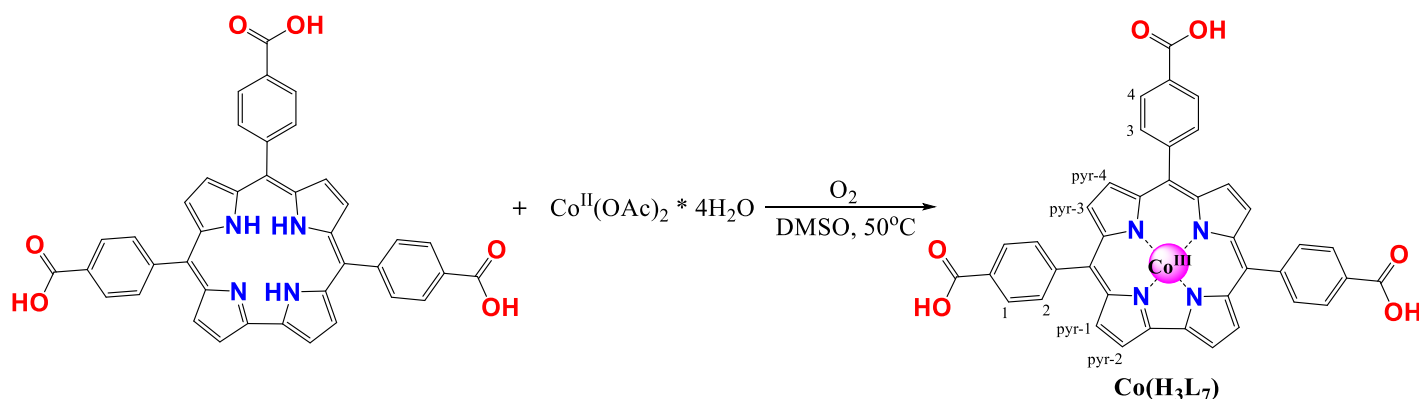
5,10,15-Tris(4-carboxyphenyl)corrole



The product was synthesized based on the already reported procedure with modifications.⁶

5,10,15-Tris(4-carboxymethylphenyl)corrole (0.2g, 0.3 mmol) was dissolved in 20 ml of THF. Subsequently, 20 ml of 4% KOH aqueous solution were added. The reaction mixture was refluxed overnight, allowed to cool to RT and acidified with 12% HCl to pH = 5-6. The reaction mixture was filtered off; it afforded a dark purple solid. Yield = 0.126g (67%).

¹H-NMR (DMSO-d₆, 500 MHz, 25 °C, NH₃ gas) δ ppm: 8.89 (d, *J* = 4.0 Hz, 2H, Pyr-H³), 8.63 (d, *J* = 4.6 Hz, 2H, Pyr-H¹), 8.49 (d, *J* = 4.0 Hz, 2H, Pyr-H⁴), 8.30 (d, *J* = 4.6 Hz, 2H, Pyr-H²), 8.27-8.14 (m, 10H, H^{1,2,4}), 8.01 (d, *J* = 7.9 Hz, 2H, H³)

[5,10,15-Tris(4-carboxyphenyl)corrolato] Co(III) (Co(H₃L₇))

The product was synthesized based on the already reported procedure with modifications.¹⁷⁸

5,10,15-Tris(4-carboxyphenyl)corrole (0.126g, 0.19 mmol) and cobalt(II) acetate tetrahydrate (0.05g, 0.20 mmol) were dissolved in 50 ml of DMSO and the mixture was heated and stirred at 50°C for 5h and then cooled to RT. The crude mixture was then poured into a cold NaCl aqueous solution (around 0.8 M), the resulting suspension was filtered, and the solid was washed three times with water that afforded a black solid. Yield = 0.124g (91.1%)

¹H-NMR (DMSO-d₆, 500 MHz, 25 °C, NH₃ gas) δ ppm: 8.80 (d, *J* = 3.8 Hz, 2H, Pyr-H³), 8.57 (d, *J* = 4.4 Hz, 2H, Pyr-H⁴), 8.37 (d, *J* = 4.4 Hz, 2H, Pyr-H¹), 8.33 (d, *J* = 4.4 Hz, 2H, Pyr-H²), 7.99-7.89 (m, 10H, H^{1,2,4}), 7.84 (d, *J* = 7.2 Hz, 2H, H³)

ESI-MS: expected *m/z* = 714.58 [M]⁺; found *m/z* = 714.10[M]⁺

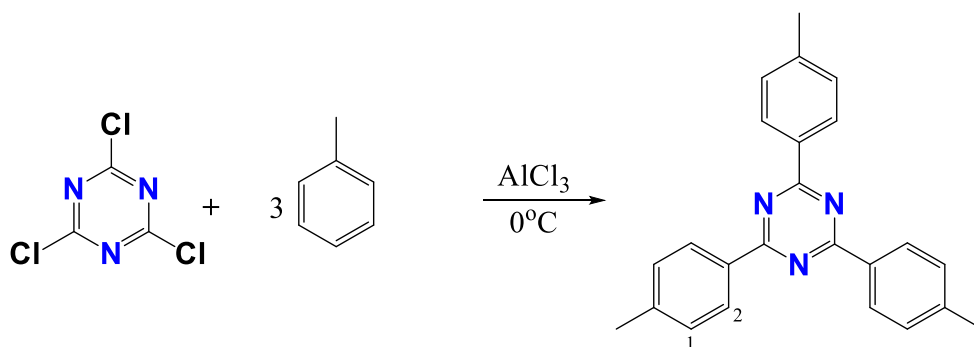
IR: 2795(wb), 1698(m), 1605(m), 1545(m), 1381(m), 1211(s), 1154(s), 1053(s), 1014(s), 952(s), 887(m), 832(m), 780(s), 720(s), 639(m), 556(m), 505(s) cm⁻¹.

Elemental Analysis: % calculated: C, 62.51%; H, 3.80%; N, 7.29% for **Co(H₃L₇)•3H₂O**

% found: C, 62.53%; H, 3.84%; N, 7.28%

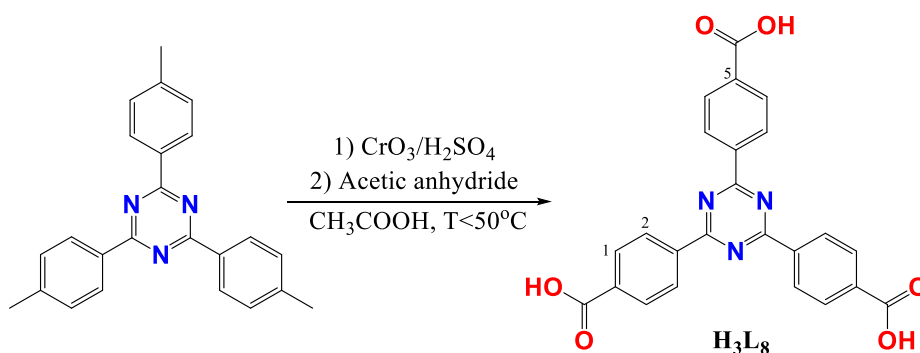


II.6. Synthesis of organic connectors

4,4',4''-(1,3,5-triazine-2,4,6-triyl)tribenzoic acid (H_3L_8)2,4,6-tri-*p*-tolyl-1,3,5-triazine

The product was synthesized according to the already reported procedure.¹⁸⁹

$^1\text{H-NMR}$ (CDCl_3 , 300 MHz, 25 °C) δ ppm: 8.65 (d, $J = 8.2$ Hz, 6H, H^1), 7.36 (d, $J = 8.1$ Hz, 6H, H^2), 2.48 (s, 9H, CH_3)

4,4',4''-(1,3,5-triazine-2,4,6-triyl)tribenzoic acid (H_3L_8)

The product was synthesized according to the already reported procedure.¹⁸⁹

$^1\text{H-NMR}$ (DMSO-d_6 , 500 MHz, 25 °C) δ ppm: 8.83 (d, $J = 8.4$ Hz, 6H, H^1), 8.20 (d, $J = 8.4$ Hz, 6H, H^2)

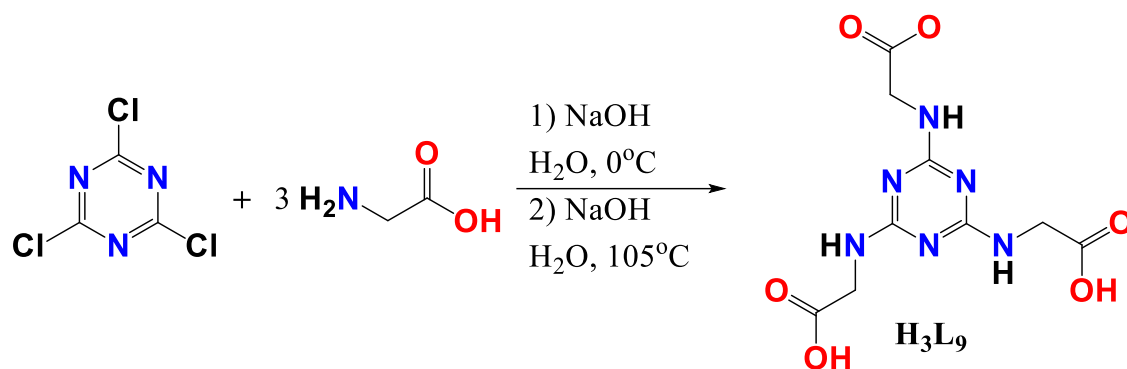
$^{13}\text{C-NMR}$ (DMSO-d_6 , 126 MHz, 25 °C) δ ppm: 171.09, 167.37, 139.17, 135.58, 130.31, 129.36

ESI-MS: expected $m/z = 441.40$ $[\text{M}]^+$; found $m/z = 442.11$ $[\text{M}]^+$

IR: 2885(wb), 2548(wb), 1694(m), 1583(m), 1518(s), 1409(m), 1360(s), 1283(s), 1107(w), 1018(m), 934(w), 879(m), 829(m), 789(s), 765(s), 693(m), 672(w), 549(m), 492(m) cm^{-1} .

Elemental Analysis: % calculated: C, 65.31%; H, 3.43%; N, 9.52%

% found: C, 65.25%; H, 3.51%; N, 9.63%

2,2',2''-((1,3,5-triazine-2,4,6-triyl)tris(azanediyl))triacetic acid (H₃L₉)

The product was synthesized according to the already reported procedure.¹⁹¹

¹H-NMR (DMSO-d₆, 500 MHz, 25 °C) δ ppm: 3.81 (s, 6H, CH₂), 6.83 (m, 3H, NH)

¹³C-NMR (DMSO-d₆, 126 MHz, 25 °C) δ ppm: 172.74, 165.86, 43.22

ESI-MS: expected $m/z = 300.23$ [M]⁺; found $m/z = 301.09$ [M]⁺

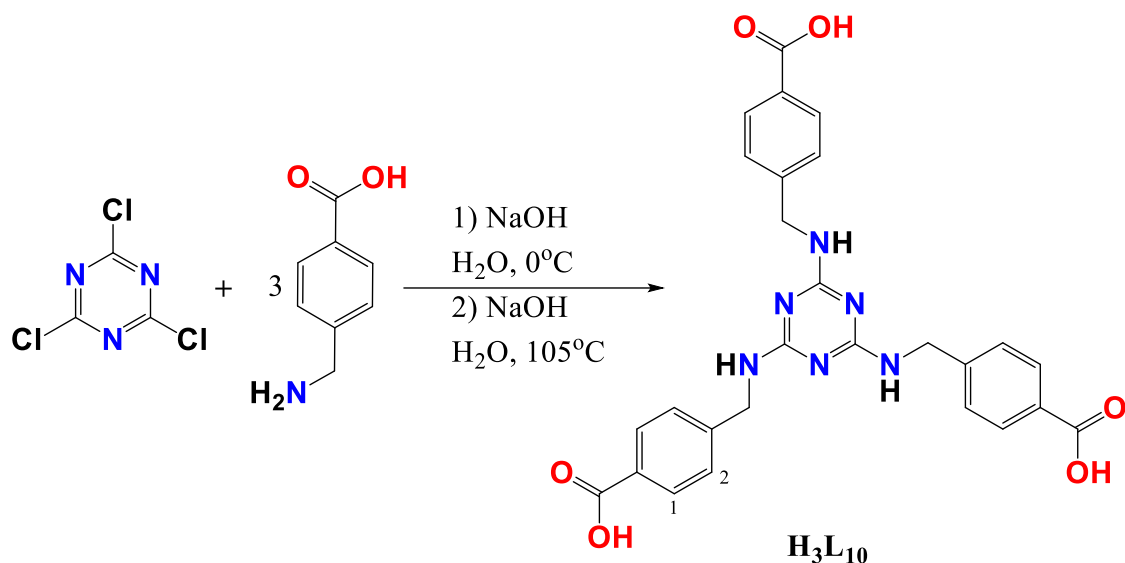
IR: 2549(mb), 1736(m), 1655(s), 1620(s), 1580(s), 1517(s), 1430(m), 1393(m), 1373(m), 1313(s), 1259(m), 1235(s), 1213(s), 1187(m), 1094(w), 1037(m), 959(m), 955(m), 900(w), 847(w), 782(s), 741(w), 686(m), 682(m), 622(m), 595(m), 562(s), 491(w), 429(m) cm⁻¹.

Elemental Analysis: % calculated: C, 35.07%; H, 3.92%; N, 27.27% for **H₃L₉•0.5H₂O**

% found: C, 35.14%; H, 3.95%; N, 27.16%



4,4',4''-(((1,3,5-triazine-2,4,6-triyl)tris(azanediyl))tris(methylene))tribenzoic acid (**H₃L₁₀**)



The product was synthesized according to the already reported procedure.¹⁹⁰

¹H-NMR (DMSO-d₆, 500 MHz, 25 °C) δ ppm: 7.85 (m, 6H, H¹), 7.37 (m, 6H, H²), 4.53 (m, 6H, CH₂)

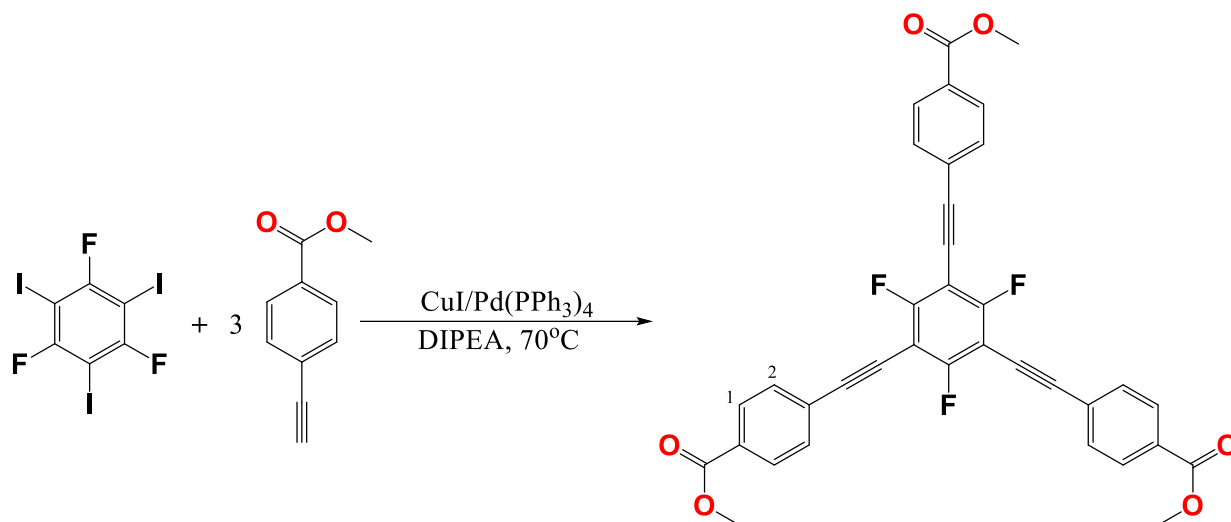
¹³C-NMR (DMSO-d₆, 126 MHz, 25 °C) δ ppm: 167.64, 146.11, 129.83, 129.52, 127.90, 127.45, 43.76

ESI-MS: expected $m/z = 528.53$ [M]⁺; found $m/z = 529.18$ [M]⁺

IR: 3278(mb), 2873(mb), 2553(wb), 1685(s), 1660(m), 1626(s), 1613(s), 1565(s), 1520(m), 1428(m), 1389(m), 1337(m), 1334(m), 1290(s), 1252(s), 1183(w), 1170(w), 1128(w), 1114(w), 1061(w), 1019(m), 939(m), 861(m), 846(m), 786(s), 752(s), 702(s), 642(m), 566(s), 551(s), 460(m) cm⁻¹.

Elemental Analysis: % calculated: C, 59.34%; H, 4.80%; N, 15.38% for **H₃L₁₀•H₂O**

% found: C, 59.33%; H, 4.80%; N, 15.43%

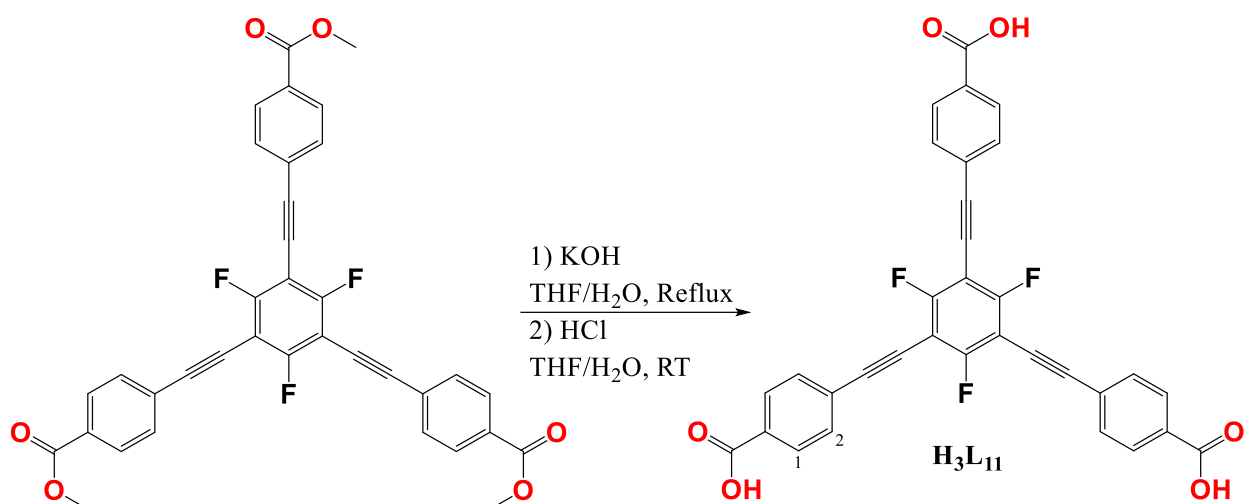
4,4',4''-((2,4,6-trifluorobenzene-1,3,5-triyl)tris(ethyne-2,1-diyl))tribenzoic acid (H₃L₁₁)*Trimethyl 4,4',4''-((2,4,6-trifluorobenzene-1,3,5-triyl)tris(ethyne-2,1-diyl))tribenzoate*

The product was synthesized based on the already reported procedure with modifications.²⁷

1,3,5-trifluoro-2,4,6-triiodobenzene (0.1g, 0.2 mmol), copper(I) iodide (0.0029g, 0.015 mmol) and Pd(PPh₃)₄ (0.0173g, 0.015 mmol) were dissolved in 30 ml of dry and degassed DIPEA. The mixture was stirred 30 minutes at RT under Ar-atmosphere. Methyl 4-ethynylbenzoate (0.1572g, 1 mmol) was added subsequently. The reaction mixture was heated 70°C for 48h and then allowed to cool to RT. The reaction mixture was portioned between CH₂Cl₂/H₂O (100/100). The water layer was extracted three times with 50 ml of CH₂Cl₂. The organic phases were collected, dried over MgSO₄ and solvents were removed under reduced pressure; it afforded an orange solid. Yield = 0.105g (88.2%).

¹H-NMR (CDCl₃, 300 MHz, 25 °C) δ ppm: 8.01 (d, *J* = 8.8 Hz, 6H, H¹), 7.59 (d, *J* = 8.7 Hz, 6H, H²), 3.93 (s, 9H, CH₃)

¹⁹F-NMR (CDCl₃, 300 MHz, 25 °C) δ ppm: -68.90 (Ar-F)

**4,4',4''-((2,4,6-trifluorobenzene-1,3,5-triyl)tris(ethyne-2,1-diyl))tribenzoic acid (H₃L₁₁)**

Trimethyl 4,4',4''-((2,4,6-trifluorobenzene-1,3,5-triyl)tris(ethyne-2,1-diyl))tribenzoate (0.105g, 0.17 mmol) was dissolved in 10 ml of THF. Subsequently, 10 ml of 4% KOH aqueous solution were added. The reaction mixture was refluxed for 5h and then allowed to cool to RT. The reaction mixture was acidified with 12% HCl to pH = 5-6, filtered off and washed two times with water; it afforded a yellowish solid. Yield = 0.090g (92.1%).

¹H-NMR (DMSO-d₆, 500 MHz, 25 °C) δ ppm: 7.98 (d, J = 8.4 Hz, 6H, H¹), 7.75 (d, J = 8.4 Hz, 6H, H²)

¹⁹F-NMR (CDCl₃, 300 MHz, 25 °C) δ ppm: -68.34 (Ar-F)

ESI-MS: expected m/z = 564.47 [M]⁺; found m/z = 565.09[M]⁺

IR: 3378(mb), 1692(w), 1467(m), 1410(s), 1305(s), 1196(s), 1179(s), 1114(m), 909(m), 882(s), 702(s), 643(m), 507(s) cm⁻¹.

Due to the low stability of H₃L₁₁ it was not possible to obtain Elemental Analysis data.

III. Synthesis of MOCs in the crystalline form

The synthesis of metal-organic cages (MOCs) was performed using all the previously discussed connectors and two main techniques: solvothermal and liquid-liquid diffusion.

- Solvothermal technique involves the reaction of a metal salt, a connector and sulfonycalix[4]arene in a solvent under high temperature and pressure in a sealed vial. The crystals form during the temperature decrease.
- Liquid-liquid diffusion technique involves the mutual diffusion of the base solution and the solution of metal salt, connector and sulfonycalix[4]arene at RT, which leads to the formation of MOCs in the crystalline form at the interface of the two solvents due to the self-assembly reaction on this interface.

Solvothermal technique

Sulfonycalix[4]arene (6 eq.), a metal salt (24 eq.) and a connector (8 eq. for triangular tridentate connectors and 12 eq. for linear bidentate connectors) in 3 ml DMF are put inside a sealed glass vessel. The vessel is heated at 80°C for one week that causes reaction and crystals formation during the temperature decrease.

Liquid-liquid diffusion technique

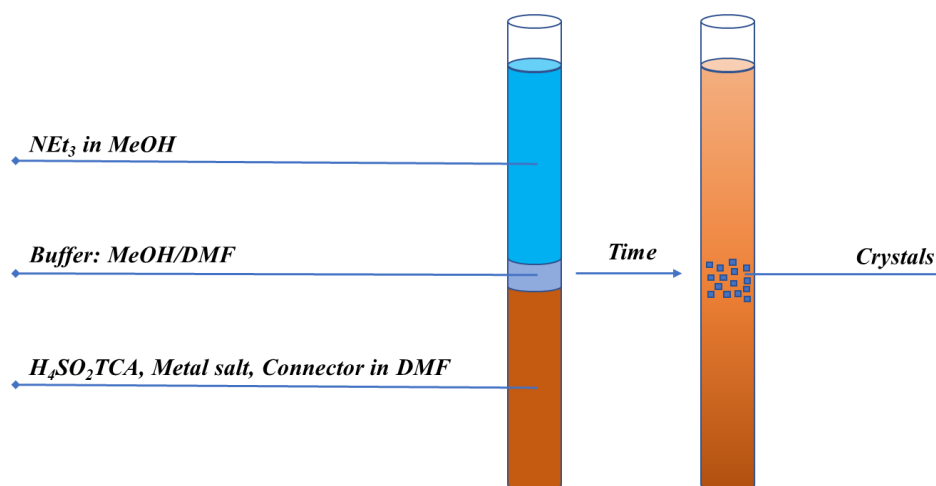
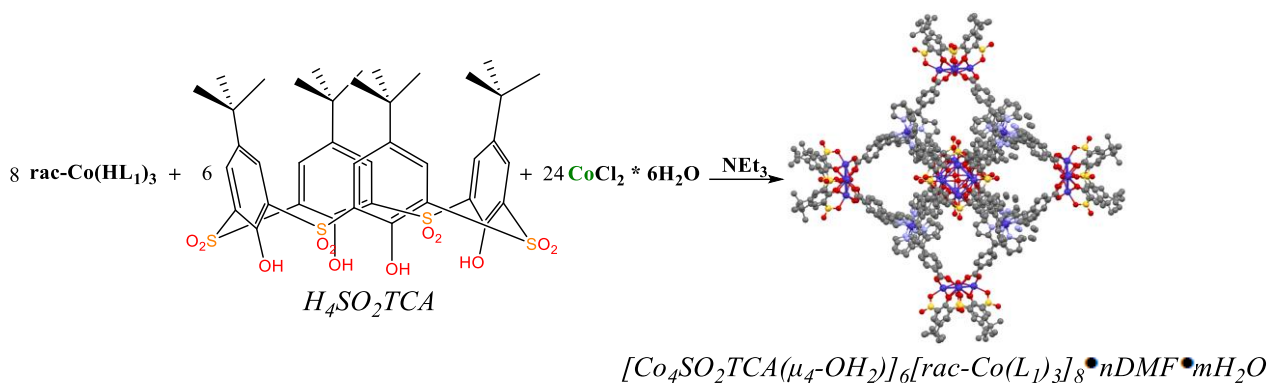


Figure 107 Liquid-liquid diffusion technique

In a diffusion tube of 10 cm length and with diameter of 1.5 cm, three layers of liquid are formed. The lower layer consists of sulfonycalix[4]arene (6 eq.), a metal salt (24 eq.) and a connector (8 eq. for triangular tridentate connectors and 12 eq. for linear bidentate connectors) in 5 ml of DMF. The buffer solution consists of the mixture 1 ml MeOH + 1 ml DMF. And the upper layer consists of triethylamine (60 eq.) solution in 3 ml of MeOH. The solutions of the reagents diffuse slowly into each other which causes crystals formation at the interface (Figure 107).



In a diffusion tube of 10 cm length and with diameter 1.5 cm, three layers of liquid are formed. The lower layer consists of sulfonylethylcalix[4]arene (0.02g, 23.55 μmol , 6 eq.), cobalt(II) chloride hexahydrate (0.0224g, 94.23 μmol , 24 eq.) and **rac-Co(HL₁)₃** (0.0296g, 31.4 μmol , 8 eq.) in 5 ml of DMF. The buffer solution consists of 1 ml MeOH + 1 ml DMF mixture. The upper layer consists of a triethylamine (0.033 ml, 235.57 μmol , 60 eq.) solution in 3 ml of MeOH. Slow liquids diffusion for 2 weeks caused the formation of large red octahedral single-crystals suitable for XRD.

Formula: $\text{C}_{624}\text{H}_{504}\text{Co}_{32}\text{N}_{48}\text{O}_{126}\text{S}_{24}$

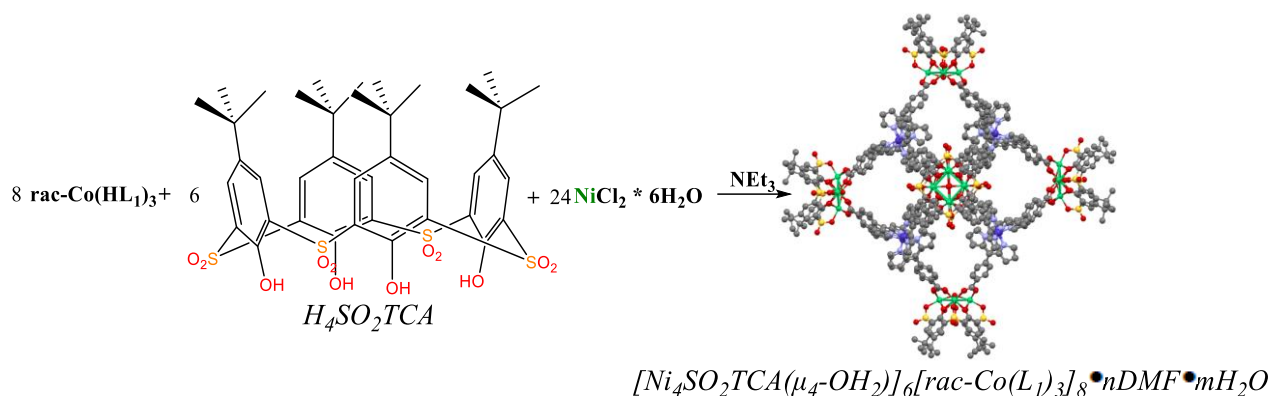
ESI-MS: calculated $m/z = 13346.1$ $[\text{M}]^-$; found $m/z = 2227.6$ $[\text{M}]^{6-}$, $[\text{M}]^- = 2227.6 \cdot z = 13365.6$

IM-MS: found $^{\text{DT}}\text{CCS}_{\text{N}_2} = 1878.5 \text{ \AA}^2$

Elemental Analysis: % calculated: C, 56.88%; H, 4.05%; N, 5.01%

% found: C, 52.52%; H, 5.05%; N, 7.48%

The differences in the calculated and the found values are related with the hygroscopicity of the samples (see details in **Chapter IV**).

$[Ni_4SO_2TCA]_6[rac-Co(L_1)_3]_8 \cdot nDMF \cdot mH_2O$ 

In a diffusion tube of 10 cm length and with diameter 1.5 cm, three layers of liquid are formed. The lower layer consists of sulfonylethylcalix[4]arene (0.02g, 23.55 μ mol, 6 eq.), nickel(II) chloride hexahydrate (0.0224g, 94.23 μ mol, 24 eq.) and **rac-Co(HL₁)₃** (0.0296g, 31.4 μ mol, 8 eq.) in 5 ml of DMF. The buffer solution consists of 1 ml MeOH + 1 ml DMF mixture. The upper layer consists of a triethylamine (0.033 ml, 235.57 μ mol, 60 eq.) solution in 3 ml of MeOH. Slow liquids diffusion for 2 weeks caused the formation of large red octahedral single-crystals suitable for XRD.

Formula: C₆₂₄H₅₀₄Co₈Ni₂₄N₄₈O₁₂₆S₂₄

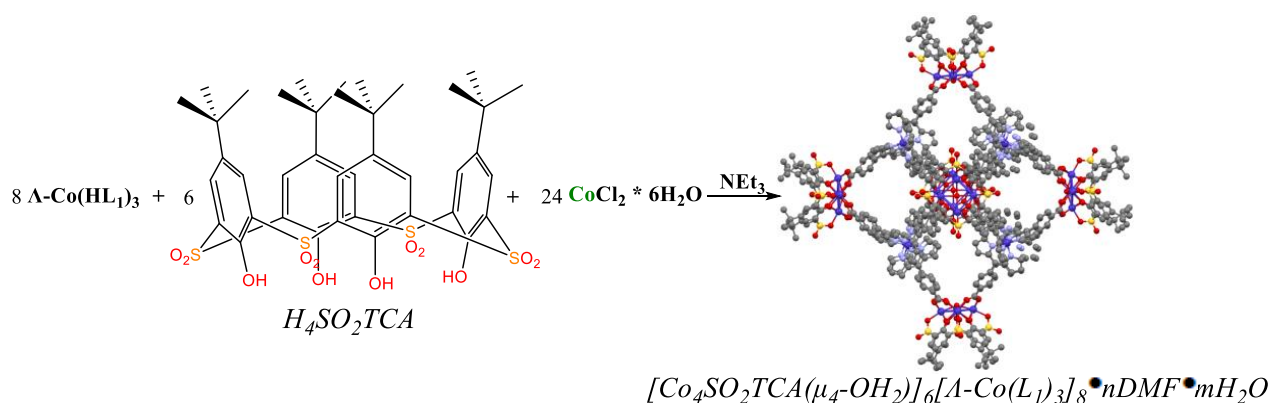
ESI-MS: calculated $m/z = 13340.7 [M]^-$; found $m/z = 2224.4 [M]^{6-}$, $[M]^- = 2224.4 * z = 13346.4$

IM-MS: found ^{DT}CCS_{N2} = 1855Å²

Elemental Analysis: % calculated: C, 56.90%; H, 4.05%; N, 5.01%

% found: C, 50.85%; H, 5.64%; N, 8.75%

The differences in the calculated and the found values are related with the hygroscopicity of the samples (see details in **Chapter IV**).



In a diffusion tube of 10 cm length and with diameter 1.5 cm, three layers of liquid are formed. The lower layer consists of sulfonylcalix[4]arene (0.02g, 23.55 μmol , 6 eq.), cobalt(II) chloride hexahydrate (0.0224g, 94.23 μmol , 24 eq.) and $\Lambda\text{-Co}(\text{HL}1)\mathbf{3}$ (0.0296g, 31.4 μmol , 8 eq.) in 5 ml of DMF. The buffer solution consists of 1 ml MeOH + 1 ml DMF mixture. The upper layer consists of a triethylamine (0.033 ml, 235.57 μmol , 60 eq.) solution in 3 ml of MeOH. Slow liquids diffusion for 2 weeks caused the formation of large red octahedral single-crystals suitable for XRD.

Formula: $\text{C}_{624}\text{H}_{504}\text{Co}_{32}\text{N}_{48}\text{O}_{126}\text{S}_{24}$

ESI-MS: calculated $m/z = 13346.1$ $[\text{M}]^-$; found $m/z = 2227.6$ $[\text{M}]^{6-}$, $[\text{M}]^- = 2227.6 \cdot z = 13393.8$

IM-MS: found $^{\text{DT}}\text{CCS}_{\text{N}_2} = 1830.0 \text{ \AA}^2$

Elemental Analysis: % calculated: C, 56.16%; H, 3.81%; N, 5.04%

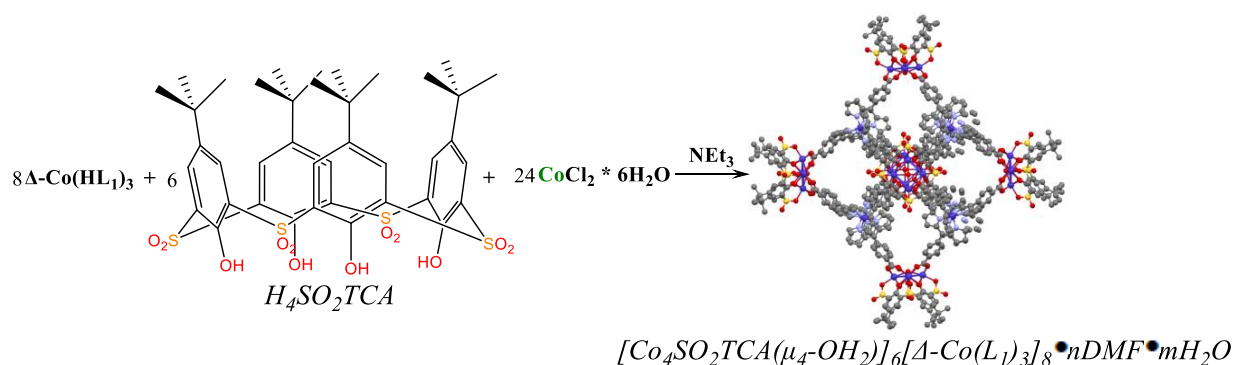
% found: C, 53.54%; H, 4.95%; N, 7.49%

The differences in the calculated and the found values are related with the hygroscopicity of the samples (see details in **Chapter IV**).

CD ($5 \cdot 10^{-5}\text{M}$, DCM, 2mm): 467 nm ($\theta = -401.79$ mdeg), 518 nm ($\theta = 433.51$ mdeg)

Chiral HPLC (ChiralPak 1A, Hexane/DCM/Ethanol = 90/5/5, flow rate = 0.5 ml/min, 450 nm): 51.06 min, ee=97%

Flack parameter: 0.422(4)



In a diffusion tube of 10 cm length and with diameter 1.5 cm, three layers of liquid are formed. The lower layer consists of sulfonylcalix[4]arene (0.02g, 23.55 μmol , 6 eq.), cobalt (II) chloride hexahydrate (0.0224g, 94.23 μmol , 24 eq.) and $\Delta\text{-Co}(\text{HL}_1)_3$ (0.0296g, 31.4 μmol , 8 eq.) in 5 ml of DMF. The buffer solution consists of 1 ml MeOH + 1 ml DMF mixture. The upper layer consists of a triethylamine (0.033 ml, 235.57 μmol , 60 eq.) solution in 3 ml MeOH. Slow liquids diffusion for 2 weeks caused the formation of large red octahedral single-crystals suitable for XRD.

Formula: $\text{C}_{624}\text{H}_{504}\text{Co}_{32}\text{N}_{48}\text{O}_{126}\text{S}_{24}$

ESI-MS: calculated $m/z = 13346.1$ $[\text{M}]^-$; found $m/z = 2227.6$ $[\text{M}]^{6-}$, $[\text{M}]^- = 2227.6 \cdot z = 13379.4$

IM-MS: found $^{\text{DT}}\text{CCS}_{\text{N}_2} = 1833.6 \text{ \AA}^2$

Elemental Analysis: % calculated: C, 56.16%; H, 3.81%; N, 5.04%

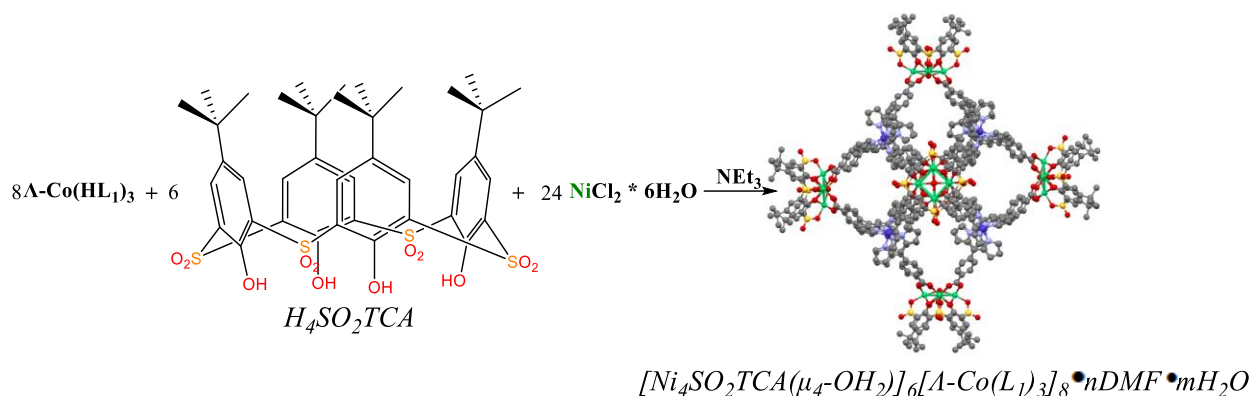
% found: C, 53.62%; H, 5.01%; N, 7.37%

The differences in the calculated and the found values are related with the hygroscopicity of the samples (see details in **Chapter IV**).

CD (5*10⁻⁵M, DCM, 2mm): 467 nm ($\theta = 418.23$ mdeg), 518 nm ($\theta = -463.17$ mdeg)

Chiral HPLC (ChiralPak 1A, Hexane/DCM/Ethanol = 90/5/5, flow rate = 0.5 ml/min, 450 nm): 28.10 min, ee=96%

Flack parameter: 0.242(5)



In a diffusion tube of 10 cm length and with diameter 1.5 cm, three layers of liquid are formed. The lower layer consists of sulfonylcalix[4]arene (0.02g, 23.55 μmol , 6 eq.), nickel (II) chloride hexahydrate (0.0224g, 94.23 μmol , 24 eq.) and $\Lambda\text{-Co}(\text{HL}_1)_3$ (0.0296g, 31.4 μmol , 8 eq.) in 5 ml of DMF. The buffer solution consists of 1 ml MeOH + 1 ml DMF mixture. The upper layer consists of a triethylamine (0.033 ml, 235.57 μmol , 60 eq.) solution in 3 ml of MeOH. Slow liquids diffusion for 2 weeks caused the formation of large red octahedral crystals suitable for XRD.

Formula: $\text{C}_{624}\text{H}_{504}\text{Co}_8\text{Ni}_{24}\text{N}_{48}\text{O}_{126}\text{S}_{24}$

ESI-MS: calculated $m/z = 13340.7$ $[\text{M}]^-$; found $m/z = 2226.2$ $[\text{M}]^{6-}$, $[\text{M}]^- = 2226.2 \cdot z = 13357.2$

IM-MS: found $^{\text{DT}}\text{CCS}_{\text{N}_2} =$ peak not resolved

Elemental Analysis: % calculated: C, 56.18%; H, 3.81%; N, 5.04%

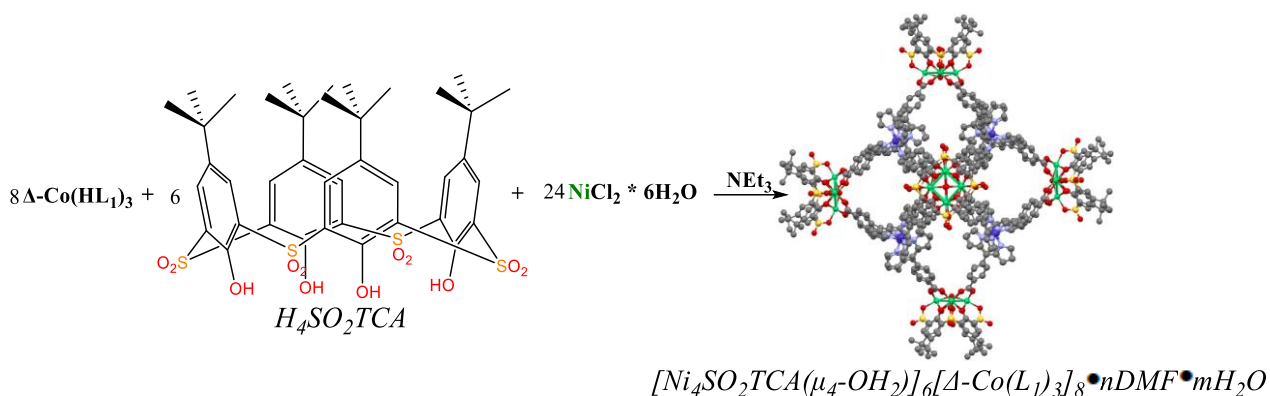
% found: C, 53.09%; H, 5.07%; N, 7.39%

The differences in the calculated and the found values are related with the hygroscopicity of the samples (see details in **Chapter IV**).

CD (5*10⁻⁵M, DCM, 2mm): 464 nm ($\theta = -395.16$ mdeg), 517 nm ($\theta = 452.06$ mdeg)

Chiral HPLC (ChiralPak 1A, Hexane/DCM/Ethanol = 90/5/5, flow rate = 0.5 ml/min, 450 nm): 51.04 min, ee=95%

Flack parameter: 0.215(5)



In a diffusion tube of 10 cm length and with diameter 1.5 cm, three layers of liquid are formed. The lower layer consists of sulfonylecalix[4]arene (0.02g, 23.55 μmol , 6 eq.), nickel(II) chloride hexahydrate (0.0224g, 94.23 μmol , 24 eq.) and $\Delta\text{-Co}(\text{HL}_1)_3$ (0.0296g, 31.4 μmol , 8 eq.) in 5 ml of DMF. The buffer solution consists of 1 ml MeOH + 1 ml DMF mixture. The upper layer consists of a triethylamine (0.033 ml, 235.57 μmol , 60 eq.) solution in 3 ml of MeOH. Slow liquids diffusion for 2 weeks caused the formation of large red octahedral single-crystals suitable for XRD.

Formula: $\text{C}_{624}\text{H}_{504}\text{Co}_8\text{Ni}_{24}\text{N}_{48}\text{O}_{126}\text{S}_{24}$

ESI-MS: calculated $m/z = 13340.7$ $[\text{M}]^-$; found $m/z = 2225.1$ $[\text{M}]^{6-}$, $[\text{M}]^- = 2225.1 \cdot z = 13350.6$

IM-MS: found $^{\text{DT}}\text{CCS}_{\text{N}_2} = 1846.1 \text{ \AA}^2$

Elemental Analysis: % calculated: C, 56.18%; H, 3.81%; N, 5.04%

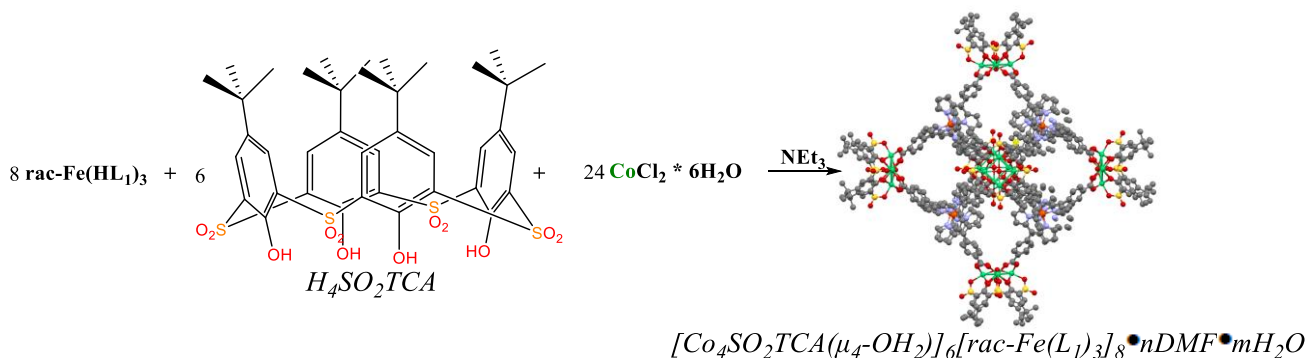
% found: C, 52.92%; H, 5.08%; N, 7.36%

The differences in the calculated and the found values are related with the hygroscopicity of the samples (see details in **Chapter IV**).

CD (5*10⁻⁵M, DCM, 2mm): 464 nm ($\theta = 421.29$ mdeg), 517 nm ($\theta = -479.56$ mdeg)

Chiral HPLC (ChiralPak 1A, Hexane/DCM/Ethanol = 90/5/5, flow rate = 0.5 ml/min, 450 nm): 28.15 min, ee=92%

Flack parameter: 0.181(4)



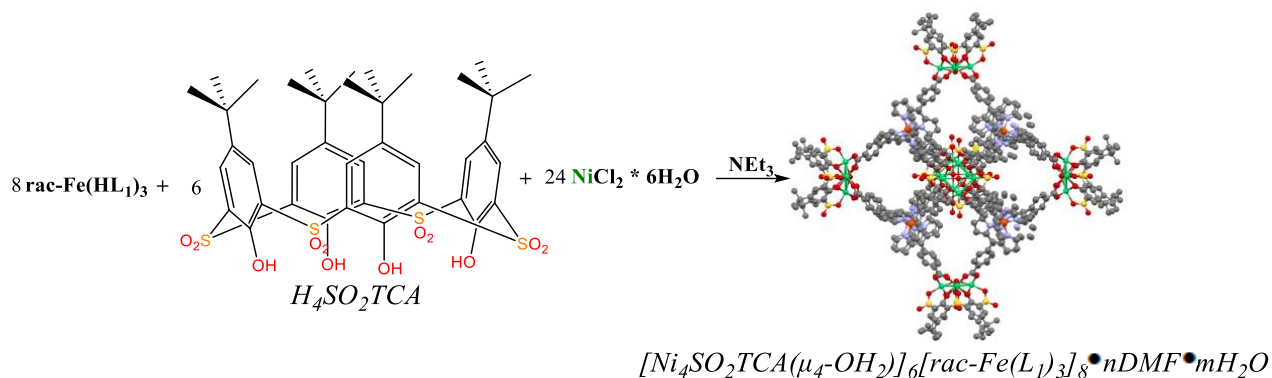
In a diffusion tube of 10 cm length and with diameter 1.5 cm, three layers of liquid are formed. The lower layer consists of sulfonylethylphenol (0.02g, 23.55 μmol , 6 eq), cobalt(II) chloride hexahydrate (0.0224g, 94.23 μmol , 24 eq.) and **rac-Fe(HL₁)₃** (0.0267g, 31.4 μmol , 8 eq.) in 5 ml of DMF. The buffer solution consists of 1 ml MeOH + 1 ml DMF mixture. The upper layer consists of a triethylamine (0.033 ml, 235.57 μmol , 60 eq.) solution in 3 ml of MeOH. Slow liquids diffusion for 2 weeks caused the formation of large red octahedral single-crystals suitable for XRD.

Formula: $\text{C}_{624}\text{H}_{504}\text{Fe}_8\text{Co}_{24}\text{N}_{48}\text{O}_{126}\text{S}_{24}$

Elemental Analysis: % calculated: C, 56.26%; H, 3.81%; N, 5.05%

% found: C, 52.52%; H, 5.05%; N, 7.48%

The differences in the calculated and the found values are related with the hygroscopicity of the samples (see details in **Chapter IV**).

$[\text{Ni}_4\text{SO}_2\text{TCA}]_6[\text{rac-Fe}(\text{L}_1)_3]_8 \cdot n\text{DMF} \cdot m\text{H}_2\text{O}$ 

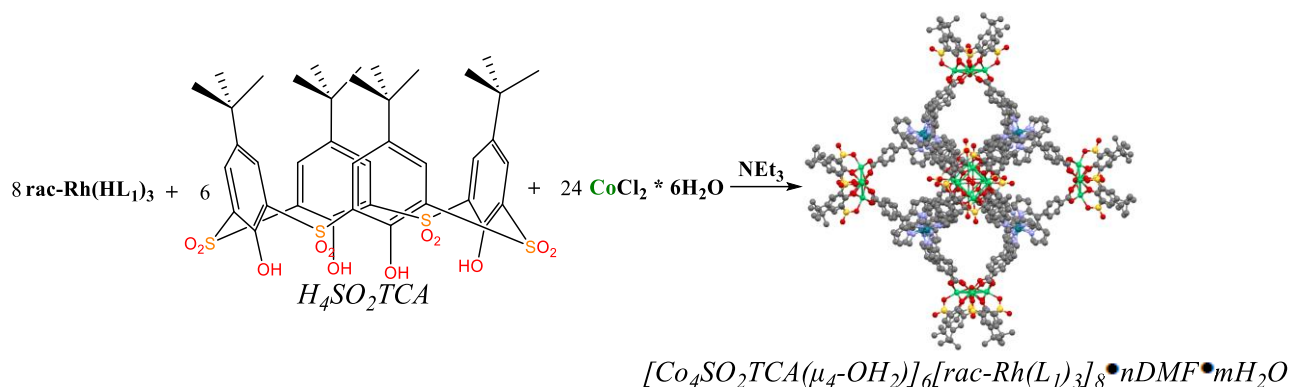
In a diffusion tube of 10 cm length and with diameter 1.5 cm, three layers of liquid are formed. The lower layer consists of sulfonylcalix[4]arene (0.02g, 23.55 μmol , 6 eq.), nickel(II) chloride hexahydrate (0.0224g, 94.23 μmol , 24 eq.) and **rac-Fe(HL₁)₃** (0.0267g, 31.4 μmol , 8 eq.) in 5 ml of DMF. The buffer solution consists of 1 ml MeOH + 1 ml DMF mixture. The upper layer consists of a triethylamine (0.033 ml, 235.57 μmol , 60 eq.) solution in 3 ml of MeOH. Slow liquids diffusion for 2 weeks caused the formation of large red octahedral single-crystals suitable for XRD.

Formula: $\text{C}_{624}\text{H}_{504}\text{Fe}_8\text{Ni}_{24}\text{N}_{48}\text{O}_{126}\text{S}_{24}$

Elemental Analysis: % calculated: C, 56.28%; H, 3.82%; N, 5.05%

% found: C, 49.72%; H, 5.32%; N, 8.15%

The differences in the calculated and the found values are related with the hygroscopicity of the samples (see details in **Chapter IV**).



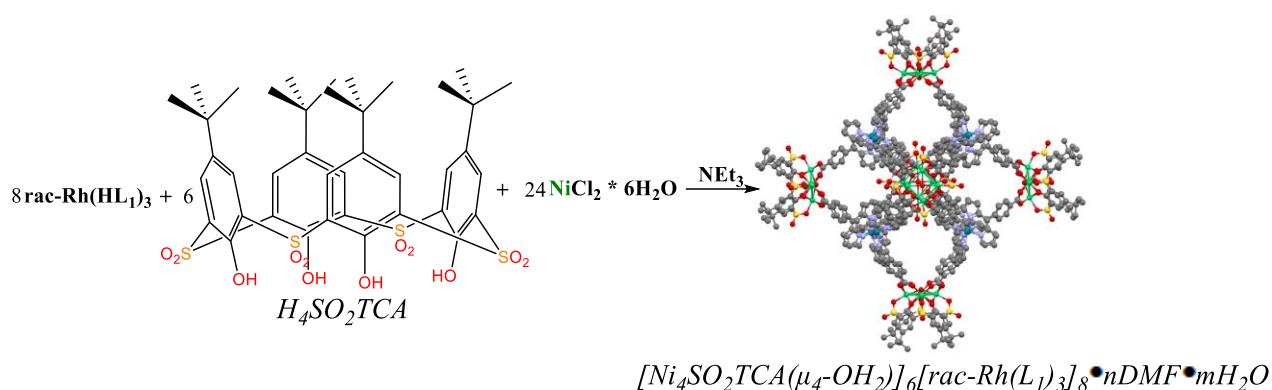
In a diffusion tube of 10 cm length and with diameter 1.5 cm, three layers of liquid are formed. The lower layer consists of sulfonylcalix[4]arene (0.02g, 23.55 μmol , 6 eq.), cobalt(II) chloride hexahydrate (0.0224g, 94.23 μmol , 24 eq.) and **rac-Rh(HL₁)₃** (0.028g, 31.4 μmol , 8 eq.) in 5 ml of DMF. The buffer solution consists of 1 ml MeOH + 1 ml DMF mixture. The upper layer consists of a triethylamine (0.033 ml, 235.57 μmol , 60 eq.) solution in 3 ml of MeOH. Slow liquids diffusion for 2 weeks caused the formation of large red octahedral single-crystals suitable for XRD.

Formula: $\text{C}_{624}\text{H}_{504}\text{Rh}_8\text{Co}_{24}\text{N}_{48}\text{O}_{126}\text{S}_{24}$

Elemental Analysis: % calculated: C, 54.71%; H, 3.71%; N, 4.91%

% found: C, 49.56%; H, 5.50%; N, 4.64%

The differences in the calculated and the found values are related with the hygroscopicity of the samples (see details in **Chapter IV**).

$$[\text{Ni}_4\text{SO}_2\text{TCA}]_6[\text{rac-Rh}(\text{L}_1)_3]_8 \cdot n\text{DMF} \cdot m\text{H}_2\text{O}$$


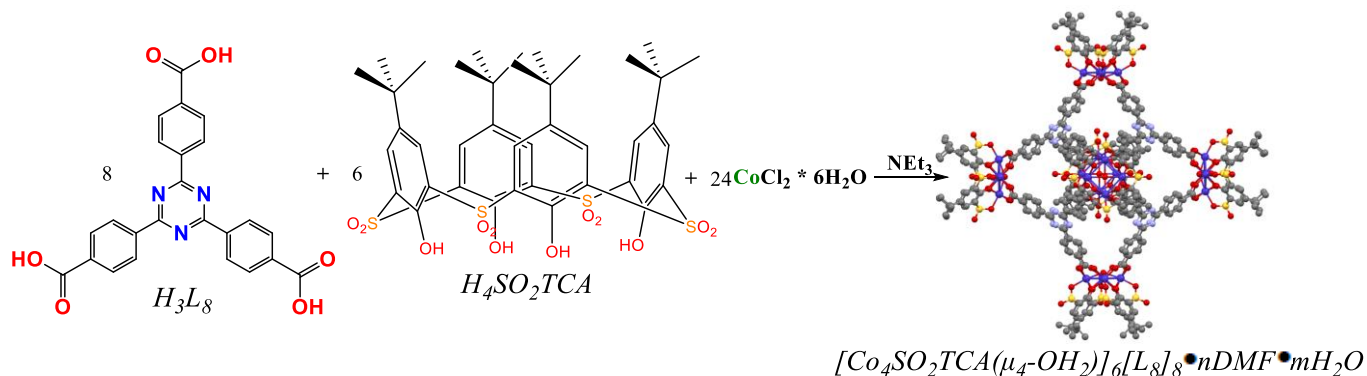
In a diffusion tube of 10 cm length and with diameter 1.5 cm, three layers of liquid are formed. The lower layer consists of sulfonycalix[4]arene (0.02g, 23.55 μmol , 6 eq.), nickel(II) chloride hexahydrate (0.0224g, 94.23 μmol , 24 eq.) and **rac-Rh(HL₁)₃** (0.028g, 31.4 μmol , 8 eq.) in 5 ml of DMF. The buffer solution consists of 1 ml MeOH + 1 ml DMF mixture. The upper layer consists of a triethylamine (0.033 ml, 235.57 μmol , 60 eq.) solution in 3 ml of MeOH. Slow liquids diffusion for 2 weeks caused the formation of large red octahedral single-crystals suitable for XRD.

Formula: $\text{C}_{624}\text{H}_{504}\text{Rh}_8\text{Ni}_{24}\text{N}_{48}\text{O}_{126}\text{S}_{24}$

Elemental Analysis: % calculated: C, 54.74%; H, 3.71%; N, 4.91%

% found: C, 48.98%; H, 5.69%; N, 7.64%

The differences in the calculated and the found values are related with the hygroscopicity of the samples (see details in **Chapter IV**).



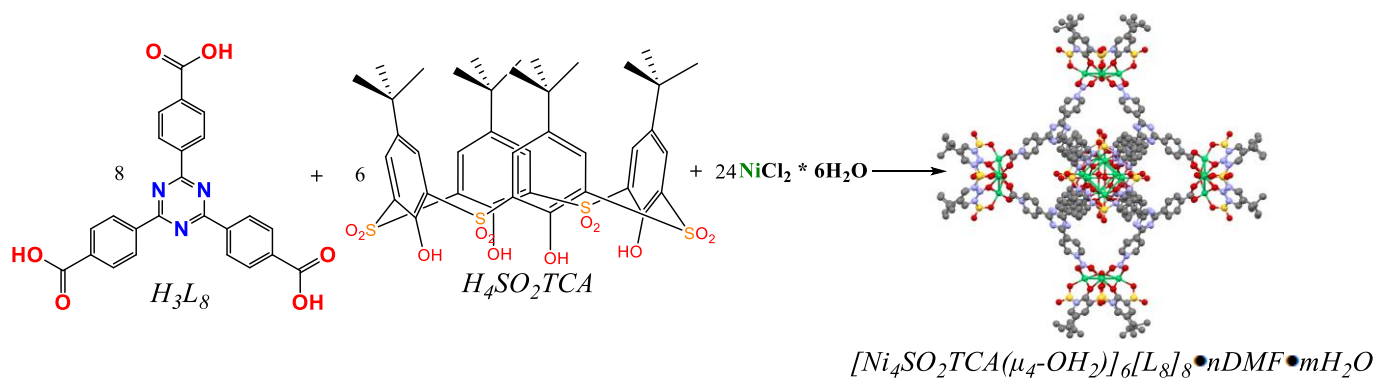
In a diffusion tube of 10 cm length and with diameter 1.5 cm, three layers of liquid are formed. The lower layer consists of sulfonycalix[4]arene (0.02g, 23.55 μmol , 6 eq.), cobalt(II) chloride hexahydrate (0.0224g, 94.23 μmol , 24 eq.) and **H₃L₈** (0.0139g, 31.4 μmol , 8 eq.) in 5 ml of DMF. The buffer solution consists of 1 ml MeOH + 1 ml DMF mixture. The upper layer consists of a triethylamine (0.033 ml, 235.57 μmol , 60 eq.) solution in 3 ml of MeOH. Slow liquids diffusion for 2 weeks caused the formation of large pink square single-crystals suitable for XRD.

Formula: $\text{C}_{432}\text{H}_{360}\text{Co}_{24}\text{N}_{24}\text{O}_{126}\text{S}_{24}$

Elemental Analysis: % calculated: C, 51.44%; H, 3.60%; N, 3.33%

% found: C, 49.34%; H, 4.15%; N, 3.60%

The differences in the calculated and the found values are related with the hygroscopicity of the samples (see details in **Chapter IV**).



Sulfonylcalix[4]arene (0.005g, 5.89 μmol , 6 eq.), nickel(II) chloride hexahydrate (0.0056g, 23.56 μmol , 24 eq.) and **H₃L₈** (0.0035g, 7.85 μmol , 8 eq.) in 3 ml DMF were put inside a sealed glass vessel. The vessel was heated at 80°C for one week that caused reaction and pale green tetrahedral single-crystals formation suitable for XRD.

Formula: $\text{C}_{432}\text{H}_{360}\text{Ni}_{24}\text{N}_{24}\text{O}_{126}\text{S}_{24}$

Elemental Analysis: % calculated: C, 51.47%; H, 3.60%; N, 3.33%

% found: C, 48.01%; H, 4.32%; N, 5.13%

The differences in the calculated and the found values are related with the hygroscopicity of the samples (see details in **Chapter IV**).

References

- (1) Zhang, D.; Ronson, T. K.; Zou, Y.-Q.; Nitschke, J. R. Metal–Organic Cages for Molecular Separations. *Nat Rev Chem* **2021**, *5* (3), 168–182. <https://doi.org/10.1038/s41570-020-00246-1>.
- (2) Pilgrim, B. S.; Champness, N. R. Metal-Organic Frameworks and Metal-Organic Cages – A Perspective. *ChemPlusChem* **2020**, *85* (8), 1842–1856. <https://doi.org/10.1002/cplu.202000408>.
- (3) Thompson, A. B.; Cope, S. J.; Swift, T. D.; Notestein, J. M. Adsorption of *n*-Butanol from Dilute Aqueous Solution with Grafted Calixarenes. *Langmuir* **2011**, *27* (19), 11990–11998. <https://doi.org/10.1021/la202508q>.
- (4) Tan, C.; Jiao, J.; Li, Z.; Liu, Y.; Han, X.; Cui, Y. Design and Assembly of a Chiral Metallosalen-Based Octahedral Coordination Cage for Supramolecular Asymmetric Catalysis. *Angew. Chem. Int. Ed.* **2018**, *57* (8), 2085–2090. <https://doi.org/10.1002/anie.201711310>.
- (5) Pellegrin, Y.; Forster, R. J.; Keyes, T. E. PH Dependent Photophysics and Role of Medium on Photoinduced Electron Transfer between Ruthenium Polypyridyl Complex and Anthraquinone. *Inorganica Chimica Acta* **2009**, *362* (6), 1715–1722. <https://doi.org/10.1016/j.ica.2008.08.008>.
- (6) Zhao, Y.; Qi, S.; Niu, Z.; Peng, Y.; Shan, C.; Verma, G.; Wojtas, L.; Zhang, Z.; Zhang, B.; Feng, Y.; Chen, Y.-S.; Ma, S. Robust Corrole-Based Metal–Organic Frameworks with Rare 9-Connected Zr/Hf-Oxo Clusters. *J. Am. Chem. Soc.* **2019**, *141* (36), 14443–14450. <https://doi.org/10.1021/jacs.9b07700>.
- (7) Huo, D.; Lin, F.; Chen, S.; Ni, Y.; Wang, R.; Chen, H.; Duan, L.; Ji, Y.; Zhou, A.; Tong, L. Ruthenium Complex-Incorporated Two-Dimensional Metal–Organic Frameworks for Cocatalyst-Free Photocatalytic Proton Reduction from Water. *Inorg. Chem.* **2020**, *59* (4), 2379–2386. <https://doi.org/10.1021/acs.inorgchem.9b03250>.
- (8) Mascal, M.; Armstrong, A.; Bartberger, M. D. Anion–Aromatic Bonding: A Case for Anion Recognition by π -Acidic Rings. *J. Am. Chem. Soc.* **2002**, *124* (22), 6274–6276. <https://doi.org/10.1021/ja017449s>.
- (9) Huang, P.; Chen, C.; Wu, M.; Jiang, F.; Hong, M. An Indium–Organic Framework for the Efficient Storage of Light Hydrocarbons and Selective Removal of Organic Dyes. *Dalton Trans.* **2019**, *48* (17), 5527–5533. <https://doi.org/10.1039/C9DT00902G>.
- (10) Gu, J.; Sun, X.; Kan, L.; Qiao, J.; Li, G.; Liu, Y. Structural Regulation and Light Hydrocarbon Adsorption/Separation of Three Zirconium–Organic Frameworks Based on Different V-Shaped Ligands. *ACS Appl. Mater. Interfaces* **2021**, *13* (35), 41680–41687. <https://doi.org/10.1021/acsami.1c11224>.
- (11) Pedersen, C. J. Cyclic Polyethers and Their Complexes with Metal Salts. *J. Am. Chem. Soc.* **1967**, *89* (26), 7017–7036. <https://doi.org/10.1021/ja01002a035>.
- (12) Lehn, J.-M. *Supramolecular Chemistry: Concepts and Perspectives: A Personal Account Built upon the George Fisher Baker Lectures in Chemistry at Cornell University [and] Lezioni Lincee, Accademia Nazionale Dei Lincei, Roma*; VCH: Weinheim ; New York, 1995.
- (13) Dietrich, B.; Lehn, J. M.; Sauvage, J. P. Diaza-polyoxa-macrocycles et macrobicycles. *Tetrahedron Letters* **1969**, *10* (34), 2885–2888. [https://doi.org/10.1016/S0040-4039\(01\)88299-X](https://doi.org/10.1016/S0040-4039(01)88299-X).
- (14) Kiggen, W.; Vögtle, F. Functionalized, Oligocyclic Large Cavities - A Novel Siderophore. *Angew. Chem. Int. Ed. Engl.* **1984**, *23* (9), 714–715. <https://doi.org/10.1002/anie.198407141>.
- (15) Quan, M. L. C.; Cram, D. J. Constrictive Binding of Large Guests by a Hemispherand Containing Four Portals. *J. Am. Chem. Soc.* **1991**, *113* (7), 2754–2755. <https://doi.org/10.1021/ja00007a060>.
- (16) Saalfrank, R. W.; Stark, A.; Peters, K.; von Schnering, H. G. The First ?Adamantoid? Alkaline Earth Metal Chelate Complex: Synthesis, Structure, and Reactivity. *Angew. Chem. Int. Ed. Engl.* **1988**, *27* (6), 851–853. <https://doi.org/10.1002/anie.198808511>.

- (17) Fujita, M.; Yazaki, J.; Ogura, K. Preparation of a Macrocyclic Polynuclear Complex, [(En)Pd(4,4'-Bpy)]₄(NO₃)₈ (En = Ethylenediamine, Bpy = Bipyridine), Which Recognizes an Organic Molecule in Aqueous Media. *J. Am. Chem. Soc.* **1990**, *112* (14), 5645–5647. <https://doi.org/10.1021/ja00170a042>.
- (18) Percástegui, E. G.; Ronson, T. K.; Nitschke, J. R. Design and Applications of Water-Soluble Coordination Cages. *Chem. Rev.* **2020**, *120* (24), 13480–13544. <https://doi.org/10.1021/acs.chemrev.0c00672>.
- (19) Fujita, M.; Tominaga, M.; Hori, A.; Therrien, B. Coordination Assemblies from a Pd(II)-Cornered Square Complex. *Acc. Chem. Res.* **2005**, *38* (4), 369–378. <https://doi.org/10.1021/ar040153h>.
- (20) Seidel, S. R.; Stang, P. J. High-Symmetry Coordination Cages via Self-Assembly. *Acc. Chem. Res.* **2002**, *35* (11), 972–983. <https://doi.org/10.1021/ar010142d>.
- (21) Saha, S.; Regeni, I.; Clever, G. H. Structure Relationships between Bis-Monodentate Ligands and Coordination Driven Self-Assemblies. *Coordination Chemistry Reviews* **2018**, *374*, 1–14. <https://doi.org/10.1016/j.ccr.2018.06.010>.
- (22) Mal, P.; Schultz, D.; Beyeh, K.; Rissanen, K.; Nitschke, J. R. An Unlockable-Relockable Iron Cage by Subcomponent Self-Assembly. *Angew. Chem. Int. Ed.* **2008**, *47* (43), 8297–8301. <https://doi.org/10.1002/anie.200803066>.
- (23) Zheng, S.-T.; Zhang, J.; Li, X.-X.; Fang, W.-H.; Yang, G.-Y. Cubic Polyoxometalate–Organic Molecular Cage. *J. Am. Chem. Soc.* **2010**, *132* (43), 15102–15103. <https://doi.org/10.1021/ja105986b>.
- (24) Liu, G.; Ju, Z.; Yuan, D.; Hong, M. In Situ Construction of a Coordination Zirconocene Tetrahedron. *Inorg. Chem.* **2013**, *52* (24), 13815–13817. <https://doi.org/10.1021/ic402428m>.
- (25) Xing, W.-H.; Li, H.-Y.; Dong, X.-Y.; Zang, S.-Q. Robust Multifunctional Zr-Based Metal–Organic Polyhedra for High Proton Conductivity and Selective CO₂ Capture. *J. Mater. Chem. A* **2018**, *6* (17), 7724–7730. <https://doi.org/10.1039/C8TA00858B>.
- (26) Takezawa, H.; Murase, T.; Resnati, G.; Metrangolo, P.; Fujita, M. Halogen-Bond-Assisted Guest Inclusion in a Synthetic Cavity. *Angew. Chem.* **2015**, *127* (29), 8531–8534. <https://doi.org/10.1002/ange.201500994>.
- (27) Bonakdarzadeh, P.; Topić, F.; Kalenius, E.; Bhowmik, S.; Sato, S.; Groessl, M.; Knochenmuss, R.; Rissanen, K. DOSY NMR, X-Ray Structural and Ion-Mobility Mass Spectrometric Studies on Electron-Deficient and Electron-Rich M₆L₄ Coordination Cages. *Inorg. Chem.* **2015**, *54* (12), 6055–6061. <https://doi.org/10.1021/acs.inorgchem.5b01082>.
- (28) Norjmaa, G.; Maréchal, J.-D.; Ujaque, G. Microsolvation and Encapsulation Effects on Supramolecular Catalysis: C–C Reductive Elimination inside [Ga₄L₆]¹²⁻ Metallocage. *J. Am. Chem. Soc.* **2019**, *141* (33), 13114–13123. <https://doi.org/10.1021/jacs.9b04909>.
- (29) Levin, M. D.; Kaphan, D. M.; Hong, C. M.; Bergman, R. G.; Raymond, K. N.; Toste, F. D. Scope and Mechanism of Cooperativity at the Intersection of Organometallic and Supramolecular Catalysis. *J. Am. Chem. Soc.* **2016**, *138* (30), 9682–9693. <https://doi.org/10.1021/jacs.6b05442>.
- (30) von Krbek, L. K. S.; Schalley, C. A.; Thordarson, P. Assessing Cooperativity in Supramolecular Systems. *Chem. Soc. Rev.* **2017**, *46* (9), 2622–2637. <https://doi.org/10.1039/C7CS00063D>.
- (31) Caulder, D. L.; Powers, R. E.; Parac, T. N.; Raymond, K. N. The Self-Assembly of a Predesigned Tetrahedral M₄L₆ Supramolecular Cluster. *Angewandte Chemie International Edition* **1998**, *37* (13–14), 1840–1843. [https://doi.org/10.1002/\(SICI\)1521-3773\(19980803\)37:13/14<1840::AID-ANIE1840>3.0.CO;2-D](https://doi.org/10.1002/(SICI)1521-3773(19980803)37:13/14<1840::AID-ANIE1840>3.0.CO;2-D).
- (32) Caulder, D. L.; Brückner, C.; Powers, R. E.; König, S.; Parac, T. N.; Leary, J. A.; Raymond, K. N. Design, Formation and Properties of Tetrahedral M₄L₄ and M₄L₆ Supramolecular Clusters¹. *J. Am. Chem. Soc.* **2001**, *123* (37), 8923–8938. <https://doi.org/10.1021/ja0104507>.

- (33) Kuehl, C. J.; Kryshenko, Y. K.; Radhakrishnan, U.; Seidel, S. R.; Huang, S. D.; Stang, P. J. Self-Assembly of Nanoscopic Coordination Cages of D_{3h} Symmetry. *Proc. Natl. Acad. Sci. U.S.A.* **2002**, *99* (8), 4932–4936. <https://doi.org/10.1073/pnas.012540799>.
- (34) Bilbeisi, R. A.; Ronson, T. K.; Nitschke, J. R. A Self-Assembled [Fe^{II}₁₂L₁₂] Capsule with an Icosahedral Framework. *Angew. Chem. Int. Ed.* **2013**, *52* (34), 9027–9030. <https://doi.org/10.1002/anie.201302976>.
- (35) Yoshizawa, M.; Tamura, M.; Fujita, M. Diels-Alder in Aqueous Molecular Hosts: Unusual Regioselectivity and Efficient Catalysis. *Science* **2006**, *312* (5771), 251–254. <https://doi.org/10.1126/science.1124985>.
- (36) Craig, G. A.; Larpent, P.; Kusaka, S.; Matsuda, R.; Kitagawa, S.; Furukawa, S. Switchable Gate-Opening Effect in Metal–Organic Polyhedra Assemblies through Solution Processing. *Chem. Sci.* **2018**, *9* (31), 6463–6469. <https://doi.org/10.1039/C8SC02263A>.
- (37) Piper, J. R.; Cletheroe, L.; Taylor, C. G. P.; Metherell, A. J.; Weinstein, J. A.; Sazanovich, I. V.; Ward, M. D. Photoinduced Energy- and Electron-Transfer from a Photoactive Coordination Cage to Bound Guests. *Chem. Commun.* **2017**, *53* (2), 408–411. <https://doi.org/10.1039/C6CC09298E>.
- (38) Li, Z.; Kishi, N.; Yoza, K.; Akita, M.; Yoshizawa, M. Isostructural M₂L₄ Molecular Capsules with Anthracene Shells: Synthesis, Crystal Structures, and Fluorescent Properties. *Chem. Eur. J.* **2012**, *18* (27), 8358–8365. <https://doi.org/10.1002/chem.201200155>.
- (39) Samanta, D.; Gemen, J.; Chu, Z.; Diskin-Posner, Y.; Shimon, L. J. W.; Klajn, R. Reversible Photoswitching of Encapsulated Azobenzenes in Water. *Proc. Natl. Acad. Sci. U.S.A.* **2018**, *115* (38), 9379–9384. <https://doi.org/10.1073/pnas.1712787115>.
- (40) Kim, T. Y.; Digal, L.; Gardiner, M. G.; Lucas, N. T.; Crowley, J. D. Octahedral [Pd₆L₈]¹²⁺ Metallosupramolecular Cages: Synthesis, Structures and Guest-Encapsulation Studies. *Chem. Eur. J.* **2017**, *23* (60), 15089–15097. <https://doi.org/10.1002/chem.201702518>.
- (41) Scherer, M.; Caulder, D. L.; Johnson, D. W.; Raymond, K. N. Triple Helicate—Tetrahedral Cluster Interconversion Controlled by Host-Guest Interactions. *Angew. Chem. Int. Ed.* **1999**, *38* (11), 1587–1592. [https://doi.org/10.1002/\(SICI\)1521-3773\(19990601\)38:11<1587::AID-ANIE1587>3.0.CO;2-R](https://doi.org/10.1002/(SICI)1521-3773(19990601)38:11<1587::AID-ANIE1587>3.0.CO;2-R).
- (42) Jiao, J.; Li, Z.; Qiao, Z.; Li, X.; Liu, Y.; Dong, J.; Jiang, J.; Cui, Y. Design and Self-Assembly of Hexahedral Coordination Cages for Cascade Reactions. *Nat Commun* **2018**, *9* (1), 4423. <https://doi.org/10.1038/s41467-018-06872-0>.
- (43) Rizzuto, F. J.; Nitschke, J. R. Stereochemical Plasticity Modulates Cooperative Binding in a CoII₁₂L₆ Cuboctahedron. *Nature Chem* **2017**, *9* (9), 903–908. <https://doi.org/10.1038/nchem.2758>.
- (44) Sawada, T.; Yoshizawa, M.; Sato, S.; Fujita, M. Minimal Nucleotide Duplex Formation in Water through Enclathration in Self-Assembled Hosts. *Nature Chem* **2009**, *1* (1), 53–56. <https://doi.org/10.1038/nchem.100>.
- (45) Kilbas, B.; Mirtschin, S.; Scopelliti, R.; Severin, K. A Solvent-Responsive Coordination Cage. *Chem. Sci.* **2012**, *3* (3), 701–704. <https://doi.org/10.1039/C1SC00779C>.
- (46) Fujita, D.; Ueda, Y.; Sato, S.; Mizuno, N.; Kumasaka, T.; Fujita, M. Self-Assembly of Tetravalent Goldberg Polyhedra from 144 Small Components. *Nature* **2016**, *540* (7634), 563–566. <https://doi.org/10.1038/nature20771>.
- (47) Bell, D. J.; Natrajan, L. S.; Riddell, I. A. Design of Lanthanide Based Metal–Organic Polyhedral Cages for Application in Catalysis, Sensing, Separation and Magnetism. *Coordination Chemistry Reviews* **2022**, *472*, 214786. <https://doi.org/10.1016/j.ccr.2022.214786>.
- (48) Zhou, J.; Yu, G.; Huang, F. Supramolecular Chemotherapy Based on Host–Guest Molecular Recognition: A Novel Strategy in the Battle against Cancer with a Bright Future. *Chem. Soc. Rev.* **2017**, *46* (22), 7021–7053. <https://doi.org/10.1039/C6CS00898D>.
- (49) Carné-Sánchez, A.; Albalad, J.; Grancha, T.; Imaz, I.; Juanhuix, J.; Larpent, P.; Furukawa, S.; MasPOCH, D. Postsynthetic Covalent and Coordination Functionalization of Rhodium(II)-

- Based Metal–Organic Polyhedra. *J. Am. Chem. Soc.* **2019**, *141* (9), 4094–4102. <https://doi.org/10.1021/jacs.8b13593>.
- (50) Taylor, C. G. P.; Metherell, A. J.; Argent, S. P.; Ashour, F. M.; Williams, N. H.; Ward, M. D. Coordination-Cage-Catalysed Hydrolysis of Organophosphates: Cavity- or Surface-Based? *Chem. Eur. J.* **2020**, *26* (14), 3065–3073. <https://doi.org/10.1002/chem.201904708>.
- (51) Cullen, W.; Metherell, A. J.; Wragg, A. B.; Taylor, C. G. P.; Williams, N. H.; Ward, M. D. Catalysis in a Cationic Coordination Cage Using a Cavity-Bound Guest and Surface-Bound Anions: Inhibition, Activation, and Autocatalysis. *J. Am. Chem. Soc.* **2018**, *140* (8), 2821–2828. <https://doi.org/10.1021/jacs.7b11334>.
- (52) Kaphan, D. M.; Levin, M. D.; Bergman, R. G.; Raymond, K. N.; Toste, F. D. A Supramolecular Microenvironment Strategy for Transition Metal Catalysis. *Science* **2015**, *350* (6265), 1235–1238. <https://doi.org/10.1126/science.aad3087>.
- (53) Zhang, D.; Ronson, T. K.; Mosquera, J.; Martinez, A.; Guy, L.; Nitschke, J. R. Anion Binding in Water Drives Structural Adaptation in an Azaphosphatrane-Functionalized Fe^{II}₄L₄ Tetrahedron. *J. Am. Chem. Soc.* **2017**, *139* (19), 6574–6577. <https://doi.org/10.1021/jacs.7b02950>.
- (54) Zhang, D.; Ronson, T. K.; Mosquera, J.; Martinez, A.; Nitschke, J. R. Selective Anion Extraction and Recovery Using a Fe^{II}₄L₄ Cage. *Angew. Chem.* **2018**, *130* (14), 3779–3783. <https://doi.org/10.1002/ange.201800459>.
- (55) Zhang, H.; Lu, Y.; Gao, W.; Lin, Y.; Jin, G. Selective Encapsulation and Separation of Dihalobenzene Isomers with Discrete Heterometallic Macrocages. *Chemistry A European J* **2018**, *24* (71), 18913–18921. <https://doi.org/10.1002/chem.201805383>.
- (56) Sun, W.; Wang, Y.; Ma, L.; Zheng, L.; Fang, W.; Chen, X.; Jiang, H. Self-Assembled Carcerand-like Cage with a Thermoregulated Selective Binding Preference for Purification of High-Purity C₆₀ and C₇₀. *J. Org. Chem.* **2018**, *83* (23), 14667–14675. <https://doi.org/10.1021/acs.joc.8b02674>.
- (57) Wu, K.; Li, K.; Hou, Y.-J.; Pan, M.; Zhang, L.-Y.; Chen, L.; Su, C.-Y. Homochiral D₄-Symmetric Metal–Organic Cages from Stereogenic Ru(II) Metalloligands for Effective Enantioseparation of Atropisomeric Molecules. *Nat Commun* **2016**, *7* (1), 10487. <https://doi.org/10.1038/ncomms10487>.
- (58) Hou, Y.-J.; Wu, K.; Wei, Z.-W.; Li, K.; Lu, Y.-L.; Zhu, C.-Y.; Wang, J.-S.; Pan, M.; Jiang, J.-J.; Li, G.-Q.; Su, C.-Y. Design and Enantioresolution of Homochiral Fe(II)–Pd(II) Coordination Cages from Stereolabile Metalloligands: Stereochemical Stability and Enantioselective Separation. *J. Am. Chem. Soc.* **2018**, *140* (51), 18183–18191. <https://doi.org/10.1021/jacs.8b11152>.
- (59) Zhu, J.; Rodríguez-Corrales, J. Á.; Prussin, R.; Zhao, Z.; Dominijanni, A.; Hopkins, S. L.; Winkel, B. S. J.; Robertson, J. L.; Brewer, K. J. Exploring the Activity of a Polyazine Bridged Ru(II)–Pt(II) Supramolecule in F98 Rat Malignant Glioma Cells. *Chem. Commun.* **2017**, *53* (1), 145–148. <https://doi.org/10.1039/C6CC07978D>.
- (60) Zhu, C.; Pan, M.; Su, C. Metal–Organic Cages for Biomedical Applications. *Isr. J. Chem.* **2019**, *59* (3–4), 209–219. <https://doi.org/10.1002/ijch.201800147>.
- (61) Jiao, Y.; Wang, J.; Wu, P.; Zhao, L.; He, C.; Zhang, J.; Duan, C. Cerium-Based M₄L₄ Tetrahedra as Molecular Flasks for Selective Reaction Prompting and Luminescent Reaction Tracing. *Chem. Eur. J.* **2014**, *20* (8), 2224–2231. <https://doi.org/10.1002/chem.201303560>.
- (62) Cui, Y.; Chen, Z.-M.; Jiang, X.-F.; Tong, J.; Yu, S.-Y. Self-Assembly and Anion Sensing of Metal–Organic [M₆L₂] Cages from Fluorescent Triphenylamine Tri-Pyrazoles with Dipalladium(II,II) Corners. *Dalton Trans.* **2017**, *46* (18), 5801–5805. <https://doi.org/10.1039/C7DT00179G>.
- (63) Rodríguez, J.; Mosquera, J.; Couceiro, J. R.; Nitschke, J. R.; Vázquez, M. E.; Mascareñas, J. L. Anion Recognition as a Supramolecular Switch of Cell Internalization. *J. Am. Chem. Soc.* **2017**, *139* (1), 55–58. <https://doi.org/10.1021/jacs.6b11103>.

- (64) Liu, C.-L.; Zhang, R.-L.; Lin, C.-S.; Zhou, L.-P.; Cai, L.-X.; Kong, J.-T.; Yang, S.-Q.; Han, K.-L.; Sun, Q.-F. Intraligand Charge Transfer Sensitization on Self-Assembled Europium Tetrahedral Cage Leads to Dual-Selective Luminescent Sensing toward Anion and Cation. *J. Am. Chem. Soc.* **2017**, *139* (36), 12474–12479. <https://doi.org/10.1021/jacs.7b05157>.
- (65) Atwood, J. L.; Brechin, E. K.; Dalgarno, S. J.; Inglis, R.; Jones, L. F.; Mossine, A.; Paterson, M. J.; Power, N. P.; Teat, S. J. Magnetism in Metal–Organic Capsules. *Chem. Commun.* **2010**, *46* (20), 3484. <https://doi.org/10.1039/c002247k>.
- (66) Gutsche, C. D. *Calixarenes Revisited*; Monographs in supramolecular chemistry; Royal Society of Chemistry: Cambridge (GB), 1998.
- (67) *Calixarenes and Beyond*, 1st ed. 2016.; Neri, P., Sessler, J. L., Wang, M.-X., Eds.; Springer International Publishing : Imprint: Springer: Cham, 2016. <https://doi.org/10.1007/978-3-319-31867-7>.
- (68) Akdas, H.; Bringel, L.; Graf, E.; Hosseini, M. W.; Mislin, G.; Pansanel, J.; De Cian, A.; Fischer, J. Thiocalixarenes: Synthesis and Structural Analysis of Thiocalix[4]Arene and of *p*-Tert-Butylthiocalix[4]Arene. *Tetrahedron Letters* **1998**, *39* (16), 2311–2314. [https://doi.org/10.1016/S0040-4039\(98\)00067-7](https://doi.org/10.1016/S0040-4039(98)00067-7).
- (69) Iki, N.; Kumagai, H.; Morohashi, N.; Ejima, K.; Hasegawa, M.; Miyanari, S.; Miyano, S. Selective Oxidation of Thiocalix[4]Arenes to the Sulfinyl- and Sulfonylcalix[4]Arenes and Their Coordination Ability to Metal Ions. *Tetrahedron Letters* **1998**, *39* (41), 7559–7562. [https://doi.org/10.1016/S0040-4039\(98\)01645-1](https://doi.org/10.1016/S0040-4039(98)01645-1).
- (70) Kajiwara, T.; Iki, N.; Yamashita, M. Transition Metal and Lanthanide Cluster Complexes Constructed with Thiocalix[n]Arene and Its Derivatives. *Coordination Chemistry Reviews* **2007**, *251* (13–14), 1734–1746. <https://doi.org/10.1016/j.ccr.2007.01.001>.
- (71) Kajiwara, T.; Kobashi, T.; Shinagawa, R.; Ito, T.; Takaishi, S.; Yamashita, M.; Iki, N. Highly Symmetrical Tetranuclear Cluster Complexes Supported by *p*-Tert-Butylsulfonylcalix[4]Arene as a Cluster-Forming Ligand. *Eur. J. Inorg. Chem.* **2006**, *2006* (9), 1765–1770. <https://doi.org/10.1002/ejic.200501086>.
- (72) Liu, M.; Liao, W.; Hu, C.; Du, S.; Zhang, H. Calixarene-Based Nanoscale Coordination Cages. *Angew. Chem. Int. Ed.* **2012**, *51* (7), 1585–1588. <https://doi.org/10.1002/anie.201106732>.
- (73) Du, S.; Hu, C.; Xiao, J.-C.; Tan, H.; Liao, W. A Giant Coordination Cage Based on Sulfonylcalix[4]Arenes. *Chem. Commun.* **2012**, *48* (73), 9177. <https://doi.org/10.1039/c2cc34265k>.
- (74) Hang, X.; Du, S.; Wang, S.; Liao, W. A 2D Metal–Calixarene Aggregate Involving in Situ Generated 5-(4-Pyridyl)Tetrazolate Ligand. *Inorganic Chemistry Communications* **2014**, *47*, 152–154. <https://doi.org/10.1016/j.inoche.2014.07.035>.
- (75) Bi, Y.; Wang, S.; Liu, M.; Du, S.; Liao, W. A Tetragonal Prismatic {Co₃₂} Nanocage Based on Thiocalixarene. *Chem. Commun.* **2013**, *49* (60), 6785. <https://doi.org/10.1039/c3cc43347a>.
- (76) Su, K.; Jiang, F.; Qian, J.; Pang, J.; Hu, F.; Bawaked, S. M.; Mokhtar, M.; Al-Thabaiti, S. A.; Hong, M. Bridging Different Co₄–Calix[4]Arene Building Blocks into Grids, Cages and 2D Polymers with Chiral Camphoric Acid. *CrystEngComm* **2015**, *17* (8), 1750–1753. <https://doi.org/10.1039/C4CE02186J>.
- (77) Su, K.; Jiang, F.; Qian, J.; Wu, M.; Gai, Y.; Pan, J.; Yuan, D.; Hong, M. Open Pentameric Calixarene Nanocage. *Inorg. Chem.* **2014**, *53* (1), 18–20. <https://doi.org/10.1021/ic4024184>.
- (78) Bi, Y.; Du, S.; Liao, W. Thiocalixarene-Based Nanoscale Polyhedral Coordination Cages. *Coordination Chemistry Reviews* **2014**, *276*, 61–72. <https://doi.org/10.1016/j.ccr.2014.06.011>.
- (79) Gosselin, A. J.; Rowland, C. A.; Bloch, E. D. Permanently Microporous Metal–Organic Polyhedra. *Chem. Rev.* **2020**, *120* (16), 8987–9014. <https://doi.org/10.1021/acs.chemrev.9b00803>.

- (80) Zhang, Y.-T.; Zhu, J.; Liu, Z.-Y.; Li, S.-B.; Huang, H.; Jiang, B.-X. Microwave-Assisted Synthesis of Zr-Based Metal-Organic Polyhedron: Serving as Efficient Visible-Light Photocatalyst for Cr(VI) Reduction. *Inorganica Chimica Acta* **2022**, *543*, 121204. <https://doi.org/10.1016/j.ica.2022.121204>.
- (81) Bi, Y.; Xu, G.; Liao, W.; Du, S.; Wang, X.; Deng, R.; Zhang, H.; Gao, S. Making a [Co₂₄] Metallamacrocycle from the Shuttlecock-like Tetranuclear Cobalt-Calixarene Building Blocks. *Chem. Commun.* **2010**, *46* (34), 6362. <https://doi.org/10.1039/c0cc01844a>.
- (82) Xiong, K.; Jiang, F.; Gai, Y.; Yuan, D.; Chen, L.; Wu, M.; Su, K.; Hong, M. Truncated Octahedral Coordination Cage Incorporating Six Tetranuclear-Metal Building Blocks and Twelve Linear Edges. *Chem. Sci.* **2012**, *3* (7), 2321. <https://doi.org/10.1039/c2sc20264f>.
- (83) Tong, H.-Y.; Liang, J.; Wu, Q.-J.; Zou, Y.-H.; Huang, Y.-B.; Cao, R. Soluble Imidazolium-Functionalized Coordination Cages for Efficient Homogeneous Catalysis of CO₂ Cycloaddition Reactions. *Chem. Commun.* **2021**, *57* (17), 2140–2143. <https://doi.org/10.1039/D0CC08098E>.
- (84) Jin, Y.; Jiang, H.; Tang, X.; Zhang, W.; Liu, Y.; Cui, Y. Coordination-Driven Self-Assembly of Anthraquinone-Based Metal–Organic Cages for Photocatalytic Selective [2 + 2] Cycloaddition. *Dalton Trans.* **2021**, *50* (24), 8533–8539. <https://doi.org/10.1039/D1DT00652E>.
- (85) Liu, M.; Liao, W. Bridging Calixarene-Based {Co₄} Units into a Square or Belt with Aromatic Dicarboxylic Acids. *CrystEngComm* **2012**, *14* (18), 5727. <https://doi.org/10.1039/c2ce25692d>.
- (86) Sun, C.-Z.; Cheng, L.-J.; Qiao, Y.; Zhang, L.-Y.; Chen, Z.-N.; Dai, F.-R.; Lin, W.; Wang, Z. Stimuli-Responsive Metal–Organic Supercontainers as Synthetic Proton Receptors. *Dalton Trans.* **2018**, *47* (30), 10256–10263. <https://doi.org/10.1039/C8DT01900B>.
- (87) Dai, F.-R.; Becht, D. C.; Wang, Z. Modulating Guest Binding in Sulfonylcalixarene-Based Metal–Organic Supercontainers. *Chem. Commun.* **2014**, *50* (40), 5385–5387. <https://doi.org/10.1039/C3CC47420H>.
- (88) Dai, F.-R.; Qiao, Y.; Wang, Z. Designing Structurally Tunable and Functionally Versatile Synthetic Supercontainers. *Inorg. Chem. Front.* **2016**, *3* (2), 243–249. <https://doi.org/10.1039/C5QI00212E>.
- (89) Qiao, Y.; Zhang, L.; Li, J.; Lin, W.; Wang, Z. Switching on Supramolecular Catalysis via Cavity Mediation and Electrostatic Regulation. *Angew. Chem.* **2016**, *128* (41), 12970–12974. <https://doi.org/10.1002/ange.201606847>.
- (90) Bhuvanewari, N.; Dai, F.-R.; Chen, Z.-N. Sensitive and Specific Guest Recognition through Pyridinium-Modification in Spindle-Like Coordination Containers. *Chem. Eur. J.* **2018**, *24* (25), 6580–6585. <https://doi.org/10.1002/chem.201705210>.
- (91) Sun, C.-Z.; Sheng, T.-P.; Dai, F.-R.; Chen, Z.-N. Sulfonylcalixaren-Based *Ortho* - Dicarboxylate-Bridged Coordination Containers for Guest Encapsulation and Separation. *Crystal Growth & Design* **2019**, *19* (2), 1144–1148. <https://doi.org/10.1021/acs.cgd.8b01633>.
- (92) Gehin, A.; Ferlay, S.; Harrowfield, J. M.; Fenske, D.; Kyritsakas, N.; Hosseini, M. W. Giant Core–Shell Nanospherical Clusters Composed of 32 Co or 32 Ni Atoms Held by 6 *p* - *Tert* - Butylthiacalix[4]Arene Units. *Inorg. Chem.* **2012**, *51* (9), 5481–5486. <https://doi.org/10.1021/ic300550v>.
- (93) Xiong, K.-C.; Jiang, F.-L.; Gai, Y.-L.; Yuan, D.-Q.; Han, D.; Ma, J.; Zhang, S.-Q.; Hong, M.-C. Chlorine-Induced Assembly of a Cationic Coordination Cage with a M5-Carbonato-Bridged MnII₂₄ Core. *Chem. Eur. J.* **2012**, *18* (18), 5536–5540. <https://doi.org/10.1002/chem.201200125>.
- (94) Hang, X.; Liu, B.; Zhu, X.; Wang, S.; Han, H.; Liao, W.; Liu, Y.; Hu, C. Discrete {Ni₄₀} Coordination Cage: A Calixarene-Based Johnson-Type (*J*₁₇) Hexadecahedron. *J. Am. Chem. Soc.* **2016**, *138* (9), 2969–2972. <https://doi.org/10.1021/jacs.6b00695>.

- (95) Yuan, D.; Zhao, D.; Sun, D.; Zhou, H.-C. An Isorecticular Series of Metal-Organic Frameworks with Dendritic Hexacarboxylate Ligands and Exceptionally High Gas-Uptake Capacity. *Angewandte Chemie* **2010**, *122* (31), 5485–5489. <https://doi.org/10.1002/ange.201001009>.
- (96) Dai, F.-R.; Wang, Z. Modular Assembly of Metal–Organic Supercontainers Incorporating Sulfonylcalixarenes. *J. Am. Chem. Soc.* **2012**, *134* (19), 8002–8005. <https://doi.org/10.1021/ja300095j>.
- (97) Fang, Y.; Xiao, Z.; Li, J.; Lollar, C.; Liu, L.; Lian, X.; Yuan, S.; Banerjee, S.; Zhang, P.; Zhou, H. Formation of a Highly Reactive Cobalt Nanocluster Crystal within a Highly Negatively Charged Porous Coordination Cage. *Angew Chem Int Ed* **2018**, *57* (19), 5283–5287. <https://doi.org/10.1002/anie.201712372>.
- (98) Du, S.; Yu, T.-Q.; Liao, W.; Hu, C. Structure Modeling, Synthesis and X-Ray Diffraction Determination of an Extra-Large Calixarene-Based Coordination Cage and Its Application in Drug Delivery. *Dalton Trans.* **2015**, *44* (32), 14394–14402. <https://doi.org/10.1039/C5DT01526J>.
- (99) Liu, M.; Du, S.; Bi, Y.; Liao, W. A Tetrahedral Coordination Cage Based on P-Tert-Butylthiacalix[4]Arene and 5-Sulfoisophthalic Acid. *Inorganic Chemistry Communications* **2014**, *41*, 96–99. <https://doi.org/10.1016/j.inoche.2014.01.009>.
- (100) Geng, D.; Han, X.; Bi, Y.; Qin, Y.; Li, Q.; Huang, L.; Zhou, K.; Song, L.; Zheng, Z. Merohedral Icosahedral M_{48} ($M = Co^{II}, Ni^{II}$) Cage Clusters Supported by Thiacalix[4]Arene. *Chem. Sci.* **2018**, *9* (45), 8535–8541. <https://doi.org/10.1039/C8SC03193B>.
- (101) Atwood, J. L.; Barbour, L. J.; Jerga, A. Storage of Methane and Freon by Interstitial van Der Waals Confinement. *Science* **2002**, *296* (5577), 2367–2369. <https://doi.org/10.1126/science.1072252>.
- (102) Morohashi, N.; Hattori, T. Selective Guest Inclusion by Crystals of Calixarenes: Potential for Application as Separation Materials. *J Incl Phenom Macrocycl Chem* **2018**, *90* (3–4), 261–277. <https://doi.org/10.1007/s10847-018-0783-3>.
- (103) Gong, W.; Chu, D.; Jiang, H.; Chen, X.; Cui, Y.; Liu, Y. Permanent Porous Hydrogen-Bonded Frameworks with Two Types of Brønsted Acid Sites for Heterogeneous Asymmetric Catalysis. *Nat Commun* **2019**, *10* (1), 600. <https://doi.org/10.1038/s41467-019-08416-6>.
- (104) Dai, F.-R.; Sambasivam, U.; Hammerstrom, A. J.; Wang, Z. Synthetic Supercontainers Exhibit Distinct Solution versus Solid State Guest-Binding Behavior. *J. Am. Chem. Soc.* **2014**, *136* (20), 7480–7491. <https://doi.org/10.1021/ja502839b>.
- (105) Zheng, W.; Yang, G.; Shao, N.; Chen, L.-J.; Ou, B.; Jiang, S.-T.; Chen, G.; Yang, H.-B. CO_2 Stimuli-Responsive, Injectable Block Copolymer Hydrogels Cross-Linked by Discrete Organoplatinum(II) Metallacycles via Stepwise Post-Assembly Polymerization. *J. Am. Chem. Soc.* **2017**, *139* (39), 13811–13820. <https://doi.org/10.1021/jacs.7b07303>.
- (106) Li, C.; Zhang, B.; Dong, Y.; Li, Y.; Wang, P.; Yu, Y.; Cheng, L.; Cao, L. A Tetraphenylethene-Based Pd_2L_4 Metallacage with Aggregation-Induced Emission and Stimuli-Responsive Behavior. *Dalton Trans.* **2020**, *49* (24), 8051–8055. <https://doi.org/10.1039/D0DT00469C>.
- (107) Zhang, J.; Deng, Y.; Wang, S.; Yang, J.; Hu, S. A Calixarene-Based Coordination Cage as an Efficient Luminescent Sensor for Fe^{3+} , MnO_4^- , NB and 2,4-DNP in Aqueous Medium. *CrystEngComm* **2023**, *25* (10), 1495–1500. <https://doi.org/10.1039/D2CE01508K>.
- (108) Bhuvanewari, N.; Annamalai, K. P.; Dai, F.-R.; Chen, Z.-N. Pyridinium Functionalized Coordination Containers as Highly Efficient Electrocatalysts for Sustainable Oxygen Evolution. *J. Mater. Chem. A* **2017**, *5* (45), 23559–23565. <https://doi.org/10.1039/C7TA05797K>.
- (109) Wang, S.; Gao, X.; Hang, X.; Zhu, X.; Han, H.; Liao, W.; Chen, W. Ultrafine Pt Nanoclusters Confined in a Calixarene-Based $\{Ni_{24}\}$ Coordination Cage for High-Efficient Hydrogen Evolution Reaction. *J. Am. Chem. Soc.* **2016**, *138* (50), 16236–16239. <https://doi.org/10.1021/jacs.6b11218>.

- (110) Matsuoka, R.; Nabeshima, T. Functional Supramolecular Architectures of Dipyrrin Complexes. *Front. Chem.* **2018**, *6*, 349. <https://doi.org/10.3389/fchem.2018.00349>.
- (111) Brückner, C.; Zhang, Y.; Rettig, S. J.; Dolphin, D. Synthesis, Derivatization and Structural Characterization of Octahedral Tris(5-Phenyl-4,6-Dipyrrinato) Complexes of Cobalt(III) and Iron(III). *Inorganica Chimica Acta* **1997**, *263* (1–2), 279–286. [https://doi.org/10.1016/S0020-1693\(97\)05700-9](https://doi.org/10.1016/S0020-1693(97)05700-9).
- (112) Hall, J. D.; McLean, T. M.; Smalley, S. J.; Waterland, M. R.; Telfer, S. G. Chromophoric Dipyrrin Complexes Capable of Binding to TiO₂: Synthesis, Structure and Spectroscopy. *Dalton Trans.* **2010**, *39* (2), 437–445. <https://doi.org/10.1039/B912332F>.
- (113) Stork, J. R.; Thoi, V. S.; Cohen, S. M. Rare Examples of Transition-Metal–Main-Group Metal Heterometallic Metal–Organic Frameworks from Gallium and Indium Dipyrrinato Complexes and Silver Salts: Synthesis and Framework Variability. *Inorg. Chem.* **2007**, *46* (26), 11213–11223. <https://doi.org/10.1021/ic7016159>.
- (114) Artigau, M.; Bonnet, A.; Ladeira, S.; Hoffmann, P.; Vigroux, A. A Free-Base Dipyrrin Capable of Forming Extended Architectures Comparable to Those of Its Metal(II) Complex Counterparts. *CrystEngComm* **2011**, *13* (23), 7149. <https://doi.org/10.1039/c1ce05913k>.
- (115) Thoi, V. S.; Stork, J. R.; Magde, D.; Cohen, S. M. Luminescent Dipyrrinato Complexes of Trivalent Group 13 Metal Ions. *Inorg. Chem.* **2006**, *45* (26), 10688–10697. <https://doi.org/10.1021/ic061581h>.
- (116) Garibay, S. J.; Stork, J. R.; Wang, Z.; Cohen, S. M.; Telfer, S. G. Enantiopure vs. Racemic Metalloligands: Impact on Metal–Organic Framework Structure and Synthesis. *Chem. Commun.* **2007**, No. 46, 4881. <https://doi.org/10.1039/b712118k>.
- (117) Cohen, S. M.; Halper, S. R. Dipyrrromethene Complexes of Iron. *Inorganica Chimica Acta* **2002**, *341*, 12–16. [https://doi.org/10.1016/S0020-1693\(02\)01176-3](https://doi.org/10.1016/S0020-1693(02)01176-3).
- (118) Halper, S. R.; Cohen, S. M. Synthesis, Structure, and Spectroscopy of Phenylacetylene Rods Incorporating *Meso*-Substituted Dipyrrin Ligands. *Chem. Eur. J.* **2003**, *9* (19), 4661–4669. <https://doi.org/10.1002/chem.200305041>.
- (119) Baudron, S. A. Dipyrrin Based Homo- and Hetero-Metallic Infinite Architectures. *CrystEngComm* **2010**, *12* (8), 2288. <https://doi.org/10.1039/c001020k>.
- (120) Shikha Singh, R.; Prasad Paitandi, R.; Kumar Gupta, R.; Shankar Pandey, D. Recent Developments in Metal Dipyrrin Complexes: Design, Synthesis, and Applications. *Coordination Chemistry Reviews* **2020**, *414*, 213269. <https://doi.org/10.1016/j.ccr.2020.213269>.
- (121) Poma, A.; Grigioni, I.; Dozzi, M. V.; Baudron, S. A.; Carlucci, L.; Hosseini, M. W.; Selli, E. A Ni-2,2'-Bisdipyrrinato Complex as a Potential Sensitizer: Synthesis and Photoelectrochemical Characterization. *New J. Chem.* **2017**, *41* (24), 15021–15026. <https://doi.org/10.1039/C7NJ03372A>.
- (122) Baudron, S. A.; Ruffin, H.; Hosseini, M. W. On Zn(II) 2,2'-Bisdipyrrin Circular Helicates. *Chem. Commun.* **2015**, *51* (27), 5906–5909. <https://doi.org/10.1039/C5CC00724K>.
- (123) Rao, P. D.; Dhanalekshmi, S.; Littler, B. J.; Lindsey, J. S. Rational Syntheses of Porphyrins Bearing up to Four Different *Meso* Substituents. *J. Org. Chem.* **2000**, *65* (22), 7323–7344. <https://doi.org/10.1021/jo000882k>.
- (124) Xu, X.; Li, S.; Liu, Q.; Liu, Z.; Yan, W.; Zhao, L.; Zhang, W.; Zhang, L.; Deng, F.; Cong, H.; Deng, H. Isolated π -Interaction Sites in Mesoporous MOF Backbone for Repetitive and Reversible Dynamics in Water. *ACS Appl. Mater. Interfaces* **2019**, *11* (1), 973–981. <https://doi.org/10.1021/acsami.8b19211>.
- (125) Telfer, S. G.; Wuest, J. D. Metallotectons: Using Enantiopure Tris(Dipyrrinato)Cobalt(III) Complexes to Build Chiral Molecular Materials. *Chem. Commun.* **2007**, No. 30, 3166. <https://doi.org/10.1039/b705212j>.
- (126) Lavie-Cambot, A.; Cantuel, M.; Leydet, Y.; Jonusauskas, G.; Bassani, D. M.; McClenaghan, N. D. Improving the Photophysical Properties of Copper(I)

- Bis(Phenanthroline) Complexes. *Coordination Chemistry Reviews* **2008**, *252* (23–24), 2572–2584. <https://doi.org/10.1016/j.ccr.2008.03.013>.
- (127) Martins, L.; Macreadie, L. K.; Sensharma, D.; Vaesen, S.; Zhang, X.; Gough, J. J.; O'Doherty, M.; Zhu, N.-Y.; R  ther, M.; O'Brien, J. E.; Bradley, A. L.; Schmitt, W. Light-Harvesting, 3rd Generation Ru^{II}/Co^{II} MOF with a Large, Tubular Channel Aperture. *Chem. Commun.* **2019**, *55* (34), 5013–5016. <https://doi.org/10.1039/C9CC00206E>.
- (128) Avdeeva, V. V.; Kubasov, A. S.; Korolenko, S. E.; Privalov, V. I.; Malinina, E. A.; Kuznetsov, N. T. Iron(II), Cobalt(II), and Nickel(II) Complexes with 1,10-Phenanthroline and 2,2'-Bipyridyl and the Macropolyhedral Borane Cluster [Trans-B20H18]²⁻ as Counterion. *Polyhedron* **2022**, *217*, 115740. <https://doi.org/10.1016/j.poly.2022.115740>.
- (129) Bron, M.; Radnik, J.; Fieber-Erdmann, M.; Bogdanoff, P.; Fiechter, S. EXAFS, XPS and Electrochemical Studies on Oxygen Reduction Catalysts Obtained by Heat Treatment of Iron Phenanthroline Complexes Supported on High Surface Area Carbon Black. *Journal of Electroanalytical Chemistry* **2002**, *535* (1–2), 113–119. [https://doi.org/10.1016/S0022-0728\(02\)01189-0](https://doi.org/10.1016/S0022-0728(02)01189-0).
- (130) Mu  oz-Becerra, K.; B  ez, D. F.; Zagal, J. H.; Bollo, S.; Toro-Labb  , A.; Venegas, R.; Recio, F. J. Reactivity Descriptors for Cu Bis-Phenanthroline Catalysts for the Hydrogen Peroxide Reduction Reaction. *Electrochimica Acta* **2020**, *357*, 136881. <https://doi.org/10.1016/j.electacta.2020.136881>.
- (131) Zeng, X.; Tavasli, M.; Perepichka, I. F.; Batsanov, A. S.; Bryce, M. R.; Chiang, C.-J.; Rothe, C.; Monkman, A. P. Cationic Bis-Cyclometallated Iridium(III) Phenanthroline Complexes with Pendant Fluorenyl Substituents: Synthesis, Redox, Photophysical Properties and Light-Emitting Cells. *Chem. Eur. J.* **2008**, *14* (3), 933–943. <https://doi.org/10.1002/chem.200700308>.
- (132) Wei, Y.; Yu, Y.; Wu, K. Highly Stable Diamondoid Network Coordination Polymer [Mn(NCP)₂]_n with Notable NLO, Magnetic, and Luminescence Properties. *Crystal Growth & Design* **2007**, *7* (11), 2262–2264. <https://doi.org/10.1021/cg070192a>.
- (133) Zhang, S.; Yang, Y.; Xia, Z.-Q.; Liu, X.-Y.; Yang, Q.; Wei, Q.; Xie, G.; Chen, S.-P.; Gao, S.-L. Eu-MOFs with 2-(4-Carboxyphenyl)Imidazo[4,5-*f*]-1,10-Phenanthroline and Ditopic Carboxylates as Coligands: Synthesis, Structure, High Thermostability, and Luminescence Properties. *Inorg. Chem.* **2014**, *53* (20), 10952–10963. <https://doi.org/10.1021/ic501253c>.
- (134) Thacker, N. C.; Ji, P.; Lin, Z.; Urban, A.; Lin, W. Phenanthroline-Based Metal–Organic Frameworks for Fe-Catalyzed C_{sp3}–H Amination. *Faraday Discuss.* **2017**, *201*, 303–315. <https://doi.org/10.1039/C7FD00030H>.
- (135) Meng, Z.; Yang, F.; Wang, X.; Shan, W.-L.; Liu, D.; Zhang, L.; Yuan, G. Trefoil-Shaped Metal–Organic Cages as Fluorescent Chemosensors for Multiple Detection of Fe³⁺, Cr₂O₇²⁻, and Antibiotics. *Inorg. Chem.* **2023**, *62* (4), 1297–1305. <https://doi.org/10.1021/acs.inorgchem.2c03639>.
- (136) Xie, L.; Luo, Z.; Zhao, Z.; Chen, T. Anticancer and Antiangiogenic Iron(II) Complexes That Target Thioredoxin Reductase to Trigger Cancer Cell Apoptosis. *J. Med. Chem.* **2017**, *60* (1), 202–214. <https://doi.org/10.1021/acs.jmedchem.6b00917>.
- (137) Zhang, H.; Song, Y.; Li, L.; Zhang, S.-Y.; Wu, Q.; Mei, W.-J.; Liu, H.-M.; Wang, X.-C. Phenanthroimidazole Derivatives Act as Potent Inducer of Autophagy by Activating DNA Damage Pathway. *Bioorganic Chemistry* **2019**, *88*, 102940. <https://doi.org/10.1016/j.bioorg.2019.102940>.
- (138) Wei, C.; He, Y.; Shi, X.; Song, Z. Terpyridine-Metal Complexes: Applications in Catalysis and Supramolecular Chemistry. *Coordination Chemistry Reviews* **2019**, *385*, 1–19. <https://doi.org/10.1016/j.ccr.2019.01.005>.
- (139) Kamata, K.; Suzuki, A.; Nakai, Y.; Nakazawa, H. Catalytic Hydrosilylation of Alkenes by Iron Complexes Containing Terpyridine Derivatives as Ancillary Ligands. *Organometallics* **2012**, *31* (10), 3825–3828. <https://doi.org/10.1021/om300279t>.

- (140) Duong, H. A.; Wu, W.; Teo, Y.-Y. Cobalt-Catalyzed Cross-Coupling Reactions of Arylboronic Esters and Aryl Halides. *Organometallics* **2017**, *36* (22), 4363–4366. <https://doi.org/10.1021/acs.organomet.7b00726>.
- (141) Limburg, J.; Vrettos, J. S.; Chen, H.; de Paula, J. C.; Crabtree, R. H.; Brudvig, G. W. Characterization of the O₂-Evolving Reaction Catalyzed by [(Terpy)(H₂O)Mn^{III}(O)₂Mn^{IV}(OH₂)(Terpy)](NO₃)₃ (Terpy = 2,2':6,2''-Terpyridine). *J. Am. Chem. Soc.* **2001**, *123* (3), 423–430. <https://doi.org/10.1021/ja001090a>.
- (142) Winter, A.; Friebe, C.; Chiper, M.; Schubert, U. S.; Presselt, M.; Dietzek, B.; Schmitt, M.; Popp, J. Synthesis, Characterization, and Electro-Optical Properties of Zn^{II} Complexes with π -Conjugated Terpyridine Ligands. *ChemPhysChem* **2009**, *10* (5), 787–798. <https://doi.org/10.1002/cphc.200800714>.
- (143) Ludlow, J. M.; Guo, Z.; Schultz, A.; Sarkar, R.; Moorefield, C. N.; Wesdemiotis, C.; Newkome, G. R. Group 8 Metallomacrocycles – Synthesis, Characterization, and Stability. *Eur. J. Inorg. Chem.* **2015**, *2015* (34), 5662–5668. <https://doi.org/10.1002/ejic.201500971>.
- (144) Breivogel, A.; Kreitner, C.; Heinze, K. Redox and Photochemistry of Bis(Terpyridine)Ruthenium(II) Amino Acids and Their Amide Conjugates – from Understanding to Applications. *Eur. J. Inorg. Chem.* **2014**, *2014* (32), 5468–5490. <https://doi.org/10.1002/ejic.201402466>.
- (145) Ashford, D. L.; Stewart, D. J.; Glasson, C. R.; Binstead, R. A.; Harrison, D. P.; Norris, M. R.; Concepcion, J. J.; Fang, Z.; Templeton, J. L.; Meyer, T. J. An Amide-Linked Chromophore–Catalyst Assembly for Water Oxidation. *Inorg. Chem.* **2012**, *51* (12), 6428–6430. <https://doi.org/10.1021/ic300061u>.
- (146) Wang, W.; Xiao, Z.; Lin, H.; Wang, R.; Zhang, L.; Sun, D. Synthesis, Structure, and Properties of a 3D Porous Zn(II) MOF Constructed from a Terpyridine-Based Ligand. *RSC Adv.* **2016**, *6* (20), 16575–16580. <https://doi.org/10.1039/C5RA27368D>.
- (147) Paul, A.; Ribeiro, A. P. C.; Karmakar, A.; Guedes da Silva, M. F. C.; Pombeiro, A. J. L. A Cu(II) MOF with a Flexible Bifunctionalised Terpyridine as an Efficient Catalyst for the Single-Pot Hydrocarboxylation of Cyclohexane to Carboxylic Acid in Water/Ionic Liquid Medium. *Dalton Trans.* **2016**, *45* (32), 12779–12789. <https://doi.org/10.1039/C6DT01852A>.
- (148) Xiong, Y.; Gao, Y.; Guo, X.; Wang, Y.; Su, X.; Sun, X. Water-Stable Metal–Organic Framework Material with Uncoordinated Terpyridine Site for Selective Th(IV)/Ln(III) Separation. *ACS Sustainable Chem. Eng.* **2019**, *7* (3), 3120–3126. <https://doi.org/10.1021/acssuschemeng.8b04875>.
- (149) Chen, M.; Wang, J.; Liu, D.; Jiang, Z.; Liu, Q.; Wu, T.; Liu, H.; Yu, W.; Yan, J.; Wang, P. Highly Stable Spherical Metallo-Capsule from a Branched Hexapodal Terpyridine and Its Self-Assembled Berry-Type Nanostructure. *J. Am. Chem. Soc.* **2018**, *140* (7), 2555–2561. <https://doi.org/10.1021/jacs.7b10707>.
- (150) Rupp, M.; Auvray, T.; Rousset, E.; Mercier, G. M.; Marvaud, V.; Kurth, D. G.; Hanan, G. S. Photocatalytic Hydrogen Evolution Driven by a Heteroleptic Ruthenium(II) Bis(Terpyridine) Complex. *Inorg. Chem.* **2019**, *58* (14), 9127–9134. <https://doi.org/10.1021/acs.inorgchem.9b00698>.
- (151) Constable, E. C.; Dunphy, E. L.; Housecroft, C. E.; Neuburger, M.; Schaffner, S.; Schaper, F.; Batten, S. R. Expanded Ligands: Bis(2,2':6,2''-Terpyridine Carboxylic Acid)Ruthenium(II) Complexes as Metallosupramolecular Analogues of Dicarboxylic Acids. *Dalton Trans.* **2007**, No. 38, 4323. <https://doi.org/10.1039/b709557k>.
- (152) Toyao, T.; Saito, M.; Dohshi, S.; Mochizuki, K.; Iwata, M.; Higashimura, H.; Horiuchi, Y.; Matsuoka, M. Development of a Ru Complex-Incorporated MOF Photocatalyst for Hydrogen Production under Visible-Light Irradiation. *Chem. Commun.* **2014**, *50* (51), 6779. <https://doi.org/10.1039/c4cc02397h>.
- (153) Zhang, X.-Y.; Xie, C.-F.; Wang, S.-Q.; Cheng, X.-M.; Zhang, Y.; Zhao, Y.; Lu, Y.; Sun, W.-Y. Coordination Polymers with 2,2':6,2''-Terpyridine Earth-Abundant Metal Complex

- Units for Selective CO₂ Photoreduction. *Inorg. Chem.* **2022**, *61* (3), 1590–1596. <https://doi.org/10.1021/acs.inorgchem.1c03348>.
- (154) Ding, Y. Fe-Zr-MOFs and Preparation Method and Application Thereof. CN115505135.
- (155) Purrello, R.; Gurrieri, S.; Lauceri, R. Porphyrin Assemblies as Chemical Sensors. *Coordination Chemistry Reviews* **1999**, *190–192*, 683–706. [https://doi.org/10.1016/S0010-8545\(99\)00106-X](https://doi.org/10.1016/S0010-8545(99)00106-X).
- (156) Rumyantseva, V. D.; Ivanovskaya, N. P.; Konovalenko, L. I.; Tsukanov, S. V.; Mironov, A. F.; Osin, N. S. Synthesis and Spectral Luminescent Characteristics of the Porphyrin Complexes with the Platinum Group Metals. *Russ J Bioorg Chem* **2008**, *34* (2), 239–244. <https://doi.org/10.1134/S1068162008020155>.
- (157) Fang, Y.; Senge, M. O.; Van Caemelbecke, E.; Smith, K. M.; Medforth, C. J.; Zhang, M.; Kadish, K. M. Impact of Substituents and Nonplanarity on Nickel and Copper Porphyrin Electrochemistry: First Observation of a Cu^{II}/Cu^{III} Reaction in Nonaqueous Media. *Inorg. Chem.* **2014**, *53* (19), 10772–10778. <https://doi.org/10.1021/ic502162p>.
- (158) Lin, Z.; Zhang, Z.-M.; Chen, Y.-S.; Lin, W. Highly Efficient Cooperative Catalysis by Co^{III} (Porphyrin) Pairs in Interpenetrating Metal-Organic Frameworks. *Angew. Chem. Int. Ed.* **2016**, *55* (44), 13739–13743. <https://doi.org/10.1002/anie.201605802>.
- (159) Mandal, T.; Das, S.; De Sarkar, S. Nickel(II) Tetraphenylporphyrin as an Efficient Photocatalyst Featuring Visible Light Promoted Dual Redox Activities. *Adv. Synth. Catal.* **2019**, *361* (13), 3200–3209. <https://doi.org/10.1002/adsc.201801737>.
- (160) Wende, H.; Bernien, M.; Luo, J.; Sorg, C.; Ponpandian, N.; Kurde, J.; Miguel, J.; Piantek, M.; Xu, X.; Eckhold, Ph.; Kuch, W.; Baberschke, K.; Panchmatia, P. M.; Sanyal, B.; Oppeneer, P. M.; Eriksson, O. Substrate-Induced Magnetic Ordering and Switching of Iron Porphyrin Molecules. *Nature Mater* **2007**, *6* (7), 516–520. <https://doi.org/10.1038/nmat1932>.
- (161) Oppeneer, P. M.; Panchmatia, P. M.; Sanyal, B.; Eriksson, O.; Ali, Md. E. Nature of the Magnetic Interaction between Fe-Porphyrin Molecules and Ferromagnetic Surfaces. *Progress in Surface Science* **2009**, *84* (1–2), 18–29. <https://doi.org/10.1016/j.progsurf.2008.12.001>.
- (162) Han, Y.; Wu, Y.; Lai, W.; Cao, R. Electrocatalytic Water Oxidation by a Water-Soluble Nickel Porphyrin Complex at Neutral PH with Low Overpotential. *Inorg. Chem.* **2015**, *54* (11), 5604–5613. <https://doi.org/10.1021/acs.inorgchem.5b00924>.
- (163) Liu, S.; Bai, J.; Huo, Y.; Ning, B.; Peng, Y.; Li, S.; Han, D.; Kang, W.; Gao, Z. A Zirconium-Porphyrin MOF-Based Ratiometric Fluorescent Biosensor for Rapid and Ultrasensitive Detection of Chloramphenicol. *Biosensors and Bioelectronics* **2020**, *149*, 111801. <https://doi.org/10.1016/j.bios.2019.111801>.
- (164) Durot, S.; Taesch, J.; Heitz, V. Multiporphyrinic Cages: Architectures and Functions. *Chem. Rev.* **2014**, *114* (17), 8542–8578. <https://doi.org/10.1021/cr400673y>.
- (165) Kawaguchi, M.; Ikeda, A.; Shinkai, S. A Novel Porphyrin–Homooxalix[3]Arene Conjugate Which Creates a C3-Symmetrical Capsular Space. *Tetrahedron Letters* **2001**, *42* (22), 3725–3728. [https://doi.org/10.1016/S0040-4039\(01\)00463-4](https://doi.org/10.1016/S0040-4039(01)00463-4).
- (166) Xue, X.; Lindstrom, A.; Li, Y. Porphyrin-Based Nanomedicines for Cancer Treatment. *Bioconjugate Chem.* **2019**, *30* (6), 1585–1603. <https://doi.org/10.1021/acs.bioconjchem.9b00231>.
- (167) Banfi, S.; Caruso, E.; Buccafurni, L.; Battini, V.; Zazzaron, S.; Barbieri, P.; Orlandi, V. Antibacterial Activity of Tetraaryl-Porphyrin Photosensitizers: An in Vitro Study on Gram Negative and Gram Positive Bacteria. *Journal of Photochemistry and Photobiology B: Biology* **2006**, *85* (1), 28–38. <https://doi.org/10.1016/j.jphotobiol.2006.04.003>.
- (168) Zhou, Y.; Li, H.; Yang, Y.-W. Controlled Drug Delivery Systems Based on Calixarenes. *Chinese Chemical Letters* **2015**, *26* (7), 825–828. <https://doi.org/10.1016/j.ccllet.2015.01.038>.

- (169) Pratiwi, R.; Ibrahim, S.; Tjahjono, D. H. Reactivity and Stability of Metalloporphyrin Complex Formation: DFT and Experimental Study. *Molecules* **2020**, *25* (18), 4221. <https://doi.org/10.3390/molecules25184221>.
- (170) Thies, S.; Bornholdt, C.; Köhler, F.; Sönnichsen, F. D.; Näther, C.; Tuczek, F.; Herges, R. Coordination-Induced Spin Crossover (CISCO) through Axial Bonding of Substituted Pyridines to Nickel-Porphyrins: σ -Donor versus π -Acceptor Effects. *Chem. Eur. J.* **2010**, *16* (33), 10074–10083. <https://doi.org/10.1002/chem.201000603>.
- (171) Gutzeit, F.; Dommaschk, M.; Levin, N.; Buchholz, A.; Schaub, E.; Plass, W.; Näther, C.; Herges, R. Structure and Properties of a Five-Coordinate Nickel(II) Porphyrin. *Inorg. Chem.* **2019**, *58* (19), 12542–12546. <https://doi.org/10.1021/acs.inorgchem.9b00348>.
- (172) Vinogradova, E. V.; Enakieva, Yu. Yu.; Gorbunova, Yu. G.; Tsivadze, A. Yu. Synthesis of Meso-Substituted Porphyrins as Precursors in Creating Highly Ordered Electroluminescent Polymer Materials. *Prot Met Phys Chem Surf* **2009**, *45* (5), 529–534. <https://doi.org/10.1134/S2070205109050050>.
- (173) Nardis, S.; Mandoj, F.; Stefanelli, M.; Paolesse, R. Metal Complexes of Corrole. *Coordination Chemistry Reviews* **2019**, *388*, 360–405. <https://doi.org/10.1016/j.ccr.2019.02.034>.
- (174) Zhu, W.; Huang, T.; Qin, M.; Li, M.; Mack, J.; Liang, X. Tuning the Synthetic Cobalt(III)Corroles Electroreductive Catalyzed Lindane Dehalogenation Reactivity through Meso-Substituents. *Journal of Electroanalytical Chemistry* **2016**, *774*, 58–65. <https://doi.org/10.1016/j.jelechem.2016.05.009>.
- (175) Fang, Y.; Ou, Z.; Kadish, K. M. Electrochemistry of Corroles in Nonaqueous Media. *Chem. Rev.* **2017**, *117* (4), 3377–3419. <https://doi.org/10.1021/acs.chemrev.6b00546>.
- (176) Ganguly, S.; Conradie, J.; Bendix, J.; Gagnon, K. J.; McCormick, L. J.; Ghosh, A. Electronic Structure of Cobalt–Corrole–Pyridine Complexes: Noninnocent Five-Coordinate Co(II) Corrole–Radical States. *J. Phys. Chem. A* **2017**, *121* (50), 9589–9598. <https://doi.org/10.1021/acs.jpca.7b09440>.
- (177) Stergiannakos, T.; Tylianakis, E.; Klontzas, E.; Trikalitis, P. N.; Froudakis, G. E. Hydrogen Storage in Novel Li-Doped Corrole Metal–Organic Frameworks. *J. Phys. Chem. C* **2012**, *116* (15), 8359–8363. <https://doi.org/10.1021/jp210975x>.
- (178) Osterloh, W. R.; Quesneau, V.; Desbois, N.; Brandès, S.; Shan, W.; Blondeau-Patissier, V.; Paolesse, R.; Gros, C. P.; Kadish, K. M. Synthesis and the Effect of Anions on the Spectroscopy and Electrochemistry of Mono(Dimethyl Sulfoxide)-Ligated Cobalt Corroles. *Inorg. Chem.* **2020**, *59* (1), 595–611. <https://doi.org/10.1021/acs.inorgchem.9b02855>.
- (179) Simkhovich, L.; Goldberg, I.; Gross, Z. CCDC 198345: Experimental Crystal Structure Determination, 2003. <https://doi.org/10.5517/CC6ND7G>.
- (180) Koszarna, B.; Gryko, D. T. Efficient Synthesis of Meso-Substituted Corroles in a H₂O–MeOH Mixture. *J. Org. Chem.* **2006**, *71* (10), 3707–3717. <https://doi.org/10.1021/jo060007k>.
- (181) Orłowski, R.; Gryko, D.; Gryko, D. T. Synthesis of Corroles and Their Heteroanalogs. *Chem. Rev.* **2017**, *117* (4), 3102–3137. <https://doi.org/10.1021/acs.chemrev.6b00434>.
- (182) El-Sayed, E.-S. M.; Yuan, D. Metal–Organic Cages (MOCs): From Discrete to Cage-Based Extended Architectures. *Chem. Lett.* **2020**, *49* (1), 28–53. <https://doi.org/10.1246/cl.190731>.
- (183) Feng, D.; Wang, K.; Su, J.; Liu, T.; Park, J.; Wei, Z.; Bosch, M.; Yakovenko, A.; Zou, X.; Zhou, H. A Highly Stable Zeotype Mesoporous Zirconium Metal–Organic Framework with Ultralarge Pores. *Angew. Chem. Int. Ed.* **2015**, *54* (1), 149–154. <https://doi.org/10.1002/anie.201409334>.
- (184) Yu, M.-H.; Liu, X.-T.; Space, B.; Chang, Z.; Bu, X.-H. Metal–Organic Materials with Triazine-Based Ligands: From Structures to Properties and Applications. *Coordination Chemistry Reviews* **2021**, *427*, 213518. <https://doi.org/10.1016/j.ccr.2020.213518>.

- (185) Leenders, S. H. A. M.; Becker, R.; Kumpulainen, T.; de Bruin, B.; Sawada, T.; Kato, T.; Fujita, M.; Reek, J. N. H. Selective Co-Encapsulation Inside an M_6L_4 Cage. *Chem. Eur. J.* **2016**, *22* (43), 15468–15474. <https://doi.org/10.1002/chem.201603017>.
- (186) Demeshko, S.; Dechert, S.; Meyer, F. Anion- π Interactions in a Carousel Copper(II)-Triazine Complex. *J. Am. Chem. Soc.* **2004**, *126* (14), 4508–4509. <https://doi.org/10.1021/ja049458h>.
- (187) Deegan, M. M.; Ahmed, T. S.; Yap, G. P. A.; Bloch, E. D. Structure and Redox Tuning of Gas Adsorption Properties in Calixarene-Supported Fe(II)-Based Porous Cages. *Chem. Sci.* **2020**, *11* (20), 5273–5279. <https://doi.org/10.1039/D0SC01833C>.
- (188) Li, Y.-L.; Alexandrov, E. V.; Yin, Q.; Li, L.; Fang, Z.-B.; Yuan, W.; Proserpio, D. M.; Liu, T.-F. Record Complexity in the Polycatenation of Three Porous Hydrogen-Bonded Organic Frameworks with Stepwise Adsorption Behaviors. *J. Am. Chem. Soc.* **2020**, *142* (15), 7218–7224. <https://doi.org/10.1021/jacs.0c02406>.
- (189) Hashemzadeh, A.; Amini, M. M.; Khavasi, H. R.; Ng, S. W. Ligand Preferences in Ytterbium Ions Complexation with Carboxylate-Based Metal-Organic Frameworks. *Journal of Coordination Chemistry* **2017**, *70* (18), 3217–3232. <https://doi.org/10.1080/00958972.2017.1375098>.
- (190) Zhu, Q.; Shen, C.; Tan, C.; Sheng, T.; Hu, S.; Wu, X. Bright Blue Emissions with Temperature-Dependent Quantum Yields from Microporous Metal-Organic Frameworks. *Chem. Commun.* **2012**, *48* (4), 531–533. <https://doi.org/10.1039/C1CC15138J>.
- (191) Wang, X.; Wang, Z.; Li, J. Effects of a Semi-bio-based Triazine Derivative on Intumescent Flame-retardant Polypropylene. *Polym Adv Technol* **2019**, *30* (5), 1259–1268. <https://doi.org/10.1002/pat.4559>.
- (192) Frontera, A.; Quiñero, D.; Deyà, P. M. Cation- π and Anion- π Interactions: Cation- π and Anion- π Interactions. *WIREs Comput Mol Sci* **2011**, *1* (3), 440–459. <https://doi.org/10.1002/wcms.14>.
- (193) Bag, P. P., Singh, Singha, S., Roymahapatra, G., S. Synthesis of Metal-Organic Frameworks (MOFs) and Their Applications to Biology, Catalysis and Electrochemical Charge Storage: A Mini Review. *Eng. Sci.* **2020**. <https://doi.org/10.30919/es8d1166>.
- (194) Wieser, C.; Dieleman, C. B.; Matt, D. Calixarene and Resorcinarene Ligands in Transition Metal Chemistry. *Coordination Chemistry Reviews* **1997**, *165*, 93–161. [https://doi.org/10.1016/S0010-8545\(97\)90153-3](https://doi.org/10.1016/S0010-8545(97)90153-3).
- (195) Mislin, G.; Graf, E.; Hosseini, M. W.; Bilyk, A.; Hall, A. K.; Harrowfield, J. M.; Skelton, B. W.; White, A. H. Thiacalixarenes as Cluster Keepers: Synthesis and Structural Analysis of a Magnetically Coupled Tetracopper(II) Square. *Chem. Commun.* **1999**, No. 4, 373–374. <https://doi.org/10.1039/a809184f>.
- (196) Kajiwara, T.; Yokozawa, S.; Ito, T.; Iki, N.; Morohashi, N.; Miyano, S. Sulfonylcalix[4]Arene as a Bis-Tridentate Facial Ligand: Syntheses and Structures of Dinuclear Complexes, $[M_2(L)(H_2O)_2(Dmf)_4]$ ($M = Co(II), Ni(II)$; $H_4L = p$ -Tert-butylsulfonylcalix[4]Arene). *Chem. Lett.* **2001**, *30* (1), 6–7. <https://doi.org/10.1246/cl.2001.6>.
- (197) Guo, Q.-L.; Ma, S.-L.; Zhu, W.-X.; Liu, Y.-C.; Zhang, J. Synthesis and Structural Characterization of a Dinuclear Copper(II) Complex With p -Tert-Butylsulfonylcalix[4]Arene. *Chin. J. Chem.* **2005**, *23* (10), 1387–1390. <https://doi.org/10.1002/cjoc.200591387>.
- (198) Dey, Avishek; Dworzak, Michael R.; Bloch, Eric D.; Yap, Glenn P. A. CCDC 2201782: Experimental Crystal Structure Determination. <https://doi.org/10.5517/CCDC.CSD.CC2CX47P>.
- (199) Henke, W.; Kremer, S.; Reinen, D. Copper(2+) in Five-Coordination: A Case of a Pseudo-Jahn-Teller Effect. 1. Structure and Spectroscopy of the Compounds $Cu(Terpy)X_2 \cdot NH_2O$. *Inorg. Chem.* **1983**, *22* (20), 2858–2863. <https://doi.org/10.1021/ic00162a018>.

- (200) Dolomanov, O. V.; Bourhis, L. J.; Gildea, R. J.; Howard, J. A. K.; Puschmann, H. *OLEX2 : A Complete Structure Solution, Refinement and Analysis Program. J Appl Crystallogr* **2009**, *42* (2), 339–341. <https://doi.org/10.1107/S0021889808042726>.
- (201) Spek, A. L. *PLATON SQUEEZE: A Tool for the Calculation of the Disordered Solvent Contribution to the Calculated Structure Factors. Acta Crystallogr C Struct Chem* **2015**, *71* (1), 9–18. <https://doi.org/10.1107/S2053229614024929>.
- (202) Khariushin, I. V.; Ovsyannikov, A. S.; Baudron, S. A.; Ward, J. S.; Kiesilä, A.; Rissanen, K.; Kalenius, E.; Kovalenko, K. A.; Fedin, V. P.; Solovieva, S. E.; Antipin, I. S.; Bulach, V.; Ferlay, S. Selective Gas Adsorption by Calixarene-Based Porous Octahedral M₃₂ Coordination Cages. *Chem. Commun.* **2022**, 58 (98), 13628–13631. <https://doi.org/10.1039/D2CC04510A>.
- (203) Flack, H. D. On Enantiomorph-Polarity Estimation. *Acta Crystallogr A Found Crystallogr* **1983**, *39* (6), 876–881. <https://doi.org/10.1107/S0108767383001762>.
- (204) *Comprehensive Sampling and Sample Preparation: Analytical Techniques for Scientists*; Pawliszyn, J., Ed.; Elsevier: Amsterdam, 2012.
- (205) Kumar, S.; Chawla, S.; Zou, M. C. Calixarenes Based Materials for Gas Sensing Applications: A Review. *J Incl Phenom Macrocycl Chem* **2017**, *88* (3–4), 129–158. <https://doi.org/10.1007/s10847-017-0728-2>.
- (206) Ananchenko, G. S.; Moudrakovski, I. L.; Coleman, A. W.; Ripmeester, J. A. A Channel-Free Soft-Walled Capsular Calixarene Solid for Gas Adsorption. *Angewandte Chemie* **2008**, *120* (30), 5698–5700. <https://doi.org/10.1002/ange.200800071>.
- (207) Du, S.; Yu, T.-Q.; Liao, W.; Hu, C. Structure Modeling, Synthesis and X-Ray Diffraction Determination of an Extra-Large Calixarene-Based Coordination Cage and Its Application in Drug Delivery. *Dalton Trans.* **2015**, 44 (32), 14394–14402. <https://doi.org/10.1039/C5DT01526J>.
- (208) Tan, H.; Du, S.; Bi, Y.; Liao, W. Two Elongated Octahedral Coordination Cages Constructed by M₄-TC4A Secondary Building Units (M = Co^{II} and Fe^{II}) and 2,2'-Bipyridine-4,4'-Dicarboxylic Acids. *Inorg. Chem.* **2014**, *53* (14), 7083–7085. <https://doi.org/10.1021/ic501012e>.
- (209) Wang, S.-M.; Yang, Q.-Y. A Copper-Based Metal-Organic Framework for Upgrading Natural Gas through the Recovery of C₂H₆ and C₃H₈. *Green Chemical Engineering* **2023**, *4* (1), 81–87. <https://doi.org/10.1016/j.gce.2022.04.006>.
- (210) He, Y.-P.; Tan, Y.-X.; Zhang, J. Tuning a Layer to a Pillared-Layer Metal–Organic Framework for Adsorption and Separation of Light Hydrocarbons. *Chem. Commun.* **2013**, 49 (96), 11323. <https://doi.org/10.1039/c3cc47286h>.
- (211) Kentish, S. E.; Scholes, C. A.; Stevens, G. W. Carbon Dioxide Separation through Polymeric Membrane Systems for Flue Gas Applications. *CHENG* **2010**, *1* (1), 52–66. <https://doi.org/10.2174/1874478810801010052>.
- (212) Ravikovitch, P. I.; Neimark, A. V. Density Functional Theory Model of Adsorption on Amorphous and Microporous Silica Materials. *Langmuir* **2006**, *22* (26), 11171–11179. <https://doi.org/10.1021/la0616146>.
- (213) Myers, A. L.; Prausnitz, J. M. Thermodynamics of Mixed-Gas Adsorption. *AIChE J.* **1965**, *11* (1), 121–127. <https://doi.org/10.1002/aic.690110125>.
- (214) Wu, Y.; Liu, Z.; Peng, J.; Wang, X.; Zhou, X.; Li, Z. Enhancing Selective Adsorption in a Robust Pillared-Layer Metal–Organic Framework via Channel Methylation for the Recovery of C₂–C₃ from Natural Gas. *ACS Appl. Mater. Interfaces* **2020**, *12* (46), 51499–51505. <https://doi.org/10.1021/acsmami.0c15267>.
- (215) Gao, S.; Morris, C. G.; Lu, Z.; Yan, Y.; Godfrey, H. G. W.; Murray, C.; Tang, C. C.; Thomas, K. M.; Yang, S.; Schröder, M. Selective Hysteretic Sorption of Light Hydrocarbons in a Flexible Metal–Organic Framework Material. *Chem. Mater.* **2016**, *28* (7), 2331–2340. <https://doi.org/10.1021/acs.chemmater.6b00443>.

- (216) He, Y.; Zhang, Z.; Xiang, S.; Fronczek, F. R.; Krishna, R.; Chen, B. A Robust Doubly Interpenetrated Metal–Organic Framework Constructed from a Novel Aromatic Tricarboxylate for Highly Selective Separation of Small Hydrocarbons. *Chem. Commun.* **2012**, 48 (52), 6493. <https://doi.org/10.1039/c2cc31792c>.
- (217) Sun, X.; Li, X.; Yao, S.; Krishna, R.; Gu, J.; Li, G.; Liu, Y. A Multifunctional Double Walled Zirconium Metal–Organic Framework: High Performance for CO₂ Adsorption and Separation and Detecting Explosives in the Aqueous Phase. *J. Mater. Chem. A* **2020**, 8 (33), 17106–17112. <https://doi.org/10.1039/D0TA04778C>.
- (218) Fan, W.; Wang, Y.; Zhang, Q.; Kirchon, A.; Xiao, Z.; Zhang, L.; Dai, F.; Wang, R.; Sun, D. An Amino-Functionalized Metal–Organic Framework, Based on a Rare Ba₁₂(COO)₁₈(NO₃)₂ Cluster, for Efficient C₃/C₂/C₁ Separation and Preferential Catalytic Performance. *Chem. Eur. J.* **2018**, 24 (9), 2137–2143. <https://doi.org/10.1002/chem.201704629>.
- (219) Fan, W.; Wang, X.; Xu, B.; Wang, Y.; Liu, D.; Zhang, M.; Shang, Y.; Dai, F.; Zhang, L.; Sun, D. Amino-Functionalized MOFs with High Physicochemical Stability for Efficient Gas Storage/Separation, Dye Adsorption and Catalytic Performance. *J. Mater. Chem. A* **2018**, 6 (47), 24486–24495. <https://doi.org/10.1039/C8TA07839D>.
- (220) Chen, C.-X.; Zheng, S.-P.; Wei, Z.-W.; Cao, C.-C.; Wang, H.-P.; Wang, D.; Jiang, J.-J.; Fenske, D.; Su, C.-Y. A Robust Metal–Organic Framework Combining Open Metal Sites and Polar Groups for Methane Purification and CO₂/Fluorocarbon Capture. *Chem. Eur. J.* **2017**, 23 (17), 4060–4064. <https://doi.org/10.1002/chem.201606038>.
- (221) Iki, N.; Kabuto, C.; Fukushima, T.; Kumagai, H.; Takeya, H.; Miyanari, S.; Miyashi, T.; Miyano, S. Synthesis of P-Tert-Butylthiacalix[4]Arene and Its Inclusion Property. *Tetrahedron* **2000**, 56 (11), 1437–1443. [https://doi.org/10.1016/S0040-4020\(00\)00030-2](https://doi.org/10.1016/S0040-4020(00)00030-2).
- (222) Morohashi, N.; Iki, N.; Sugawara, A.; Miyano, S. Selective Oxidation of Thiacalix[4]Arenes to the Sulfinyl and Sulfonyl Counterparts and Their Complexation Abilities toward Metal Ions as Studied by Solvent Extraction. *Tetrahedron* **2001**, 57 (26), 5557–5563. [https://doi.org/10.1016/S0040-4020\(01\)00482-3](https://doi.org/10.1016/S0040-4020(01)00482-3).
- (223) Bodige, S.; MacDonnell, F. M. Synthesis of Free and Ruthenium Coordinated 5,6-Diamino-1,10-Phenanthroline. *Tetrahedron Letters* **1997**, 38 (47), 8159–8160. [https://doi.org/10.1016/S0040-4039\(97\)10223-4](https://doi.org/10.1016/S0040-4039(97)10223-4).
- (224) Stublla, A.; Potvin, P. G. Ruthenium(II) Complexes of Carboxylated Terpyridines and Dipyrzinylypyridines. *Eur. J. Inorg. Chem.* **2010**, 2010 (19), 3040–3050. <https://doi.org/10.1002/ejic.201000122>.

Annexes

Table of content

<u>I. Crystallographic part</u>	249
<u>I.1. Crystallographic data of MOCs</u>	249
<u>I.2. Crystallographic data of metallocalixarenes</u>	256
<u>I.3. Crystallographic data of metal-organic complexes</u>	258
<u>II. Gas adsorption</u>	259
<u>II.1. Isotherms fit by virial equation</u>	259
<u>II.2. Calculations of Henry constants</u>	261
<u>II.3. Calculations of heats of adsorption</u>	261
<u>II.4. Calculations of IAST selectivity of adsorption</u>	262

I. Crystallographic part

I.1. Crystallographic data of MOCs

Structure refinement:

The data collection and reduction were performed using the program CrysAlisPro, with an empirical absorption correction method using spherical harmonics correction and a numerical absorption correction based on gaussian integration over a multifaceted crystal model. The structure was solved with intrinsic phasing (*ShelXT*)¹ and refined by full-matrix least squares on F^2 using the *Olex2* software,²⁰⁰ which uses the *ShelXL-2015* module.² Anisotropic displacement parameters were assigned to non-H atoms. All hydrogen atoms were refined using riding models with $U_{\text{eq}}(\text{H})$ of $1.5U_{\text{eq}}(\text{C})$ for sp^3 hybridized carbons and $U_{\text{eq}}(\text{H})$ of $1.2U_{\text{eq}}(\text{C})$ for sp^2 hybridized carbons.

As a result of supramolecular and highly porous nature, MOCs displayed rapid falloff of the reflection intensities, even with prolonged exposure times using Cu radiation, with no reflections whatsoever observed beyond 0.87\AA resolution. This necessitated moderate modelling using a range of restraints and constraints to account for the geometric (DFIX, DANG, FLAT) and thermal parameters (DELU, SIMU, RIGU, EADP) within parts of the structure, especially when disorder was found to be present as with the racemic $M(L_1)_3$ nodes. The solvents present in MOCs could not be modelled and were accounted using a Solvent Mask generated by the BYPASS or PLATON SQUEEZE modules within *Olex2* software.³

¹ Sheldrick, G. M. *SHELXT* – Integrated Space-Group and Crystal-Structure Determination. *Acta Crystallogr A Found Adv* **2015**, *71* (1), 3–8. <https://doi.org/10.1107/S2053273314026370>.

² Sheldrick, G. M. Crystal Structure Refinement with *SHELXL*. *Acta Crystallogr C Struct Chem* **2015**, *71* (1), 3–8. <https://doi.org/10.1107/S2053229614024218>

³ Dolomanov, O. V.; Bourhis, L. J.; Gildea, R. J.; Howard, J. A. K.; Puschmann, H. *OLEX2*: A Complete Structure Solution, Refinement and Analysis Program. *J Appl Crystallogr* **2009**, *42* (2), 339–341. <https://doi.org/10.1107/S0021889808042726>.



[Co₄SO₂TCA(μ₄-OH₂)₆[rac-Co(L₁)₃]₈				
Formula = C ₆₂₄ H ₅₀₄ Co ₃₂ N ₄₈ O ₁₂₆ S ₂₄			Molecular weight = 13345 Da	
Unit cell parameters				
α	90°	a	37.1152(8) Å	Volume 228095(11) Å ³
β	90°	b	37.1152(8) Å	
γ	120°	c	191.198(3) Å	
Crystal system	trigonal			
Space group	R3c			
T	120.01K			
Wavelength	1.5418 Å			
Crystal size	0.278 x 0.262 x 0.227 mm			
Z	6			
Absorption coefficient	3.228			
F(000)	41040			
Theta range	2.730° – 41.778°			
h,k,l max	42, 31, 195			
h,k,l min	-38, -42, -215			
Reflections collected	378068			
Max. and min. transmission	0.005, 0.053			
Data / restraints / parameters	38980/352/1459			
Goodness-of-fit on F ²	1.162			
Final R indexes I ≥ 2σ (I)	R1 = 0.1365, wR2 = 0.3780			
Final R indexes All data	R1 = 0.1674, wR2 = 0.3467			
Largest diff. peak and hole	1.078 and -0.587 eÅ ⁻³			

[Ni₄SO₂TCA(μ₄-OH₂)₆[rac-Co(L₁)₃]₈				
Formula = C ₆₂₄ H ₅₀₄ Co ₈ Ni ₂₄ N ₄₈ O ₁₂₆ S ₂₄			Molecular weight = 13321 Da	
Unit cell parameters				
α	90°	a	36.9039(4) Å	Volume 224992(5) Å ³
β	90°	b	36.9039(4) Å	
γ	120°	c	190.7619(15) Å	
Crystal system	trigonal			
Space group	R3c			
T	120K			
Wavelength	1.5418 Å			
Crystal size	0.382 x 0.242 x 0.239 mm			
Z	6			
Absorption coefficient	1.567			
F(000)	41184			
Theta range	2.6840, 60.7890			
h, k, l max	41, 40, 155			
h, k, l min	-37, -42, -214			
Reflections collected	356939			
Max. and min. transmission	0.293, 0.688			
Data / restraints / parameters	39074/161/1489			
Goodness-of-fit on F ²	1.096			
Final R indexes I ≥ 2σ (I)	R1 = 0.0778, wR2 = 0.2747			
Final R indexes All data	R1 = 0.0941, wR2 = 0.2573			
Largest diff. peak and hole	0.453 and -0.429 eÅ ⁻³			



[Co₄SO₂TCA(μ₄-OH₂)₆[Δ-Co(L₁)₃]₈				
Formula = C ₆₂₄ H ₅₀₄ Co ₃₂ N ₄₈ O ₁₂₆ S ₂₄			Molecular weight = 13345 Da	
Unit cell parameters				
α	90°	a	37.0736(6) Å	Volume 226898(8) Å ³
β	90°	b	37.0736(6) Å	
γ	120°	c	190.622(3) Å	
Crystal system	trigonal			
Space group	R32			
T	120K			
Wavelength	1.5418 Å			
Crystal size	0.432 x 0.34 x 0.301 mm			
Z	6			
Absorption coefficient	3.245			
F(000)	41040			
Theta range	2.127, 61.168			
h, k, l max	42, 35, 211			
h, k, l min	-40, -41, -216			
Reflections collected	331644			
Data / restraints / parameters	77167/321/2296			
Goodness-of-fit on F ²	0.892			
Final R indexes I ≥ 2σ (I)	R1 = 0.0830, wR2 = 0.2531			
Final R indexes All data	R1 = 0.1476, wR2 = 0.2070			
Largest diff. peak and hole	0.568 and -0.526 eÅ ⁻³			

[Co₄SO₂TCA(μ₄-OH₂)₆[Δ-Co(L₁)₃]₈				
Formula = C ₆₂₄ H ₅₀₄ Co ₃₂ N ₄₈ O ₁₂₆ S ₂₄			Molecular weight = 13345 Da	
Unit cell parameters				
α	90°	a	37.9778(10) Å	Volume 237538(13) Å ³
β	90°	b	37.9778(10) Å	
γ	120°	c	190.170(4) Å	
Crystal system	trigonal			
Space group	R32			
T	120K			
Wavelength	1.5418 Å			
Crystal size	0.376 x 0.344 x 0.236			
Z	6			
Absorption coefficient	3.100			
F(000)	41040			
Theta range	2.7130, 49.7270			
h, k, l max	35, 38, 191			
h, k, l min	-38, -25, -186			
Reflections collected	298743			
Data / restraints / parameters	57138/294/2257			
Goodness-of-fit on F ²	0.985			
Final R indexes I ≥ 2σ (I)	R1 = 0.0873, wR2 = 0.2756			
Final R indexes All data	R1 = 0.1282, wR2 = 0.2420			
Largest diff. peak and hole	0.517 and -0.564 eÅ ⁻³			



[Ni₄SO₂TCA(μ₄-OH₂)₆[Λ-Co(L₁)₃]₈				
Formula = C ₆₂₄ H ₅₀₄ Co ₈ Ni ₂₄ N ₄₈ O ₁₂₆ S ₂₄			Molecular weight = 13321 Da	
Unit cell parameters				
α	90°	a	37.0388(3) Å	Volume 225939(5)Å ³
β	90°	b	37.0388(3) Å	
γ	120°	c	190.1726(19) Å	
Crystal system	trigonal			
Space group	R32			
T	120K			
Wavelength	1.5418 Å			
Crystal size	0.347 x 0.3 x 0.273 mm			
Z	6			
Absorption coefficient	1.561			
F(000)	41184			
Theta range	2.6690, 64.0440			
h, k, l max	32, 42, 216			
h, k, l min	-42, -39, -214			
Reflections collected	290455			
Data / restraints / parameters	77139/384/2274			
Goodness-of-fit on F ²	0.923			
Final R indexes I ≥ 2σ (I)	R1 = 0.0554, wR2 = 0.1492			
Final R indexes All data	R1 = 0.0848, wR2 = 0.1319			
Largest diff. peak and hole	0.513 and -0.447 eÅ ⁻³			

[Ni₄SO₂TCA(μ₄-OH₂)₆[Λ-Co(L₁)₃]₈				
Formula = C ₆₂₄ H ₅₀₄ Co ₈ Ni ₂₄ N ₄₈ O ₁₂₆ S ₂₄			Molecular weight = 13321 Da	
Unit cell parameters				
α	90°	a	36.9578(6) Å	Volume 224892(8)Å ³
β	90°	b	36.9578(6) Å	
γ	120°	c	190.122(2) Å	
Crystal system	trigonal			
Space group	R32			
T	120K			
Wavelength	1.5418 Å			
Crystal size	0.454 x 0.321 x 0.212 mm			
Z	6			
Absorption coefficient	1.568			
F(000)	41184			
Theta range	2.7010, 59.6550			
h, k, l max	37, 41, 215			
h, k, l min	-41, -41, -214			
Reflections collected	309391			
Data / restraints / parameters	76366/109/2270			
Goodness-of-fit on F ²	1.023			
Final R indexes I ≥ 2σ (I)	R1 = 0.0549, wR2 = 0.1680			
Final R indexes All data	R1 = 0.0861, wR2 = 0.1495			
Largest diff. peak and hole	0.424 and -0.451 eÅ ⁻³			



Unit cell parameters of $[\text{Co}_4\text{SO}_2\text{TCA}(\mu_4\text{-OH}_2)]_6[\text{rac-Fe}(\text{L}_1)_3]_8$				
Formula = $\text{C}_{624}\text{H}_{504}\text{Fe}_8\text{Co}_{24}\text{N}_{48}\text{O}_{126}\text{S}_{24}$			Molecular weight = 13321 Da	
α	90°	a	36.9 Å	Volume 226077 Å ³
β	90°	b	36.9 Å	
γ	120°	c	191.2(2) Å	
Crystal system	trigonal			
Space group	R3c			

Unit cell parameters of $[\text{Co}_4\text{SO}_2\text{TCA}]_6[\text{rac-Rh}(\text{L}_1)_3]_8$				
Formula = $\text{C}_{624}\text{H}_{504}\text{Rh}_8\text{Co}_{24}\text{N}_{48}\text{O}_{126}\text{S}_{24}$			Molecular weight = 13698 Da	
α	90°	a	37.4 Å	Volume 232307 Å ³
β	90°	b	37.4 Å	
γ	120°	c	191.4 Å	
Crystal system	trigonal			
Space group	R3c			

$[\text{Ni}_4\text{SO}_2\text{TCA}(\mu_4\text{-OH}_2)]_6[\text{rac-Fe}(\text{L}_1)_3]_8$				
Formula = $\text{C}_{624}\text{H}_{504}\text{Fe}_8\text{Ni}_{24}\text{N}_{48}\text{O}_{126}\text{S}_{24}$			Molecular weight = 13316 Da	
Unit cell parameters				
α	90°	a	37.2723(3) Å	Volume 229719(4) Å ³
β	90°	b	37.2723(3) Å	
γ	120°	c	190.9387(9) Å	
Crystal system	trigonal			
Space group	R3c			
T	120K			
Wavelength	1.5418 Å			
Crystal size	0.419 x 0.28 x 0.17 mm			
Z	6			
Absorption coefficient	1.464			
F(000)	41136			
Theta range	2.6820, 51.7860			
h, k, l max	37, 37, 190			
h, k, l min	-36, -37, -159			
Reflections collected	373451			
Data / restraints / parameters	26769/661/1469			
Goodness-of-fit on F ²	1.314			
Final R indexes I >= 2σ (I)	R1 = 0.1010, wR2 = 0.3494			
Final R indexes All data	R1 = 0.1225, wR2 = 0.3273			
Largest diff. peak and hole	0.609 and -0.498 eÅ ⁻³			



[Ni₄SO₂TCA(μ₄-OH₂)₆[rac-Rh(L₁)₃]₈				
Formula = C ₆₂₄ H ₅₀₄ Rh ₈ Ni ₂₄ N ₄₈ O ₁₂₆ S ₂₄			Molecular weight = 13692 Da	
Unit cell parameters				
α	90°	a	37.2759(3) Å	Volume 230232(4) Å ³
β	90°	b	37.2759(3) Å	
γ	120°	c	191.3281(13) Å	
Crystal system	trigonal			
Space group	R3c			
T	120K			
Wavelength	1.5418 Å			
Crystal size	0.419 x 0.28 x 0.17			
Z	6			
Absorption coefficient	1.550			
F(000)	42048			
Theta range	2.6840, 71.4880			
h, k, l max	38, 43, 227			
h, k, l min	-44, -38, -180			
Reflections collected	252480			
Data / restraints / parameters	45195/561/1469			
Goodness-of-fit on F ²	1.057			
Final R indexes I ≥ 2σ (I)	R1 = 0.0764, wR2 = 0.2813			
Final R indexes All data	R1 = 0.0912, wR2 = 0.2621			
Largest diff. peak and hole	0.679 and -0.546 eÅ ⁻³			

[Co₄SO₂TCA(μ₄-OH₂)₆[L₈]₈				
Formula = C ₄₃₂ H ₃₆₀ Co ₂₄ N ₂₄ O ₁₂₀ S ₂₄			Molecular weight = 9992 Da	
Unit cell parameters				
α	90°	a	33.0404(10) Å	Volume 59041(4) Å ³
β	90°	b	33.0404(10) Å	
γ	90°	c	54.083(2) Å	
Crystal system	tetragonal			
Space group	I 4/m			
T	120K			
Wavelength	1.5418 Å			
Crystal size	0.502 x 0.409 x 0.312 mm			
Z	2			
Absorption coefficient	3.233			
F(000)	10320			
Theta range	2.6730, 55.3560			
h, k, l max	33, 35, 50			
h, k, l min	-25, -35, -57			
Reflections collected	72847			
Data / restraints / parameters	19170/99/733			
Goodness-of-fit on F ²	1.027			
Final R indexes I ≥ 2σ (I)	R1 = 0.0858, wR2 = 0.3117			
Final R indexes All data	R1 = 0.1510, wR2 = 0.2686			
Largest diff. peak and hole	0.544 and -0.292 eÅ ⁻³			



[Ni₄SO₂TCA(μ₄-OH₂)₆[L₈]₈				
Formula = C ₄₃₂ H ₃₆₀ Ni ₂₄ N ₂₄ O ₁₂₀ S ₂₄			Molecular weight = 9986 Da	
Unit cell parameters				
α	90°	a	32.5402(7) Å	Volume 57065(3) Å ³
β	90°	b	32.5402(7) Å	
γ	90°	c	53.8929(13) Å	
Crystal system	tetragonal			
Space group	I 4/m			
T	120K			
Wavelength	1.5418 Å			
Crystal size	0.351 x 0.281 x 0.212			
Z	2			
Absorption coefficient	1.076			
F(000)	10368			
Theta range	1.9520, 73.5070			
h, k, l max	39, 22, 66			
h, k, l min	-40, -40, -67			
Reflections collected	189192			
Data / restraints / parameters	29635/222/733			
Goodness-of-fit on F ²	1.029			
Final R indexes I >= 2σ (I)	R1 = 0.0895, wR2 = 0.2982			
Final R indexes All data	R1 = 0.1144, wR2 = 0.2632			
Largest diff. peak and hole	0.708 and -0.566 eÅ ⁻³			



I.2. Crystallographic data of metallocalixarenes

Structure refinement:

The structures of metallocalixarenes and metal-organic complexes were solved using the program SHELXT-2018.⁴ The refinement and all further calculations were carried out using SHELXL-2018.

The H-atoms were included in calculated positions and treated as riding atoms using SHELXL default parameters.

The non-H atoms were refined anisotropically, using weighted full-matrix least-squares on F².

A semi-empirical absorption correction was applied using SADABS in APEX3; transmission factors: $T_{\min}/T_{\max} = \text{xxxx/yyyy}$.

⁴ Sheldrick, G. M. Crystal Structure Refinement with *SHELXL*. *Acta Crystallogr C Struct Chem* **2015**, *71* (1), 3–8. <https://doi.org/10.1107/S2053229614024218>

Parameter/ Complex	[Co ₂ SO ₂ TCA]• 4DMF	[Cu ₂ SO ₂ TCA]• 4DMF	[Ni ₄ (SO ₂ TCA) ₂]• 4DMF	[Fe ₄ (SO ₂ TCA) ₂]• 4DMF	[Fe ₂ SO ₂ TCA]Cl ₂ • 4DMF	[CoSO ₂ TCA]• 3DMF
Formula	C ₅₂ H ₇₆ Co ₂ N ₄ O ₁₈ S ₄	C ₅₂ H ₇₂ Cu ₂ N ₄ O ₁₆ S ₄	C ₉₂ H ₁₂₄ Ni ₄ N ₄ O ₃₂ S ₈	C ₉₂ H ₁₂₄ Fe ₄ N ₄ O ₁₆ S ₄	C ₅₂ H ₇₂ Cl ₂ Fe ₂ N ₄ O ₁₈ S ₄	C ₄₉ H ₆₅ CoN ₃ O ₁₅ S ₄
Molecular weight	1291 Da	1264 Da	2289 Da	2288 Da	1320 Da	1123 Da
α	77.315(2)	95.758(5)	90	90	90	90
β	80.3770(10)	111.389(4)	106.5540(10)	106.524(2)	96.169(3)	102.991(2)
γ	82.5430(10)	115.093(7)	90	90	90°	90
a	12.2835(4)Å	11.4011(12)Å	13.5274(3)Å	13.5086(5)Å	12.6284(10)Å	18.9762(8)Å
b	12.3441(6)Å	11.8719(12)Å	23.7673(5)Å	23.6785(10)Å	12.4129(8)Å	11.7053(5)Å
c	13.6387(7)Å	13.4331(14)Å	21.1500(4)Å	21.1072(8)Å	22.776(2)Å	25.1624(11)Å
Volume	1979.82(16)Å ³	1461.4(3)Å ³	6518.1(2)Å ³	6472.6(4)Å ³	3549.5(5)Å ³	5446.07Å ³
Crystal system	triclinic	triclinic	monoclinic	monoclinic	monoclinic	monoclinic
Space group	<i>P</i> -1	<i>P</i> -1	<i>P</i> 21/n	<i>P</i> 21/n	<i>P</i> 21/n	<i>P</i> 21/c
T	173K	296.15K	173K	296.15K	296.15K	296.15K
Wavelength	0.71073Å	0.71073Å	0.71073Å	0.71073Å	0.71073Å	0.71073Å
Crystal size	0.120 x 0.120 x 0.100	? x ? x ?	? x ? x ?	? x ? x ?	? x ? x ?	? x ? x ?
Z	1	2	2	4	4	4
Absorption coefficient	0.597	2.306	0.766	0.308	0.687	0.514
F(000)	838	740	2552	2131	1239	2108
Theta range	2.52, 24.90	3.416, 55.764	2.26, 25.93	2.648, 55.292	3.536, 56.096	3.322, 55.146
h, k, l max	14, 16, 17	14, 15, 17	17, 31, 27	17, 30, 27	16, 10, 30	24, 15, 32
h, k, l min	-11, -16, -17	-14, -15, -16	-17, -31, -20	-17, -30, -27	-16, -15, 30	-24, -13, -32
Reflections collected	35715	9148	62823	118050	27832	80086
Data / restraints / parameters	8969/3/471	4942/0/347	15568/21/712	15061/0/655	8476/0/181	12561/0/289
Goodness-of-fit on F ²	1.017	1.528	1.033	2.510	2.347	1.336
Final R indexes I ≥ 2σ (I)	wR2=0.1127 R1=0.0419	wR2= 0.2050 R1= 0.0714	wR2= 0.1750 R1= 0.0620	wR2= 0.3563 R1= 0.1167	wR2=0.3004 R1=0.0962	wR2=0.2101 R1=0.0855
Final R indexes All data	wR2=0.1252 R1= 0.0576	wR2=0.2259 R1= 0.0967	wR2=0.1965 R1= 0.0895	wR2=0.3711 R1=0.1517	wR2=0.3170 R1 =0.1093	wR2= 0.2342 R1= 0.1399
Largest diff. peak and hole	0.386, -0.334	2.798, -0.808	1.761, -1.235	6.140, -0.860	1.800, -1.330	1.030, -0.640



I.3. Crystallographic data of metal-organic complexes

Parameter/Complex	Pd(HL ₁) ₂	[CuHL ₅]Cl ₂
Formula	C ₃₂ H ₂₀ N ₄ O ₄ Pd	C ₂₂ H ₁₅ Cl ₂ CuN ₃ O ₂
Molecular weight	631	488
α	90	111.191(2)
β	97.9740(10)	97.792(2)
γ	90	107.205(2)
a	16.2889(6)Å	11.1018(5)Å
b	6.9627(2)Å	11.1582(4)Å
c	15.0949(5)Å	11.1923(5)Å
Volume	1695.43(10)Å ³	1188.21(9)Å ³
Crystal system	monoclinic	triclinic
Space group	<i>P</i> 21/ <i>c</i>	<i>P</i> -1
T	120K	173K
Wavelength	0.71073Å	0.71073Å
Crystal size	0.220 x 0.120 x 0.100	0.120 x 0.120 x 0.100
Z	2	2
Absorption coefficient	0.605	1.180
F(000)	796	574
Theta range	2.53, 28.73	2.43, 25.52
h, k, l max	22, 9, 20	15, 14, 15
h, k, l min	-22, -9, -20	-15, -11, -15
Reflections collected	80032	58035
Data / restraints / parameters	4394/2/243	6513/0/354
Goodness-of-fit on F ²	1.02	1.06
Final R indexes I >= 2σ (I)	wR2 = 0.0674, R1 = 0.0255	wR2 = 0.1645, R1 = 0.0549
Final R indexes All data	wR2 = 0.0701, R1 = 0.0283	wR2 = 0.1813, R1 = 0.0764
Largest diff. peak and hole	1.017, -0.612	2.295, -0.800



II. Gas adsorption

II.1. Isotherms fit by virial equation

Gas adsorption isotherms at for $[M_4SO_2TCA(\mu_4-OH_2)]_6[rac-Co(L_1)_3]_8$ ($M = Co^{II}, Ni^{II}$) 273K and 298K were fitted by virial equation (Equation 1) in order to calculate Henry constants and isosteric heats of adsorption through use of virial coefficients.

$$\ln p = \ln n + \frac{1}{T} \sum_i A_i \times n^i + \sum_j B_j \times n^j$$

Equation 1 Virial equation

Here, p – is the pressure expressed in Torr; n – is the amount adsorbed in mmol/g; T – temperature in K; A and B - virial coefficients; i and j – number of coefficients required to adequately describe the isotherms.

The virial coefficients in the virial equation for gas adsorption are mathematical parameters that describe the non-ideal behaviour of gases when they are adsorbed onto a solid surface. They are summarized in Table 28.

Gas	Virial coefficients	
	$[Co_4SO_2TCA]_6[rac-Co(L_1)_3]_8$	$[Ni_4SO_2TCA]_6[rac-Co(L_1)_3]_8$
C_2H_2	$A_0 = -3531.3 \pm 36.98$ (1.047%) $A_1 = 248.258 \pm 2.631$ (1.06%) $B_0 = 10.0926 \pm 0.1237$ (1.226%)	$A_0 = -3741.53 \pm 37.08$ (0.9909%) $A_1 = 254.844 \pm 2.505$ (0.9832%) $B_0 = 10.6634 \pm 0.1239$ (1.162%)
C_2H_4	$A_0 = -3298.93 \pm 24.89$ (0.7546%) $A_1 = 337.79 \pm 2.315$ (0.6854%) $B_0 = 9.36013 \pm 0.08321$ (0.8889%)	$A_0 = -3537.13 \pm 22.44$ (0.6344%) $A_1 = 347.085 \pm 2.035$ (0.5864%) $B_0 = 10.0898 \pm 0.07492$ (0.7425%)
C_2H_6	$A_0 = -3450.41 \pm 43.52$ (1.261%) $A_1 = 413.873 \pm 4.241$ (1.025%) $B_0 = 9.38848 \pm 0.1448$ (1.543%)	$A_0 = -3723.56 \pm 29.67$ (0.7967%) $A_1 = 419.06 \pm 2.797$ (0.6674%) $B_0 = 10.2747 \pm 0.09859$ (0.9596%)
CO_2	$A_0 = -3365.16 \pm 42.58$ (1.265%) $A_1 = 191.612 \pm 3.539$ (1.847%) $B_0 = 10.4926 \pm 0.1433$ (1.365%)	$A_0 = -3497.17 \pm 65.48$ (1.872%) $A_1 = 201.389 \pm 5.285$ (2.624%) $B_0 = 10.833 \pm 0.2201$ (2.032%)
CH_4	$A_0 = -1406.62 \pm 43.83$ (3.116%) $A_1 = 222.827 \pm 12.99$ (5.829%) $B_0 = 5.38465 \pm 0.1504$ (2.793%)	$A_0 = -1781.33 \pm 28.14$ (1.58%) $A_1 = 315.761 \pm 8.088$ (2.562%) $B_0 = 6.56696 \pm 0.09607$ (1.463%)
N_2	$A_0 = -839.886 \pm 105.9$ (12.61%) $A_1 = 479.414 \pm 104.1$ (21.72%) $B_0 = 4.70149 \pm 0.3666$ (7.798%)	$A_0 = -868.507 \pm 158.7$ (18.27%) $A_1 = 1322.24 \pm 186.6$ (14.11%) $B_0 = 4.70937 \pm 0.5502$ (11.68%)

Table 28 Virial coefficients A_i and B_j for gas adsorption isotherms at 273K and 298K for $[M_4SO_2TCA(\mu_4-OH_2)]_6[rac-Co(L_1)_3]_8$ ($M = Co^{II}, Ni^{II}$)

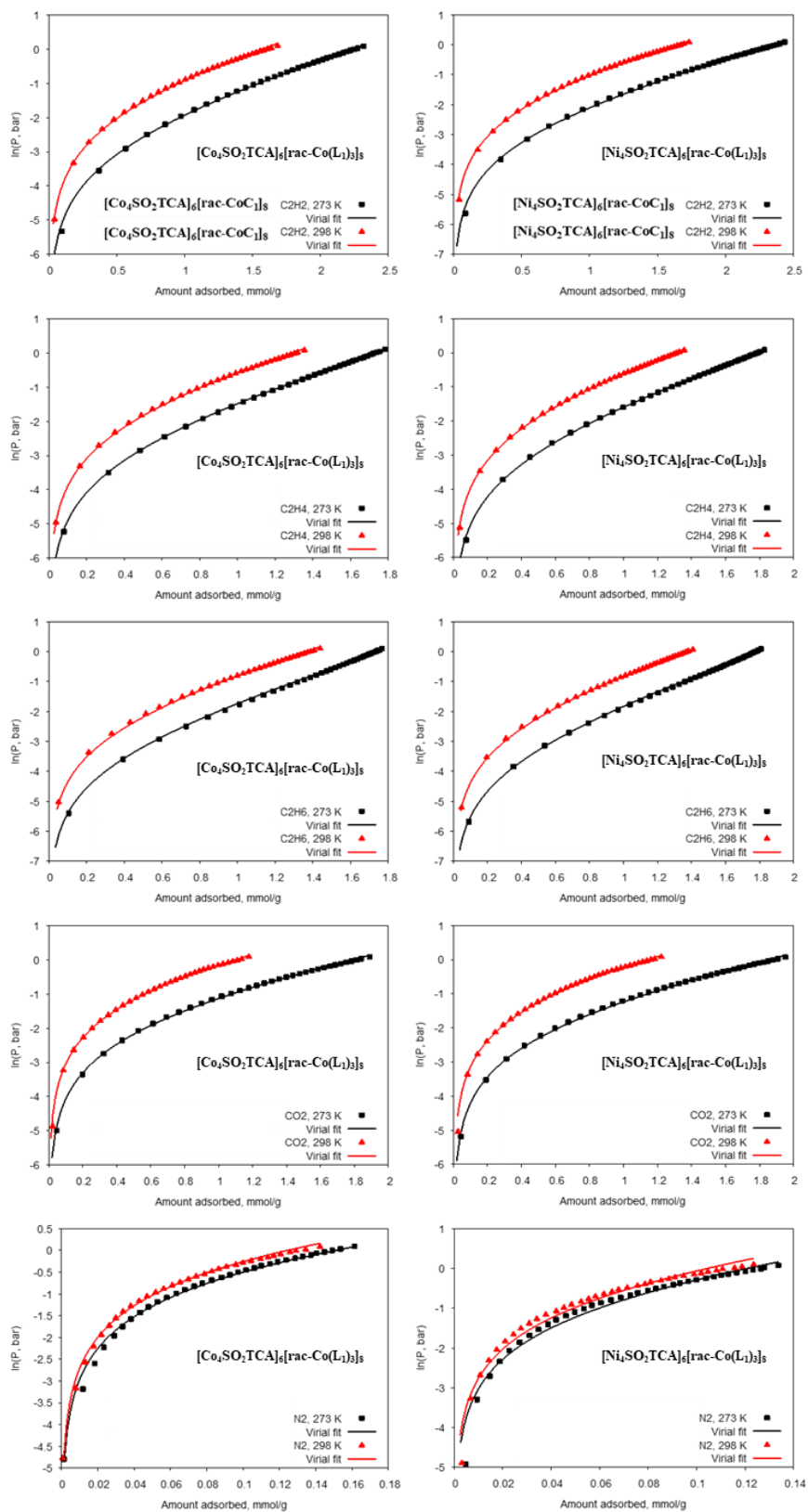


Figure 108 Fits of isotherms of all measured gases by virial equations for $[M_4SO_2TCA(\mu_4-OH_2)_6[rac-Co(L_1)_3]_8$ ($M = Co^{II}, Ni^{II}$)

II.2. Calculations of Henry constants

Henry constants for gas adsorption for $[M_4SO_2TCA(\mu_4-OH_2)]_6[rac-Co(L_1)_3]_8$ ($M = Co^{II}$, Ni^{II}) were calculated using virial coefficients by Equation 2:

$$K_h = \exp \left[\frac{-A_0}{T} - B_0 \right]$$

Equation 2

Here, K_h – Henry constant; T – temperature in K; A_0 and B_0 - virial coefficients

Henry constants for gas adsorption for $[M_4SO_2TCA(\mu_4-OH_2)]_6[rac-Co(L_1)_3]_8$ ($M = Co^{II}$, Ni^{II}) at 273K and 298K are summarized in the Table 29:

Gas/Temperature	273K	298K
$[Co_4SO_2TCA]_6[rac-Co(L_1)_3]_8$		
C ₂ H ₂	17.04	5.76
C ₂ H ₄	15.14	5.50
C ₂ H ₆	25.62	8.88
CO ₂	6.22	2.21
CH ₄	0.79	0.51
N ₂	0.20	0.15
$[Ni_4SO_2TCA]_6[rac-Co(L_1)_3]_8$		
C ₂ H ₂	20.79	6.59
C ₂ H ₄	17.46	5.89
C ₂ H ₆	28.71	9.15
CO ₂	7.17	2.45
CH ₄	0.956	0.553
N ₂	0.217	0.166

Table 29 Henry constants for $[M_4SO_2TCA(\mu_4-OH_2)]_6[rac-Co(L_1)_3]_8$ ($M = Co^{II}$, Ni^{II}) at 273K and 298K in mmol/(g*bar)

II.3. Calculations of heats of adsorption

Isosteric heats of adsorption were calculated using virial coefficients by Equation 3:

$$Q_{st} = -R \times \sum_i A_i \times n^i$$

Equation 3

Here, Q_{st} – coverage-dependent isosteric heat of adsorption; R – universal gas constant; A - virial coefficient; i – number of coefficients required to adequately describe the isotherms.

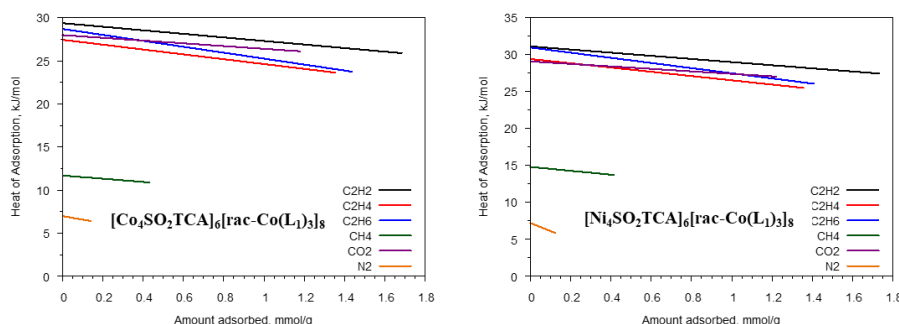


Figure 109 Graphs of isosteric heats of adsorption of all measured gases on $[M_4SO_2TCA(\mu_4-OH_2)]_6[rac-Co(L_1)_3]_8$ ($M = Co^{II}$, Ni^{II})



II.4. Calculations of IAST selectivity of adsorption

Ideal Adsorbed Solution Theory (IAST) calculations were used to estimate selectivity factors at different gas mixture compositions and total pressures. The relationship between P , y_i and x_i (P — the total pressure of the gas phase, y_i — mole fraction of the i -component in gas phase, x_i — mole fraction of the i -component in adsorbed state) is defined according to Equation 4:

$$\int_{p=0}^{p=\frac{Py_1}{x_1}} n_1(p) d \ln p = \int_{p=0}^{p=\frac{Py_2}{x_2}} n_1(p) d \ln p$$

Equation 4

Selectivity factors were calculated according to Equation 5:

$$IAST \text{ selectivity} = \frac{y_2/x_2}{y_1/x_1} = \frac{x_1(1 - y_1)}{y_1(1 - x_1)}$$

Equation 5

Formation de nanocontainers multimétalliques moléculaires

Résumé

Ce projet a permis d'obtenir une nouvelle série originale de 12 cages métallo-organiques (MOCs) octaédriques à base de calixarène. Cette série se compose de deux groupes : (i) 10 MOCs basés sur des connecteurs métalloorganiques de type tris(dipyrrine), et (ii) 2 MOCs basés sur des connecteurs purement organiques de type triazine. Les structures et les caractéristiques de ces MOCs ont été analysées à l'aide de diverses techniques, telles que la Diffraction de RX sur monocristal, l'ATG et la Spectrométrie de masse. Ces cages présentent une porosité significative allant jusqu'à 71%. En outre, les propriétés d'adsorption de gaz de certains de ces MOCs ont été étudiées pour une série de gaz, y compris des hydrocarbures légers. Au cours de ces expériences, les MOCs ont démontré une excellente absorption de gaz (avec une surface BET d'environ 425 m²/g) et une sélectivité d'adsorption de gaz IAST calculée supérieure à celle de nombreux systèmes pour des mélanges de gaz équimolaires, tels que C₂H₆/CH₄. Ces cages présentent donc un grand potentiel pour la conception de systèmes de séparation sélective des gaz. En outre, la structure inhérente des MOCs obtenus leur confèrent des propriétés de reconnaissance potentiellement intéressantes.

Mots-clés : Cages métallo-organiques, Structure DRX, porosité, sélectivité de l'adsorption de gaz.

Résumé en anglais

In this project, a novel series of 12 octahedral calixarene-based metal-organic cages (MOCs) were obtained. This series consists of two groups: (i) 10 MOCs based on tris(dipyrin) metal-organic connectors, and (ii) 2 MOCs based on purely organic triazine connectors. The structures and characteristics of these MOCs were analyzed using various techniques, such as single-crystal XRD, TGA, and MS, and were found to exhibit significant porosity up to 71%. Moreover, the gas adsorption properties of some of these MOCs were investigated for a range of gases, including light hydrocarbons. In these experiments, the MOCs demonstrated excellent gas uptakes (with BET surface area around 425 m²/g) and superior to many systems calculated IAST gas adsorption selectivity towards equimolar gas mixtures, such as C₂H₆/CH₄. Thus, these MOCs exhibit a great potential for the design of selective gas separation systems. Additionally, these MOCs have the potential to be explored for other properties, such as recognition properties, related to their inherent structure.

Keywords: Metal-organic cages, single-crystals XRD, porosity, gas adsorption selectivity